A Monte Carlo Approach to Radiation Hydrodynamics in Stellar Outflows

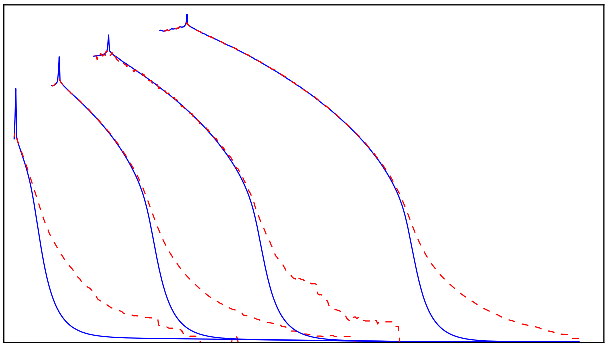

Dissertation

Ulrich M. Nöbauer

TECHNISCHE UNIVERSITÄT MÜNCHEN

MAX-PLANCK-INSTITUT FÜR ASTROPHYSIK

A Monte Carlo Approach to Radiation Hydrodynamics in Stellar Outflows

Ulrich Matthias Nöbauer

Vollständiger Abdruck der von der Fakultät für Physik der Technischen Universität München zur Erlangung des akademischen Grades eines

Doktors der Naturwissenschaften (Dr. rer. nat.)

genehmigten Dissertation.

Vorsitzende(r): Univ.-Prof. Shawn Bishop, Ph.D.

Prüfer der Dissertation:

1. Hon.-Prof. Dr. Wolfgang Hillebrandt
2. Univ.-Prof. Dr. Wilhelm Zwerger

Die Dissertation wurde am 05.06.2014 bei der Technischen Universität München eingereicht und durch die Fakultät für Physik am 29.07.2014 angenommen.

Abstract

A new approach for the numerical solution of radiation hydrodynamical problems in astrophysical environments is introduced. The distinguishing feature is the incorporation of a time-dependent Monte Carlo radiative transfer scheme, which is coupled to a finite-volume fluid dynamical calculation. The accuracy of the resulting method is confirmed in a series of test calculations and its utility for astrophysical studies is demonstrated by investigating the radiation–matter coupling in Type Ia supernovae and in hot-star winds.

Zusammenfassung

In dieser Arbeit wird ein neuer Ansatz zum numerischen Lösen von strahlungshydrodynamischen Problemen in der Astrophysik vorgestellt. Die Methode zeichnet sich durch das Einbinden von zeitabhängigen Monte Carlo Strahlungstransporttechniken aus, die an eine Hydrodynamikrechnung gekoppelt werden. In einer Reihe von Testrechnungen wird die Genauigkeit der entwickelten Methode sichergestellt. Anhand von strahlungshydrodynamischen Untersuchungen in Typ Ia Supernovae und in Winden von heißen Sternen wird die Nützlichkeit der Methode für astrophysikalische Studien demonstriert.

Contents

List of Figures

List of Tables

List of Constants

Physical Constants:[1]

Boltzmann constant	k_{B}	$1.380\,648\,8 \times 10^{-16}\,\mathrm{erg\,K^{-1}}$
elementary charge	e	$4.803\,204\,50 \times 10^{-10}\,\mathrm{statC}$
electron mass	m_e	$9.109\,382\,91 \times 10^{-28}\,\mathrm{g}$
gravitational constant	G	$6.673\,84 \times 10^{-8}\,\mathrm{cm^3\,g^{-1}\,s^{-2}}$
proton mass	m_p	$1.672\,621\,777 \times 10^{-24}\,\mathrm{g}$
Planck constant	h	$6.626\,069\,57 \times 10^{-27}\,\mathrm{erg\,s}$
radiation constant	a_{R}	$7.565\,731 \times 10^{-15}\,\mathrm{erg\,cm^{-3}\,K^{-4}}$
speed of light	c	$2.997\,924\,580 \times 10^{10}\,\mathrm{cm\,s^{-1}}$
Stefan-Boltzmann constant	σ_{R}	$5.670\,373 \times 10^{-5}\,\mathrm{erg\,s^{-1}\,cm^{-2}\,K^{-4}}$
Thomson cross section	σ_{T}	$6.652\,458\,734 \times 10^{-25}\,\mathrm{cm^2}$

Astrophysical Quantities:[2]

solar mass	$M_{\odot}$	$1.989 \times 10^{33}\,\mathrm{g}$
solar radius	$R_{\odot}$	$6.955\,08 \times 10^{10}\,\mathrm{cm}$
solar luminosity	$L_{\odot}$	$3.845 \times 10^{33}\,\mathrm{erg\,s^{-1}}$
solar absolute bolometric magnitude	$m_{\odot}$	4.74

---

[1] CODATA 2010 recommended values (Mohr et al., 2012).

[2] Values taken from Allen's Astrophysical Quantities, 4th Edition (Cox, 2000).

1. Introduction

1.1. Numerical Modelling in Astrophysics

Large-scale computer simulations have emerged as an important contribution to modern astrophysical research[1]. Examples cover a vast range of astrophysics, from calculations concerned with the atmosphere of our own Sun (e.g. Stein & Nordlund, 1998) to simulations exploring the formation of the large-scale structure in the Universe (for example the “Millennium run”, Springel et al. 2005). Since reproducing the conditions prevalent in astrophysical environments in the laboratory is extremely challenging, astronomical research mainly relies on two disciplines complementing each other: gathering insights about the nature of astrophysical objects and systems through direct observations on the one hand, and developing theoretical models for astrophysical phenomena and testing their plausibility on the other hand. Whether a particular theoretical description of an astrophysical phenomenon provides an adequate representation of physical reality is ultimately based on comparisons between the predictions derived from the theoretical model and actual observational data. Due to the high complexity of astrophysical systems, however, the theoretical approach increasingly relies on large numerical simulations to determine the evolution and the structure of these systems.

Given the vast scales of astrophysical objects, modelling efforts typically use the continuity description of the dynamics of many-body systems within the framework of fluid dynamics. To predict the observable appearance of the modelled astrophysical object and enable a comparison with data, the evolution of the electromagnetic radiation field has to be determined. The theory of radiative transfer provides powerful tools for this task. What may appear to be two separate problems at first sight, form in reality a highly coupled system. Due to the interactions with the ambient material, e.g. by radiative heating and cooling processes, the radiation field influences the dynamics of the system. Conversely, dynamical changes in the state of the ambient material affect the way photons propagate through the system. Only in cases where the consequences of these mutual influences are negligible, can fluid dynamics and radiative transfer be treated separately. Once the coupling becomes appreciable, the coevolution of the radiation field and of the ambient material has to be solved. Radiation hydrodynamics constitutes the theoretical foundation for such calculations.

In this work we introduce a new approach to numerically solve the coupled coevolution of the radiation–matter state in astrophysical applications. The key feature of our radiation hydrody-

---

[1] A critical assessment of this development is presented in the essay by Heng (2014).

namical approach is the incorporation of Monte Carlo radiative transfer techniques. Thus, our scheme may benefit from the same advantages that have established the Monte Carlo approach as a very successful technique for pure radiative transfer problems. In particular, the capacity to treat complex interaction physics and the facility to handle arbitrary geometrical configurations render the Monte Carlo technique, and in turn our Monte Carlo-based radiation hydrodynamical approach, very attractive for astrophysical modelling. In the development of our approach, we take particular care to mitigate the major drawback of Monte Carlo methods, namely the introduction of statistical fluctuations. For this, we adopt and improve the volume-based estimator formalism, first proposed by Lucy (1999a). The concern about the effect of stochastic fluctuations, together with the high demand for computational power, which often accompanies Monte Carlo calculations, seems to have restricted the application of the Monte Carlo approach mainly to pure radiative transfer problems in astrophysics. Only recently, has the use of Monte Carlo techniques for radiation hydrodynamical applications been attempted, for example by Haworth & Harries (2012), Noebauer et al. (2012), in which we present a first implementation of our method, and Roth & Kasen (2014).

We conceive our Monte Carlo-based approach as a general-purpose method. For the scope of this work, however, we limit its astrophysical application to the investigation of radiation hydrodynamical processes in Type Ia supernovae and to the study of hot-star winds, as an example for radiatively-driven mass outflows. In the following chapters, we review the theoretical concepts, which are relevant for radiation hydrodynamics, introduce our numerical scheme in detail and present its applications. To emphasise the significance of radiation hydrodynamics in astrophysics and to highlight the need for developing techniques to solve such problems, we briefly survey some astrophysical examples, in which the radiation–matter coupling is dynamically important.

1.2. Radiation Hydrodynamics in Astrophysics

The effect of the radiation field on the dynamical behaviour of an astrophysical system is twofold. Firstly, through interactions with the surrounding fluid material, the radiation may exert an appreciable pressure and affect the momentum balance of the ambient material. Secondly, due to emission and absorption processes, efficient energy transfer between the radiation field and its surroundings may occur. This mechanism affects the total energy budget of the fluid material. In some astrophysical applications only one or the other effect may be important, while in other incarnations of the radiation hydrodynamical coupling, both mechanisms are dynamically important. Some of these astrophysical phenomena are reviewed in the following. Naturally, this list is incomplete and not intended as an exhaustive overview, but as an emphasis of the importance of radiation hydrodynamics and its modelling in astrophysics.

Momentum transfer plays a crucial role and is the dominant dynamical effect in the case radiatively-launched mass outflows. In many cases the accelerating effect derives from the interaction of the radiation field with many atomic line transitions. Such line-driven winds are encountered in hot stars, cataclysmic variables, active galactic nuclei or young stellar objects. A more detailed discussion of this topic follows in Chapter 6, in which we investigate such winds with our radiation hydrodynamical approach.

In the formation process of massive stars, the influence of the radiative pressure is of particular importance. Not only may it power and launch outflows but it also interferes with the mass accretion stream, which feeds the growth of the protostar. The radiative pressure associated with the luminosity of the protostars counteracts the gravitational pull and should interrupt the mass accretion flow for stellar masses that are much below the most massive stars observed (see, for example, Krumholz et al., 2009). A number of effects are proposed that may potentially decrease the efficiency of the radiative feedback on the accretion stream (see, for example, the review by McKee & Ostriker, 2007, and references therein). For example, radiation-driven Rayleigh-Taylor instabilities may facilitate the escape of radiation through the accretion stream. Indeed, recent fully three-dimensional[2] radiation hydrodynamical simulations (Krumholz et al., 2009) indicated that the "[...] radiation pressure does not halt accretion" (from Krumholz et al., 2009).

Rather than momentum transfer, energy exchange is of most dynamical importance in the solar photosphere. Convection in this layer, and thus the granulation pattern visible on the surface of the Sun is driven by radiative heating and cooling effects (see, for example, Nordlund, 1982; Stein & Nordlund, 1998). While the buoyant ascent of parcels of hot gas from below the surface initially proceeds adiabatically, at a certain point radiative losses become appreciable. The temperature drop due to radiative cooling is amplified by the strong temperature dependence of the absorption opacity of the material. Thus, radiative losses increase as the temperature decreases. Once the parcel of gas has cooled, it descends and is heated again by turbulent mixing (see Nordlund, 1982). As a consequence of these processes, detailed (magneto-) radiation hydrodynamical calculations accounting for the radiative heating and cooling processes (e.g. Stein & Nordlund, 1998; Vögler et al., 2005) have to be performed to study convection in the solar photosphere and investigate its visible manifestation, the surface granulation pattern.

In contrast to all of the above examples, both the radiative influences on the momentum and energy balance have to be accounted for in the study of radiation-dominated accretion discs. As demonstrated by Shakura & Sunyaev (1973), the inner regions of accretion discs are supported by radiation pressure whenever they radiate at a significant fraction of the Eddington limit (see also Hirose et al., 2009; Jiang et al., 2013b). However, it was also found that, according to the highly successful model of Shakura & Sunyaev (1973), in which turbulent motion is assumed to be the main source of viscosity, such radiation-dominated discs are thermally unstable (e.g. Shakura & Sunyaev, 1976; Piran, 1978). The instability is caused by variations in the viscous heating rate, which cannot be compensated by the cooling rate, to which radiative processes contribute significantly. Consequently, recent detailed (magneto-)[3] radiation hydrodynamical

---

[2] Necessary to account for the proper growth rate of these instabilities.

[3] Including the magnetic effects is important, since the magneto-rotational instability (Balbus & Hawley, 1991) provides a mechanism to induce turbulence in the disc (see Balbus & Hawley 1991 and discussion in Jiang et al. 2013b).

calculations investigating the thermal stability of radiation dominated discs include both the energy and momentum coupling (see Hirose et al., 2009; Jiang et al., 2013b).

Also in the supernova environment, the second astrophysical system in which we investigate radiation hydrodynamical effects with our approach, both energy and momentum coupling are important. In the case of core-collapse supernovae, a strong radiation-mediated shock wave disrupts the dying star. The region in front of the shock is significantly heated by the radiation field and compressed by the strong radiation pressure (see overview by Mihalas & Mihalas, 1984, §105). Such radiative shocks may also form during a potential interaction of the supernova ejecta with circumstellar material. In Chapter 5, a more detailed discussion of radiation hydrodynamical effects in the supernova field is provided.

This limited survey highlights two important aspects: radiation hydrodynamical processes play a crucial role in a variety of different astrophysical systems and numerical schemes aspiring for a broad applicability should incorporate both the energy and momentum coupling effects. Since we ultimately aim to formulate such a general-purpose strategy for the numerical solution of radiation hydrodynamical problems in astrophysics, we account for the full coupling in our Monte Carlo-based approach.

1.3. Thesis Overview and Structure

The detailed description of our method and its application to supernovae and line-driven winds is structured as follows: in Chapter 2, an introduction to the theoretical concepts of fluid dynamics, radiative transfer and their combination in terms of radiation hydrodynamics is provided. There, we also present a number of solution strategies for radiative transfer problems, which are also used in radiation hydrodynamical calculations. The following part, Chapter 3, is dedicated to an in-depth description of the numerical techniques we use for our Monte Carlo radiation hydrodynamical scheme. In this methodology section, we focus particularly on a detailed introduction of all relevant Monte Carlo techniques. Also, some alternative numerical approaches to radiation hydrodynamics are discussed in this section. An overview of the implementation of these techniques is provided at the end of Chapter 3. In the following part, Chapter 4, we report on the results of the thorough and extensive testing and verification procedure to which our numerical method has been subjected. The first astrophysical applications are described in the following two chapters: in Chapter 5, we present Type Ia supernova-related calculations and in Chapter 6 simulations of radiatively-launched mass outflows are discussed. In particular, we address the radiative influence on the expansion of Type Ia ejecta, apply our method to Type Ia supernova ejecta interacting with circumstellar material and address line-driven hot-star winds. By choosing the stellar winds application and the interacting supernova scenario, we cover both systems in which either momentum exchange or energy transfer constitute the dominant dynamical processes and test the performance of our scheme under these conditions. We summarise our findings in Chapter 7 and provide an outlook on future projects.

2. Theory

The temporal coevolution of the radiation field and the fluid state of the surrounding material is macroscopically captured in the theory of *radiation hydrodynamics*. In the following the basic concepts of this framework are sketched. Since our numerical implementation requires a successive treatment of the fluid state and the radiation field, the theoretical discussion begins with an introduction to the basic hydrodynamical equations governing an ideal fluid, followed by an outline of the main principles of radiative transfer. In the final part of this presentation, the actual radiation hydrodynamical equations are derived, by incorporating the effect of the radiation field in the fluid dynamical equations. This structuring is also loosely based on the organisation of Mihalas & Mihalas (1984), the standard reference for radiation hydrodynamics, featuring an exhausting discussion of this topic in the context of astrophysical applications. We draw extensively on this textbook but also on Chandrasekhar (1960), LeVeque (2002), Castor (2007) and Clarke & Carswell (2007) throughout the following presentation of standard physics. We refer the reader to these textbooks for a rigorous derivation of the concepts and equations. Here, we present the physical motivation for the equations and discus their implications and their relevance with regard to our radiation hydrodynamical scheme. We stress that this only constitutes a repetition of well-known physical concepts and is solely intended to provide an adequate theoretical backdrop for understanding our numerical scheme later on in Chapter 3.

2.1. Restriction to One-Dimensional Geometries

Before presenting the various theoretical concepts of radiation hydrodynamics, we emphasise that solving the full problem poses an ambitious challenge. One reason lies in the high dimensionality of the parameter space. The full radiation hydrodynamical equations contain quantities which depend on the three spatial coordinates, time, frequency and two angles, describing a propagation direction. Fortunately, the complexity of the radiation hydrodynamical calculations may be simplified under certain circumstances. If the investigated systems feature inherent symmetries, which allow the reduction to effectively one-dimensional geometries, the spatial dependence is simplified dramatically. In astrophysical studies, such situations are frequently encountered. The spherical shape of many astrophysical objects favours a treatment of these environments in a spherical coordinate system. If they are additionally symmetric with respect to the radial axis, thus invariant to changes in the two angular coordinates, the geometrical dependence may be converted into a one-dimensional problem. Sometimes, even the reduction to plane-parallel geometries is valid, for example if only a thin outer layer of a spherical object is considered. Since all astrophysical applications we are presenting in the scope of this work feature such symmetries, we restrict the implementation of our radiation hydrodynamical framework to plane-parallel and spherically symmetric problems. However, we emphasise that this step is taken merely to reduce the complexity of the calculations and to facilitate the computational treatment. The adopted simplifications do not represent a shortcoming of the theory or of the developed numerical concepts. In fact, they could be readily applied to the general case. However, the resulting increase in computational and implementation effort is beyond the scope of this work.

In general, the position in one-dimensional configurations is already fully determined by one scalar parameter, x or r, which is measured along the symmetry axis. Any direction relative to the symmetry axis may be specified by the enclosed angle θ. More commonly, the cosine of this angle,

$$\mu = \cos\theta, \tag{2.1}$$

is used for this purpose. The differential operators, gradient and divergence, reduce to

$$\nabla A(\mathbf{x}, t) \rightarrow \begin{cases} \frac{\partial}{\partial x} A(x,t) & \text{plane parallel} \\ \frac{\partial}{\partial r} A(r,t) & \text{spherically symmetric} \end{cases} \tag{2.2}$$

and

$$\nabla \cdot \mathbf{A}(\mathbf{x}, t) \rightarrow \begin{cases} \frac{\partial}{\partial x} A_x(x,t) & \text{plane parallel} \\ \frac{1}{r^2}\frac{\partial}{\partial r} \left(r^2 A_r(r,t)\right) & \text{spherically symmetric} \end{cases} \tag{2.3}$$

respectively. Here, the explicit appearance of the radius in the divergence term accounts for the change in the surface of the spherical shells.

Despite the restriction to one-dimensional configurations in our radiation hydrodynamical framework, we introduce and derive in the following chapters the governing equations in their general form, which applies to arbitrary geometries. For the equations upon which the numerical implementation rests, the one-dimensional correspondents are presented as well.

2.2. Fluid Dynamics

The theory of fluid dynamics is a cornerstone of modelling astrophysical phenomena. Instead of considering the microscopic constituents of astrophysical gases and fluids, the vast length scales on which they are encountered lend themselves to a macroscopic continuum description. In this treatment, the motion of individual particles is not followed, but mean characteristics, such as density, bulk motion and pressure are defined and their macroscopic temporal and spatial variations are considered. Fluid dynamics provides a description of how these properties evolve. One very appealing feature of this approach is that the details of microscopic physics, such as the collisions between matter constituents are excluded from this consideration but are encoded in an *equation of state*. This relation connects the mean characteristics of the fluid with its thermodynamic properties, such as its temperature and internal energy. Thanks to this "outsourcing" of microphysics, a large number of astrophysical environments with vastly different conditions, ranging from the interior of stars, over the interstellar medium (ISM) to entire galaxies, may be described with similar fluid dynamical methods (see Clarke & Carswell, 2007, chap. 1.1).

2.2.1. Fluid Elements

In order to define average quantities, such as the density, a sufficiently large number of individual particles has to be considered. For this purpose, hypothetical control volumes, so-called *fluid elements*, are introduced (see, e.g., Clarke & Carswell, 2007). These fluid elements have to fulfil a number of requirements to be suitable for the averaging process. The spatial extent, l_{elem}, should be small compared to the characteristic length scale, l_{system}, of the investigated system, so that all systematic variations in the mean quantities may be neglected on the level of the fluid element. However, the element must be large enough to encompass a sufficient number of individual particles to minimise statistical fluctuations. Also, it should be large compared to the mean free path λ of the matter constituents with respect to collisions among one another. This additional requirement ensures that the random microscopic motion of the matter particles in the fluid element forms a distribution that maximises entropy for a certain temperature (Clarke & Carswell, 2007). Naturally, this constraint may also be interpreted as a necessary condition for the definition of a temperature. The far-reaching consequence in both cases, however, lies in the ability to construct an equation of state.

To summarise, a fluid or gas with particle number density n, in which fluid elements fulfilling

$$\begin{aligned} l_{\mathrm{system}} \gg l_{\mathrm{elem}} &\gg \lambda, \\ l_{\mathrm{elem}}^3 n &\gg 1. \end{aligned} \tag{2.4}$$

can be defined, may be described by continuous average properties such as density, bulk velocity and pressure. It is worth emphasising that these fluid properties have no explicit dependence on the entirely conceptual fluid elements. Essentially, they only serve as an indicator of whether or not a system may be treated within the framework of collisional fluid dynamics. In the case of a very dilute gas, or of a system investigated on microscopic length scales, this treatment is not possible, as a set of appropriate fluid elements [according to Eq. (2.4)] cannot be defined.

2.2.2. Conservation Laws

Having introduced the definition of mean fluid quantities, such as density ρ, velocity u and total energy e, fluid dynamics addresses the temporal evolution of these properties. The solution to this problem, in the non-relativistic case, is encoded in the three fundamental physical conservation laws, namely of mass, momentum and energy (see, e.g., Clarke & Carswell, 2007). An arbitrary volume[1] V encloses fluid material of mass $\int_V \mathrm{d}V' \rho$. Due to the absence of any processes creating or destroying mass within the control volume, only an imbalance of in- and outflows to this volume changes the enclosed mass. The rate of mass flow through the surface of the control volume is determined by the product of material density and velocity. Consequently, the following equality describing mass conservation within the volume V for the time interval $[t_0, t_1]$ may be formulated:

$$\int_V \mathrm{d}V[\rho(\mathbf{x}, t_1) - \rho(\mathbf{x}, t_0)] = -\int_{t_0}^{t_1} \mathrm{d}t \int_{\partial V} \mathrm{d}\mathbf{S} \cdot \rho(\mathbf{x}, t)\mathbf{u}(\mathbf{x}, t). \tag{2.5}$$

Here, $\mathrm{d}\mathbf{S}$ denotes an infinitesimal surface element and ∂V the surface of the control volume. Replacing the difference on the left hand side by an integral over a partial differential and using the divergence theorem yields

$$\int_{t_0}^{t_1} \mathrm{d}t \int_V \mathrm{d}V \frac{\partial}{\partial t}\rho(\mathbf{x}, t) = -\int_{t_0}^{t_1} \mathrm{d}t \int_V \mathrm{d}V \nabla \cdot \rho(\mathbf{x}, t)\mathbf{u}(\mathbf{x}, t). \tag{2.6}$$

Provided that the fluid quantities are continuous (c.f. LeVeque, 2002, chap. 2), the above formulation of mass conservation, which has to hold for arbitrary control volumes and time intervals, may be expressed as

$$\frac{\partial}{\partial t}\rho(\mathbf{x}, t) + \nabla \cdot [\rho(\mathbf{x}, t)\mathbf{u}(\mathbf{x}, t)] = 0, \tag{2.7}$$

which is commonly referred to as the *continuity equation*. Hyperbolic[2] partial differential equations of this form and in general of[3]

$$\frac{\partial}{\partial t}\mathbf{Q}(\mathbf{x}, t) + \frac{\partial}{\partial x}\mathbf{F}(\mathbf{Q}) = 0 \tag{2.8}$$

are called *conservation laws* with $\mathbf{Q}$ being the vector of the so-called *conserved quantities* and $\mathbf{F}$ being a vector-valued flux function[4]. The conservation form is an important concept. Provided that hyperbolic partial differential equations can be cast in this form, the class of high-resolution finite-volume schemes may be used to construct a numerical solution (see LeVeque, 2002). This family of numerical techniques constitutes a very common and successful strategy in astrophysical fluid dynamical problems and will be adopted here as well. We defer a detailed description of the finite-volume approach to the discussion of the numerical techniques.

---

[1] Unrelated to the control volumes discussed in the context of fluid elements.

[2] Partial differential equations are called hyperbolic if the matrix A in $\frac{\partial}{\partial t}\mathbf{Q} + \mathsf{A}\frac{\partial}{\partial x}\mathbf{Q} = 0$ is diagonalisable and has real eigenvalues (see, for example, LeVeque, 2002, chap. 2.9).

[3] The multidimensional version of this equation involves a flux vector for each spatial dimension (see, for example, Miniati & Colella, 2007, eq. 1).

[4] Strictly speaking, the continuity equation is in conservation form for the quantities density ρ and momentum density $\rho\mathbf{u}$.

2.2.3. Fluid Dynamical Equations

In analogy to deriving the continuity equation from the principle of mass conservation, four additional hyperbolic partial differential equations can be formulated based on momentum and energy conservation. Compared to mass conservation, however, not only in- and outflows have to be considered but also the possibility to induce and remove momentum and energy by exerting an external force, described by the force density $\mathbf{f}$. In addition, the flux function is further complicated by the action of the thermodynamic pressure p. Taking these extra terms into account and including also the continuity equation, the set of gas-dynamic equations reads (see, e.g., Clarke & Carswell, 2007)

$$\frac{\partial}{\partial t}\rho + \nabla \cdot (\rho\,\mathbf{u}) = 0, \tag{2.9}$$

$$\frac{\partial}{\partial t}(\rho\,\mathbf{u}) + \nabla \cdot (\rho\,\mathbf{u} \otimes \mathbf{u}) + \nabla p = \mathbf{f}, \tag{2.10}$$

$$\frac{\partial}{\partial t}(\rho\,e) + \nabla \cdot (\mathbf{u}\rho e + \mathbf{u}p) = \mathbf{u} \cdot \mathbf{f}. \tag{2.11}$$

Here and in the following we drop the explicit dependence of the fluid quantities on time and location for the sake of readability. Nevertheless, all fluid quantities are assumed to be functions of time and position unless explicitly stated otherwise. In the energy equation, the total specific energy e is used, which involves a bulk kinetic contribution and the internal energy density ε

$$e = \frac{1}{2}\mathbf{u} \cdot \mathbf{u} + \frac{\varepsilon}{\rho}. \tag{2.12}$$

In the absence of any external force ($\mathbf{f} = 0$), the set of fluid dynamics equations, as presented by Eqs. (2.9) to (2.11), is in conservation form for the conserved variables density, the components of the momentum density vector $\rho\,\mathbf{u}$ and the total energy density $\rho\,e$ [see Eq. (2.8)]. However, due to the appearance of the thermodynamic pressure, this system is not yet fully determined, but has to be closed by an additional constraint. This is provided by an appropriate equation of state, relating the internal energy density to the thermodynamic pressure. For an ideal gas, the equation of state is given by

$$p = (\gamma - 1)\varepsilon. \tag{2.13}$$

Here, γ denotes the adiabatic index, which is equal to 5/3 for an ideal monoatomic gas.

2.2.4. Eulerian and Lagrangian Reference Frames

The fluid dynamical equations as derived above [see Eqs. (2.9) to (2.11)] are cast in the *Eulerian form*. Here, the spatial coordinate $\mathbf{x}$ identifies a location in a fixed frame, in which the fluid moves with speed $\mathbf{u}$. Consequently, the fluid properties describe a parcel of fluid that currently resides at this location. A different, and in some respects more natural way of describing a fluid, is to consider changes of individual fluid parcels. This amounts to defining a reference frame that is advected, i.e. comoves with the fluid. From a computational point of view, this approach, often termed the *Lagrangian description*, is of considerable merit since a class of numerical schemes featuring excellent advection behaviour is based on this formulation (see, for example, Castor, 2007, chap. 2.4). Fluid dynamics in the Lagrangian frame follows

$$\frac{\mathrm{D}}{\mathrm{D}t}\rho + \rho\nabla\cdot\mathbf{u} = 0, \tag{2.14}$$

$$\rho\frac{\mathrm{D}}{\mathrm{D}t}\mathbf{u} + \nabla p = \mathbf{f}, \tag{2.15}$$

$$\rho\frac{\mathrm{D}}{\mathrm{D}t}e + \nabla\cdot(p\mathbf{u}) = \mathbf{u}\cdot\mathbf{f}, \tag{2.16}$$

with all quantities measured with respect to the fluid parcels[5]. This typically involves introducing a labelling scheme a, for example by assigning each parcel its initial location or in the one dimensional case the enclosed mass. The coordinate location is now a function of this labelling $\mathbf{x}(a,t)$, i.e. on which parcel is considered, and the Lagrangian quantities relate to the corresponding Eulerian fluid properties by

$$q(a,t) = q(\mathbf{x}(a,t)). \tag{2.17}$$

The equations presented above already demonstrate the merit of the Lagrangian description, namely the absence of any advective terms. To avoid confusion with Eulerian time derivatives, the temporal changes in this formulation are denoted with capital letters and are often referred to as *substantial derivatives*. Expressed in the Eulerian frame, the additional advective contribution has to be included (see, e.g., Clarke & Carswell, 2007)

$$\frac{\mathrm{D}}{\mathrm{D}t} = \frac{\partial}{\partial t} + \mathbf{u}\cdot\nabla, \tag{2.18}$$

which accounts for the fluid parcel changing its fixed-frame coordinate position.

2.2.5. Note on Ideal Fluids in Astrophysics

We will conclude this brief overview of basic theoretical concepts of fluid dynamics with a few remarks on the validity of the derived equations. Fluid dynamics as formulated by the equations (2.9) to (2.11) and (2.14) to (2.16) neglects all viscous effects and thus only applies to *ideal fluids*. Using the ideal fluid concept in astrophysical applications is generally warranted by the large dimensions of the involved systems. On these length scales, the viscosity of the fluid material is negligible and its effects outmatched by the inertial terms. For example, for the radiative zone of the sun, the Reynolds number, a characteristic measure of the importance of the inertial with respect to viscous terms, is 3×10^{12} (see Edelmann, 2014). Furthermore, the numerical schemes that are typically used to solve astrophysical fluid dynamics problems introduce an inherent

---

[5] Note that the equations as presented above are not in conservation from. See, for example, Colella & Woodward (1984) for a conservative formulation in one-dimensional problems with respect to the mass coordinate.

numerical viscosity which is usually much larger than the physical one (see, for example, test calculations performed by Edelmann 2014). Those arguments are in favour of solving the fluid dynamical equations for ideal fluids rather than those for real fluids, which include the much more complicated Navier-Stokes equation. Note, that in contrast to common discussions of ideal fluids in terrestrial applications (e.g. Landau & Lifshitz, 1959), the incompressible approximation ($\nabla \cdot \mathbf{u} = 0$) is not used. In astrophysics, supersonic flows, which show a high compressibility compared to subsonic ones, are frequently encountered (Clarke & Carswell, 2007). For this reason, we retain the compressible formulation in our radiation hydrodynamical approach as presented in Sections 2.2.3 and 2.2.4.

2.3. Theory of Radiative Transfer

Often, observing and interpreting the radiation signals from an astrophysical object is the only means of studying its properties. This, however, requires a firm understanding of how the observed radiation is formed and how it interacts with its surroundings – in short how the radiation field propagates and evolves. A macroscopic answer to these questions may be found in the theory of *radiative transfer*, whose essence will be outlined in the following sections. This presentation is tailored to the needs of radiation hydrodynamical calculations and focuses in particular on the concepts that our numerical implementation are based on. More exhaustive summaries of the field of radiative transfer can be found in the standard literature, for example in the text books by Chandrasekhar (1960), Mihalas (1978), Rybicki & Lightman (1979), Mihalas & Mihalas (1984) and Castor (2007) from which the following outline extensively draws.

2.3.1. Specific Intensity

In the theory of radiative transfer, the most fundamental quantity that characterises the radiation field is the *specific intensity.* It is best defined via a parcel of radiative energy (see, e.g., Mihalas & Mihalas, 1984, §63), more specifically by the amount of radiative energy $\mathrm{d}\mathcal{E}$ stored in a pencil beam that in the time $\mathrm{d}t$ passes through the surface $\mathrm{d}\mathbf{S}$ along the propagation direction $\mathbf{n}$ into the solid angle $\mathrm{d}\Omega$ and whose frequency lies in the bin $[\nu, \nu + \mathrm{d}\nu]$

$$\mathrm{d}\mathcal{E} = I(\mathbf{x}, t; \mathbf{n}, \nu)\mathrm{d}\mathbf{S} \cdot \mathbf{n}\, \mathrm{d}t\, \mathrm{d}\nu\, \mathrm{d}\Omega. \tag{2.19}$$

The above definition provides a macroscopic description of the radiation field. However, the characterisation may also be based on the microscopic picture of an ensemble of photons. This ensemble is described by the photon distribution function $f_{\mathrm{R}}(\mathbf{x}, \mathbf{n}, t; \mathbf{n}, \nu)$, denoting the number of photons in a certain phase space volume, in particular the photons at location $\mathbf{x}$ and time t, lying in the frequency interval $[\nu, \nu + \mathrm{d}\nu]$ and propagating along the direction $\mathbf{n}$ into the solid angle $\mathrm{d}\Omega$. The connection between the microscopic and macroscopic picture is achieved via the relation

$$I(\mathbf{x},\mathbf{n},t;\mathbf{n},\nu) = ch\nu f_{\mathrm{R}}(\mathbf{x},\mathbf{n},t;\mathbf{n},\nu), \tag{2.20}$$

which is a direct consequence of each photon carrying the energy $h\nu$ and propagating with the speed of light c. The theory of radiative transfer provides a description of how the radiation field, characterised by the specific intensity, evolves.

2.3.2. Moments of the Specific Intensity

Before turning to the equation which encodes the evolution of the specific intensity, we scrutinise the radiation field further by introducing additional characteristics, such as the radiative energy, its flux and its pressure. These properties prove to be very helpful in quantifying the interaction between the radiation field and the surrounding material in the radiation hydrodynamical formulation.

All of the quantities mentioned above are closely related to the specific intensity and may be derived from its so-called *moments* (see, e.g., Mihalas & Mihalas, 1984, §64 to §66). These are defined by solid angle integrals of the specific intensity weighted by the propagation direction to a certain power. For example, the zeroth-order moment is given by

$$J(\mathbf{x},t;\nu) = \frac{1}{4\pi}\oint \mathrm{d}\Omega\, I(\mathbf{x},t;\mathbf{n},\nu) \tag{2.21}$$

and yields the *mean intensity*. Substituting the photon distribution function [see Eq. (2.20)], reveals the close connection of the mean intensity with the energy density of the radiation field

$$E(\mathbf{x},t;\nu) = h\nu \oint \mathrm{d}\Omega\, f_{\mathrm{R}}(\mathbf{x},t;\mathbf{n},\nu). \tag{2.22}$$

These quantities only differ by a multiplicative factor:

$$E(\mathbf{x},t;\nu) = \frac{4\pi}{c} J(\mathbf{x},t;\nu). \tag{2.23}$$

The components of the radiative flux measure the rate at which radiative energy is streaming through unit surfaces which lie along the corresponding coordinate axis. In the microscopic picture, this may be expressed as

$$\mathbf{F}(\mathbf{x},t;\nu) = ch\nu \oint \mathrm{d}\Omega\, f_{\mathrm{R}}(\mathbf{x},t;\nu)\mathbf{n}. \tag{2.24}$$

Consequently, the radiative flux may be constructed from the first moment of the specific intensity

$$\mathbf{H}(\mathbf{x},t;\nu) = \frac{1}{4\pi}\oint \mathrm{d}\Omega\, I(\mathbf{x},t;\nu)\mathbf{n}, \tag{2.25}$$

using the identity

$$\mathbf{F}(\mathbf{x},t;\nu) = 4\pi\mathbf{H}(\mathbf{x},t;\nu). \tag{2.26}$$

The flux is of particular interest in radiation hydrodynamics as it provides a measure for the momentum content of the radiation field, expressed by the momentum density $\mathcal{G}$. Since each photon of frequency ν propagating along direction $\mathbf{n}$ carries a momentum $h\nu/c\,\mathbf{n}$, the momentum density amounts to

$$\mathcal{G}(\mathbf{x},t;\mathbf{n}) = \frac{1}{c^2}\mathbf{F}(\mathbf{x},t;\mathbf{n}). \tag{2.27}$$

With the momentum of the radiation field established, a radiative pressure may be defined for the photon ensemble, by analogy to a collection of classical particles where it essentially measures the transport of momentum. In particular, the entries of the *radiative pressure tensor* P specify the rates with which the components i of the photon momentum vector are being carried along the coordinate axis j and are given by

$$P^{ij}(\mathbf{x},t;\nu) = \oint \mathrm{d}\Omega\, f_\mathrm{R}(\mathbf{x},t;\mathbf{n},\nu)(h\nu/cn^i)(cn^j). \tag{2.28}$$

Aside from a multiplicative factor, the radiative pressure tensor is equal to the second moment of the specific intensity

$$\mathsf{K}(\mathbf{x},t;\nu) = \frac{1}{4\pi}\oint \mathrm{d}\Omega\, I(\mathbf{x},t;\nu)\mathbf{n}\otimes\mathbf{n}, \tag{2.29}$$

$$\mathsf{P}(\mathbf{x},t;\nu) = \frac{4\pi}{c}\mathsf{K}(\mathbf{x},t;\nu). \tag{2.30}$$

The radiative pressure tensor collapses to a particularly simple shape in the case of an isotropic radiation field, i.e. $I(\mathbf{x},t;\mathbf{n},\nu) \to I(\mathbf{x},t;\nu)$. Here, not only are all off-diagonal elements zero, but also the diagonal entries share the value

$$P^{ii} = \frac{1}{3}E(\mathbf{x},t;\nu). \tag{2.31}$$

This result is commonly used to include the effect of radiation in equations of state (see, for example, Timmes & Arnett, 1999).

All quantities presented here are monochromatic, but frequency-integrated counterparts exist for each of them, for example, the total radiation field energy density

$$E(\mathbf{x},t) = \int_0^\infty \mathrm{d}\nu\, E(\mathbf{x},t;\nu) = c^{-1}\int_0^\infty \mathrm{d}\nu \oint \mathrm{d}\Omega I(\mathbf{x},t;\mathbf{n},\nu). \tag{2.32}$$

To distinguish monochromatic and frequency-integrated quantities, a commonly encountered notation indicates the former by a ν subscript, i.e. $J(\mathbf{x},t;\nu) \to J_\nu(\mathbf{x},t)$.

2.3.3. Radiative Transfer Equation

When propagating through material, the photons interact with their environment, for example by scattering on free electrons, by being absorbed in an atomic line transition or by being destroyed by the process of electron-positron pair creation. All such interaction channels have to be accounted for when formulating the equation governing radiative transfer. Despite the complex microphysics of these interactions, their effects, essentially removing or injecting radiative energy from or into a beam of radiation, may be captured by two material functions, referred to as opacity χ and emissivity ξ (see, e.g., Mihalas & Mihalas, 1984, §72). More precisely, the energy decrease during time $\mathrm{d}t$ in the frequency interval $[\nu, \nu + \mathrm{d}\nu]$ of a beam intersecting a parcel of matter of length $\mathrm{d}s$ in the direction $\mathbf{n}$ perpendicular to the surface element $\mathrm{d}S$ and covering the solid angle $\mathrm{d}\Omega$ is given by the following expression:

$$\mathrm{d}\mathcal{E} = \chi(\mathbf{x}, t; \mathbf{n}, \nu) I(\mathbf{x}, t; \mathbf{n}, \nu) \mathrm{d}S\, \mathrm{d}s\, \mathrm{d}t\, \mathrm{d}\nu\, \mathrm{d}\Omega. \tag{2.33}$$

Correspondingly, the emissivity is defined by the reverse process of increasing the energy in the beam within the material element $\mathrm{d}S\, \mathrm{d}s$ by

$$\mathrm{d}\mathcal{E} = \xi(\mathbf{x}, t; \mathbf{n}, \nu) \mathrm{d}S\, \mathrm{d}s\, \mathrm{d}t\, \mathrm{d}\nu\, \mathrm{d}\Omega. \tag{2.34}$$

Returning to the original definition of the specific intensity [see Eq. (2.19)], the radiative transfer equation may be formulated in terms of conservation of energy. Consider a slab of material on which radiation is impinging (c.f. Mihalas & Mihalas, 1984, §76). The difference between the incident and emergent energy stems from the source and sink terms within the slab, as determined by Eqs. (2.33) and (2.34). This yields the *transfer equation*

$$\left(\frac{1}{c}\frac{\partial}{\partial t} + \frac{\partial}{\partial s}\right) I(\mathbf{x}, t; \mathbf{n}, \nu) = \xi(\mathbf{x}, t; \mathbf{n}, \nu) - \chi(\mathbf{x}, t; \mathbf{n}, \nu) I(\mathbf{x}, t; \mathbf{n}, \nu). \tag{2.35}$$

Here, $\partial/\partial s$ measures changes of the radiation field properties along the propagation direction. In a Cartesian coordinate system, this may be expressed as

$$\frac{\partial}{\partial s} = \mathbf{n} \cdot \nabla. \tag{2.36}$$

In the above discussion, only absorption and emission have been considered. However, scattering interactions may be trivially included, by interpreting these processes as an absorption followed instantaneously by a re-emission event (see, e.g., Mihalas & Mihalas, 1984, §72). Thus, the total opacity consists in general of a true absorption, χ^{abs}, and a scattering component, χ^{scat},

$$\chi(\mathbf{x}, t; \mathbf{n}, \nu) = \chi^{\mathrm{abs}}(\mathbf{x}, t; \mathbf{n}, \nu) + \chi^{\mathrm{scat}}(\mathbf{x}, t; \mathbf{n}, \nu). \tag{2.37}$$

Likewise, the total emissivity involves a contribution from scattering interactions and from true emission processes

$$\xi(\mathbf{x}, t; \mathbf{n}, \nu) = \xi^{\mathrm{true}}(\mathbf{x}, t; \mathbf{n}, \nu) + \xi^{\mathrm{scat}}(\mathbf{x}, t; \mathbf{n}, \nu). \tag{2.38}$$

In general, the material functions are complicated entities which may involve detailed atomic physics deliberations. However, if the radiation field is in *thermal equilibrium* with its surroundings, a simple expression for the emissivity may be derived (see, e.g., Mihalas & Mihalas, 1984, §67, 68 and 72). Under such conditions, the radiation field resembles that of a black body. This means that the specific intensity may be expressed by the *Planck function*, which only depends on the local temperature and the frequency

$$B(T; \nu) = \frac{2h\nu^3}{c^2} \frac{1}{e^{h\nu/k_{\mathrm{B}}T} - 1}. \tag{2.39}$$

This is an immediate consequence of the photon field being governed by the Bose-Einstein statistics. This *thermal* radiation field is perfectly isotropic, implying that both the specific and the mean intensity are equal to the Planck function. Moreover, the frequency-integrated intensity takes a particularly simply form, known as the *Stefan-Boltzmann law*

$$B(T) = \frac{\sigma_{\mathrm{R}}}{\pi} T^4, \tag{2.40}$$

with σ_{R} denoting the Stefan-Boltzmann constant. As the radiation field does not undergo any temporal or spatial variations in thermal equilibrium, the left hand side of the transfer equation [see Eq. (2.35)] vanishes, leading to a direct relation between the emissivity and the equilibrium state of the radiation field

$$\xi^{\mathrm{eq}}(\nu) = \chi(\nu) B(T; \nu). \tag{2.41}$$

The frequency-integrated counterpart of the true emissivity for this case is often referred to as *thermal emission* and is given by

$$\xi^{\mathrm{th}} = \chi \frac{\sigma_{\mathrm{R}}}{\pi} T^4. \tag{2.42}$$

Strictly speaking, all considerations mentioned above are only valid for thermal equilibrium, i.e. for a uniform global temperature T. However, if the temperature varies on scales much larger than the ones set by the photon–matter interactions, i.e. the photon mean path and interaction time scale, the radiation field will adjust itself to the equilibrium state corresponding to the local temperature (see, e.g., Mihalas & Mihalas, 1984, §72). In this case of *local thermodynamic equilibrium* (LTE), the above derivation may still be applied but now with a temperature featuring a spatial, and possibly a temporal, dependence.

2.3.4. Frame Transformations

Calculations involving the radiation field, such as determining the moments of the specific intensity, are significantly simplified if the radiation field is isotropic. This already became apparent during the presentation of the thermal radiation field in the previous section. Consequently, identifying the conditions under which some of the quantities involved in radiative transfer calculations may be treated as isotropic is advantageous. From atomic physics, we learn that most interaction processes may be considered as isotropic in the particular frame of reference in which the interaction partners are at rest (see, e.g., Mihalas & Mihalas, 1984, §72). Moreover, the thermal radiation field may only be expressed in the simple form derived above when measured in this particular frame. However, such a frame defies in general a global definition due to variation in the fluid velocity. Nevertheless, a local construction of a fluid rest frame may be attempted at every location. The result of this approach is often referred to as the local *comoving frame* (CMF) to be clearly distinguishable from the *lab frame* (LF) in which the observer is typically at rest. The concept of the CMF is very important for radiative transfer and radiation hydrodynamics calculations. This refers to a common strategy for the numerical solution of such problems, which employs a so-called *mixed-frame* formulation by defining the spatial and temporal discretisation in the LF but by treating the interaction processes in their natural frame, the CMF. However, to follow this strategy, a set of rules specifying how to relate these two frames and the quantities defined within them have to be found. This section is dedicated to presenting the most important transformation laws with respect to our purposes.

Since photons, as the constituents of the radiation field, are highly relativistic particles, concepts from the theory of special relativity have to be borrowed to derive the desired transformation rules even though the considered fluid velocities still warrant a classical, i.e. non-relativistic, treatment of fluid dynamics (for a relativistic description of fluid dynamics see, for example, Mihalas & Mihalas, 1984). In special relativity, two frames moving with speed $\mathbf{u}$ relative to each other are connected by the Lorentz transformation[6]

$$\mathsf{L} = \begin{pmatrix} \gamma & \gamma\boldsymbol{\beta} \\ -\gamma\boldsymbol{\beta} & \mathbb{I} + (\gamma - 1)\beta^{-2}\boldsymbol{\beta}\otimes\boldsymbol{\beta} \end{pmatrix}, \tag{2.43}$$

introducing the standard parameters of special relativity

$$\boldsymbol{\beta} = \frac{\mathbf{u}}{c}, \tag{2.44}$$

$$\gamma = \frac{1}{\sqrt{1-\beta^2}}. \tag{2.45}$$

Applying the Lorentz transformation [Eq. (2.43)] to the four-vector comprising the photon frequency and its momentum vector

$$M^\alpha = (h\nu/c)(1, \mathbf{n}), \tag{2.46}$$

---

[6] Note that in presenting special relativistic concepts, we adopt the notation of Mihalas & Mihalas (1984). In particular, the Minkowski metric features a −1 in its 00 component.

the well-known expressions for the *Doppler shift* and the *angle aberration*

$$\nu_0 = \nu\gamma(1 - \mathbf{n}\cdot\boldsymbol{\beta}), \tag{2.47}$$

$$\mathbf{n_0} = \frac{\nu}{\nu_0}\left[\mathbf{n} - \gamma\boldsymbol{\beta}\left(1 - \frac{\gamma\mathbf{n}\cdot\boldsymbol{\beta}}{\gamma+1}\right)\right] \tag{2.48}$$

of a photon with frequency ν, which propagates along the direction $\mathbf{n}$ in the LF where the fluid flows with speed $\mathbf{u}$, are obtained (see, e.g., Mihalas & Mihalas, 1984, §89). Here, the zero subscript is introduced to label all quantities which are measured in the CMF, a common convention which is followed throughout this work.

For one-dimensional geometries, the Doppler shift and angle aberration reduce to

$$\nu_0 = \nu\gamma(1 - \beta\mu), \tag{2.49}$$

$$\mu_0 = \frac{\mu - \beta}{1 - \beta\mu}. \tag{2.50}$$

From these expressions, the behaviour of the infinitesimal solid angle element $\mathrm{d}\Omega = \mathrm{d}\phi\mathrm{d}\mu$ and the frequency interval may be derived:

$$\mathrm{d}\nu_0 = \left(\frac{\nu_0}{\nu}\right)\mathrm{d}\nu, \tag{2.51}$$

$$\mathrm{d}\mu_0 = \left(\frac{\nu}{\nu_0}\right)^2\mathrm{d}\mu, \tag{2.52}$$

$$\mathrm{d}\phi_0 = \mathrm{d}\phi. \tag{2.53}$$

With the knowledge of the transformation behaviour of these infinitesimal elements, the transformation laws governing the material functions, the specific intensity and its moments may be obtained. The validity of these expressions may be checked by performing a number of hypothetical photon counting experiments. This approach dates back to Thomas (1930) and is, for example, summarised in Mihalas & Mihalas (1984, §90). The underlying principle is given by the frame invariance of the number of photons passing through a certain surface element. After accounting for the relative motion of the surface element in a different frame and the transformation behaviour of the infinitesimal elements, the following relation between the specific intensity in the CMF and the LF is found

$$I_0(\mu_0, \nu_0) = \left(\frac{\nu_0}{\nu}\right)^3 I(\mu, \nu). \tag{2.54}$$

By analogy, the following laws governing the reference frame transformation of opacity and emissivity may be obtained (e.g. Castor, 1972):

$$\chi_0(\nu_0) = \left(\frac{\nu}{\nu_0}\right)\chi(\mu,\nu), \tag{2.55}$$

$$\eta_0(\nu_0) = \left(\frac{\nu_0}{\nu}\right)^2 \eta(\mu,\nu). \tag{2.56}$$

$$\tag{2.57}$$

Here, we have already incorporated the fact that in the CMF the material functions may be treated as isotropic[7]. The remaining transformation laws, applicable to the frequency-integrated moments of the radiation force, may be found by applying the relations already presented. Specifically, the mean intensity in the CMF is defined (for one-dimensional problems):

$$J_0 = \frac{1}{4\pi}\int_0^\infty \mathrm{d}\nu_0 \int_0^{2\pi} \mathrm{d}\phi_0 \int_{-1}^{1} \mathrm{d}\mu_0 I_0(\mu_0,\nu_0). \tag{2.58}$$

Inserting the transformation laws Eqs. (2.51) to (2.54) and recalling the definition of the moments of the specific intensity, Eqs. (2.21), (2.25) and (2.29), the CMF mean intensity may be expressed in terms of LF quantities as

$$J_0 = \gamma^2(J - 2\beta H + \beta^2 K). \tag{2.59}$$

Accounting for the angle aberration Eq. (2.50), the transformation behaviour for the higher moments may also be found (see, e.g., Mihalas & Mihalas, 1984, §91):

$$H_0 = \gamma^2[H(1+\beta^2) - \beta(J+K)], \tag{2.60}$$

$$K_0 = \gamma^2(K - 2\beta H + \beta^2 J). \tag{2.61}$$

For weakly-relativistic flows, with which we work and in which

$$\begin{aligned} &\beta \ll 1, \\ &\gamma = 1 + \mathcal{O}(\beta^2), \end{aligned} \tag{2.62}$$

these transformation laws for the frequency-integrated moments reduce to the first-order expressions (see, e.g., Castor, 1972):

$$J_0 = J - 2\beta H + \mathcal{O}(\beta^2), \tag{2.63}$$

$$H_0 = H - \beta(J+K) + \mathcal{O}(\beta^2), \tag{2.64}$$

$$K_0 = K - 2\beta H + \mathcal{O}(\beta^2). \tag{2.65}$$

---

[7] Isotropy in the CMF is only an approximation for some processes, for example electron scattering.

This concludes the presentation of the most important reference frame transformation laws between the CMF and the LF. In Appendix A, these rules are summarised together with their inverse counterparts for the one-dimensional case as a quick reference.

2.3.5. Moments of the Transfer Equation

The moments of the transfer equation are obtained by integrating it with respect to the solid angle (see, e.g., Mihalas & Mihalas, 1984, §78). However, we immediately consider the frequency integrated incarnations of these expressions, yielding

$$\frac{\partial}{\partial t}E(\mathbf{x},t) + \nabla \cdot \mathbf{F}(\mathbf{x},t) = \int_0^\infty \mathrm{d}\nu \oint \mathrm{d}\Omega[\xi(\mathbf{x},t;\mathbf{n},\nu) - \chi(\mathbf{x},t;\mathbf{n},\nu)I(\mathbf{x},t;\mathbf{n},\nu)] \tag{2.66}$$

as the zeroth moment. In light of the discussion of physical conservation laws and their formulation as partial differential equations (see Section 2.2.2), the above expression may be interpreted as the conservation of radiative energy. The left hand side comprises the overall temporal change of the radiative energy content and its accumulation due to flux gradients. Any imbalance between these terms must be compensated by the action of source and sink terms, which are captured on the right hand side in terms of opacity and emissivity. Thus, the right hand side of the equation describes how much energy is effectively removed from or added to the radiative pool. Naturally, this net energy increase or decrease is provided at the cost or benefit of the surrounding fluid energy content and therefore constitutes a key quantity for radiation hydrodynamics.

Based on the first moment of the radiative transfer equation, a similar expression may be formulated for the momentum content of the radiation field. Integrating with respect to $\mathrm{d}\Omega\mathbf{n}/4\pi$ and dividing by c results in

$$\frac{1}{c^2}\frac{\partial}{\partial t}\mathbf{F}(\mathbf{x},t) + \nabla \cdot \mathsf{P}(\mathbf{x},t) = \frac{1}{c}\int_0^\infty \mathrm{d}\nu \oint \mathrm{d}\Omega[\xi(\mathbf{x},t;\mathbf{n},\nu) - \chi(\mathbf{x},t;\mathbf{n},\nu)I(\mathbf{x},t;\mathbf{n},\nu)]\mathbf{n}. \tag{2.67}$$

Recalling the definition of the momentum of the radiation field [see Eq. (2.27)] and the interpretation of the pressure tensor as a momentum flux, this relation may be viewed as a formulation of momentum conservation. Again, the source and sink terms on the right hand side capture the amount of momentum transferred between the radiation field and the surrounding fluid material, providing the other key quantity for radiation hydrodynamics.

For the following formulation of the radiation hydrodynamical equations, it is convenient to introduce a new quantity, called the *radiation force* G^α (see, e.g., Mihalas & Mihalas, 1984, §91). The zeroth component of this four-vector encodes the energy transfer between the radiation field and the surrounding material as formulated in Eq. (2.66)

$$G^0(\mathbf{x},t) = -\frac{1}{c}\int_0^\infty \mathrm{d}\nu \oint \mathrm{d}\Omega[\xi(\mathbf{x},t;\mathbf{n},\nu) - \chi(\mathbf{x},t;\mathbf{n},\nu)I(\mathbf{x},t;\mathbf{n},\nu)] \tag{2.68}$$

and the spatial components the momentum transfer terms of Eq. (2.67)

$$\mathbf{G}(\mathbf{x},t) = -\frac{1}{c}\int_0^\infty \mathrm{d}\nu \oint \mathrm{d}\Omega[\xi(\mathbf{x},t;\mathbf{n},\nu) - \chi(\mathbf{x},t;\mathbf{n},\nu)I(\mathbf{x},t;\mathbf{n},\nu)]\mathbf{n}. \tag{2.69}$$

The terminology is motivated by the appearance of these quantities as body force terms in the radiation hydrodynamical equations, which is already reflected in their dimensionality (force density [erg cm^{-4}]). The components of the radiation force translate between the CMF and the LF according to (see, e.g. Mihalas, 2001)

$$G_0^0 = \gamma(G^0 - \boldsymbol{\beta}\cdot\mathbf{G}), \tag{2.70}$$

$$\mathbf{G}_0 = \mathbf{G} - \gamma\left(G^0 - \gamma\frac{\boldsymbol{\beta}\cdot\mathbf{G}}{\gamma+1}\right)\boldsymbol{\beta}. \tag{2.71}$$

For one-dimensional geometries, these simplify to

$$G_0^0 = \gamma(G^0 - \beta G^1), \tag{2.72}$$

$$G_0^1 = \gamma(G^1 - \beta G^0), \tag{2.73}$$

which may be verified with the relations presented in Section 2.3.4. In the CMF, the radiation force terms reduce to a simple form since the material functions are isotropic in this frame. The resulting expressions

$$G_0^0 = \frac{1}{c}\int_0^\infty \mathrm{d}\nu_0[c\chi_0(\nu_0)E_0(\nu_0) - 4\pi\xi_0(\nu_0)], \tag{2.74}$$

$$\mathbf{G}_0 = \frac{1}{c}\int_0^\infty \mathrm{d}\nu_0\chi_0(\nu_0)\mathbf{F}_0(\nu_0), \tag{2.75}$$

are used in determining the momentum and energy transfer terms in our mixed-frame approach to radiation hydrodynamics (see Section 3.4.5).

2.3.6. Solving Radiative Transfer

Before turning to the presentation of the radiation hydrodynamical equations, we briefly comment on solving the pure radiative transfer problem. This is of particular interest, since many of the relevant concepts also apply to the more general problem of radiation hydrodynamics. Here we do not provide an exhaustive overview of the numerous approaches to the problem[8]. Instead, we aim at highlighting the complexity of the general radiative transfer problem and present a few selected solution techniques, introducing general concepts that are relevant for many approaches.

In principle, the state of the radiation field is determined by a partial differential equation for each propagation direction. The complexity of the problem now arises from the angle and frequency redistributing effects of the material functions. In particular, in the case of scattering

---

[8] For a broader review of analytic and numerical solution techniques, see, for example, Castor (2007).

interactions, the corresponding emissivity depends on the complete angle-dependent distribution of the radiation field (see, e.g., Mihalas, 1978, chap. 2-1). Also a strong non-local coupling may be introduced by this type of interaction because radiation may stream freely for a time before scattering. Thus, the region influencing the emissivity at a certain location may not only span all directions but also be quite extended. Formulating a solution to the radiative transfer problem is further complicated by the additional dependence of the material functions on the fluid state, in particular on density and temperature (see, e.g., Mihalas & Mihalas, 1984, §73). Even in pure radiative transfer applications, the effect the radiation field has on these fluid quantities, e.g. in raising the temperature by radiative heating, may not be neglected and introduces a complex feedback cycle. Following this line of argument, one easily appreciates the challenge of solving radiative transfer problems and may recognise that an analytic, and sometimes even a numerical, solution is only found after reducing the complexity. Typical examples for such simplifications, which are also often combined, include considering the steady-state solution, examining the problem in two or one-dimensional geometries or with so-called *grey* (i.e. frequency-independent) material functions or assuming strict LTE conditions.

However, despite these difficulties, a formal solution for the transfer equation may be derived. We briefly present this solution for the steady-state case (c.f. Chandrasekhar, 1960) and refer the reader to the literature, e.g. to Mihalas & Mihalas (1984), for the general, time-dependent formal solution. For stationary problems, the radiative transfer equation may be cast into the following form

$$\frac{1}{\chi_\nu}\frac{\mathrm{d}I_\nu}{\mathrm{d}s} = S_\nu - I_\nu. \tag{2.76}$$

This introduces the *source function* as the ratio of emissivity and opacity

$$S_\nu = \frac{\xi_\nu}{\chi_\nu} \tag{2.77}$$

and the *optical depth*

$$\tau(s, s') = \int_{s'}^{s} \mathrm{d}\tilde{s}\,\chi(\tilde{s}) \tag{2.78}$$

defined between two points s' and s on the radiation beam. Since the opacity may be viewed as the inverse of the mean free photon path, the optical depth measures the average number of interactions a photon would experience along its trajectory. With these definitions, the formal solution to Eq. (2.76) may be expressed as (see, e.g., Chandrasekhar, 1960, chap. 7)

$$I_\nu(s) = I_\nu(0)\mathrm{e}^{-\tau_\nu(s,0)} + \int_0^s \mathrm{d}s' S_\nu(s') e^{\tau_\nu(s,s')}\chi_\nu(s'). \tag{2.79}$$

Clearly, the solution describes the extinction of the initial radiation field at the origin of the beam and the cumulative contribution of the source terms along it. However, it is obvious that this formulation is of little practical use, since the source function is often not known a priori but itself depends on the intensity.

In practice, solutions to the transfer equations are commonly found by approximate methods. For example, the evolution of the radiation field may only be considered on a limited set of rays, which are cast along different propagation directions through the medium. The frequency dependence may be mitigated by only considering a number of frequency intervals, over which the quantities are assumed to be constant. Such techniques are often referred to as methods of *short or long characteristics*, depending on their numerical realisation (see, e.g., Castor, 2007, chap. 11.9).

A prominent example for the long characteristics method, applied to the slab geometry, dates back to Feautrier (1964). Here, the two even and odd combinations of the specific intensity parallel and anti-parallel to a particular ray μ are introduced

$$\begin{aligned} j(\mu) &= \frac{1}{2}[I(\mu) + I(-\mu)], \\ h(\mu) &= \frac{1}{2}[I(\mu) - I(-\mu)]. \end{aligned} \tag{2.80}$$

Assuming isotropy in the material functions, the time-independent transfer equations for these two quantities may be derived from Eq. (2.76)

$$\mu \frac{\mathrm{d}h}{\mathrm{d}\tau} = j - S, \tag{2.81}$$

$$\mu \frac{\mathrm{d}j}{\mathrm{d}\tau} = h. \tag{2.82}$$

These are combined into a single second order ordinary differential equation

$$\mu^2 \frac{\mathrm{d}^2 j}{\mathrm{d}\tau^2} = j - S, \tag{2.83}$$

for which a discrete counterpart may be formulated as (see Castor, 2007, chap. 5.6)

$$\mu_k^2 \frac{j_{i-1,k} - 2j_{i,k} + j_{i+1,k}}{\Delta\tau^2} = j_{i,k} - S_i. \tag{2.84}$$

According to this equation, the stationary radiative transfer problem may be solved along a number of rays $\{\mu_k\}$, which are cast through the computational domain.

In the short characteristics approach (Mihalas et al., 1978; Olson & Kunasz, 1987; Kunasz & Auer, 1988), the rays are not defined with respect to the entire domain, but on the basis of each individual grid cell. At each grid vertex, the values of the material functions are assumed to be directly accessible. From each vertex a bundle of rays is cast through the cells. At the intersection with the adjacent cell interfaces, the rays are terminated and the values for the material functions interpolated from the neighbouring vertices. This basic procedure allows again to advance the radiation field quantities at each grid node. In case some of the material functions are not directly accessible but depend on the radiation field itself, accelerated lambda iteration methods (Cannon, 1973) are often employed to solve the radiative transfer problem (e.g. Davis et al., 2012).

As an alternative to considering the radiative transfer equation itself, its solid angle-integrated moments may be solved instead. In these approaches, a closure relation is necessary to avoid the successive introduction of higher moments. Since the transfer equation involves the spatial gradient term with an explicit dependence on the propagation direction, each moment of the transfer equation always also introduces the next higher moment of the specific intensity, thus never achieving a fully determined system of integro-differential equations. Commonly this hierarchy is terminated after the first moment by introducing a relation between the radiative pressure tensor and the radiative energy. Of course this closure is achieved at the cost of introducing a new variable, the so-called *Eddington tensor* (see, e.g., Castor, 2007, chap. 11.5)

$$\mathsf{f}_\mathrm{E} = \mathsf{P}/E, \tag{2.85}$$

or for one-dimensional problems, the *Eddington factor* (see, e.g., Castor, 2007, chap. 5.4)

$$f_\mathrm{E} = P/E. \tag{2.86}$$

Introducing this new variable, however, has not yet solved the problem. Since its value is not known a priori, it has to be found through iterative procedures or by relying on ad-hoc assumptions. The class of methods using an iterative approach is referred to as variable Eddington factor/tensor approach (VEF/VET) (see, for example, Mihalas 1978, chap. 1.4, Castor 2007, chap. 11.5). The so-called *Eddington approximation* is often employed to avoid the iterative procedure. In this approximation, the radiative pressure and energy are related by the factor 1/3. As already mentioned above, an isotropic radiation field exactly fulfils this relation [see Eq. (2.31)]. Also, in the diffusion approximation, in which the radiation field is expanded with respect to powers of the mean free path χ^{-1} (see, e.g., Castor, 2007, chap. 4.4), the Eddington approximation becomes exact. However, as stressed by Castor (2007, chap. 4.4), working with the resulting diffusion equations constitutes a more serious physical restriction than is imposed by the Eddington approximation itself.

Monte Carlo techniques, which constitute a cornerstone of our approach to radiation hydrodynamics, provide a description of the radiation field through a probabilistic interpretation of the transfer equation (see, e.g., Kalos & Whitlock, 2008, chap. 6). As a substantial part of the following numerics chapter is dedicated to an in-depth description of our Monte Carlo scheme, we defer a discussion of the rationale behind this approach to Section 3.4. For the moment, we stress that it aims at a direct solution of the transfer equation, which conceptually renders a reduction in the complexity level or the need for a closure relation redundant. The limitation of this approach lies rather in the introduction of statistical fluctuations, which have to be controlled.

2.4. Radiation Hydrodynamics

In the last part of this theory review, we merge the concepts presented so far and consider the coevolution of the radiation field and the fluid state. The resulting radiation hydrodynamical equations are the foundation of our numerical approach. Since many of the relevant ideas have already been introduced earlier, this discussion is brief. Moreover, the formulation of the final set of equations governing the evolution of the radiation hydrodynamical state foreshadows our numerical solution approach and thus deviates from commonly encountered presentations, e.g. Mihalas & Mihalas (1984, §93, 94 and 96).

2.4.1. Modified Fluid Dynamical Equations

During the discussion of radiative transfer, the terms specifying the amount of energy and momentum transferred between the radiation field and the surrounding fluid have already been identified as the radiation force components (see Section 2.3.5). Thus, the only remaining task is to include these terms in the fluid energy and momentum balance equations. Here, they act as external source and sink terms and are therefore included as an additional body force. The resulting "extended" fluid equations may be formulated as (see Mihalas & Mihalas, 1984, §94)

$$\rho \frac{\mathrm{D}}{\mathrm{D}t}\mathbf{u} + \nabla p = \mathbf{f} + \mathbf{G} - \frac{\mathbf{u}}{c} G^0, \tag{2.87}$$

$$\rho \frac{\mathrm{D}}{\mathrm{D}t} e + \nabla \cdot (\mathbf{u} p) = \mathbf{u} \cdot \mathbf{f} + c G^0. \tag{2.88}$$

Despite using the so-called *pseudo Lagrangian* notation by employing the substantial derivative, the dependent quantities are still defined in the Eulerian frame. Also, we have retained the effect of a general body force $\mathbf{f}$, since some of the applications discussed later in this thesis require the inclusion of an external gravitational field, which may be interpreted as an external source term of this type. It is important to note that these equations are only correct to $\mathcal{O}(u/c)$. The relativistically correct covariant formulation of the radiation hydrodynamical equations may be found, for example, in Mihalas & Mihalas (1984, §94). There, the authors also point out that on the fluid flow time scale the last term on the right hand side of the momentum equation is always at maximum of order $\mathcal{O}(u/c)$ compared to $\mathbf{G}$. Consequently, we neglect this term, since for all applications that we address it may be assumed that $u \ll c$.

2.4.2. Radiation Hydrodynamical Equations

The equations presented above only describe the evolution of the fluid energy and momentum in the presence of a radiation field. To obtain a full set of equations, we recall that the equation of mass conservation is unaffected by the radiation field and that the strength of the radiation force may be calculated according to the right hand sides of the radiative energy and momentum equations [see Eqs. (2.68) and (2.69)] once the evolution of the radiation field is established. By including the radiative transfer equation and an appropriate equation of state[9] to relate thermodynamic pressure and fluid internal energy, an appropriate set of radiation hydrodynamical equations is found:

$$p = \frac{1}{\gamma - 1}\left(\frac{e}{\rho} - \frac{1}{2}\mathbf{u}\cdot\mathbf{u}\right), \tag{2.89}$$

$$\frac{\mathrm{D}}{\mathrm{D}t}\rho + \rho\nabla\cdot\mathbf{u} = 0, \tag{2.90}$$

$$\rho\frac{\mathrm{D}}{\mathrm{D}t}\mathbf{u} + \nabla p = \mathbf{f} + \mathbf{G}, \tag{2.91}$$

$$\rho\frac{\mathrm{D}}{\mathrm{D}t}e + \nabla\cdot(\mathbf{u}p) = \mathbf{u}\cdot\mathbf{f} + cG^0, \tag{2.92}$$

$$\left(\frac{1}{c}\frac{\partial}{\partial t} + \mathbf{n}\cdot\nabla\right) I = \xi - \chi I, \tag{2.93}$$

$$G^0 = \frac{1}{c}\int_0^\infty \mathrm{d}\nu \oint \mathrm{d}\Omega(\chi I - \xi), \tag{2.94}$$

$$\mathbf{G} = \frac{1}{c}\int_0^\infty \mathrm{d}\nu \oint \mathrm{d}\Omega(\chi I - \xi)\mathbf{n}. \tag{2.95}$$

The additional contribution to the momentum equation has already been neglected here [compare Eq. (2.87) and Eq. (2.91)]. As mentioned at the outset of this section, the system differs from that commonly found in the literature: often, the zeroth and first moment of the transfer equation are listed together with an appropriate closure (see discussion in Mihalas & Mihalas, 1984, chap. 7.3). However, we have already stated that the Monte Carlo technique offers a direct solution to the radiative transfer problem, thus releasing us from the need to follow the moments approach or a comparable scheme. Within the scope of this work, only one-dimensional radiation hydrodynamical problems are addressed. For this purpose, the one-dimensional counterparts of the radiation hydrodynamical equations are listed in Appendix B for completeness.

---

[9] For all applications discussed in the scope of this work, the ideal gas description is sufficient.

3. Numerics

The complexity of the radiation hydrodynamical equations inhibits the formulation of an analytic solution for most practical applications. Instead, a numerical approach has to be pursued. There is no universal scheme for this task, but a variety of different techniques exists, each with its own benefits and drawbacks. However, independent of the accepted numerical approach, approximations have to be adopted and errors are inevitably introduced. Thus, it is essential to identify the appropriate numerical technique which excels in the physical regime of interest and which introduces errors within acceptable limits. This definition is intentionally vague since these criteria vary from application to application.

We have developed a new approach to radiation hydrodynamics in astrophysical environments, specifically designed for mass-outflow problems, which couples a Monte Carlo radiative transfer method with a finite-volume fluid dynamical scheme by means of operator splitting. This chapter is dedicated to an in-depth description of our approach and the numerical techniques involved. In particular, all technical terms which have been used above to characterise our approach are systematically introduced and explained in this chapter. We begin with a (limited) overview of different solution techniques for radiation hydrodynamics and of how our approach relates to them. Afterwards, we introduce the operator-splitting concept, which separates the radiation hydrodynamics problem into a series of subproblems. The rest of the chapter deals with the techniques we employ to solve these subproblems, namely the finite-volume approach for fluid dynamics and the Monte Carlo approach to radiative transfer. Part of this description may be found in abbreviated from in Noebauer et al. (2012), in which the principle methodology of our approach is outlined.

3.1. Overview of Radiation Hydrodynamical Approaches

In astrophysical modelling, a number of different techniques are employed to address radiation hydrodynamical problems. For example, Blinnikov & Bartunov (1993) and Blinnikov & Sorokina (2000) developed a fully implicit numerical solution to the radiation hydrodynamics equations and have applied the resulting astrophysical one-dimensional code Stella very successfully in the field of supernova studies, in particular to shock breakouts in Type II explosions (e.g. Blinnikov et al., 2000) and to ejecta–circumstellar material interactions (e.g. Chugai et al., 2004b). The implicit approach to radiation hydrodynamics has the advantage of providing stable results even under circumstances in which the radiation hydrodynamical state changes rapidly (see discussion in Section 3.2.5). However, the numerical realisation of the implicit time stepping is quite complex and requires comparatively high computational effort (see discussion in Section 3.2.1). These costs may even prohibit a fully three-dimensional and frequency-dependent treatment of radiation hydrodynamics. Other strategies follow an explicit time-marching scheme, which is conceptually simpler and often also computationally cheaper than the implicit approach. Here, radiation hydrodynamics is typically broken down into a series of subproblems consisting of a separate treatment of fluid dynamics, radiative transfer and their influence on each other. The benefit of this technique lies in the ability to access the vast pool of standard numerical methods available to address the first two subproblems. For example, the (magneto-) radiation hydrodynamical code ZEUS[1] couples a flux-limited diffusion scheme, which includes a variable Eddington tensor (Stone et al., 1992; Turner & Stone, 2001; Hayes & Norman, 2003; Hayes et al., 2006), with a finite-differencing fluid dynamical method (see Stone & Norman, 1992, for the description of the module solving two-dimensional fluid dynamics). Its successor, the state-of-the-art multi-purpose finite-volume magneto-hydrodynamics code ATHENA[2] (Stone et al., 2008) also contains, in its most recent implementation (Jiang et al., 2012), a radiative transfer module. It is based on a short characteristics VET approach (Davis et al., 2012) and has been used within the ATHENA framework to study radiation-dominated discs (Jiang et al., 2013b). This listing is by no means complete but already reflects the diversity of numerical techniques used to solve radiation hydrodynamics. We propose a new approach, which also relies on the separation into the subproblems of fluid dynamics and radiative transfer. The novelty of our method lies in the incorporation of Monte Carlo radiative transfer methods.

With regard to the solution of the radiative transfer equations, the Monte Carlo approach follows an entirely different strategy than all the techniques mentioned before. Instead of discretising the relevant equations on a computational grid and addressing their discrete representation (see discussion on numerical grids in Section 3.2.1), the evolution of the radiation field is solved by tracking the propagation history of a large number of test particles. There is a long history of harnessing Monte Carlo techniques to solve various transport problems. In particular, in the reactor physics community, this probabilistic approach is widely used for the treatment of neutron transport (see, for example, the book by Dupree & Fraley, 2002). Widespread use of the Monte Carlo radiative transfer technique has been inhibited in the past by its high demand for computational power. However, with the increasing availability of computational resources this factor has become a less important concern. Together with seminal works by Fleck & Cummings (1971); Abbott & Lucy (1985) and Lucy (1999a), this has led to an increasing number of highly successful applications of the Monte Carlo approach in astrophysical radiative transfer problems, for example time-dependent, three-dimensional, multi-frequency spectral-synthesis calculations for Type Ia supernova explosions (e.g. Kasen et al., 2006; Kromer & Sim, 2009).

---

[1] The original `Fortran` version of this code may be obtained at `http://www.astro.princeton.edu/~jstone/zeus.html`.

[2] The magneto-hydrodynamical modules are publicly available at `https://trac.princeton.edu/Athena/`

In general, Monte Carlo techniques excel in the treatment of problems with arbitrary three-dimensional geometries and in cases which require the inclusion of complex interaction physics, in particular scattering interactions (see also discussion in, e.g., House & Avery, 1968; Roth & Kasen, 2014). These properties render the Monte Carlo approach very compelling since one or both features often may not be realised within the deterministic techniques outlined above. For example, multidimensional problems are difficult to address with fully implicit radiation hydrodynamical schemes, such as Stella, because the involved matrices become very large and computationally challenging. Moreover, incorporating scattering interactions is still challenging for radiative transfer schemes which are based on the characteristics approach. However, recent progress has been achieved on this field, for example by Hayek et al. (2010) and Davis et al. (2012). Naturally, using the Monte Carlo approach offers not only advantages. The benefits come at the cost of introducing statistical fluctuations, a downside which is caused by the finite number of statistical samples. The magnitude of the fluctuations may be mitigated by investing a higher computational effort to increase the sample size, a strategy which is obviously limited by the available computational resources. Undeniably, these disadvantages of statistical noise and of high demand for computation power have inhibited the use of Monte Carlo techniques in the radiation hydrodynamical context, despite their success in pure radiative transfer applications.

Despite these concerns, the benefits of the Monte Carlo approach clearly warrant investigating the feasibility of incorporating this technique into radiation hydrodynamical calculations. Consequently, we have devised a radiation hydrodynamical scheme which relies as one cornerstone on a Monte Carlo method and intends to retain the advantageous properties of this radiative transfer approach in the solution of the radiation–matter coevolution. Astrophysical problems such as the interaction of a supernova ejecta with a fractal circumstellar material or the emergence of a clumpy wind from hot stars or accretion discs due to radiative processes support this strategy. A detailed study of these problems requires including detailed microphysics and treating complex geometrical configurations. In our radiation hydrodynamical approach, we incorporate the full coupling between the radiative and gas energy and momentum pools. This prominent feature sets us apart from earlier studies of Monte Carlo radiation hydrodynamical techniques (Nayakshin et al., 2009; Acreman et al., 2010; Haworth & Harries, 2012). There, simplified treatments of the radiation–matter coevolution are adopted, which are appropriate for the astrophysical environments under investigation. For example, Nayakshin et al. (2009) mainly focus on the momentum coupling when interfacing a Monte Carlo method with a cosmological smoothed particle hydrodynamics (SPH, see Gingold & Monaghan 1977; Lucy 1977; Monaghan 1992) code. Another example of a Monte Carlo-SPH approach is presented by Acreman et al. (2010). Here, the Monte Carlo radiative transfer code Torus (Harries, 2000, 2011) is used in conjunction with a SPH method to study circumstellar discs. The radiation–matter coupling is realised by only updating the fluid temperature according to the heating and cooling terms determined in the radiative transfer calculation. Also Haworth & Harries (2012) neglect the momentum coupling when incorporating a Monte Carlo photoionisation calculation into a fluid dynamical method to investigate triggered star formation. Here, the radiation–matter coevolution is realised by adjusting the gas temperature according to the ion fractions and associated ionisation temperatures found in the Monte Carlo calculation. In contrast to that, we strive to develop a more generic Monte Carlo approach to radiation hydrodynamics, which may be applied to energy and momentum-dominated environments alike. For this purpose we explicitly include both the full energy and momentum transfer terms, a strategy similar to the approach followed by Kasen et al. (2011) to study pair-instability supernovae. This also holds for the very recent presentation of a general-purpose Monte Carlo radiation hydrodynamics method by Roth & Kasen (2014). The design of their method is similar to our approach, as published in Noebauer et al. (2012), but with a strong focus on implicit Monte Carlo methods (see Section 3.4.6).

3.2. Operator Splitting

3.2.1. Numerical Discretisation

Numerical approaches to a physical problem, such as fluid dynamics, captured in terms of a system of partial differential equations, only provide approximate solutions in terms of an ensemble of discrete samples, discontinuous both in space and time. The inherent discretisation scheme varies depending on the numerical solution technique, but typically involves a breakdown of the continuous flow of time into a series of discrete intervals (see, e.g., Bodenheimer et al., 2007, chap. 2.3)

$$\Delta t^n = t^{n+1} - t^n. \tag{3.1}$$

In addition to this time discretisation, the continuous spatial dependence has to be approximated by introducing a discrete subdivision (see, e.g., Bodenheimer et al., 2007, chap. 2.3). In grid-based[3] techniques, this is achieved by defining a computational mesh consisting, in the one-dimensional case, of a series of grid cells with width

$$\Delta x_i = x_{i+1} - x_i. \tag{3.2}$$

This discretisation scheme constitutes the point of reference for the definition of a set of discrete values, $\{Q_i^n\}$, which serves as an approximate representation of the continuous fluid properties. For example, in the so called *finite-difference* approach (see, e.g., Ames, 1992, for a presentation of various finite-difference schemes), the discrete values are interpreted as an approximation to the fluid quantities at the nodes of the space–time grid

$$Q_i^n \approx Q(x_i, t^n). \tag{3.3}$$

---

[3] In contrast to grid-free methods, such as the smoothed particle hydrodynamics technique SPH (Gingold & Monaghan, 1977; Lucy, 1977; Monaghan, 1992), which are not discussed in the scope of this work.

The approximate character stems from the fact that, within the numerical algorithm, the exact information about the continuous dependence of the quantities is lost, even though the initial discretisation $Q_i^0 = Q(x_i, 0)$ may be performed precisely. Figure 3.1 illustrates the finite difference discretisation strategy. Naturally, in the case of radiative transfer, the discretisation scheme has to be extended to include the dependence on the propagation direction and frequency. In the course of this chapter, we will present a different approach for representing fluid properties on a computational grid, the so-called *finite-volume* approach (see LeVeque, 2002, for a description of finite-volume methods), which offers a very efficient and accurate numerical treatment of fluid dynamics (see Section 3.3).

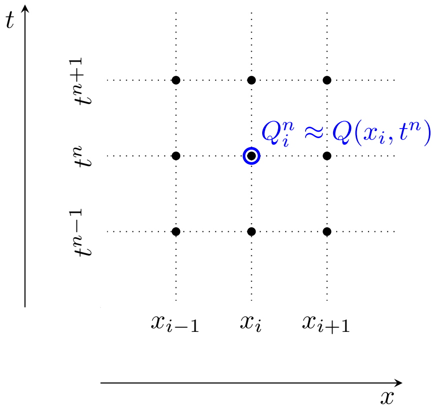

Figure 3.1.: Principle of the finite-difference discretisation in one spatial dimension. All quantities are represented by the corresponding values at the grid nodes.

In general two different strategies exist to advance the quantities to the next time snapshot. *Explicit* numerical schemes solve the temporal evolution of the system by relying only on the already accessible information of previous time snapshots

$$Q_i^{n+1} = F(\{Q_i^n\}). \tag{3.4}$$

The braces indicate that the function may depend on the information of multiple grid points. In contrast to Eq. (3.4), *implicit* approaches are based on algorithms which require a knowledge of the system at the future time snapshot (see, e.g., Ames, 1992, for a presentation of various explicit and implicit techniques to solve partial differential equations)

$$Q_i^{n+1} = F(\{Q_i^{n+1}\}, \{Q_i^n\}). \tag{3.5}$$

The difference between these approaches is graphically highlighted in Fig. 3.2, where two representative stencils are shown, linking all discrete grid points which are needed to determine the new value Q_i^{n+1}.

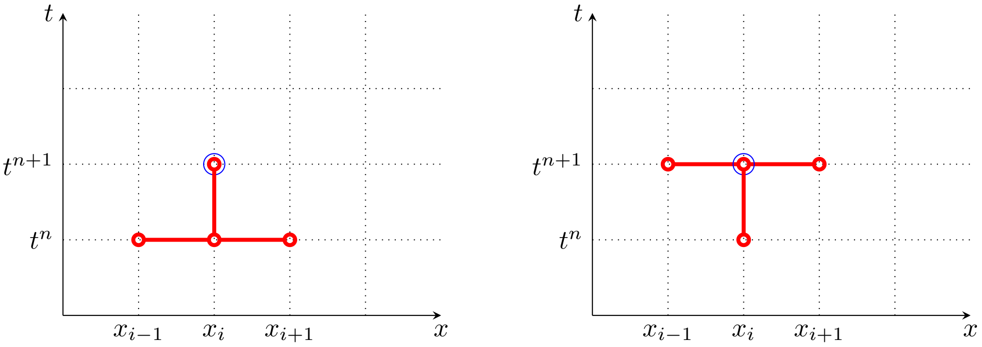

Figure 3.2.: Representative stencils for explicit (left panel) and implicit (right panel) time-marching schemes. All grid points which are needed to determine the value Q_i^{n+1} (highlighted in blue) are linked.

Due to this implicit dependence, the corresponding numerical algorithms are quite complex and also computationally expensive to solve. However, they permit advancing the system over much larger time steps compared to the simpler explicit schemes[4] (see, e.g., Ames, 1992). Since our radiation hydrodynamical approach is based on an explicit time marching scheme, the following presentation will only introduce concepts relevant for this strategy.

3.2.2. Source Terms

For a system of hyperbolic partial differential equations, such as the ideal fluid dynamical equations, the family of finite-volume techniques provides a very successful solution approach (e.g. LeVeque, 2002). Typically, these methods rely on the conservative formulation of the equations. However, cases are often encountered in which additional contributions, so-called *source terms*, have to be considered and prohibit casting the differential equations in conservative form. We have already accounted for such source terms in the presentation of the fluid dynamical equations by incorporating the generic external force density $\mathbf{f}$, which, for example, may describe an external gravitational field. Of course, the radiation hydrodynamical equations for the fluid energy and momentum also involve such source terms in the form of the components of the radiation force vector G^α. In such cases, a strategy has to be devised to account for the action of these source terms.

3.2.3. Principles of the Fractional Step Method

The *fractional step* method (e.g. LeVeque, 2002, chap. 17.3), often also referred to as *operator splitting*, is a very popular approach to include source terms. Here, the problem encoded in the hyperbolic equations is split into a set of individual processes which are treated successively

---

[4] As an example for a fully implicit fluid dynamical approach, which was specifically designed to circumvent the time step constraint of explicit methods in low Mach number flows, see Miczek (2013).

and independently of each other. This is best illustrated at the simple example of a reactive flow (following LeVeque, 2002, chap. 17.2). In particular, the advection of a decaying tracer substance with decay constant λ and of concentration q in a uniform fluid flow of constant speed $\bar{u}$ is considered. The evolution of the concentration is governed by

$$\frac{\partial}{\partial t} q + \bar{u} \frac{\partial}{\partial x} q = -\lambda q. \tag{3.6}$$

Obviously, the equation would reduce to its conservative form in the absence of the source term on the right hand side with the flux function

$$F(x,t) = \bar{u}\, q(x,t). \tag{3.7}$$

In the fractional step method, the advective and the decay processes are separated

$$\frac{\partial}{\partial t} q + \frac{\partial}{\partial x} F = 0, \tag{3.8}$$

$$\frac{\partial}{\partial t} q + \lambda q = 0, \tag{3.9}$$

and treated successively to determine the final concentration value. Hereby, each step introduces intermediate values for the considered quantities which serve as the input for the solution of the successive subproblem. In the case at hand, the concentration is advanced in time for the period Δt with the fractional step method by first determining an intermediate concentration $q^\star$ in solving the advection process. In the following step, the decay subproblem is addressed, relying on the intermediate concentration as the starting point. Only after this second step, the final value for the tracer concentration at the new time $t + \Delta t$ is obtained.

The practical result of this approach, often referred to as *Godunov splitting*, which may be generalised to partial differential equations of the type

$$\frac{\partial}{\partial t} q + (\mathcal{A} + \mathcal{B}) q = 0 \tag{3.10}$$

with arbitrary differential operators $\mathcal{A}$ and $\mathcal{B}$, lies in the ability to solve each subproblem with the numerical tool best suited for the task. The enormous benefit of this becomes apparent in the case of radiation hydrodynamics. Here, the formulation of a successful numerical solution technique for the full system of equations is extremely challenging, but a multitude of efficient numerical methods to address the two subproblems of fluid dynamics and radiative transfer already exists. Naturally, there is a catch: the separation into subproblems and their successive treatment introduces errors. In the case of Godunov splitting, the flavour of the fractional step method discussed above, the magnitude of this so-called *splitting error* formally scales linearly with the length of the time interval Δt over which the equation is evolved. Only in the case of commuting differential operators, i.e. $\mathcal{AB} = \mathcal{BA}$, the splitting error exactly vanishes (see LeVeque, 2002, chap. 17.3 for a detailed derivation and discussion of the splitting errors). The method may be improved by alternating the order in which the subproblems are solved, effectively replacing the procedure $\mathcal{ABABAB}\ldots$ by $\mathcal{ABBAAB}\ldots$. The resulting *Strang Splitting* scheme (after Strang, 1968) is a second-order method, since formally the splitting error decreases quadratically with the time step length. In practice, however, the two splitting approaches exhibit comparable accuracy, since the leading order error terms in the formally first-order Godunov scheme are often very small (see LeVeque, 2002, chap. 17.5).

3.2.4. Operator Splitting for Radiation Hydrodynamics

In our approach, we rely on the Godunov splitting scheme to separate changes due to fluid dynamical effects from those induced by the action of the radiation field. This amounts to identifying

$$\mathcal{A}q \to \nabla \cdot (\rho \mathbf{u} \otimes \mathbf{u}) + \nabla p, \tag{3.11}$$

$$\mathcal{B}q \to -\mathbf{u} \cdot \mathbf{G} \tag{3.12}$$

in case of the momentum balance and analogously for the energy equation

$$\mathcal{A}q \to \nabla \cdot (\rho \mathbf{u} e + \mathbf{u} p), \tag{3.13}$$

$$\mathcal{B}q \to c G^0. \tag{3.14}$$

Strictly speaking, another substep is introduced between these two operations, solving the radiative transfer problem and determining the radiation force. The resulting general splitting scheme may be summarised as follows: we begin by considering the pure fluid dynamical problem in the absence of the radiation field. Intermediate values for the fluid state are determined. In the following step, radiative transfer is treated as an isolated problem. It is solved by assuming static fluid conditions described by the intermediate values, yielding the new radiation field state and the radiation force. Finally, the fluid momentum and energy are updated according to the components of the radiation force

$$\Delta(\rho \mathbf{u}) = \Delta t \mathbf{G}, \tag{3.15}$$

$$\Delta(\rho e) = \Delta t c G^0. \tag{3.16}$$

This concludes the process of advancing the radiation–matter state for the time interval Δt. The entire process is graphically illustrated in Fig. 3.3 (c.f. Noebauer et al., 2012, fig. 1).

3.2.5. Importance of Characteristic Time Scales

The general order of accuracy of the Godunov splitting approach, namely the splitting error decreasing linearly with Δt, does not provide any information about the absolute magnitude of the introduced error. To keep these deviations within acceptable limits and prevent a breakdown

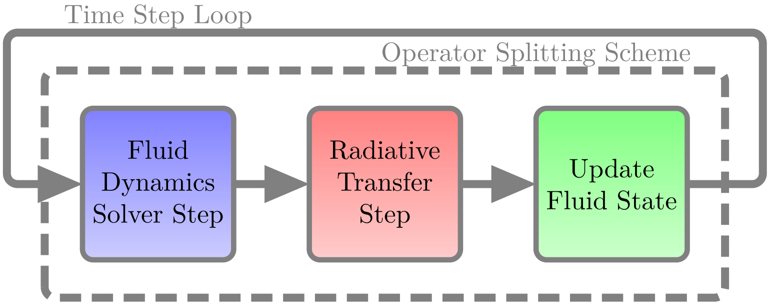

Figure 3.3.: Our Godunov Splitting approach to radiation hydrodynamics. Each simulation cycle consists of a separate treatment of fluid dynamics and radiative transfer. In the final phase, the energy and momentum of the fluid are updated according to the radiation force [see Eqs. (3.15) and (3.16)].

of the numerical solution, the basic design of the fractional step method has to be kept in mind: specifically the assumption that during the intermediate steps, concerned with one of the separated physical processes, all quantities associated with the remaining processes are inert. This approximation is only sensible if the real physical changes in these quantities are small, which corresponds to considering the problem on time scales much smaller than the characteristic scales associated with the expected changes. Obeying this restriction ensures that all subprocesses may react to changes in the physical properties induced by any of the other processes.

Unfortunately, the example of the reactive flow is ill-suited to illustrate the seriousness of violating this time scale constraint. Since the two operators describing advection and decay commute in this simple case, no immediate errors are introduced by separating these processes. However, if, for example, a radiative cooling term $\dot{A}$ is included, the situation changes drastically. Since the cooling rate typically exhibits a strong dependence on the gas temperature – T^4 in case of thermal emission – large errors are introduced if the operator-splitting scheme is applied on time scales larger than the cooling time. The cooling process sets the characteristic time for depleting the entire internal energy reservoir by means of radiative cooling (see, for example, Harries, 2011)

$$t_{\mathrm{cool}} = \frac{\varepsilon}{\dot{A}}. \tag{3.17}$$

Since the cooling rate cannot adapt to changes in the gas temperature, non-physical results will be obtained if the characteristic time scale is not resolved. In fact, the entire internal energy pool may be drained in the radiative cooling splitting step if $\Delta t \geq t_{\mathrm{cool}}$. In reality, however, the cooling rate would have reacted to a drop in gas temperature, thus cushioning the continued depletion of internal energy (see van Marle & Keppens, 2011, for a discussion of radiative cooling in astrophysics and its numerical implementation). This brief illustration points out one of the potential limitations of the splitting approach, namely the need to resolve all characteristic time scales of the investigated system (see also Sekora & Stone, 2010, for a radiation hydrodynamics-specific discussion). Particularly in the regime of *stiff source terms*, i.e. in cases of very short time scales introduced by the source terms (LeVeque, 2002, chap. 17.10), the need to reduce the time step for advancing the physical quantities seriously impedes the efficient use of the splitting approach. In such cases, alternative coupling schemes are best devised (see Miniati & Colella, 2007; Sekora & Stone, 2010, for a discussion of stiff source terms in finite volume hydrodynamics). We defer a detailed presentation of such methods to the later discussion of energy-dominated shocks in supernova ejecta (see Section 5.3.5).

3.3. Finite-Volume Approach to Fluid Dynamics

Many grid-based numerical techniques to solve fluid dynamics problems fall into one of two families[5], depending on the underlying form of the equations. A numerical scheme may aim to solve fluid dynamics by approximating the partial differential equations with finite differences. This class is referred to as *finite-difference* schemes and stands in contrast to the so-called *finite-volume* approach, which originates from the integral formulation of fluid dynamics as conservation laws (see LeVeque, 2002, for an exhausting overview of finite-volume methods). Members of this second family have the significant benefit of conserving mass, momentum and energy by construction. Moreover, finite-volume schemes naturally capture fluid discontinuities such as compression shocks, while additional effort may have to be invested in detecting and treating these phenomena within the finite-difference approach. This is a direct consequence of the fact that discontinuous fluid states are possible solutions to the integral equations, on which the finite-volume approach is based, but not to their differential counterparts. Both formulations are only equivalent in the absence of discontinuities. This restriction to smooth flows is also implicitly assumed when performing the transition between the integral and differential formulation (see Section 2.2.2). However, the integral formulation is the more fundamental concept since it is based on physical conservation laws (c.f. LeVeque, 2002, chap. 1.2.2).

Due to its advantages, many state-of-the-art astrophysical fluid dynamics codes rely on the finite-volume approach, for example Arepo (Springel, 2010), Athena (Stone et al., 2008), Enzo[6] (Bryan et al., 2014), Pluto[7] (Mignone et al., 2007) or Ramses[8] (Teyssier, 2002), to name just a few. In light of the success of the finite-volume framework we also adopt this technique to solve the fluid dynamical subproblem in our radiation hydrodynamical approach. This section explains the finite-volume approach in detail and introduces all relevant numerical techniques. More information about this approach and the related concepts may be found in the excellent textbooks by LeVeque (2002) and by Toro (2009).

---

[5] In this work, we do not cover alternative approaches, such as spectral methods (see, for example, Canuto, 1988) or finite-element schemes (see, for example, Ames, 1992).

[6] `http://enzo-project.org/`

[7] `http://plutocode.ph.unito.it/index.html`

[8] `http://www.ics.uzh.ch/~teyssier/ramses/RAMSES.html`

3.3.1. Finite-Volume Discretisation

The family of finite-volume techniques originates from the integral formulation of the fluid dynamical equations. Following (LeVeque, 2002, chap. 4), we briefly summarise the derivation of the fundamental equations. Recalling Section 2.2.2 and the general derivation of fluid dynamics from physical conservation principles, the temporal integration of the flux difference through the boundaries of the control volume yields the volume-integrated conserved quantities Q at a new point in time

$$\int_{x_{i-1/2}}^{x_{i+1/2}} \mathrm{d}x\, Q(x, t^{n+1}) - \int_{x_{i-1/2}}^{x_{i+1/2}} \mathrm{d}x\, Q(x, t^{n}) = -\int_{t^n}^{t^{n+1}} \mathrm{d}t\, [F(Q(x_{i+1/2}, t)) - F(Q(x_{i-1/2}, t))]. \tag{3.18}$$

Here, we have already reduced the problem to a one-dimensional geometry, introduced the temporal discretisation, t^n, t^{n+1}, and identified the control volume with one grid cell of the computational domain which is bordered by the left and right interfaces, $x_{i-1/2}$ and $x_{i+1/2}$ respectively. This result motivates a discretisation scheme in which the discrete values Q_i^n of the fluid properties are interpreted as an approximation to their corresponding mean values, averaged with respect to the cell volume of the spatial mesh

$$Q_i^n \approx \frac{1}{\Delta x_i} \int_{x_{i-1/2}}^{x_{i+1/2}} \mathrm{d}x\, Q(x, t^n). \tag{3.19}$$

Figure 3.4 illustrates this discretisation process. The right hand side of Eq. (3.18) may be dealt with analogously to the approximate representation of its left hand side. In particular, a time-averaged numerical flux function is defined by

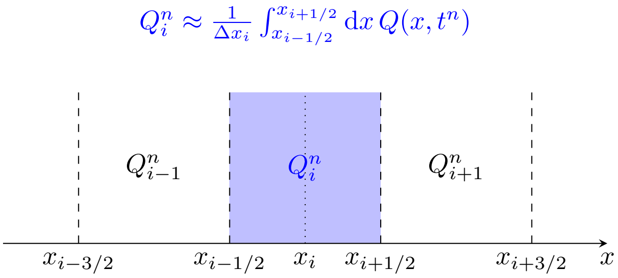

Figure 3.4.: Principles of the finite-volume discretisation in one spatial dimension. All quantities are represented by their corresponding cell average mean values.

$$F_{i\pm1/2}^n \approx \frac{1}{\Delta t^n} \int_{t^n}^{t^{n+1}} \mathrm{d}t\, F(Q(x_{x\pm1/2}, t)) \tag{3.20}$$

allowing for the formulation of a discrete version of the integral equation (3.18)

$$Q_i^{n+1} = Q_i^n - \frac{\Delta t}{\Delta x}(F_{i+1/2}^n - F_{i-1/2}^n). \tag{3.21}$$

This constitutes the foundation for any numerical finite-volume technique, which solves this equation by providing a prescription of how to construct the flux functions from the discrete volume-averaged values of the fluid quantities. Commonly, the flux function only depends on the fluid properties in the two adjacent cells (LeVeque, 2002, chap. 4.1), thus

$$F_{i-1/2}^n = \mathcal{F}(Q_{i-1}^n, Q_i^n). \tag{3.22}$$

The exact functional form of the numerical flux varies depending on the chosen scheme, but is guided by the aim of obtaining results which are in accordance with the analytic solution. This concept is referred to as convergence and is introduced in detail in one of the following sections, Section 3.3.3.

3.3.2. Boundary Conditions

With Eqs. (3.21) and (3.22), the fluid state may be advanced to a later time, using the current fluid state in the cell of interest and those adjacent. Obviously, this recipe requires the specification of an initial fluid state, $\{Q_i^0\}$. Moreover, so-called *boundary conditions* (see, for example, LeVeque, 2002, chap. 7) have to be imposed to close the system at the boundaries of the computational domain, $i = 0, N$. Otherwise the numerical flux function Eq. (3.22) remains undetermined. For the boundary treatment, a number of *ghost cells* are introduced and attached at the edges of the computational domain. Using the fluid state in these additional cells, the numerical flux may be calculated. The number of ghost cells which are introduced depends on the functional dependence of the numerical flux function. In the case of Eq. (3.22) one ghost cell at each edge of the computational domain is sufficient. The fluid state in the ghost cells is not evolved according to the finite-volume scheme but following the imposed boundary conditions. These prescriptions vary from application to application and are ideally chosen to mimic the physical conditions which are expected to prevail at the location of the boundary. If the computational domain is, for example, bounded by a rigid wall, the expected reflection of the fluid flow may be realised by imposing *reflecting boundary conditions*, in which all vector quantities, such as the flow velocity, are mirrored,

$$Q_{a-i} = -Q_{a+i}, \tag{3.23}$$

and the remaining scalar values, such as density and pressure, are copied:

$$Q_{a-i} = Q_{a+i}. \tag{3.24}$$

Here, we assume that the index a marks the location of the left boundary of the computational domain. Other common examples for boundary conditions include supersonic outflows, in which the fluid state in the ghost cells is assumed to be constant and equal to the adjacent cell of the domain, or inflow conditions, in which the ghost cells are filled with predefined (potentially also time-dependent) values for the fluid properties. Also, periodic boundaries, with the ghost cells containing copies of the fluid state at the opposite side of the computational domain, are frequently encountered (see LeVeque, 2002, chap. 7, for a more detailed description of the boundary conditions mentioned here).

3.3.3. Convergence and the CFL Criterion

The utility of numerical schemes is primarily decided upon their ability to produce *convergent* results, which in the limit of an ever finer spatial and temporal discretisation match the analytic solution to the investigated problem. In general, the numerical scheme has to fulfil two requirements to reach convergence, namely *consistency* and *stability* (LeVeque, 2002, chap. 4.4). The consistency constraint refers to the discretised expressions underlying the numerical approach and requires them to accurately represent the analytic equations locally. For example, in the finite-volume approach, the employed numerical fluxes should turn into the integral expressions on the right hand side of Eq. (3.18) in the limit of infinite temporal and spatial resolution. Stability refers to the error introduced by the numerical scheme and the temporal and spatial discretisation. In particular, the errors introduced in each time-marching step should not accumulate to a total error which diverges at any time. This criterion may be investigated in detail for each numerical scheme with the techniques of stability analysis (see, e.g., LeVeque, 2002, chap. 8). Independently of the outcome of such an analysis, there is one requirement any explicit finite-volume technique has to necessarily fulfil to achieve stability. This so-called *CFL criterion* is named after the authors of a seminal paper (Courant et al., 1928), in which this condition was first formulated. This criterion relates the numerical and physical domain of dependence. In general, the physical domain of dependence for a fluid quantity Q at the location x and time t consists of all points by which it may have been influenced. Consequently, the extent of this region is set by the maximum speed with which information may propagate. For example, in a subsonic flow, the domain of dependence forms a cone spanning to the left and right as shown in Fig. 3.5 since sound waves may reach the point of interest from both directions. The numerical domain of dependence is defined analogously as the set of discrete points on the computational mesh which may influence the point of interest. However, here the domain of dependence is not necessarily given by the signal speed but by the particular resolution of the temporal and spatial discretisation of the computational domain. This discrepancy between the physical and the "numerical signal speed", given by $\Delta x/\Delta t$, is considered in the CFL criterion, which states that any numerical finite-volume scheme may only converge if the numerical domain of depen-

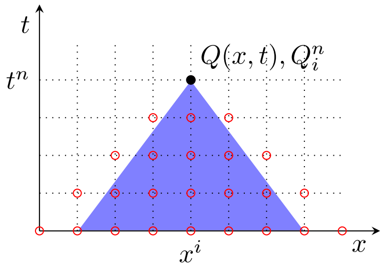

Figure 3.5.: Illustration of the physical domain of dependence in a subsonic flow (blue shaded region). For comparison, the numerical domain of dependence is also shown (red circles), assuming a numerical flux according to Eq. (3.22). For simplicity, we assume that the sound speed is constant in space and time and that the flow is stationary everywhere.

dence contains the physical one (LeVeque, 2002, chap. 4.4). This may be identified with the requirement that the numerical signal propagation speed always exceeds the physical one

$$\frac{\Delta x}{\Delta t} \geq s_{\max}. \tag{3.25}$$

This clearly sets a limit to the length of the time step in the explicit time-marching scheme, which is directly linked to the spatial resolution. If ever finer structures are to be numerically resolved, a larger number of time steps have to be invested to advance the fluid state to a given physical time.

In the CFL criterion, $s_{\max}$ denotes the maximum physical signal propagation speed. A common approach used in numerical schemes to estimate this value considers the maximum velocity of sound waves, the propagation of linear perturbations of the fluid state. However, in the non-linear regime, information may be transported supersonically, for example by shock waves. Thus, a rigorous determination of the maximum signal speed is based on the propagation velocities of these nonlinear waves. Finally, we emphasise that the CFL criterion is only a necessary but by no means a sufficient condition for stability (LeVeque, 2002). This discrepancy is commonly taken into account approximately by introducing a fudge factor C_{CFL}, which further reduces the length of the time step. Typical values for this factor are 0.5 or 0.8 (e.g. Woodward & Colella, 1984; Sekora & Stone, 2010).

3.3.4. Godunov's Approach

Godunov (1959) presented a novel approach to numerically solve the fluid dynamical equations in the finite-volume formulation. From this revolutionary concept, an entire family of highly successful computational fluid dynamical methods has evolved. These *Godunov methods* still lie at the heart of many current state-of-the-art simulations of astrophysical fluid flows, for example when modelling structure formation (e.g. Vogelsberger et al., 2014), the birth of stars (e.g. Krumholz et al., 2007, 2009) or supernova explosions (e.g. Janka & Mueller, 1996; Röpke, 2005). Due to the overwhelming success of the Godunov method, our fluid dynamical solver step also adopts such a scheme.

The basic algorithm of Godunov's approach may be summarised in the three words algorithm *reconstruct, evolve, average*, which, abbreviated as *REA*, is another common name for this family of numerical techniques (see LeVeque, 2002, chap. 4.9). In the reconstruction step, an approximation to the true continuous character of the fluid properties is obtained from the discrete values $\{Q_i^n\}$ by a set of polynomials $\{\tilde{Q}_i^n(x)\}$, defined in each cell. In the original approach by Godunov, piecewise constant functions were employed. Higher accuracy may be achieved by employing higher-order reconstruction schemes (see LeVeque, 2002, chap. 6), such as piecewise linear segments or the piecewise parabolic method (Colella & Woodward 1984, see Section 3.3.5). The reconstructed fluid properties are evolved for the duration of the time step in the second step of the algorithm. Since the piecewise defined reconstruction polynomials do not generally match at the cell interfaces, this step involves the solution to fluid dynamics for a series of discontinuous initial conditions. This is equivalent to solving a series of so-called *Riemann-problems*, the generic term for the challenge posed by a system of hyperbolic partial differential equations with constant initial conditions separated by a discontinuity (see, for example, LeVeque, 2002, chap. 1.2.1). The appeal of Godunov's approach lies in the fact that even for the complex case of the fluid dynamical equations, the Riemann problem is well understood, and solutions may be determined quite easily by exact or approximate techniques (see Section 3.3.6). The solution to the Riemann problem of ideal compressible fluid dynamics is self-similar, i.e. constant along rays $x/t = \text{const}$, and consists of three characteristic waves which emerge from the discontinuity, $Q^{\mathrm{RP}}(x/t)$. The resulting combined wave pattern $\bar{Q}(x,t)$ is then used in the averaging process at the end of the algorithm to obtain the discrete representation of the fluid quantities in terms of volume-averaged values

$$Q_i^{n+1} = \frac{1}{\Delta x_i} \int_{x_{i-1/2}}^{x_{i+1/2}} \mathrm{d}x\, \bar{Q}(x, t^{n+1}). \tag{3.26}$$

This, however, is only valid if the waves have not yet interacted, leading to the time step constraint

$$\Delta t \leq \frac{1}{2} \frac{\Delta x}{s_{\max}}. \tag{3.27}$$

This basic concept may be improved by observing that, in the REA approach, the time-averaged fluxes through the cell interfaces may be determined exactly from $\bar{Q}(x,t)$. Recalling the self-similar character of the solution to the Riemann problem, a numerical flux function may be defined as (LeVeque, 2002, chap. 4.11)

$$F_{i-1/2}^n = \frac{1}{\Delta t} \int_{t^n}^{t^{n+1}} \mathrm{d}t\, \bar{Q}(x_{i-1/2}, t) = Q_{i-1/2}^{\mathrm{RP}}(0). \tag{3.28}$$

Here, we have used the fact that the interface lies on the ray $x/t = 0$ and that the solution of the Riemann problem is time-independent along this trajectory. From the flux differences, the new fluid state is calculated according to Eq. (3.21) and the time step constraint is mitigated to the normal CFL criterion, Eq. (3.25). This modified formulation of Godunov's method builds the foundation of many computational fluid dynamics approaches and also lies at the heart of our fluid dynamical splitting step. In the following we briefly introduce the high-order reconstruction scheme and the Riemann solver.

3.3.5. Reconstruction Scheme: PPM

Godunov's original approach involves the simplest reconstruction scheme which is based on piecewise constant segments. Of all the techniques, this most intuitively leads to Riemann problems at the cell interfaces. However, it generally also suffers from low physical accuracy and should be abandoned in favour of higher-order schemes. The natural extension of the piecewise constant approach is to use linear functions instead. Here, however, a generic difficulty inherent to all higher-order reconstruction schemes appears, namely the introduction of spurious oscillations at sharp discontinuities, such as shocks (see, e.g., LeVeque, 2002, chap. 6). In such regions, suppression of these oscillations is commonly achieved by reducing the order of the reconstruction scheme back to constant segments, since this mimics the physical situation around discontinuities most closely. For this purpose, so called *slope limiters* are used, algorithms which automatically detect discontinuities and reduce the reconstruction order (see, e.g., LeVeque, 2002, chap. 6). A further improvement of the linear reconstruction scheme employs second-order polynomials, for example the *piecewise parabolic method* (PPM) developed by Colella & Woodward (1984). This technique is widely used in astrophysical studies, for example of supernova explosions (Janka & Mueller, 1996; Röpke, 2005) and jets (Marti et al., 1997). Its utility for the modelling of astrophysical fluid flows is further attested by the large number of astrophysical codes that include PPM as one of their high-resolution capabilities, such as ATHENA (Stone et al., 2008), ENZO (Bryan et al., 2014) or FLASH[9] (Fryxell et al., 2000). Therefore we rely on this method for our fluid dynamical implementation as well.

In the PPM scheme, the true continuous character of the fluid properties in a grid cell is approximated by constructing parabolas based on the information in the cell and the two adjacent ones. A special algorithm is used to enforce the monotonicity of the parabolas, i.e. it ensures that they do not contain any extrema within the grid cell. This step introduces discontinuities between the parabolas of different cells at the corresponding interfaces. In the final step, the parabolic reconstruction functions are integrated over the region which may influence the corresponding grid cell interface over the course of the time step. This yields constant left and right states at each interface, which constitute the initial conditions for the series of Riemann problems. Particular care is taken at fluid discontinuities. A flattening algorithm is designed to detect shocks and interpolates linearly between the fluid state obtained from the parabolic reconstruction and one based on constant segments. The full details of this algorithm are described by Colella & Woodward (1984). The lengthy presentation of formulae therein unfortunately contains a

---

[9] `http://www.flash.uchicago.edu/site/index.shtml`

number of typos, listed in Appendix C. It should also be noted that the slope-limiting mechanism proposed by Colella & Woodward (1984) and sketched above fails to preserve extrema in the fluid state. This will be encountered again in the code verification process (see Chapter 4), in particular when verifying the advection behaviour. Despite this downside, we still use the traditional limiter, since our main focus rests on establishing the radiation hydrodynamical coupling and not in maximising the performance in advection-dominated cases. A different limiter has been proposed by Colella & Sekora (2008), which retains the local extrema and exhibits better accuracy in advection processes.

3.3.6. Riemann Problem and Riemann Solver

Providing piecewise constant initial conditions featuring a discontinuity for a set of hyperbolic partial differential equations is generally referred to as the *Riemann Problem* (see, for example, LeVeque, 2002, chap. 1.2.1). This is of particular interest for Godunov's approach to fluid dynamics, since a Riemann Problem is posed at each grid cell interface by the constant left and right states which are determined in the reconstruction step. The solution to the Riemann Problem of ideal fluid dynamics is well-known: it consists of three waves, which originate from the initial discontinuity. The wave pattern evolves in a self-similar manner, which implies a constant fluid state along the characteristics $x/t = \text{const}$. The central wave, propagating with the lowest speed, is always a contact discontinuity, over which only the density of the fluid changes. The two other elementary waves bracket the central area around the contact discontinuity, referred to as "star" region, and are either shocks or rarefaction fans. Figure 3.6 shows a typical elementary wave pattern of a Riemann problem, with the rarefaction fan running to the left and a shock to the right. In contrast to a contact discontinuity, all three fluid properties change their value across a shock. Physically, the shock wave compresses the fluid and constitutes the conversion of kinetic into thermal energy. This process is caused by viscous effects, thus results in an irreversible increase of entropy across the shock. The changes in the fluid properties do not occur abruptly but within a thin transition layer, whose extent is set by the viscous properties of the fluid. However, since the width of this layer is of the order of the mean free paths (see, e.g., Mihalas & Mihalas, 1984, § 57), the mathematical description of shocks in terms of sharp discontinuities within the ideal fluid dynamical framework is warranted. The inverse process of expanding the fluid is not mediated by a discontinuity, a so-called *rarefaction shock* which is physically prohibited on thermodynamic grounds, but by a rarefaction wave. Here, the fluid properties change smoothly between the head and the tail of the wave, connecting the fluid state near the contact discontinuity with the region outside the expanding rarefaction fan.

Despite the precise knowledge about the wave patterns which may emerge from the initial discontinuity, the solution to a particular setup of the Riemann problem may not be immediately read-off from the initial condition. Each elementary wave uniquely connects the initial left or right state with the star region, setting the fluid properties in this zone. The challenge stems from identifying a consistent state in the star region which satisfies the conditions posed by attaching

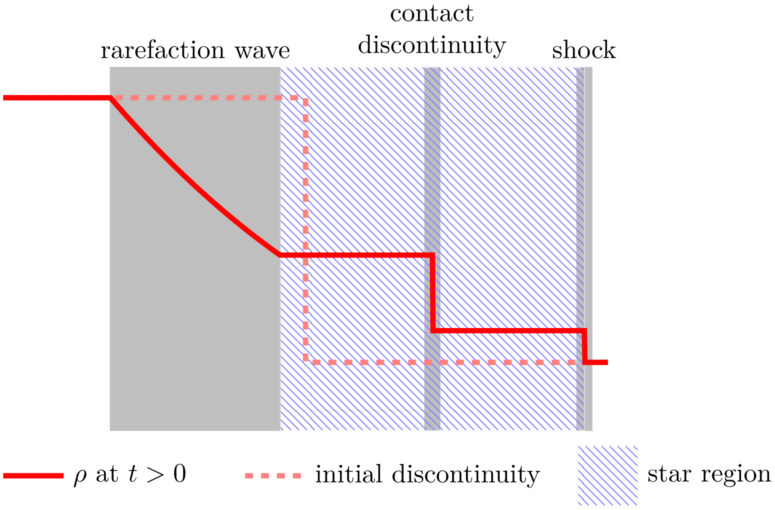

Figure 3.6.: Example for a typical elementary wave pattern (solid red) emerging from the initial discontinuity of the Riemann problem (dashed light red). The density is schematically displayed for a setup which corresponds to the Sod-Shocktube (Sod, 1978). The "star" region is highlighted by the blue striped region.

the two elementary waves. For this task, so-called *Riemann solvers* are employed, which either use an iterative procedure or work with approximate formulations of the problem. A detailed description of many different Riemann solvers is given in the excellent book by Toro (2009). In that work, the author also describes an "exact" Riemann solver, which solves for the conditions in the star regions by using a Newton-Raphson root-finding algorithm. The terminology "exact" is set in quotation marks to highlight that, although the problem is addressed without resorting to approximate simplifications, the solution is not provided in terms of a closed analytic expression, but is found by relying on numerical techniques. Due to the iterative root finding process and the associated numerical costs, this exact Riemann solver is typically not employed in numerical simulations of fluid dynamics. Moreover, formulating a first initial guess to commence the iterative procedure which leads to convergent results is challenging (see discussion in Toro, 2009, chap. 4.3.2). Instead of using this exact solution scheme, approximate Riemann solvers are usually employed in large scale numerical simulations, in which computational efficiency is essential (e.g. in ATHENA). These techniques may, for example, approximate the emergent wave pattern by only accounting for a subset of the possible elementary waves (two-shock solver or two-rarefaction solver, Toro, 2009, chaps. 9.4.1 and 9.4.2), reduce the complexity of the underlying fluid dynamical equations (Roe's method: Roe, 1981; Toro, 2009, chap. 11) or approximate the flux in the star region (HLL and HLLC family Harten et al., 1983; Toro et al., 1994; Toro, 2009, chap. 10). Further references and a detailed description and motivation for these approaches and various other Riemann solver may be found in Toro (2009). Here, we only present the family of

HLL techniques, since we employ the approximate Riemann solver HLLC in our finite-volume fluid dynamical algorithm.

The terminology of these techniques derives from the initials of the authors[10] originally proposing an approximate Riemann solver that is based on estimating the maximum signal propagation speeds of the two elementary waves. Assuming that these velocities may be derived by some approximate expressions, Harten et al. (1983) proposed to determine the fluxes from the simplified situation of two waves propagating with speeds s_L and s_R, separating an intermediate regime from the initial left and right states. This situation may be summarised by

$$Q(x,t) = \begin{cases} Q_\mathrm{L} & \text{if} \quad x/t < s_\mathrm{L} \\ Q_\mathrm{HLL} & \text{if} \quad s_\mathrm{L} < x/t < s_\mathrm{R} \\ Q_\mathrm{R} & \text{if} \quad x/t > s_\mathrm{R} \end{cases} \tag{3.29}$$

and is sketched in Fig. 3.7. Note that the coordinate system is chosen such that the initial discontinuity resides at $x = 0$. A value for the fluid state in the intermediate region at time t may be found exactly by considering a control volume with boundaries $x_\mathrm{L} \leq s_\mathrm{L} t$ and $x_\mathrm{R} \geq s_\mathrm{R} t$, extending beyond the reach of the fastest emerging wave (see Toro, 2009, chap. 10.2.2). Due to the underlying conservation laws and the particular form of the initial configuration, the volume integration of the fluid quantity at time t may be expressed as (see Toro, 2009, chap. 10.2.2, for more details on the following integral relations)

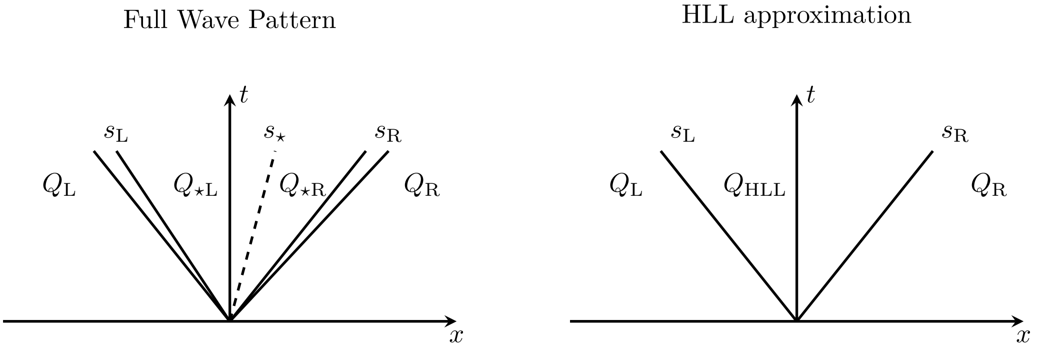

Figure 3.7.: Illustration of the HLL approximation (adapted from Toro 2009, figs. 10.2 and 10.3). In the left panel, the full elementary wave pattern is depicted in terms of the associated characteristics. The central contact discontinuity is marked by the dashed line. Since each bracketing wave may either be a shock or rarefaction fan, two characteristic lines are shown on each side of the initial discontinuity. In the HLL Riemann solver, the central region is approximated by one constant state, Q_HLL, neglecting the existence of the contact discontinuity.

$$\int_{x_\mathrm{L}}^{x_\mathrm{R}} \mathrm{d}x \, Q(x,t) = x_\mathrm{R} Q_\mathrm{R} - x_\mathrm{L} Q_\mathrm{L} + t(F_\mathrm{L} - F_\mathrm{R}). \tag{3.30}$$

---

[10] Harten, Lax and van Leer

Here, $F_{\mathrm{L,R}}$ denote the conserved fluxes for the constant left and right states of the initial condition. The volume integration may be split into contributions from the left and right boundary to the corresponding fastest waves and an integration over the region enclosed by these waves

$$\int_{x_\mathrm{L}}^{x_\mathrm{R}} \mathrm{d}x\, Q(x,t) = \int_{x_\mathrm{L}}^{s_\mathrm{L}t} \mathrm{d}x\, Q(x,t) + \int_{s_\mathrm{L}t}^{s_\mathrm{R}t} \mathrm{d}x\, Q(x,t) + \int_{s_\mathrm{R}t}^{x_\mathrm{R}} \mathrm{d}x\, Q(x,t). \tag{3.31}$$

Evaluating the integrals and including the result of Eq. (3.30), the volume average over the region between the two fastest waves may be formulated as

$$\frac{1}{t(s_\mathrm{R}-s_\mathrm{L})}\int_{ts_\mathrm{L}}^{ts_\mathrm{R}} \mathrm{d}x\, Q(x,t) = \frac{s_\mathrm{R}Q_\mathrm{r} - s_\mathrm{L}Q_\mathrm{L} + F_\mathrm{L} - F_\mathrm{R}}{s_\mathrm{R}-s_\mathrm{L}}. \tag{3.32}$$

and identified with the intermediate state Q_HLL. In the HLL approach, the numerical intercell flux is constructed relying on this intermediate state

$$F_{i-1/2} = \begin{cases} F_\mathrm{L} & \text{if} \quad 0 \leq s_\mathrm{L} \\ F_\mathrm{HLL} & \text{if} \quad s_\mathrm{L} \leq 0 \leq s_\mathrm{R} \\ F_\mathrm{R} & \text{if} \quad 0 \geq s_\mathrm{R} \end{cases}. \tag{3.33}$$

The flux in the intermediate region is not simply given by $F_\mathrm{HLL} = F(Q_{HLL})$, but derived from applying Rankine-Hugoniot[11] conditions at the fastest waves

$$F_\mathrm{HLL} = F_\mathrm{K} + s_\mathrm{K}(Q_\mathrm{HLL} - Q_\mathrm{K}). \tag{3.34}$$

Here, the subscript may represent either of the two sides $\mathrm{K} \in [\mathrm{L},\mathrm{R}]$. Combining both jump conditions and the expression for the intermediate state Eq. (3.29), the flux in this region may be directly calculated from the initial conditions

$$F_\mathrm{HLL} = \frac{s_\mathrm{R}F_\mathrm{L} - s_\mathrm{L}F_\mathrm{R} + s_\mathrm{L}s_\mathrm{R}(Q_\mathrm{R} - Q_\mathrm{L})}{s_\mathrm{R}-s_\mathrm{L}}, \tag{3.35}$$

provided the fastest signal speed is accessible.

The approximate character of the solution technique for Riemann problems presented above lies in the assumption that the left and right waves propagate at the maximum signal propagation speed and that they encompass an intermediate region which may be described by one effective fluid state. This approach implicitly relies on the ability to estimate the velocity of the two waves beforehand. Algorithms for this procedure have been proposed for example by Davis (1988) and Einfeldt (1988), resulting in HLL Riemann solvers which were successfully employed in Godunov type schemes (see Toro, 2009, chap. 10.1). However, due to neglecting the presence of the central wave and the associated density jump, the pure HLL technique performs poorly

---

[11] These jump conditions are typically used to connect the fluid state immediately in front of and behind a shock front (see, for example, Toro, 2009, chap. 2.4.2).

when dealing with contact discontinuities or other intermediate waves (see Toro, 2009, chaps. 10.1 and 10.3). This deficit may be remedied by accounting for the third wave, as already proposed in the original HLL paper (Harten et al., 1983) and implemented by Toro et al. (1994). The resulting scheme is referred to as HLLC[12] and constitutes the means by which the intercell flux is determined in our fluid dynamical substep. Below, we briefly present the equations which govern the determination of the numerical fluxes and introduce the wave speed estimates we employ. For a thorough derivation of these equations we refer the reader to the original publications Toro et al. (1994) and Batten et al. (1997) and the summary found in Toro (2009).

In the HLLC approach, a contact discontinuity, which is moving with speed $s_\star$, is taken into account and the intermediate region is split into two parts left and right of it

$$Q(x,t) = \begin{cases} Q_\mathrm{L} & \text{if} \quad x/t < s_\mathrm{L} \\ Q_{\star\mathrm{L}} & \text{if} \quad s_\mathrm{L} < x/t < s_\star \\ Q_{\star\mathrm{R}} & \text{if} \quad s_\star < x/t < s_\mathrm{R} \\ Q_\mathrm{R} & \text{if} \quad x/t > s_\mathrm{R} \end{cases} . \tag{3.36}$$

Similarly, the HLLC intercell flux calculation takes the four possible fluid states into account

$$F(x,t) = \begin{cases} F_\mathrm{L} & \text{if} \quad 0 < s_\mathrm{L} \\ F_{\star\mathrm{L}} & \text{if} \quad s_\mathrm{L} < 0 < s_\star \\ F_{\star\mathrm{R}} & \text{if} \quad s_\star < 0 < s_\mathrm{R} \\ F_\mathrm{R} & \text{if} \quad 0 > s_\mathrm{R} \end{cases} . \tag{3.37}$$

The velocity of the contact discontinuity may be estimated in different ways, for example as described by Batten et al. (1997). We follow their suggestion and determine the central wave speed by

$$s_\star = \frac{\rho_\mathrm{R} u_\mathrm{R}(s_\mathrm{R} - u_\mathrm{R}) - \rho_\mathrm{L} u_\mathrm{L}(s_\mathrm{L} - u_\mathrm{L}) + p_\mathrm{L} - p_\mathrm{R}}{\rho_\mathrm{R}(s_\mathrm{R} - u_\mathrm{R}) - \rho_\mathrm{L}(s_\mathrm{L} - u_\mathrm{L})} . \tag{3.38}$$

With the velocity of the contact discontinuity determined, the fluid properties in the left and right part of the intermediate region may be successively determined. In the following only the expressions governing the region left of the contact discontinuity are presented. The corresponding properties on the right may be found by simply exchanging the subscripts. Following again Batten et al. (1997), the density may be calculated from

$$\rho_{\star\mathrm{L}} = \rho_\mathrm{L} \frac{s_\mathrm{L} - u_\mathrm{L}}{s_\mathrm{L} - s_\star} \tag{3.39}$$

---

[12] The C stands for contact discontinuity.

and the pressure, which is constant across the central discontinuity, from

$$p_\star = \rho_\mathrm{L}(u_\mathrm{L} - s_\mathrm{L})(u_\mathrm{L} - s_\star) + p_\mathrm{L}. \tag{3.40}$$

With the momentum and energy density given by

$$(\rho u)_{\star\mathrm{L}} = \frac{(s_\mathrm{L} - u_\mathrm{L})\rho_\mathrm{L} u_\mathrm{L} + (p_\star - p_\mathrm{L})}{s_\mathrm{L} - s_\star}, \tag{3.41}$$

$$(\rho e)_{\star\mathrm{L}} = \frac{(s_\mathrm{L} - u_\mathrm{L})\rho_\mathrm{L} e_\mathrm{L} - p_\mathrm{L} - u_\mathrm{L} + p_\star s_\star}{s_\mathrm{L} - s_\star}, \tag{3.42}$$

all necessary fluid properties are accessible to determine the flux in the intermediate region with

$$F_{\star\mathrm{L}} = F_\mathrm{L} + s_\mathrm{L}(Q_{\star\mathrm{L}} - Q_\mathrm{L}). \tag{3.43}$$

For the calculation of the final HLLC intercell flux Eq. (3.37) only an appropriate scheme to estimate the left and right wave speeds remains to be formulated. Various techniques exist to obtain approximate values for these velocities (see Toro, 2009, chap. 10.5), for example the approach advocated by Batten et al. (1997), which we adopt in our implementation of the HLLC solver.

In this approach, the wave speeds are estimated by determining the minimum and maximum propagation velocities of acoustic waves in the constant left and right states

$$\begin{aligned} s_\mathrm{L} &= \min[\lambda_1(Q_\mathrm{L}), \lambda_1(Q_\mathrm{R})], \\ s_\mathrm{R} &= \max[\lambda_3(Q_\mathrm{L}), \lambda_3(Q_\mathrm{R})]. \end{aligned} \tag{3.44}$$

Here, λ_i denote the three eigenvalues of the pseudo-linearised system of ideal fluid dynamical equations

$$\begin{aligned} \lambda_1 &= u - a, \\ \lambda_2 &= u, \\ \lambda_3 &= u + a, \end{aligned} \tag{3.45}$$

which are also the propagation velocities of finite-amplitude disturbances, so-called *simple waves* (see, for example Mihalas & Mihalas, 1984, §55). The quantity a denotes the speed of sound at which small amplitude pressure perturbations of the fluid state, i.e. sound waves, propagate (e.g. Mihalas & Mihalas, 1984, chap. 5.1). As suggested already by Davis (1988), this first estimate may be improved by a further comparison

$$\begin{aligned} s_\mathrm{L} &= \min[\lambda_1(Q_\mathrm{L}), \lambda_1(Q^\mathrm{Roe})], \\ s_\mathrm{R} &= \max[\lambda_3(Q^\mathrm{Roe}), \lambda_3(Q_\mathrm{R})], \end{aligned} \tag{3.46}$$

with an hypothetical intermediate state based on the so-called Roe-average (e.g. Toro, 2009, chap. 11.2.1)

$$Q^{\mathrm{Roe}} = \frac{\sqrt{\rho_{\mathrm{L}}}Q_{\mathrm{L}} + \sqrt{\rho_{\mathrm{R}}}Q_{\mathrm{R}}}{\sqrt{\rho_{\mathrm{L}}} + \sqrt{\rho_{\mathrm{R}}}}. \tag{3.47}$$

We follow Stone et al. (2008) and employ the wave speeds obtained from this improved estimate to complete the implementation of the HLLC Riemann solver for our fluid dynamical calculation.

3.3.7. Summary of the Finite-Volume Algorithm

We conclude the presentation of the numerical fluid dynamical techniques by providing a brief summary of how these methods join together and form the hydrodynamical substep of the splitting scheme. Determining the temporal evolution of the fluid state commences by reconstructing the fluid properties from their discrete average values $\{Q_i^n\}$ using the piecewise parabolic method (see Section 3.3.5). In this step, at each interface left and right states are determined which define a series of Riemann problems. These are addressed with the HLLC Riemann solver (see Section 3.3.6) which yields the intercell fluxes $\{F_{i+1/2}^n\}$. Relying on these numerical fluxes, the new values of the volume-averaged fluid properties $\{Q_i^{n+1}\}$ are determined according to Eq. (3.21). This concludes our fluid dynamical splitting step. The ensuing radiative transfer calculation is detailed in the remaining part of this chapter.

3.4. Monte Carlo Radiative Transfer

A distinguishing feature of our radiation hydrodynamical approach lies in incorporating Monte Carlo radiative transfer techniques. Their advantages in dealing with arbitrary geometrical configurations and complex interaction physics have established Monte Carlo techniques as very successful tools for the solution of pure radiative transfer problems, for example for the calculation of supernova observables (e.g. Mazzali & Lucy, 1993; Lucy, 2005; Kasen et al., 2006; Sim, 2007; Kromer & Sim, 2009), the ionisation state and emergent spectra of cataclysmic variables (e.g. Long & Knigge, 2002; Noebauer et al., 2010) and of active galactic nuclei (e.g. Sim et al., 2008, 2010) and for the structure of hot-star winds (e.g. Abbott & Lucy, 1985; Vink et al., 1999, 2000; Sim, 2004). By relying on this probabilistic approach we aim at retaining these benefits in radiation hydrodynamical calculations. In the following, we provide an in-depth description of the Monte Carlo approach to radiative transfer and present all techniques which finally constitute the corresponding step in the splitting scheme. We note that the discussion in this chapter is restricted to the core techniques which apply to all calculations presented in this work. Features which are implemented to accommodate the physical requirements of the different astrophysical applications will be introduced in the corresponding sections.

3.4.1. Monte Carlo Principles

Many techniques to numerically solve the radiative transfer problem rely on discretising the underlying equations with respect to their spatial, temporal, directional and frequency dependence. For example, in the short-characteristics method (Mihalas, 1978; Olson & Kunasz, 1987; Kunasz & Auer, 1988), all radiation field properties are first represented on a computational mesh, discretising space and time. In each cell, the radiative transfer equations are then solved along a number of rays with different propagation direction. Rules exist to connect the constructed solutions across grid cells (see Section 2.3.6, for a more detailed discussion). In the non-grey case, also the frequency dependence has to be discretised, for example by introducing an appropriate number of frequency or opacity bins.

In contrast to this strategy, the Monte Carlo approach introduces a discretisation of the radiation field which is motivated by its microphysical interpretation as an ensemble of photons. However, the discretisation is not performed on the level of single photons but by defining a large number of Monte Carlo quanta, each representing photon bundles and parcels of radiative energy (see Section 3.4.3). Each of these quanta, commonly referred to as *packets*, is assigned an energy, frequency and direction information, corresponding to the properties of the radiation field. They are then propagated through the medium and simulate physical radiation–matter interactions in accordance with the corresponding material functions (see Section 3.4.4). With their collective propagation behaviour, the packets simulate the temporal evolution of the radiation field as captured in the transfer equation. By performing all these processes in a probabilistic fashion, an adequate statistical representation of the microphysical situation is achieved. From the ensemble of interaction histories and packet trajectories, which are determined in the propagation step, the relevant radiation field properties may be reconstructed (see Section 3.4.5).

From these fundamental principles of the Monte Carlo approach the benefits of this technique (see again discussion in, e.g., House & Avery, 1968; Roth & Kasen, 2014), which have been highlighted on various occasions, may already be motivated. One challenge in radiative transfer calculations is posed by complex non-local source functions (see discussion in Section 2.3.6). In the Monte Carlo approach, this difficulty is circumvented by letting the packets perform the physical interactions directly. The same rules governing the photon propagation on the microscopic level and describing the angle and frequency redistribution are applied to the packets. Thus, many different interaction channels, even processes which formally may not be categorised as true absorption or scattering events (e.g. Compton scattering or non-resonant line interactions), may be incorporated. Moreover, for scattering processes, this technique automatically enforces energy conservation, a property which is not trivially obtained when including formal source functions in deterministic approaches. Complex geometrical configurations also do not pose any limitation onto the Monte Carlo approach since this only affects locating the Monte Carlo packets in the computational domain and determining distances to adjacent grid cells. The propagation of one packet is unaffected by the action of all other packets, mimicking the bosonic character of the photons the packets represent. Consequently, Monte Carlo calculations are ideal for parallel processing, since the work load of propagating packets may simply be distributed among the processing cores without worrying about feedback effects between the different packet pools. In view of these benefits, the significant drawback of the Monte Carlo approach should not go unmentioned. Representing the radiation field by a large but finite number of packets inevitably introduces statistical fluctuations in the reconstructed radiation field properties. This statistical noise has to be controlled in order to identify the true physical variations of the radiation field properties. Unfortunately, the fluctuations are governed by Poisson statistics and thus decrease with the inverse square of the sample size (see, e.g., Kalos & Whitlock, 2008). As a consequence, the computational effort may have to be increased significantly to achieve a noticeable reduction in the Monte Carlo noise. However, the increasing availability of computational resources and the development of sophisticated reconstruction techniques (e.g. Lucy, 1999a, 2003, 2005) reduce the significance of this limitation and render the Monte Carlo technique an attractive approach to radiative transfer. A number of recent highly successful applications of the method are a testimony to this statement (see Section 3.4) and warrant harnessing the benefits of the Monte Carlo approach also in radiation hydrodynamical calculations (Nayakshin et al., 2009; Acreman et al., 2010; Haworth & Harries, 2012; Noebauer et al., 2012; Roth & Kasen, 2014).

In the following sections, the fundamental Monte Carlo techniques, which assemble into the radiative transfer step of the splitting scheme as outlined in Fig. 3.8 (c.f. Noebauer et al., 2012, fig. 1), are described in detail. In Section 3.4.3, the determination of the initial packet population is described. This packet ensemble constitutes the basis for the first radiative transfer step. At

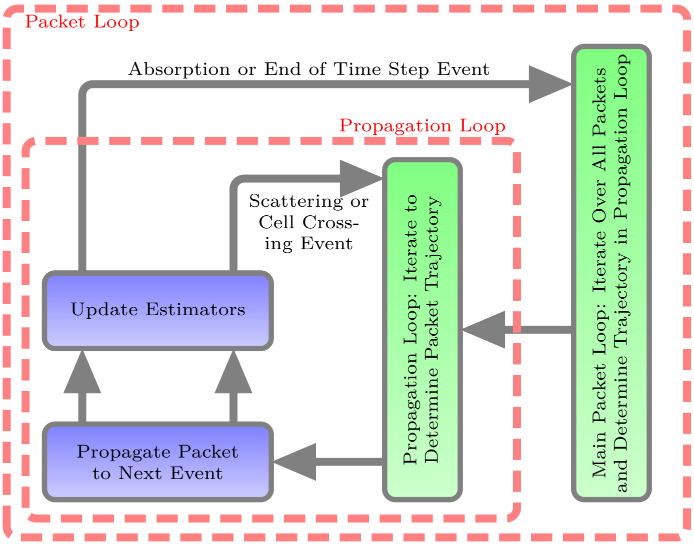

Figure 3.8.: Illustration of the core of the Monte Carlo radiative transfer step. Each packet of the initial population is treated separately and its trajectory determined by identifying and performing all numerical and physical events it encounters during its propagation. The Monte Carlo estimators are updated for each trajectory segment.

the onset of this and any following simulation cycle, the effective opacities of the so-called *implicit Monte Carlo* approach (Fleck & Cummings, 1971) are calculated based on the current fluid state (see Section 3.4.6). Afterwards, the amount of radiative energy injected into the radiation field due to the emissivity of the medium is determined and distributed over a number of newly created packets (see Section 3.4.4). These together with the initial packet population constitute the general pool of packets which have to be processed in the propagation step. During this process, the propagation trajectory is determined for each individual packet. Advancing the packet to the next numerical or physical event until it either reaches the end of the time step, escapes the computational domain or is absorbed, the packet pool is successively treated (see Section 3.4.4). During each trajectory segment, the estimators for the radiation field characteristics are updated (see Section 3.4.5). In this process, the radiation force components are determined, which update the fluid momentum and energy at the end of the time step (see Section 3.2.4). All packets which survive the propagation cycle, are recorded and constitute the initial packet population in the next radiative transfer step (see. Section 3.4.4).

3.4.2. Random Sampling

The probabilistic nature of the Monte Carlo approach requires the assignment of discrete values according to probability distributions describing the underlying physics. For example, each Monte Carlo packet has to be given an initial propagation direction which has to be assigned in accordance with the overall angular dependence of the initial radiation field. This assignment is typically referred to as *random sampling* and may be performed with various techniques (see, e.g., Kalos & Whitlock, 2008, chap. 3). All of these methods provide rules of how to translate a set of values governed by one probability distribution into representative samples of the distribution of interest. This is ideal for numerical calculations, since so-called *random number generators* exist which provide uniformly distributed values z between $[0, 1]$ and which may be used for the sampling purpose. In the following, two important techniques are briefly presented since they are used in our Monte Carlo radiative transfer scheme.

A probability distribution $f_X(x)$ is the continuous analogue to the discrete probability of a random variable X taking the value x. The corresponding cumulative distribution function $F_X(x)$ describes the likelihood that the random variable takes any value up to x

$$F_X(x) = \int_{-\infty}^{x} \mathrm{d}x' \, f_X(x') \tag{3.48}$$

and is a monotonic function increasing from zero to one. The most basic technique of random sampling relies on equating the cumulative distribution functions of the reference distribution and the one of interest. In particular, a discrete value x representing the probability distribution $f_X(x)$ may be calculated from the random number z by requiring that the corresponding cumulative probability functions are equal

$$F_X(x) = F_Z(z). \tag{3.49}$$

Consequently, this random sampling technique requires an analytic inversion of the cumulative distribution function $F(x)$. For example, in the case of an isotropic radiation field, $f_\mu(\mu) = \frac{1}{2}$, the propagation direction is assigned by resolving

$$\int_{-1}^{\mu} \mathrm{d}\mu' \, \frac{1}{2} = \int_{0}^{z} \mathrm{d}z' \, 1 \tag{3.50}$$

which yields

$$\mu = 2z - 1. \tag{3.51}$$

However, complex distributions may be encountered for which the corresponding cumulative distribution functions cannot be trivially inverted. An example may be the drawing of initial packet frequencies in accordance with a thermal radiation field, governed by the Planck distribution. In such cases, the rejection method may be used to perform the random sampling process. In its simplest version, often denoted as *von Neumann rejection sampling* (von Neumann, 1951), pairs of random numbers are drawn (z_x, z_y), which are mapped onto the support and the image of the probability distribution

$$\begin{aligned} x_{\mathrm{trial}} &= (b - a) z_x + a \\ y_{\mathrm{trial}} &= (y_{\mathrm{max}} - y_{\mathrm{min}}) z_y + y_{\mathrm{min}}. \end{aligned} \tag{3.52}$$

Here, we assume that $f_X(x)$ is only defined on the interval $[a, b]$ and that

$$y_{\mathrm{min}} < f_X(x) < y_{\mathrm{max}} \quad \text{for all } x \text{ in } [a, b] \tag{3.53}$$

holds. The value x_{trial} is then accepted as a valid sample of the probability distribution if the corresponding value y_{trial} fulfils

$$y_{\mathrm{trial}} \leq f_X(x_{\mathrm{trial}}). \tag{3.54}$$

Otherwise, the value is rejected and new pairs are drawn until the condition is met. This simple algorithm, which is illustrated in Fig. 3.9, allows us to sample even very complex distribution functions, but may suffer from computational inefficiency in cases where a large number of pairs have to be drawn until a value is accepted. Adaptive rejection techniques (e.g. Gilks & Wild, 1992) address this shortcoming but are not used in this work.

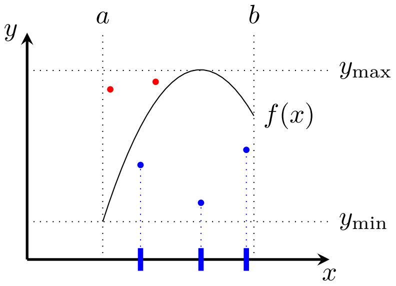

Figure 3.9.: Illustration of the von Neumann rejection sampling strategy. The sampled distribution function is shown as the black solid line. Five representative pairs of random numbers are displayed, the rejected ones in red and the accepted ones in blue. The values for the random variable obtained in this process are highlighted on the x-axis.

3.4.3. Discretisation and Initialisation

The basic discretisation strategy inherent to the Monte Carlo radiative transfer approach was introduced in Section 3.4.1. Here, the details of these procedures are presented, together with the necessary techniques to initialise a Monte Carlo radiative transfer simulation. It should be noted that, although the fundamental feature of the Monte Carlo method lies in representing the radiation field by the packet ensemble, a discretisation of space and time is generally required as well. In the context of radiation hydrodynamics, this computational mesh naturally coincides with the grid defined in the finite-volume approach and provides a discretisation of the relevant material properties, such as opacity and emissivity.

Two general strategies of representing the radiation field in terms of Monte Carlo quanta exist. Both techniques are geared to different interpretations of the radiation field. In early applications of the Monte Carlo method to astrophysical radiative transfer problems[13] (including Avery & House, 1968; Auer, 1968; Magnan, 1968; Caroff et al., 1972; Lucy, 1983), the discretisation scheme was inspired by the microphysical picture of the radiation field as an ensemble of photons. In this formulation of the Monte Carlo approach, “machine photons” are introduced, which represent the radiation field (House & Avery, 1968). These machine photons are interpreted as describing entire bundles of physical photons. The properties of the radiation field are reconstructed by counting the relevant events performed during the propagation of the machine photons. A weighting scheme may also be introduced (see, for example, Avery & House, 1968; House & Avery, 1968), in which each machine photon is assigned an importance factor, which may change during the propagation, depending on the occurring interaction events (*biasing*, see House & Avery 1968). Though intuitive, this photon-based discretisation scheme bears the risk of becoming computationally expensive, since the photon packet number is generally not conserved if non-resonant or non-coherent processes are to be treated. In particular in cases of

---

[13] See House & Avery (1968), for a detailed review of the early uses of the Monte Carlo approach in the astrophysical context.

encountering interaction channels which increasingly redistribute to lower frequencies, a large number of packets has to be introduced to represent the growing number of low-frequency photons (Abbott & Lucy, 1985; Lucy, 1999a). A more efficient discretisation approach was first proposed and introduced by Abbott & Lucy (1985). Here, packets are interpreted as parcels of radiative energy. The authors note that one is at liberty to freely choose the amount of energy, ε_ν, the packets represent at initialisation. An efficient technique, which avoids treating a large number of infrared packets, is obtained by insisting that each packet represents the same amount of radiative energy, $\varepsilon_\nu = \text{const}$. Lucy (1999a) extended the approach by introducing the indivisible energy packet concept. This strategy is motivated by the observation that interactions between the radiation field and the surrounding material conserve energy but not necessarily the number of photons. Consequently, in the indivisible packet formalism, packets are insisted to be re-emitted at the same energy when they interact. Since frequency changes are still permitted, packets have to be interpreted as representing a varying number of physical photons during their simulation lifetime. The advantage of using this indivisible packet concept lies in the ease with which energy conservation may be realised in situations of radiative equilibrium (Lucy, 1999a). In follow-up works (Lucy, 2003, 2005), the approach was generalised to include non-resonant interaction channels. Due to the success of the constant packet energy formalism, e.g. in the calculation of stellar winds (Abbott & Lucy, 1985; Lucy & Abbott, 1993), accretion disc winds (Long & Knigge, 2002; Sim, 2005; Sim et al., 2008, 2010; Noebauer et al., 2010) or supernova observables (Lucy, 2005; Sim, 2007; Kromer & Sim, 2009), we adopt this concept in our implementation.

Prior to the start of the Monte Carlo radiative transfer calculation, the initial packet population representing the radiation field at the beginning of the simulation has to be defined. For this purpose and the ensuing propagation process, adopting a mixed-frame approach similar to the discussion in Section 2.3.4 is beneficial. Since the packet propagation process requires the determination of distances within the discrete temporal and spatial mesh, this is best performed in the lab frame, where the computational grid is typically defined. However, all processes associated with microphysical phenomena, thus the entire interaction machinery, is treated most conveniently in the local rest frame of the fluid, since all expressions associated with atomic physics take a particularly simple form in the CMF. Within this mixed-frame strategy, the initial packet population has to be defined and prepared in the LF. For the initialisation process, the total radiative energy content, $\mathcal{E}$, in the computational domain at the onset of the simulation is distributed equally onto a large number of packets, N, each carrying an energy of

$$\varepsilon = \mathcal{E}/N. \tag{3.55}$$

The packets are uniformly distributed over the corresponding grid cells with the initial location drawn by

$$x_{\mathrm{emit}} = \begin{cases} z\Delta x & \text{planar symmetry} \\ z^{\frac{1}{3}}\Delta r & \text{spherical symmetry} \end{cases}. \tag{3.56}$$

Each packet is also assigned a propagation direction and, in non-grey calculations, a frequency. These values are chosen by sampling the corresponding probability distributions which capture the directional and the frequency dependence of the initial radiation field by using the random sampling methods described in Section 3.4.2.

In many applications we will rely on the LTE assumption to determine the initial packet population. Under these conditions, the radiative energy may be readily determined in each cell from the gas temperature of the fluid material according to the Stefan-Boltzmann law, Eq. (2.40). This relation and any other properties of the thermal radiation field listed in Section 2.3.3 are only strictly valid in the CMF. Thus, to perform the LF packet initialisation, a reference frame transformation has to be carried out. In case of the radiative energy content in cell i, this amounts to

$$\mathcal{E}_i = VE_i = V\gamma^2\left(1+\frac{1}{3}\beta^2\right)E_{0,i} \tag{3.57}$$

already taking Eq. (2.59) and the isotropy of the thermal radiation field in the CMF into account. Despite this isotropy, the angle aberration effect introduces a dependence on the propagation direction in the LF. From Eq. (2.54) the frequency integrated specific intensity in the LF may be found:

$$I(\mu) = \frac{B(T)}{\gamma^4(1-\beta\mu)^4}. \tag{3.58}$$

The non-isotropy of the radiation field has to be accounted for when assigning the initial propagation direction of the Monte Carlo packets. Instead of sampling the simple uniform distribution [see Eq. (3.50)], the probability density (see Noebauer et al., 2012)

$$f_\mu(\mu) = \frac{3}{2}\frac{1}{\gamma^6}\frac{1}{3+\beta^2}\frac{1}{(1-\beta\mu)^4} \tag{3.59}$$

is used. This distribution is quite complex but yields the relativistically correct angle assignment, compatible with the specific intensity, Eq. (3.58). However, in situations where the fluid velocity is much smaller than the speed of light, simplified versions may be used, for example by only accounting for first-order effects

$$f_\mu(\mu) = \frac{1}{2}(1+4\mu\beta). \tag{3.60}$$

These probability distributions may be either sampled by relying on the rejection technique or directly by inverting the corresponding cumulative distribution functions. Unfortunately, the resulting sampling routines are quite complex, for example in the relativistically correct case

$$\mu = \frac{1}{\beta}\left[1 - \left(2\beta\gamma^6(3+\beta^2)z + \frac{1}{(1+\beta)^3}\right)^{-\frac{1}{3}}\right]. \tag{3.61}$$

In the absence of any fluid motion, LF and CMF coincide, the probability density Eq. (3.59) collapses to the uniform distribution and the simple sampling rule Eq. (3.51) is retained.

The entire process of determining the initial packet properties in the LF seems laborious. In particular in the LTE initialisation scheme, one may argue that due to the trivial angular dependence of the thermal radiation field in the CMF, the packet properties are best drawn in the CMF. However, the obvious strategy of isotropically assigning the packet propagation direction

$$\mu_0 = 2z - 1, \tag{3.62}$$

letting each packet carry the radiative energy ε_0 and transforming these packet properties into the LF according to the rules laid out in Section 2.3.4, fails to reproduce the desired radiation field features in the LF. As a consequence, all initial packet properties are assigned according to the LF techniques introduced in this section.

For calculations which are performed in the grey approximation, the assignment of initial packet energy and propagation direction concludes the initialisation process of the packet pool at the onset of the simulation. If the spectral dependence of the radiation field is taken into account, each packet additionally has to be associated with a frequency (see, e.g. Lucy, 1999a). We defer a detailed description of this process to the discussion of the stellar wind application where we first make use of non-grey calculations (see Chapter 6). Independently of the frequency consideration, the initial packet pool is defined and the propagation cycles, constituting the single radiative transfer steps, may be commenced.

3.4.4. Packet Propagation

Launching Monte Carlo packets through the computational domain and determining their propagation trajectories serves a single purpose: from the interaction histories and packet paths the properties of the radiation field may be reconstructed and its new state at the end of the time step determined. In radiation hydrodynamical applications, this allows us to calculate the radiation force. Packets are allowed to perform physical radiation–matter interactions in analogy to real photons during their propagation history to describe the correct temporal evolution of the radiation field. This section explains the packet propagation procedure (see also, e.g., Lucy, 1999a, 2003, 2005; Noebauer et al., 2012; Roth & Kasen, 2014, for descriptions of the basic time-dependent Monte Carlo packet propagation procedure). We will restrict our discussion to the treatment of grey absorption and scattering interactions. In the later presentation of the stellar wind application, the generalisation to non-grey interaction channels will be introduced (see Chapter 6).

At the beginning of each radiative transfer step, all packets from the initial population, which corresponds to the state of the radiation field at the onset of the simulation cycle, are launched through the computational domain along their initial propagation direction. Along their straight trajectories, packets may pass through the interfaces of the spatial discretisation, perform physical radiation–matter interactions and finally reach the end of the time step (see, e.g. Lucy, 1999a, 2005; Noebauer et al., 2012). All of these numerical and physical events are accompanied by changes in the instantaneous packet properties and in the direction of the propagation trajectory. After having completed determining the propagation history of a particular packet, a new packet is considered and the entire process repeated until the complete packet population has been updated.

The main challenge of the packet propagation process is the identification of the series of events a packet experiences along its trajectory. The simplest of these events are owed to the spatial and temporal discretisation of the computation domain. Since packets propagate with the speed of light c and due to the limited duration of the time step, Δt, a packet may cover at maximum a distance of[14]

$$l_{\mathrm{EoT}} = c\Delta t. \tag{3.63}$$

After that, the propagation is interrupted and the properties of the packet recorded. In the next time step it contributes to the initial packet population and resumes its propagation.

When crossing through the interfaces of the spatial discretisation into an adjacent grid cell, the packet properties have to be adjusted to the new material state in this cell. In particular, changes in the local opacity, which determine the location of physical interactions, have to be taken into account. The distance to the next interface may be calculated at any instance of the propagation from the geometry of the computational mesh. In planar symmetry, the adjacent grid cell is reached either on the right through the interface at x_r, or on the left at x_l, after covering the distance[15]

$$l_{\mathrm{GCC}} = \begin{cases} \frac{x_r - x}{\mu} & \text{if} \quad \mu > 0 \\ \frac{x_l - x}{\mu} & \text{if} \quad \mu < 0. \end{cases} \tag{3.64}$$

The situation is slightly more complicated if the underlying geometry has spherical symmetry. Here, the parameter μ, which describes the cosine of the angle between the symmetry axis r and the packet trajectory l, changes during the propagation (see Fig. 3.10). If a packet started at the location r_i along the direction μ_i, it reaches the point

$$r_f = \sqrt{r_i^2 + l^2 + 2 l r_i \mu_i} \tag{3.65}$$

---

[14] EoT abbreviates end of time step.

[15] The abbreviation GCC derives from *grid cell crossing.*

after covering the distance l, with the trajectory now enclosing the angle cosine

$$\mu_f = \frac{l + r_i \mu_i}{r_f} \tag{3.66}$$

with the symmetry axis. After some algebraic manipulation, the distance to the next spherical shell, either inwards at r_l or outwards at r_r, may be calculated from

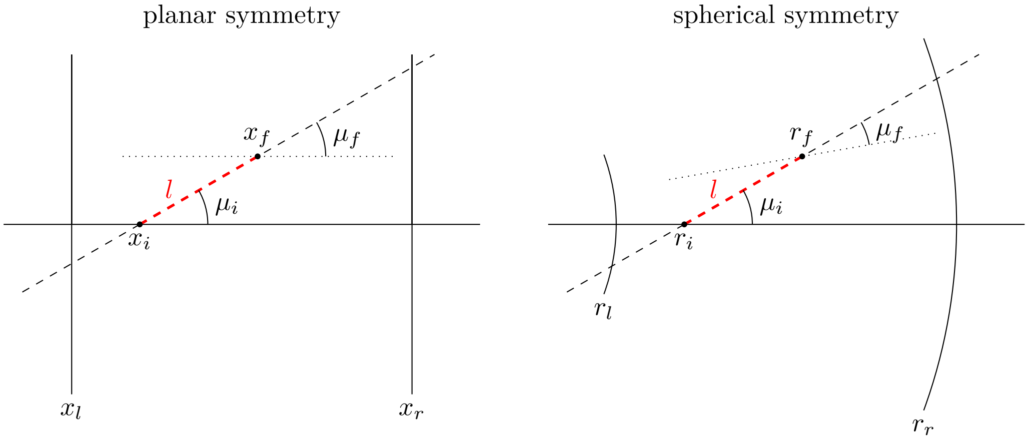

Figure 3.10.: Illustration of the Monte Carlo propagation process in planar (left panel) and spherical symmetry (right panel). The packet starts at x_i (r_i) and propagates along the direction μ_i for a distance of l (highlighted in red) to reach the location x_f (r_f). The change of the angular parameter μ during this process in the spherical case is apparent. The dotted lines mark the direction of the symmetry axis at the final packet location.

$$l_{\mathrm{GCC}} = \begin{cases} -\mu_i r_i - \sqrt{\mu_i^2 r_i^2 - r_i^2 + r_l^2} & \text{if} \quad \mu_i \leq -\sqrt{1 - \left(\frac{r_l}{r_i}\right)^2} \\ -\mu_i r_i + \sqrt{\mu_i^2 r_i^2 - r_i^2 + r_r^2} & \text{else.} \end{cases} \tag{3.67}$$

More important than the numerical events are, from a physical point of view, the radiation–matter interactions performed by the Monte Carlo packets. Since the ensemble of Monte Carlo packets only constitutes a representation of the radiation field in the statistical sense, the interaction procedure has to be carried out in a probabilistic fashion. In particular, the exact location and the nature of the interaction events a packet simulates are determined in a series of random number experiments. The distance to the next physical interaction may be calculated by sampling

$$f_l(l) = \chi \mathrm{e}^{-\chi l}, \tag{3.68}$$

yielding the assignment (see, e.g. Lucy, 1999a; Noebauer et al., 2012)

$$l_{\mathrm{PIE}} = -\frac{\log z}{\chi}, \tag{3.69}$$

in which the abbreviation derives from *physical interaction event.* The sampling routine is a direct result of the general extinction law

$$I(l) = I(0)\mathrm{e}^{-\chi l}. \tag{3.70}$$

which captures the drop in intensity due to absorption when passing through a slab of material of width l and with the opacity χ. After having covered a distance equal to Eq. (3.69), a packet undergoes a physical interaction event. The nature of the simulated interaction, being a scattering or absorption, is determined by comparing the relative strengths of these two interaction channels (see, e.g., Lucy, 1999a; Noebauer et al., 2012). Specifically, a packet scatters if the random number experiment yields

$$z \leq \frac{\chi^{\mathrm{scat}}}{\chi^{\mathrm{abs}} + \chi^{\mathrm{scat}}}. \tag{3.71}$$

The determination of the new packet properties after the scattering interaction relies on the principle of energy conservation. Assuming isotropic and resonant scattering processes, the incident and emergent packet energies, ε_0^i and ε_0^f, are equal in the CMF (see, e.g., Lucy, 2005; Noebauer et al., 2012)

$$\varepsilon_0^i = \varepsilon_0^f. \tag{3.72}$$

Using the transformation rules, the post-scattering packet energy in the LF may be determined directly from the incident and emergent propagation directions

$$\varepsilon^f = \gamma^2(1 + \beta\mu_0^f)(1 - \beta\mu^i)\varepsilon^i. \tag{3.73}$$

Here, the new propagation direction in the CMF is determined by sampling the isotropic probability distribution Eq. (3.51) and afterwards transformed into the LF by means of Eq. (2.48). If the condition of the random number experiment Eq. (3.71) is not fulfilled, the packet experiences an absorption. The packet trajectory is terminated at the interaction location and the packet discarded from the following propagation process. The complementing effect to removing Monte Carlo packets from the simulation in absorption events is caused by the emissivity of the material. To capture this additional source of radiative energy, a number of new Monte Carlo packets is injected into the simulation in the course of the time step. Specifically,

$$N_{\mathrm{emit}} = \eta\frac{\Delta V \Delta t}{\varepsilon} \tag{3.74}$$

packets are created in a particular cell and added to the packet census and treated analogously (see, e.g., Noebauer et al., 2012; Roth & Kasen, 2014). However, in contrast to the initial population, each packet is injected at a time chosen according to

$$t_{\mathrm{emit}} = z\Delta t \tag{3.75}$$

at a random location [see Eq. (3.56)].

After having introduced the distances associated with all possible numerical and physical events, i.e. reaching the end of the time step (l_{EoT}), passing over a grid cell interface (l_{GCC}) and simulating a physical interaction event (l_{PIE}), the propagation process reduces to advancing the packet for the shortest of these pathlengths and performing the associated changes in the packet properties. This sequence is repeated until the packet has either reached the end of the time step, has left the computational domain through one of its boundaries or has been destroyed in an absorption event. After that, a new packet is considered and its propagation history determined. The packet propagation process concludes when all packets from the initial census and the ones injected due to the emissivity have been treated in this fashion. From the resulting ensemble of interaction histories and packet trajectories the properties of the radiation field may be reconstructed employing the techniques which are detailed in the next section.

3.4.5. Reconstruction Schemes

The bulk of the computational effort associated with the Monte Carlo approach is spent in calculating the packet trajectories during the propagation process. However, the Monte Carlo routine is incomplete without developing a prescription of how to distil properties of the radiation field, such as its mean intensity, flux or pressure, from the ensemble of packet interaction histories. Due to the probabilistic nature of the Monte Carlo approach, the reconstructed quantities are subject to statistical fluctuations, which limit their accuracy. Thus it is advisable to devise a reconstruction scheme which minimises the Monte Carlo noise. For this purpose we adopt the so-called *volume-based estimator* formalism of Lucy (1999a, 2003, 2005) and extend it to suit our radiation hydrodynamical needs. In the following, we first introduce a simple and intuitive reconstruction scheme based on counting instantaneous packet properties. Afterwards the estimator formalism is presented and its superiority with respect to the noise level in the reconstructed quantities illustrated.

A simple reconstruction technique may be readily devised by considering a temporal snapshot of the simulation. Then, measures for the radiation field quantities in a cell may be intuitively obtained by counting all packets which are currently in the cell and summing over their respective properties – in case of the radiative energy content by considering the packet energies:

$$E_i = \frac{1}{\Delta V_i} \sum_j \varepsilon_j. \tag{3.76}$$

Here, the summation only includes packets which reside within the grid cell boundaries, thus $x_j \in [x_{i-1/2}, x_{i+1/2}]$. With the fundamental relation between energy and mean intensity, the latter may be readily reconstructed

$$J_i = \frac{1}{4\pi} \frac{c}{\Delta V_i} \sum_j \varepsilon_j. \tag{3.77}$$

By restricting the summation to only include packets whose propagation directions lie in a certain directional bin $\mu \in [\mu_k, \mu_k + \Delta\mu_k]$, the specific intensity may be obtained within the counting framework

$$I_i(\mu_k)\Delta\mu_k = \frac{1}{2\pi}\frac{c}{\Delta V_i}\sum_{j,k}\varepsilon_{j,k}. \tag{3.78}$$

The factor 2 is introduced to fulfil the relation between specific and mean intensity

$$J_i = \frac{1}{2}\sum_{\Delta\mu_k} I_i(\mu_k)\Delta\mu_k. \tag{3.79}$$

In analogy to these direct results, all higher moments of the specific intensity may be reconstructed. For example, in case of the first and second moment by using

$$H_i = \frac{1}{4\pi}\frac{c}{\Delta V_i}\sum_j \varepsilon_j\mu_j, \tag{3.80}$$

$$K_i = \frac{1}{4\pi}\frac{c}{\Delta V_i}\sum_j \varepsilon_j\mu_j^2. \tag{3.81}$$

All forms presented above are effectively counting experiments and are thus subject to the statistical fluctuations inherent to this type of stochastic processes. Namely, the deviation from the expectation value varies with the inverse square root of the number of samples included in the counting (Kalos & Whitlock, 2008, chap. 2.7). One may immediately imagine situations in which this behaviour becomes problematic, for example when facing regions with varying optical depth. Packets will be trapped in areas of high optical depth, leading to small fluctuations in the reconstructed quantities there. However, at the same time, the packet population in cells with low optical depth will be seriously depleted and any quantity reconstructed by summing over the packet census at the end of the time step will suffer from a severe level of Monte Carlo noise. This problem generally worsens regarding the determination of energy and momentum transfer terms, the crucial quantities for radiation hydrodynamics. In the direct counting picture, these transfer terms may be reconstructed by recording all interactions events and balancing the incident and emergent packet energies and momenta. With the Monte Carlo packet carrying an energy and momentum of ε and $\varepsilon\mu/c$ along the coordinate axis, the radiation force terms may be calculated

$$G^0 = \frac{1}{\Delta V_i c\Delta t}\sum_j \varepsilon_j^I - \varepsilon_j^F \tag{3.82}$$

$$G^1 = \frac{1}{\Delta V_i c\Delta t}\sum_j \varepsilon_j^I\mu_j^I - \varepsilon_j^F\mu_j^F, \tag{3.83}$$

where the summation runs over all interaction events happening in the cell i and the superscripts I (initial) and F (final) denote the incident and emergent packet properties respectively. Particularly in regions with low optical depth, the above reconstruction of the radiation force suffers from very high shot noise. In the extreme case, $\tau \to 0$, packets pass cells without interacting, yielding a zero radiation force. Thus any formalism which increased the number of contributions to the summation while at the same time retaining the number of Monte Carlo quanta is preferable to the intuitive but potentially noisy direct counting approach.

Lucy (1999a) proposed a new reconstruction technique which mitigates the deficits of the direct counting formalism. In a series of successive publications (Lucy, 2003, 2005) this technique was refined and extended. The fundamental principle behind the introduced *volume-based estimator* scheme lies in the insight that over a time step Δt every packet which resides at any instance in the investigated cell contributes to a certain extent to the time and volume-averaged radiation field quantities. Specifically, an estimator for the radiative energy content of a grid cell may be obtained by summing over all packets that somehow found themselves in that cell. Denoting the residence time of the packet in the cell with δt, each contribution to the summation is weighted by the relative residence time $\delta t/\Delta t$, yielding the estimator (Lucy, 1999a)

$$E_i = \frac{1}{\Delta V_i} \sum_j \varepsilon_j \frac{\delta t_j}{\Delta t}. \tag{3.84}$$

Strictly speaking, the residence times in the summation have to be interpreted as the time intervals during which the packet properties remain unchanged. Thus, they may be identified with all trajectory elements lying in the cell and connecting two numerical or physical events. This subtlety may be clearly highlighted by translating the residence time intervals via the packet propagation speed c into trajectory segments of length l_j, yielding the estimator (Lucy, 1999a)

$$E_i = \frac{1}{\Delta V_i c \Delta t} \sum_j \varepsilon_j l_j \tag{3.85}$$

We emphasise again that the summation runs over all packet trajectory segments which lie within the investigated cell i. Relying on the cell volume as the basis for the construction of the Monte Carlo estimator distinguishes this approach from earlier techniques (e.g. Och et al., 1998), which are based on control surfaces (see Lucy, 1999a).

In analogy to formulating a direct counting measure for the mean intensity, a volume-based estimator for J_i may be found (Lucy, 1999a):

$$J_i = \frac{1}{4\pi \Delta V_i \Delta t} \sum_j \varepsilon_j l_j. \tag{3.86}$$

Higher moments are reconstructed by including the propagation direction cosine

$$H_i = \frac{1}{4\pi \Delta V_i \Delta t} \sum_j \varepsilon_j l_j \mu_j, \tag{3.87}$$

$$K_i = \frac{1}{4\pi \Delta V_i \Delta t} \sum_j \varepsilon_j l_j \mu_j^2. \tag{3.88}$$

Finally, the specific intensity is again found within the estimator formalism by restricting the summation to trajectory segments which point into the direction contained in the interval $[\mu_k, \mu_k + \Delta\mu_k]$,

$$I_i(\mu_k)\Delta\mu_k = \frac{1}{2\pi}\frac{1}{\Delta V_i}\sum_{j,k}\varepsilon_{j,k}l_{j,k}. \tag{3.89}$$

In the original formulation of the volume estimator scheme, Lucy (1999a) also provided a recipe to calculate the rate of absorbed energy in a Monte Carlo simulation. The proposed technique does not rely on a summation over all events that actually occurred during the simulation. Instead, all possible interaction events are taken into account, each weighted by its probability of occurrence. Specifically, given the absorption opacity χ^{abs} and the corresponding mean free path $1/\chi^{\mathrm{abs}}$, a packet would on average undergoes $l\chi^{\mathrm{abs}}$ interactions along a path of length l and thus contribute with $\varepsilon l\chi^{\mathrm{abs}}$ to the total amount of absorbed radiative energy. Extending this idea to the calculation of energy and momentum transfer terms, the radiative force components in a purely absorbing medium may be found through the volume estimators

$$G^0 = \frac{1}{\Delta V_i c\Delta t}\sum_j \varepsilon_j l_j \chi^{\mathrm{abs}} - \frac{4}{c}\gamma\chi^{\mathrm{abs}}\sigma_{\mathrm{R}}T^4, \tag{3.90}$$

$$G^1 = \frac{1}{\Delta V_i c\Delta t}\sum_j \varepsilon_j \mu_j l_j \chi^{\mathrm{abs}} - \frac{4}{c}\beta\gamma\chi^{\mathrm{abs}}\sigma_{\mathrm{R}}T^4. \tag{3.91}$$

Besides the packet summation, an additional, negative contribution appears in these estimators. This corresponds to the effect of the emissivity which injects energy and momentum into the radiation field. For the current discussion we have assumed that only the thermal LTE emissivity of the medium contributes [see Eq. (2.42)] and have already determined the corresponding LF values of emitted energy and momentum using the appropriate transformation laws (see Section 2.3.4).

Incorporating scattering interactions into this picture is slightly more challenging since capturing the re-emission contribution analytically is generally non-trivial. Nevertheless, an estimator for the energy and momentum transfer mediated by scattering interactions may be formulated (Noebauer et al., 2012). In the formulation of the absorption estimators we identified $l\chi^{\mathrm{abs}}$ as the number of interactions a packet experiences along the segment l. In the case of scatterings, a packet would be immediately re-emitted, now with the properties ε^f, μ^f [see Eq. (3.73)]. Thus, a packet may be interpreted as contributing $\varepsilon l\chi^{\mathrm{scat}}$ to the absorbed energy and simultaneously $\varepsilon^f l\chi^{\mathrm{scat}}$ to the re-injected energy. With this insight, estimators for the radiation force in purely scattering media may be derived, yielding (Noebauer et al., 2012)

$$G^0 = \frac{1}{\Delta V_i c\Delta t}\sum_j \chi^{\mathrm{scat}} l_j(\varepsilon_j - \varepsilon_j^f), \tag{3.92}$$

$$G^1 = \frac{1}{\Delta V_i c\Delta t}\sum_j \chi^{\mathrm{scat}} l_j(\varepsilon_j\mu_j - \varepsilon_j^f\mu_j^f). \tag{3.93}$$

Combining these results with the previously derived pure absorption estimators, a general reconstruction rule for the energy and momentum transfer terms may be obtained

$$G^0 = \frac{1}{\Delta V_i c \Delta t} \sum_j l_j [(\chi^{\rm scat} + \chi^{\rm abs})\varepsilon_j - \chi^{\rm scat} \varepsilon_j^f] - \frac{4}{c} \gamma \chi^{\rm abs} \sigma_{\rm R} T^4, \tag{3.94}$$

$$G^1 = \frac{1}{\Delta V_i c \Delta t} \sum_j l_j [(\chi^{\rm scat} + \chi^{\rm abs})\varepsilon_j \mu_j - \chi^{\rm scat} \varepsilon_j^f \mu_j^f] - \frac{4}{c} \beta \gamma \chi^{\rm abs} \sigma_{\rm R} T^4. \tag{3.95}$$

Our strategy to include scattering interactions may be generalised to any emission process which cannot be expressed by a closed analytic expression. Thus, the estimator formalism for the radiation force constitutes a powerful tool to deal with generic interaction processes. We revisit this concept later, when considering resonant line interactions in the stellar wind environment (see Section 6.2.7).

Despite the general applicability of Eqs. (3.94) and (3.95), they are unnecessarily complex for the simple case of grey material functions, describing thermal emission, isotropic absorption and resonant, isotropic scattering. In such situations, the simple form of the radiation force in the CMF [see Eqs. (2.74) and (2.75)] may be exploited to construct estimators. In particular, the energy transfer terms may be obtained by combining the estimators for mean intensity and flux in the CMF appropriately and multiplying with CMF opacities.

The required values for the CMF radiation field quantities may either be determined from the LF estimators for the first three moments using the transformation laws Eqs. (2.59) and (2.60), or reconstructed directly. For this we may use the same estimator recipes as in the LF, since the derived volume-based estimators are relativistically correct. Consider, for example, the mean intensity in the LF and express all quantities by the corresponding CMF values. Relying on the invariance of the “space-time” element $\Delta V \Delta t$ and using the transformation law for the length of the trajectory element (c.f. Lucy, 2005)

$$l = \gamma(1 + \beta\mu_0) l_0, \tag{3.96}$$

the following expression is obtained:

$$J = \frac{1}{4\pi \Delta V \Delta t} \sum \gamma^2 (1 + \beta\mu_0)^2 \varepsilon_0 l_0. \tag{3.97}$$

This may be expanded to

$$J = \gamma^2 \left(\frac{1}{4\pi \Delta V \Delta t} \sum \varepsilon_0 l_0 + 2\beta \frac{1}{4\pi \Delta V \Delta t} \sum \varepsilon l_0 \mu_0 + \beta^2 \frac{1}{4\pi \Delta V \Delta t} \sum \varepsilon_0 l_0 \mu_0^2 \right), \tag{3.98}$$

which matches exactly the expected transformation behaviour of the mean intensity Eq. (A.8), after using estimator formulae for the first three moments Eqs. (3.86) to (3.88) in the CMF. The correct transformation behaviour of the remaining estimators may be verified in the same fashion. As a consequence, values for the LF and CMF radiation field quantities may be calculated simultaneously from the packet propagation histories determined in the LF by simply transforming the LF estimator increments

$$\Delta J_0 = \Delta J \gamma^2 (1 - \beta\mu)^2, \tag{3.99}$$

$$\Delta H_0 = \Delta J_0 \frac{\mu - \beta}{1 - \beta\mu}, \tag{3.100}$$

$$\Delta K_0 = \Delta H_0 \frac{\mu - \beta}{1 - \beta\mu}. \tag{3.101}$$

For the estimators for the CMF values of the first two moments of the specific intensity, the radiation force components may be reconstructed by (Noebauer et al., 2012)

$$G_0^0 = \frac{4\pi}{c} \chi_0^{\mathrm{abs}} [J_0 - B(T)], \tag{3.102}$$

$$G_0^1 = \frac{4\pi}{c} (\chi_0^{\mathrm{abs}} + \chi_0^{\mathrm{scat}}) H_0, \tag{3.103}$$

and the ensuing transformation into the LF

$$\begin{aligned} G^0 &= \gamma(G_0^0 + \beta G_0^1), \\ G^1 &= \gamma(G_0^1 + \beta G_0^0). \end{aligned} \tag{3.104}$$

After having presented the volume-based estimators for all relevant radiation field properties, the significant benefit of this approach should be emphasised once more. Since again all packets in the cell contribute, the reconstruction is less noisy compared to a direct counting approach and problems in optically thin regions are mitigated (see discussion in Lucy, 1999a).

Before concluding the discussion of Monte Carlo reconstruction schemes, we briefly sketch how to generalise the estimator formalism to spherically symmetric calculations. In the previous section, Section 3.4.4, we noted that the angle parameter μ changes along the packet trajectory in spherical symmetry (see Fig. 3.10). This variability has to be accounted for in all estimators, by replacing any explicit appearance of the propagation direction by its average value with respect to the trajectory length l

$$\bar{\mu}(l) = \frac{1}{l} \int_0^l \mathrm{d}l' \, \mu(l). \tag{3.105}$$

Employing Eqs. (3.65) and (3.66), the mean propagation direction may be expressed by the initial and final radial position of the trajectory segment

$$\bar{\mu}(l) = \frac{r_f - r_i}{l}. \tag{3.106}$$

3.4.6. Implicit Monte Carlo

In general, the Monte Carlo technique performs best for applications with low or moderate optical depth. Since all interaction processes have to be followed individually, the computational efficiency of standard Monte Carlo approaches suffers in optically thick regions. Moreover, the Monte Carlo results will be subject to large fluctuations in this regime, since both the absorption and emission terms, which enter the estimator with opposite sign, are very large. Related to this problem, very short time steps have to be applied in this regime in order to resolve the rapid changes in the emissivity. Fleck & Cummings (1971) presented an *implicit Monte Carlo* (IMC) approach specifically tailored to alleviate some of these challenges. In particular, the proposed technique features a higher accuracy in optically thick calculations and allows for the use of larger time steps, since it partly anticipates the reaction of the ambient material to the evolution of the radiation field. Given these benefits, many recent Monte Carlo radiative transfer approaches incorporate this technique (e.g. Kasen et al., 2011; Abdikamalov et al., 2012; Wollaeger et al., 2013; Roth & Kasen, 2014). We follow these examples and include this approach into our Monte Carlo radiation hydrodynamical method as well. A different strategy to address the optically thick regime was offered by Gentile (2001), who developed a Monte Carlo diffusion scheme (DDMC for discrete diffusion Monte Carlo)[16]. Here, we do not elaborate this technique further but note that recent efforts aim at the development of hybrid schemes, combining the benefits of both DDMC and IMC (e.g. Densmore et al., 2007, 2012; Abdikamalov et al., 2012).

In regions of high optical depth, a great deal of computational power is spent in following the absorption and injection of a large number of Monte Carlo packets, when in fact only the small difference between these contributions simulates the effective energy and momentum transfer terms. The implicit Monte Carlo technique introduces an effective scattering channel replacing this absorption-emission balance, retaining only the imbalance in terms of an effective absorption opacity. This replacement introduces a higher accuracy, since the absorption and successive emission event occur at the same physical location. In the optically thick regime this constitutes a better description of reality than spreading the emission process uniformly over space and time (Fleck & Cummings, 1971). The values of these effective opacities are obtained by solving the radiative transfer and internal energy equation implicitly by introducing appropriate time-centred values for the internal energy and specific intensity.

Due to the implicit solution, this technique also soothes the restriction on the duration of the simulation step. In fact, Fleck & Cummings (1971) demonstrate that their approach is formally unconditionally stable. This is very important in the radiation hydrodynamical context, since the characteristic time scales of the radiative source terms [see Eq. (3.122)] are often much shorter than the fluid flow scale, captured by the CFL criterion. Exactly for this reason, we include the implicit Monte Carlo technique in our radiation hydrodynamical approach. In their recent publication of a similar numerical technique for radiation hydrodynamics, Roth & Kasen (2014) highlight the benefits of the implicit Monte Carlo scheme, which constitutes a cornerstone of their method. Fleck & Cummings (1971) provide a detailed derivation and description of the implicit scheme, also for non-grey application. Here, we only briefly sketch the technique for the grey case.

---

[16] See also Densmore et al. (2007), Cleveland et al. (2010) and Densmore et al. (2012) for a further development of DDMC.

Assuming that grey absorption processes and thermal emission are the only radiation–matter interactions, the one-dimensional radiative transfer problem may be described by [see Eqs. (2.35) and (2.40)][17]

$$\frac{1}{c}\frac{\partial}{\partial t}I + \mu\frac{\partial}{\partial x}I + \chi I = \frac{1}{2}\chi c a_{\mathrm{R}} T^4, \tag{3.107}$$

$$\frac{\partial}{\partial t}\varepsilon = \chi\left(\int_{-1}^{1}\mathrm{d}\mu\, I - c a_{\mathrm{R}} T^4\right) + S. \tag{3.108}$$

Here, ε denotes the internal energy density of the ambient material and $a_{\mathrm{R}} = 4\sigma_{\mathrm{R}}/c$ the radiation constant. We also drop the superscript $^{\mathrm{abs}}$ and implicitly assume that χ describes the absorption opacity. Also, S is introduced, representing all additional source terms inducing changes in the internal energy other than from radiative effects. In the case of radiation hydrodynamics, the fluid dynamical changes of the internal energy may be captured by this quantity. Introducing the equilibrium radiation field energy density

$$E_{\mathrm{R}} = a_{\mathrm{R}} T^4 \tag{3.109}$$

and its relation to the internal energy pool[18]

$$\beta^{-1} = \frac{\partial \varepsilon}{\partial E_{\mathrm{R}}}, \tag{3.110}$$

which for the ideal gas case reduces to

$$\beta = \frac{4E_{\mathrm{R}}}{\varepsilon}, \tag{3.111}$$

the radiative transfer problem may be expressed as

$$\frac{1}{c}\frac{\partial}{\partial t}I + \mu\frac{\partial}{\partial x}I + \chi I = \frac{1}{2}\chi c E_{\mathrm{R}}, \tag{3.112}$$

$$\frac{\partial}{\partial t}E_{\mathrm{R}} = \beta\chi\left(\int_{-1}^{1}\mathrm{d}\mu\, I - c E_{\mathrm{R}}\right) + S. \tag{3.113}$$

Fleck & Cummings (1971) proposed to solve Eq. (3.107) by replacing the instantaneous value for the radiative energy by a time-centred value, $\tilde{E}_{\mathrm{R}}$. For the time interval $[t^n, t^{n+1}]$, the time-centring is achieved by linearly interpolating between the values at the beginning and the end of the interval

$$\tilde{E}_{\mathrm{R}} = \alpha E_{\mathrm{R}}^{n+1} + (1-\alpha)E_{\mathrm{R}}^{n}. \tag{3.114}$$

---

[17] Note that we follow Fleck & Cummings (1971) in this presentation and implicitly perform the angle average with respect to the rotational symmetry of the problem, i.e. we use the specific intensity $\frac{1}{2\pi}\int_0^{2\pi} I \rightarrow I$.

[18] We adopt the notation of Fleck & Cummings (1971) and emphasise that β should not be confused with the relativity parameter.

Relying on the information of the new time step lends this technique its implicit character. The time-centred radiative energy is found by formally integrating Eq. (3.113) and replacing the instantaneous values of β, χ, I and S with their time-averaged counterparts, which are indicated with bars and λ and γ superscripts. The symbols express the possibility of employing different time-centring techniques for the different quantities. After the integration, Eq. (3.113) reads

$$E_{\mathrm{R}}^{n+1} - E_{\mathrm{R}}^{n} = \Delta t \bar{\beta}\bar{\chi}\left(\int \mathrm{d}\mu I^{\lambda} - c[\alpha E_{\mathrm{R}}^{n+1} + (1-\alpha)E_{\mathrm{R}}^{n}]\right) + \bar{\beta}S^{\gamma}\Delta t, \tag{3.115}$$

which finally yields an explicit expression for the time-centred energy

$$\tilde{E} = \frac{\alpha\bar{\beta}\bar{\chi}\Delta t}{1+\alpha\bar{\beta}c\Delta t\bar{\chi}}\int \mathrm{d}\mu\, I^{\lambda} + \frac{E_{\mathrm{R}}^{n}}{1+\alpha\bar{\beta}c\Delta t\bar{\chi}} + \frac{\alpha\bar{\beta}\Delta t S^{\gamma}}{1+\alpha\bar{\beta}c\Delta t\bar{\chi}}. \tag{3.116}$$

If the instantaneous values for the specific intensity, the opacity and β are re-inserted, a modified transfer equation is obtained

$$\begin{aligned}\frac{1}{c}\frac{\partial}{\partial t}I + \mu\frac{\partial}{\partial x}I + \chi I = {}& \frac{1}{2}\chi\left(\frac{\alpha\beta c\Delta t\chi}{1+\alpha\beta c\Delta t\chi}\int \mathrm{d}\mu I\right)\\ &+ \frac{1}{2}\left(\frac{c\chi E_{\mathrm{R}}^{n}}{1+\alpha\beta c\Delta t\chi} + \frac{\chi\alpha\beta c\Delta t S^{\gamma}}{1+\alpha\beta c\Delta t\chi}\right).\end{aligned} \tag{3.117}$$

After identifying the effective absorption and scattering opacities and introducing the Fleck factor f_F,

$$\chi_{\mathrm{eff}}^{\mathrm{abs}} = \frac{1}{1+\alpha\beta c\Delta t\chi}\chi \equiv f_F\chi \tag{3.118}$$

$$\chi_{\mathrm{eff}}^{\mathrm{scat}} = \frac{\alpha\beta c\Delta t\chi}{1+\alpha\beta c\Delta t\chi}\chi \equiv (1-f_F)\chi \tag{3.119}$$

the transfer equation resembles that of an isotropic scattering problem

$$\begin{aligned}\frac{1}{c}\frac{\partial}{\partial t}I + \mu\frac{\partial}{\partial x}I + (\chi_{\mathrm{eff}}^{\mathrm{abs}} + \chi_{\mathrm{eff}}^{\mathrm{scat}})I = {}& \frac{1}{2}\chi_{\mathrm{eff}}^{\mathrm{scat}}\int \mathrm{d}\mu\, I\\ &+ \frac{1}{2}\chi_{\mathrm{eff}}^{\mathrm{abs}}ca_{\mathrm{R}}T^4 + \frac{1}{2}\frac{\chi_{\mathrm{eff}}^{\mathrm{scat}}}{\chi}S^{\gamma}.\end{aligned} \tag{3.120}$$

Using the Fleck factor, the notation simplifies to

$$\begin{aligned}\frac{1}{c}\frac{\partial}{\partial t}I + \mu\frac{\partial}{\partial x}I + \chi I = {}& \frac{1}{2}(1-f_F)\chi\int \mathrm{d}\mu\, I\\ &+ \frac{1}{2}f_F\chi ca_{\mathrm{R}}T^4 + \frac{1}{2}(1-f_F)S^{\gamma}.\end{aligned} \tag{3.121}$$

The magnitude of the effective opacities is directly tuned to the relative importance of the radiative to internal energy and to the strength of the coupling between these pools. This is captured by β and $c\Delta t\chi$, which may be interpreted as the duration of the time step measured in units of the characteristic interaction time scale, $1/(c\chi)$. With increasing importance of the radiative energy pool or stronger coupling, i.e. higher values of β and of $c\Delta\chi$ respectively, the effective scattering opacity increases (see Fig. 3.11). Fleck & Cummings (1971) emphasise the clear advantage of the formulation of Eq. (3.120) over the original pure absorption problem. The Monte Carlo solution to this formulation of the equations is well-behaved, also for $\Delta t \to \infty$, in which case it reduces to a pure scattering problem. It should also be highlighted that the implicit Monte Carlo approach is not restricted to optically thick environments but remains valid and accurate in the free streaming limit.

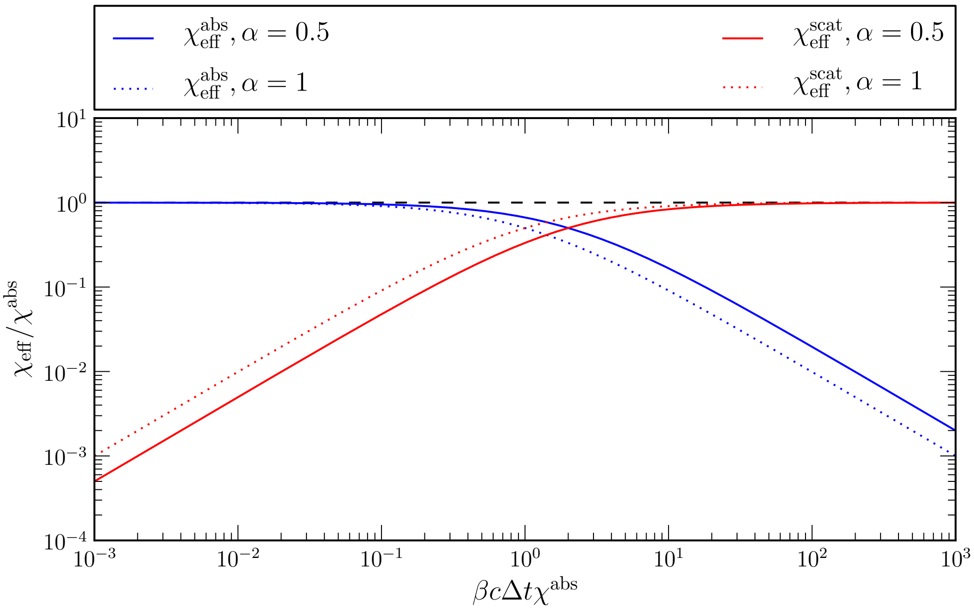

Figure 3.11.: Dependence of the effective scattering opacities on the relative strength of the radiative-to-internal energy (β) and on the radiation–matter coupling ($c\Delta t\chi$). All effective opacities are displayed in units of the true absorption opacity (dashed black line).

To incorporate the implicit scheme in our Monte Carlo formulation we follow the suggestions of Fleck & Cummings (1971) and determine at the onset of the radiative transfer step the effective scattering and absorption opacities according to Eqs. (3.118) and (3.119). Here, we use the state of the fluid at the beginning of the radiative transfer step to determine β. Following Fleck & Cummings (1971), we employ $\alpha = 0.5$ unless $\alpha\beta\Delta t\chi c$ is large, in which case α is set to 1. The Monte Carlo routine is then performed according to the techniques presented in Sections 3.4.3 to 3.4.5, but using the effective opacities in the interaction machinery. We note that unlike Roth & Kasen (2014) we do not include S in our calculation. Following the operator-split idea, we interpret the radiative transfer step as an isolated problem and thus set $S = 0$ (but see discussion in Section 5.3.4).

3.4.7. Characteristic Time Scales

The concept of characteristic time scales associated with source terms has already been introduced in Section 3.2.5 and has been touched upon during the presentation of the implicit Monte Carlo technique in the previous section. A number of characteristic time scales have to be taken into account when incorporating the effect of the radiation field into radiation hydrodynamical calculations by means of operator-splitting. Harries (2011) defined the characteristic cooling

$$t_{\mathrm{cool}} = -\frac{\varepsilon}{cG^0_{\mathrm{abs}}} \tag{3.122}$$

and equilibration time

$$t_{\mathrm{eq}} = \frac{\varepsilon_{\mathrm{eq}} - \varepsilon}{cG^0_{\mathrm{abs}}} \tag{3.123}$$

scales, which have to be resolved in the explicit techniques. Otherwise, non-physical states with negative internal energy may be induced by the numerical scheme and the evolution towards an equilibrium situation may not be properly followed. In the definition of the characteristic time scales, the subscript of the radiation force signifies that only absorption opacities and corresponding emissivities are taken into account. Also, the equilibrium internal energy corresponds to the situation where the gas temperature is equivalent to the radiation temperature, following from

$$T_{\mathrm{eq}} = \left(\frac{\pi J}{\sigma_{\mathrm{R}}}\right)^{\frac{1}{4}}. \tag{3.124}$$

In addition to the direct cooling and heating processes, another effect has to be considered. Imagine a region in the computational domain which strongly emits radiative energy. If this energy subsequently freely streams over some distance and is later absorbed at some other location, two patches of the computational domain are brought into causal contact. In light of the stability discussion in Section 3.3.3, we have to ensure that this process is properly resolved by the temporal discretisation. In other words, this communication process has to be restricted to neighbouring cells. The relevant time scale for this effect is set by the speed with which radiative energy is transported through the computational domain. This is not necessarily given by the light crossing time

$$t_{\mathrm{cross}} = \frac{\Delta x}{c}, \tag{3.125}$$

since radiation–matter interactions slow down the photon propagation. In the extreme case, the radiative energy transport is governed by the diffusion time scale

$$t_{\mathrm{cross}} = \sqrt{3}\frac{\chi}{c}. \tag{3.126}$$

Even though the transport time scale may be very short in optically thin regions, the small interaction probabilities in this case render the constraint less stringent.

3.5. Implementation

After this detailed description of the relevant numerical techniques, we outline their implementation into a computer code. We also comment briefly on differences to previous reports on preliminary implementations of our Monte Carlo radiation hydrodynamics scheme (Noebauer, 2011; Noebauer et al., 2012).

3.5.1. Current Numerical Implementation

Based on the fluid dynamics and radiative transfer techniques introduced in this chapter, we have written a one-dimensional radiation hydrodynamical code for astrophysical applications, referred to as MCRH. The main programming language is `C` and the code relies heavily on the `GNU` scientific library (`GSL`[19]). In particular we use the `GSL` implementation of the *Mersenne twister* generator (Matsumoto & Nishimura, 1998) to provide random numbers for the Monte Carlo radiative transfer calculation. In our operator-splitting scheme, we first solve fluid dynamics with the finite-volume methods outlined in Section 3.3 and then address radiative transfer with the Monte Carlo techniques of Section 3.4. The code can operate on geometrical meshes which are either in plane-parallel or spherical symmetry. The grid is either statically defined or moves with the fluid flow, mimicking the Eulerian or Lagrangian description of fluid dynamics. Apart from the fact that the grid interfaces are changing position during the radiative transfer step, the different numerical grid implementations have no conceptual influence on the Monte Carlo simulation. For the fluid dynamical calculation, we use the implementation of the original PPM algorithm (Colella & Woodward 1984, see Section 3.3.5), written by Philipp Edelmann in the course of his diploma project (Edelmann, 2010), and have combined it with a HLLC Riemann solver (Toro et al. 1994, see Section 3.3.6). We rely on the particular realisation according to Batten et al. (1997). For testing purposes we have also incorporated the option to use a constant reconstruction scheme and the “exact” Riemann solver of Toro (2009). The Monte Carlo radiative transfer simulation is based on the indivisible energy packet formalism of Abbott & Lucy (1985) and Lucy (1999a). The basic implementation operates in the grey approximation. Later, we present an extension of this scheme that includes frequency-dependent resonance-line interactions to address the radiative acceleration in stellar winds (see Chapter 6). Important radiation field properties are reconstructed by using volume-based Monte Carlo estimators following Lucy (1999a), Lucy (2003) and Lucy (2005) (see Section 3.4.5). Additionally, we have incorporated the possibility to reconstruct the radiation quantities with the direct counting technique to verify the estimator results. The radiative transfer step may either be performed in the traditional explicit fashion or using the implicit technique of Fleck & Cummings (1971, see Section 3.4.6). According to the

---

[19] We use version 1.15. The documentation and source code may be obtained at `https://www.gnu.org/software/gsl/`.

values for the radiation force, G^0 and G^1, determined in the radiative transfer calculation, the fluid energy and momentum are updated in the final step of the splitting algorithm:

$$\Delta u = \Delta t \frac{G^1}{\rho}, \tag{3.127}$$

$$\Delta e = \Delta t \frac{cG^0}{\rho}. \tag{3.128}$$

We explicitly enforce that true scattering interactions do not change the internal energy of the ambient material. For this purpose, only the fluid momentum is updated according to the radiation force in pure scattering calculations. The total material energy change results from variations in the kinetic energy pool only:

$$\Delta e = \frac{1}{2}\left[(u + \Delta u)^2 - u^2\right]. \tag{3.129}$$

3.5.2. Comparison with Previous Work

Some of the foundations for interfacing a Monte Carlo radiative transfer machinery with a fluid dynamical method were laid during the preceding diploma project (Noebauer, 2011). The current radiation hydrodynamical implementation bears little resemblance with the rudimentary code presented therein. Among the most significant changes and improvements are the inclusion of spherically symmetric grids, the incorporation of the implicit Monte Carlo scheme, the replacement of the k-packet treatment of absorption interactions (after Lucy 2003; see Noebauer 2011, chap. 3.2.5) by the more accurate and powerful direct treatment of this interaction channel, the development of more accurate Monte Carlo estimators, in particular for scattering interactions, the use of a relativistically correct initialisation scheme and the reliance on a more robust Riemann solver. Part of these extensions developed in the course of this PhD project have already been presented in Noebauer et al. (2012). Moreover, an entirely new set of sophisticated test calculations is set up, chosen and designed to carefully verify each aspect of the radiation hydrodynamical approach. The associated testing processes reach far beyond the basic calculations performed in Noebauer (2011). Now, the accuracy of the code implementation is assessed by deriving quantitative fidelity measures, comparing the results with analytic and approximate solutions and confronting the outcome with simulations performed with alternative numerical codes. In the next chapter, we present these test calculations in detail.

4. Test and Verification Calculations

The previous chapters have been dedicated to the introduction of the theoretical foundation of radiation hydrodynamics and the description of our numerical approach. Before using the resulting scheme for the modelling of astrophysical radiation hydrodynamical problems, we carefully examine the physical accuracy of the proposed technique and review its computational efficiency. We are particularly interested in the effect of the stochastic fluctuations, which are inherent to the Monte Carlo scheme, on the overall performance, stability and accuracy. In the course of this process, we also explore how many Monte Carlo quanta are required to achieve satisfactory results. These tasks are performed in a series of well-defined test problems for which the solution is either accessible in terms of analytic formulations or approximate expressions. By comparing with the results obtained with alternative fluid dynamics, radiative transfer and radiation hydrodynamics codes, we position our proposed method in terms of accuracy and performance within the realm of numerical approaches to radiation hydrodynamics.

The verification and validation process is a crucial step in the development of new numerical schemes and also in the re-implementation of already known techniques. By applying the numerical code to well-defined test problems and comparing the results with the analytic solution, the physical accuracy of the proposed numerical scheme can be established. Moreover, this process serves to isolate the physical parameter regime in which the numerical methods excel and to identify the circumstances under which they should not be applied. In addition, the test calculations help in assessing the computational costs of the techniques. In cases of using already established numerical approaches, the verification process is equally important. In this situation, its prime purpose lies in ensuring the correct implementation of the numerical methods. Since our Monte Carlo radiation hydrodynamics method incorporates well-known fluid dynamics techniques, such as PPM and HLLC, but constitutes in its entirety a new approach to solve the radiation–matter coevolution, we pursue in the verification process all of the above mentioned objectives.

For the testing process, a set of simple and well-defined problems is required, for which the solution is either known analytically or is available in terms of approximate expressions. Moreover, these test calculations should probe different aspects of the numerical approach, in order to provide a differential analysis of the proposed method. For the sub-problems of fluid dynamics and radiative transfer a large number of test problems is available (see Sections 4.1 and 4.2), fulfilling both requirements. The situation is slightly more challenging for the full radiation hydrodynamical problem, since only a handful of suitable verification problems are known (see Section 4.3) as pointed out by Ensman (1994). Many of the test calculations presented here are considered "standard" and are frequently used when introducing new numerical frameworks. Thus, repeating these simulations and confronting the outcome with published results or with calculations that are obtained with other available numerical approaches, the proposed technique may be set into context to other radiation hydrodynamical methods regarding performance and accuracy.

In the following, we present the results of our code verification process, starting with investigating the fluid dynamical and radiative transfer sub-problems separately (see Section 4.1 and Section 4.2 respectively). After establishing the correct working of these steps, the full radiation hydrodynamical scheme is verified in a final set of test calculations (see Section 4.3). Note that some of these simulations have already been presented in Noebauer et al. (2012). Also, if not mentioned otherwise, all test calculations rely on an ideal gas equation of state with $\gamma = 5/3$ and the mean molecular weight of neutral hydrogen and are performed on Eulerian grids.

4.1. Fluid Dynamics Tests

The performance of numerical fluid dynamics methods is typically tested by considering so-called *shocktube* problems (see Section 4.1.2). These constitute the physical realisation of the Riemann problem and consist of two initially constant fluid states which are separated by a diaphragm. After removing the diaphragm, the two states come into contact and form the typical elementary wave pattern (see Section 3.3.6). Using this type of setup has the advantage that the full non-linear properties of the fluid dynamical problem are tested and that an analytic solution is accessible, at least for the simple cases of only one initial discontinuity[1]. In addition to the shocktube problems, other common hydrodynamical tests include the propagation of linear waves (e.g. Sekora & Stone, 2010), the advection of passive scalars (see Section 4.1.1) and the self-similar evolution of blast waves (see Section 4.1.3).

Our fluid dynamical splitting step relies on well-known numerical schemes whose numerical properties have been extensively studied and whose physical accuracy have been established. Thus, the main purpose of testing our fluid dynamical module lies in verifying the correct implementation of the numerical techniques outlined in Section 3.3. In all the fluid dynamics tests presented in the following, the radiative transfer module is deactivated.

4.1.1. Advection

First we investigate the performance of the Mcrh hydrodynamics solver in the linear regime. For this purpose, we consider the advection of a tracer substance by the constant fluid flow[2]. In the absence of any gradients in the thermodynamic pressure and in a stationary flow with no

---

[1] See Woodward & Colella (1984) for a famous shocktube problem with two initial jumps in the fluid state.

[2] We implicitly assume that the tracer material has no influence on the dynamics of the fluid, i.e. we consider a *passive scalar*.

spatial velocity variations, the density may be interpreted as the advected tracer. In this case, the fluid dynamical equations reduce to

$$\frac{\partial}{\partial t}\rho + u\frac{\partial}{\partial x}\rho = 0. \tag{4.1}$$

With $u = \text{const}$, the evolution of the density is given by a simple translation of its initial profile $\rho(x, t = 0) = \rho_0(x)$:

$$\rho(x, t) = \rho_0(x - ut). \tag{4.2}$$

Testing and verifying the advection properties of a numerical fluid dynamics approach is of particular important, since advection processes always contribute to the full fluid dynamical evolution. For example, resolving and maintaining contact discontinuities is closely related to the ability of numerical schemes to accurately deal with advection.

We use the propagation of a Gaussian density pulse to test the advection behaviour of our PPM scheme and verify its correct implementation. We consider a plane-parallel box of length $L = 1\,\mathrm{cm}$, subdivided into 128 grid cells, in which the fluid material moves with the speed $u = 1\,\mathrm{cm\,s^{-1}}$. The initial density profile contains a Gaussian spike and has the shape

$$\rho_0(x) = 1 + \exp\left(-256(x - 0.5)^2\right). \tag{4.3}$$

We ensure the absence of any thermodynamic pressure gradients by adjusting the temperature profile:

$$T_0(x) \sim \rho_0(x)^{-1}. \tag{4.4}$$

To mimic an infinite extent of the fluid material, we employ periodic boundary conditions. This implies that the fluid state in the ghost cells is an exact copy of the properties of the outermost region at the opposite side of the computational domain. From Eq. (4.2) we expect that, in the absence of any numerical errors, after each passage through the computation domain, i.e. after $\Delta t = 1\,\mathrm{s}$, the density pulse coincides with the initial setup. In Fig. 4.1, the results of the advection simulation are shown for $t = 2\,\mathrm{s}$ and compared with the analytic solution. To better judge the fidelity of our calculations, we also include the results of two other numerical PPM implementations, PROMETHEUS[3] (Fryxell et al., 1989) and ATHENA (Stone et al., 2008), into the comparison. Our calculated density profile matches the expected Gaussian shape very well[4] and also agrees with the results of the two reference calculations. Only in the peak region of the Gaussian pulse some flattening in the numerical results obtained with MCRH and PROMETHEUS occurs (see blow-up in Fig. 4.1). This is a well-known property of PPM and may be remedied by using the improved limiter of Colella & Sekora (2008). Since ATHENA incorporates this

---

[3] Like our fluid dynamical method, this multidimensional and multi-purpose hydrodynamics code relies on the finite-volume prescription and uses the PPM reconstruction scheme.

[4] Note that we switch off the discontinuity detection capability of PPM (Colella & Woodward, 1984, eqs. 1.15 - 1.17, 3.2). Otherwise, the algorithm wrongly distorts the Gaussian pulse. This behaviour of PPM was commented on by Woodward et al. (2013, Appendix) as well.

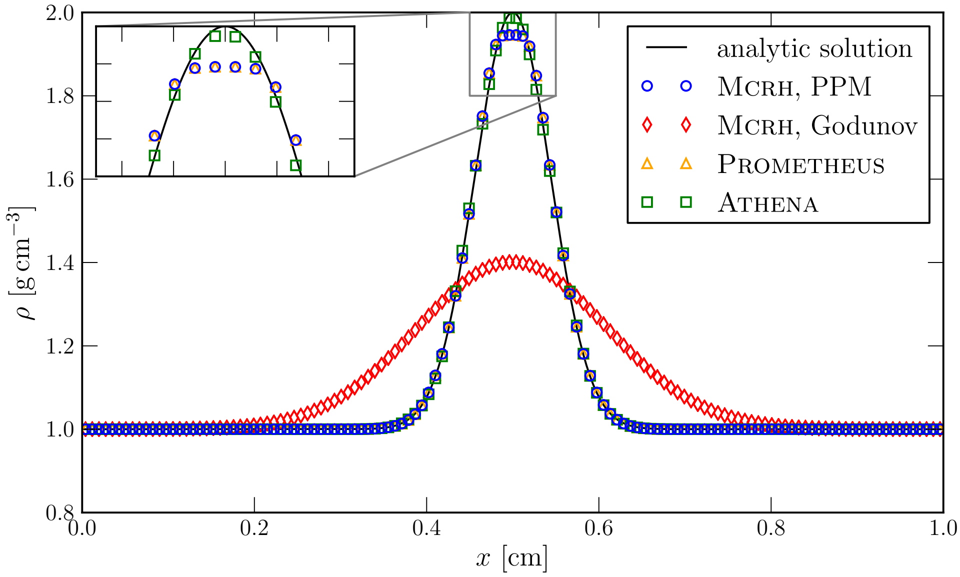

Figure 4.1.: Results of the advection of a Gaussian density pulse after $t = 2\,\mathrm{s}$. The analytic solution according to Eq. (4.2) is plotted as the solid black line. The MCRH results are shown by the blue circles for the calculation with PPM and red diamonds for the simulation with the constant reconstruction scheme. As a comparison, the results of corresponding calculations with PROMETHEUS and ATHENA are included by the yellow triangles and green squares. The blow-up shows a zoom-in to the peak region of the Gaussian pulse and illustrates the benefits of the improved limiter of Colella & Sekora (2008), which is incorporated in ATHENA.

algorithm, the corresponding numerical results reproduce the solution near the extremum much better. To illustrate the benefits of a high-order scheme, Fig. 4.1 also includes the results of a MCRH simulation that uses the simple constant reconstruction algorithm. The high dispersion of the Gaussian pulse after only two passages clearly highlights the advantage of high-order reconstruction schemes in retaining an accurate solution in smooth regions.

The confrontation between the numerical results and the analytic solution in Fig. 4.1 already suggests the correct implementation of the fluid dynamical techniques in the linear regime. To fortify this statement, we quantify the numerical error and investigate its dependence on the spatial resolution. Commonly, error assessments in computational fluid dynamics are based on the L_p norm, which is generally defined as (e.g. LeVeque, 2002, chap. 8.1.1)

$$L_p(\Delta Q) = \left(\sum_i \Delta x_i |\Delta Q_i|^p \right)^{1/p} . \tag{4.5}$$

Here, ΔQ_i denotes the error in the fluid property Q in the cell i. If a convergent numerical scheme has been constructed (see Section 3.3.3), the overall error vanishes with increasing grid resolution. The rate with which the error decreases is commonly referred to as the *order* n of a numerical scheme (e.g. LeVeque, 2002, chap. 8.5)

$$L_p(\Delta Q) \sim \Delta x^n + \mathcal{O}(\Delta x^{n+1}). \tag{4.6}$$

We follow Sekora & Stone (2010) and estimate the convergence rate, R, and thus the order of our scheme via Richardson extrapolation,

$$R = \frac{\log L_p(\Delta Q^r) / \log L_p(\Delta Q^{r+1})}{\log \Delta x^r / \log \Delta x^{r+1}}, \tag{4.7}$$

which relates the error of two calculations with increasing resolution, r and $r+1$. In Fig. 4.2, we compare the L_2 numerical error and the associated convergence rate of the results obtained with our PPM implementation with calculations performed with PROMETHEUS and ATHENA. With the observed convergence rate of roughly 2.5 for all three numerical implementations of PPM, the numerical error behaves as expected given the labelling of this method as a high-order scheme. Note that the improved limiter does not affect the convergence rate significantly but reduces the absolute deviations slightly (see left panel in Fig. 4.2). In summary, the observed error convergence in the advection problem and the excellent agreement of our MCRH results with the analytic solution and with other PPM implementations support and verify the correct behaviour of our numerical realisation of fluid dynamics, at least in the linear regime.

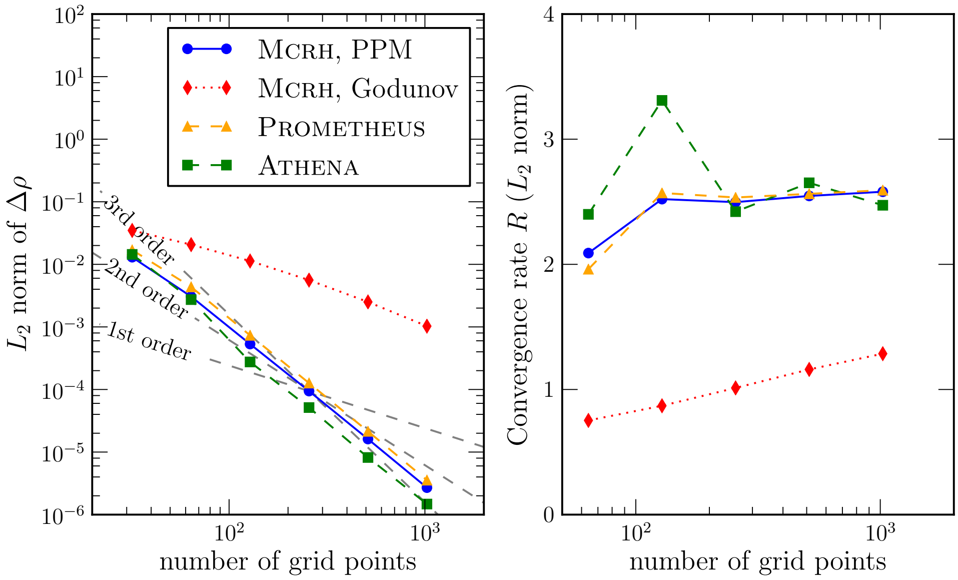

Figure 4.2.: The absolute error for the Gaussian advection test (see Fig. 4.1) is shown in the left panel for a number of different resolutions as measured by the L_2 norm. For this, the computational domain of length $L = 1\,\mathrm{cm}$ is discretised by an increasing number of grid cells. On the right, the corresponding convergence rate is shown. For comparison, the results of simulations with PROMETHEUS and ATHENA are also displayed. To guide the eye, first, second and third order convergence rates are indicated by dashed black lines.

4.1.2. Sod-Shocktube

A particular setup for a shocktube problem was proposed by Sod (1978) and has been used extensively for the verification of numerical approaches to fluid dynamics. We use this application to test the performance of our PPM implementation in the non-linear regime. Following Sod (1978), we define a Riemann problem with[5]

$$\begin{aligned} \rho_l &= 1, \quad \rho_r = 0.1 \\ u_l &= 0, \quad u_r = 0 \\ p_l &= 1, \quad p_r = 0.125 \end{aligned} \tag{4.8}$$

in a plane-parallel box with $L = 1\,\mathrm{cm}$ and the discontinuity at the centre

$$\begin{pmatrix} \rho_0 \\ u_0 \\ p_0 \end{pmatrix} = \begin{cases} \begin{pmatrix} \rho_l \\ u_l \\ p_l \end{pmatrix} & \text{for} \quad x \leq \frac{L}{2} \\ \begin{pmatrix} \rho_r \\ u_r \\ p_r \end{pmatrix} & \text{for} \quad x > \frac{L}{2}. \end{cases} \tag{4.9}$$

For this particular choice of initial conditions, an elementary wave pattern with a rarefaction fan propagating to the left and with a shock moving to the right emerges. As mentioned in Section 3.3.6, both waves enclose a contact discontinuity, which in this case also moves to the right. In Fig. 4.3, the wave pattern calculated with the fluid dynamical module for a box with 128 cells is displayed in terms of the density, clearly showing the three elementary waves. The final fluid state at $t = 0.2\,\mathrm{s}$ is compared with the exact solution in Fig. 4.4, exhibiting excellent agreement. The analytic solution for this Riemann problem is determined with the techniques detailed in Toro (2009, chap. 4).

The deviation from the analytic solution and its evolution with increasing spatial resolution is displayed in Fig. 4.5. Here, we also show the results obtained from a corresponding calculation with ATHENA. In both cases, the error decreases with higher resolution, but only exhibits roughly first order convergence. This stems from the fact that the error in shocktube problems is generally dominated by the deviations at the discontinuities. Here, the PPM algorithm reduces the reconstruction algorithm to the lower-order constant scheme in order to avoid spurious oscillations. Thus, a low convergence rate is expected (see Woodward & Colella, 1984, for a discussion of convergences rates of PPM in non-linear problems). Consequently, the behaviour of MCRH in the non-linear regime, as revealed by the Sod-Shocktube problem, gives further confidence into our implementation of the fluid dynamical solver.

---

[5] In cgs units.

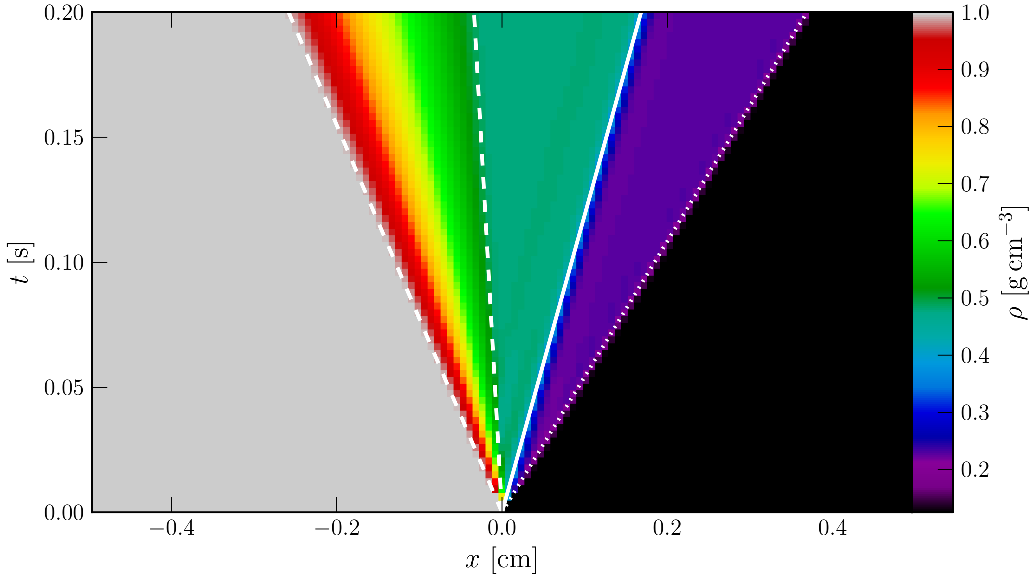

Figure 4.3.: Evolution of the density in the Sod-Shocktube problem as determined with our fluid dynamical implementation. The elementary wave pattern is clearly visible, consisting of a rarefaction wave propagating to the left, a contact discontinuity and a shock wave, both moving to the right. The theoretical characteristics for the elementary waves of the Riemann problem are highlighted by the white lines – the solid line denotes the central contact discontinuity, the dashed lines mark head and tail of the rarefaction fan and the expected shock position is shown by the dotted line.

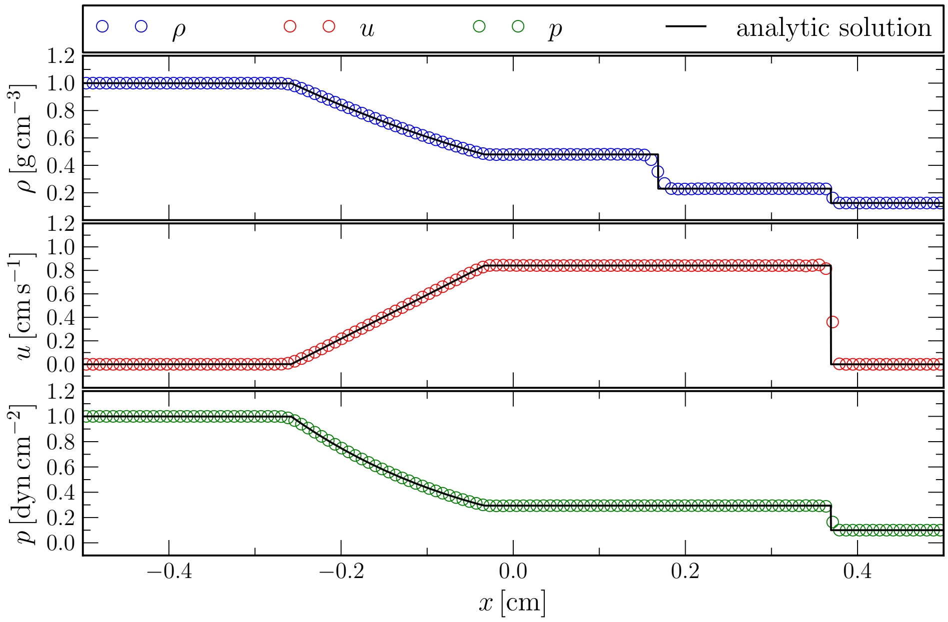

Figure 4.4.: Fluid state at the final snapshot, $t = 0.2\,\mathrm{s}$ for the Sod-Shocktube problem. The solid black lines depict the expected density, velocity and pressure profiles, determined with the methods of Toro (2009, chap. 4). Overplotted are the results obtained in our fluid dynamical calculations, showing excellent agreement with the exact solution.

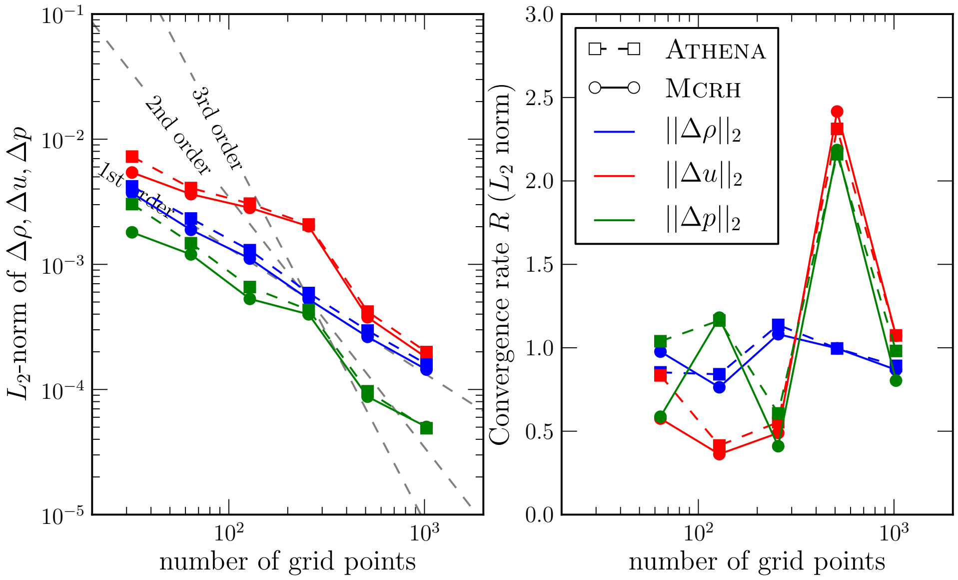

Figure 4.5.: Evolution of the deviation between the calculated and expected fluid state (density in blue, velocity in red, pressure in green) in the Sod-Shocktube problem with increasing grid resolution (left panel). We compare our results obtained with MCRH (solid, circles) with the corresponding calculations performed with ATHENA (dashed, squares). In both cases and for all fluid properties, first order convergence is observed, which is expected for problems with a discontinuous fluid state. The convergence rate as measured by the L_2 norm is shown in the right panel.

4.1.3. Taylor-Sedov Blast Wave

In the final verification calculation for the fluid dynamical module of MCRH we focus on its ability to handle spherically symmetric flows. For this purpose we consider the so-called Taylor-Sedov blast wave, a common test problem for multidimensional fluid dynamical methods. A self-similar solution for this problem of a point explosion in a cold ambient medium was independently found by von Neumann (1941), Taylor (1941) and Sedov (1946). Initiated by the instantaneous injection of a predefined amount of energy at one location, which then acts as the centre of the explosion, a spherical shock front propagates through the ambient material. After time t, the blast wave reaches the location[6]

$$R_s = \left(\frac{Et^2}{\alpha\rho_0}\right)^{\frac{1}{5}}, \tag{4.10}$$

measured from the explosion centre. Here, α is a constant that depends on the adiabatic index of the fluid material. A full discussion of the self-similar solution may, for example, be found in Sedov (1959), Landau & Lifshitz (1959) and Castor (2007). Kamm (2000) outlines a numerical scheme to construct Sedov solutions.

We use the Taylor-Sedov blast wave to verify the correct behaviour of our fluid dynamical implementation in spherically symmetric flow geometries. However, instead of directly generating the blast wave by the injection of energy in the central radial shell, we follow Buchler et al. (1997) and initiate the simulation with a pre-established explosion profile and verify its self-similar evolution. For this, we consider a sphere with $R_{\max} = 7 \times 10^{19}\,\mathrm{cm}$ and divide it into 256 equidistant shells. An initial Sedov profile is constructed with the numerical routine of Wongwathanarat (2014) for $t_0 = 3.4 \times 10^{10}\,\mathrm{s}$, a deposited energy of $E = 10^{51}\,\mathrm{erg\,cm^{-3}}$ and an ambient medium with the constant fluid state $\rho_0 = 1 \times 10^{-25}\,\mathrm{g\,cm^{-3}}$, $u_0 = 0$ and $P = 1.4 \times 10^{-13}\,\mathrm{dyn\,cm^{-2}}$. This particular choice of parameters represents the setup of a Taylor-Sedov test calculation presented by Wongwathanarat et al. (2010). The evolution of the initial fluid state is followed using the hydrodynamical module of MCRH and is shown in Fig. 4.6, clearly demonstrating the spreading of the spherical shock front. After reaching the time $t = 2.36 \times 10^{11}\,\mathrm{s}$, the calculated profiles of the fluid properties are compared with the self-similar solution, again determined with the routine of Wongwathanarat (2014). As illustrated by Fig. 4.7, the MCRH results agree very well with the theoretical solution of the problem. Only in the region around $r = 5 \times 10^{19}\,\mathrm{cm}$, small deviations are present. These are artefacts of the initialisation process, specifically of mapping the analytic solution onto the finite-volume grid. In Fig. 4.6, the origin of these deviations at the initial location of the blast wave and the following propagation are clearly visible in the fluid velocity panel. However, the strength of these artefacts decreases with increasing grid resolution, giving additional support to a relation with the initial mapping process.

---

[6] In the expression for the shock radius, we implicitly assume a constant initial density profile and a spherical expansion. For the more general case of a power-law density profile (first investigated by Korobeilnikov et al. 1961) and for the blast wave propagation in planar and cylindrical geometries, see for example Sedov (1959); Book (1994); Kamm (2000) and Kamm & Timmes (2007).

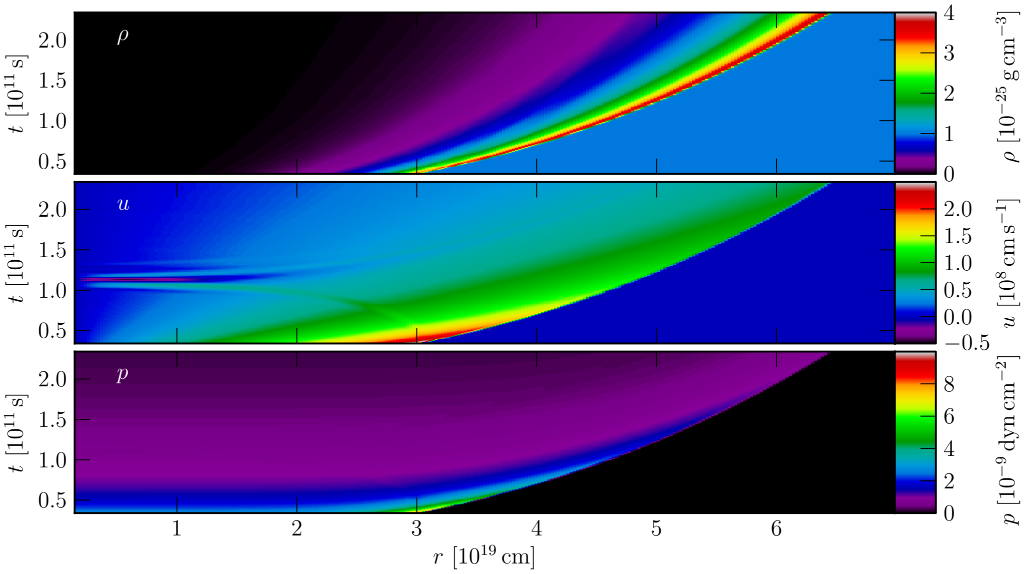

Figure 4.6.: The three panels show the evolution of the fluid state in the Taylor-Sedov Blast Wave test. The density, velocity and gas pressure (from top to bottom) are colour-coded and displayed in the $r \times t$ plane.

The excellent overall agreement of the calculated fluid properties with the analytic solution, in particular at the spherical shock front, further supports our fluid dynamical implementation and together with the preceding test calculations strongly suggests a correct numerical realisation of the hydrodynamical techniques presented in Section 3.3. In the following, we investigate the accuracy and performance of the radiative transfer step and its coupling to the fluid dynamical calculation.

4.2. Radiative Transfer Tests

In the testing of the radiative transfer module, we focus on investigating the packet propagation process and the accurate determination of the radiation field properties within the estimator reconstruction scheme. We also take this opportunity to scrutinise the Monte Carlo noise behaviour of our scheme. For this purpose, we consider the test problems presented in Harries (2011) and in Abdikamalov et al. (2012), repeating some of these calculations. Here, we deactivate the fluid dynamical evolution in Mcrh and only test its radiative transfer module.

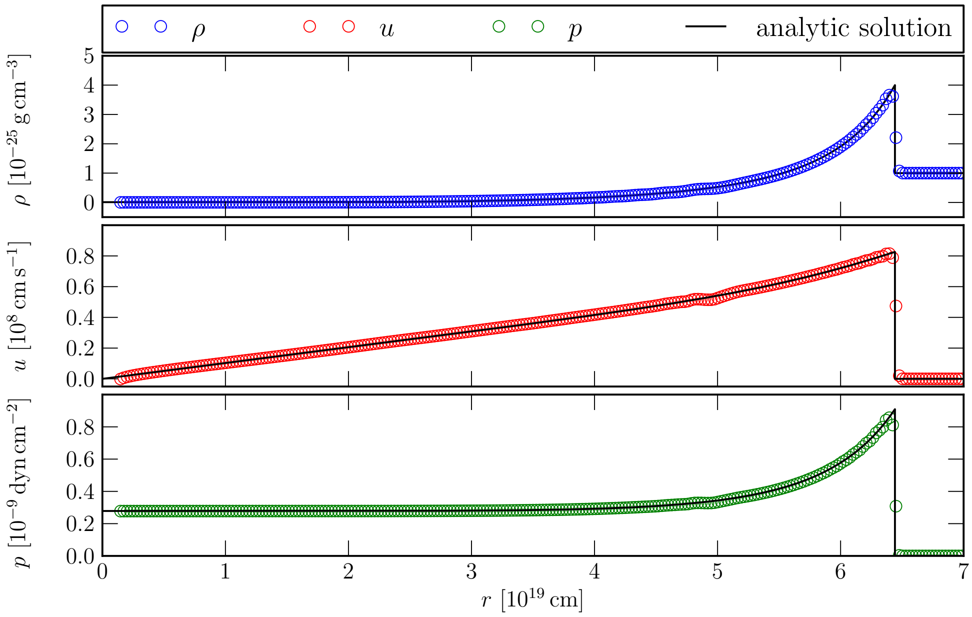

Figure 4.7.: Comparison between the final MCRH snapshot at $t = 2.36 \times 10^{11}$ s (coloured circles) of the Taylor-Sedov Blast Wave calculation and the theoretical self-similar solution (solid black line). The panels show, from top to bottom, the fluid density (blue), velocity (red) and gas pressure (green).

4.2.1. Optically Thick Diffusion

A particularly instructive problem to verify the correct behaviour of the Monte Carlo packet propagation routine is posed by the dispersion of a Gaussian energy pulse in the diffusion limit. Only if all aspects of the propagation process, i.e. determining distances to grid cell interfaces, calculating interaction locations and storing packet properties at the end of a time step, are implemented correctly, the expected evolution of the initial radiative energy profile is obtained. Harries (2011) formulated the Gaussian diffusion problem as a test case for Monte Carlo codes in planar symmetry and Abdikamalov et al. (2012) presented the corresponding simulation in spherical symmetry. We repeat these calculations in order to verify the performance of the radiative transfer module in both geometrical configurations.

In the diffusion limit ($\tau \rightarrow \infty$) and in a purely scattering medium with constant opacities, the radiative transfer equation reduces to[7]

$$\frac{\partial}{\partial t} E(\mathbf{x}, t) - D \nabla^2 E(\mathbf{x}, t) = 0, \tag{4.11}$$

with the diffusion constant

$$D = \frac{c}{3\chi}. \tag{4.12}$$

In this limit, a Gaussian energy pulse, centred around $\mathbf{x}_0$, evolves according to (e.g. Swesty & Myra, 2009; Abdikamalov et al., 2012; Sumiyoshi & Yamada, 2012)

$$E(\mathbf{x}, t) = E_0 \left(\frac{t_0}{t_0 + t} \right)^{\omega} \exp\left(- \frac{|\mathbf{x} - \mathbf{x}_0|^2}{4D(t_0 + t)} \right), \tag{4.13}$$

which may be directly verified by inserting into Eq. (4.11). Here, E_0 denotes the initial height of the Gaussian profile and t_0 is related to its initial width d_0 via

$$d_0 = \sqrt{4Dt_0}. \tag{4.14}$$

The exponent ω depends on the dimensionality N of the problem:

$$\omega = N/2. \tag{4.15}$$

Thus, for the plane-parallel application, it equals 1/2 and for the spherical case 3/2.

Following Abdikamalov et al. (2012), we perform the test calculations in a spherical computational domain which extends from $r = 0$ to $r = 3 \times 10^7\,\mathrm{cm}$. Radiative matter interactions are restricted to scatterings, which are described by a constant opacity of $\chi = 2 \times 10^{-4}\,\mathrm{cm}^{-1}$. The resulting total optical depth of $\tau = 6 \times 10^3$ warrants the use of the diffusion approximation. The

---

[7] See, for example, Mihalas & Mihalas (1984, §80) or Castor (2007, chap. 4.4) for a derivation of the diffusion approximation.

initial radiative energy profile is centred[8] at $r = 0$, has the properties $E_0 = 10^3\,\mathrm{erg\,cm^{-3}}$ and $d_0 = 10^6\,\mathrm{cm}$ and is discretised by 2×10^5 Monte Carlo packets. The dispersion of this energy pulse in spherical symmetry is followed with our Monte Carlo radiative transfer scheme and shown in Fig. 4.8. The same figure also displays the corresponding results for a calculation in a plane-parallel configuration. In contrast to Noebauer et al. (2012), we also initiate this simulation with an pre-established Gaussian pulse analogously to the spherical calculation. Again, we place the centre of the initial profile at $x_0 = 0$ and consider the domain from $x = -3 \times 10^7\,\mathrm{cm}$ to $x = 3 \times 10^7\,\mathrm{cm}$. Since now the full pulse is treated, the number of Monte Carlo packets is doubled (4×10^5 packets) to achieve the same statistics as in the spherical case. As illustrated by the comparison in Fig. 4.8, the agreement between the Monte Carlo results and the theoretical expectation according to Eq. (4.13) is excellent, suggesting the correct working of the basic Monte Carlo machinery both in plane-parallel and spherical geometry.

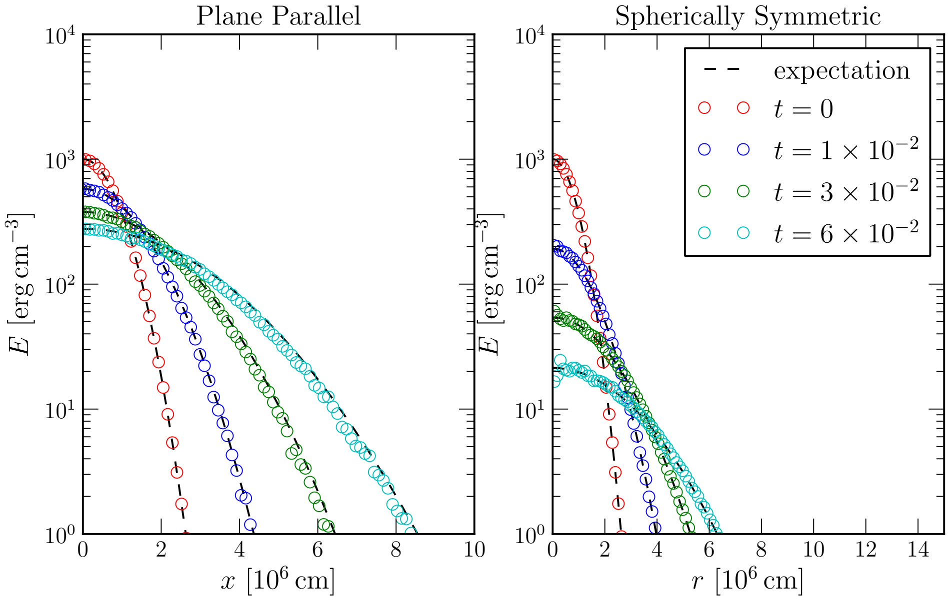

Figure 4.8.: Diffusion of a Gaussian radiative energy profile in plane-parallel (left panel) and spherically symmetric (right panel) geometry. For a number of snapshots, the calculated radiative energy profile (open circles) is compared in both cases with the analytic solution (dashed black) to the problem according to Eq. (4.13). For the plane-parallel calculation, only one half of the pulse ($x \geq 0$) is displayed.

---

[8] Note that Eq. (4.13) is only valid for spherical diffusion if $\mathbf{x}_0 = 0$. This may be easily checked by inserting this expression into the spherical counterpart to Eq. (4.11) with $\nabla^2 = \frac{1}{r^2}\frac{\partial}{\partial r}\left(r^2 \frac{\partial}{\partial r}\right)$.

4.2.2. Scattering Atmosphere

The reconstruction routines and the associated challenge of controlling the statistical fluctuations inherent to the Monte Carlo approach are equally important to the propagation-related processes. An instructive test problem, ideally suited to investigate these aspects, is posed by the homogeneous, grey scattering atmosphere (e.g. Abdikamalov et al., 2012). In this problem, a central source emits radiation at luminosity L_0 into a spherical shell of material which extends up to r_{max} and in which the incident radiation may scatter isotropically. Hummer & Rybicki (1971) showed that in case of a power-law opacity

$$\chi = r^{-n} \tag{4.16}$$

with $n > 1$, the stationary solution has a constant luminosity throughout the atmosphere. Thus, in addition to investigating the reconstruction method and the Monte Carlo noise, this problem serves as a test case for the performance of the propagation scheme in the presence of non-uniform opacities. We follow Abdikamalov et al. (2012) and consider a spherical domain of radius $r_{\mathrm{max}} = 5 \times 10^6\,\mathrm{cm}$. For the central source, we carve out a small sphere of $r_{\mathrm{source}} = 1 \times 10^2\,\mathrm{cm}$ and inject radiative energy at luminosity $L_0 = 6.5 \times 10^{48}\,\mathrm{erg\,s^{-1}}$ through this inner boundary. Thus, a number of new packets, corresponding to the energy injection rate, are newly created at the lower boundary during each time step. They are launched uniformly over the time step and along an initial propagation direction sampled from[9] (see, e.g., Lucy, 1999a)

$$\mu = \sqrt{z}. \tag{4.17}$$

The power law index for the scattering opacity is set to $n = 1.1$ and the computational domain is subdivided into 200 grid cells. Using the Mcrh radiative transfer module, the evolution of the injected radiative energy is followed until a stationary state has established. This is shown in Fig. 4.9 in terms of the measured luminosity

$$L(r) = 4\pi r^2 F(r), \tag{4.18}$$

which is determined from the reconstructed first moment of the specific intensity, together with the expected constant luminosity, L_0. The measured values agree with the analytic solution to the problem, however, clearly exhibit the typical Monte Carlo behaviour by fluctuating about the exact solution. The strength of these fluctuations decreases, as expected, if the number of packets and thus the sample size in the underlying Monte Carlo counting experiments increases. Figure 4.10 quantifies this statement by displaying the standard deviation in the luminosity with different numbers of packets. Our results clearly follow the expected trend and decrease with the inverse square root of the sample size. In Fig. 4.10 we also show the variance in the luminosity when applying the direct counting reconstruction scheme. Again, the deviation decreases with

---

[9] This implies that no limb darkening (e.g. Mihalas, 1978, chap. 3.3) is present.

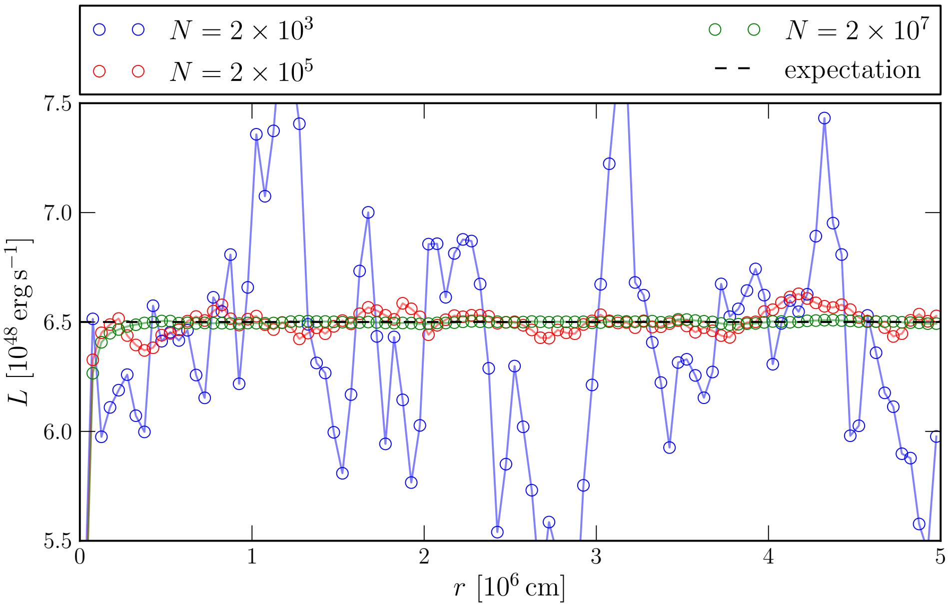

Figure 4.9.: Calculated luminosity in the Scattering Atmosphere Test. The analytic solution, given by $L(r) = L_0$, is shown as the dashed black line. In colour, the results of calculations with different numbers of Monte Carlo packets representing the steady state are shown. These calculations already indicate the decrease in the Monte Carlo noise with increasing sample size, a result which is properly quantified in Fig. 4.10.

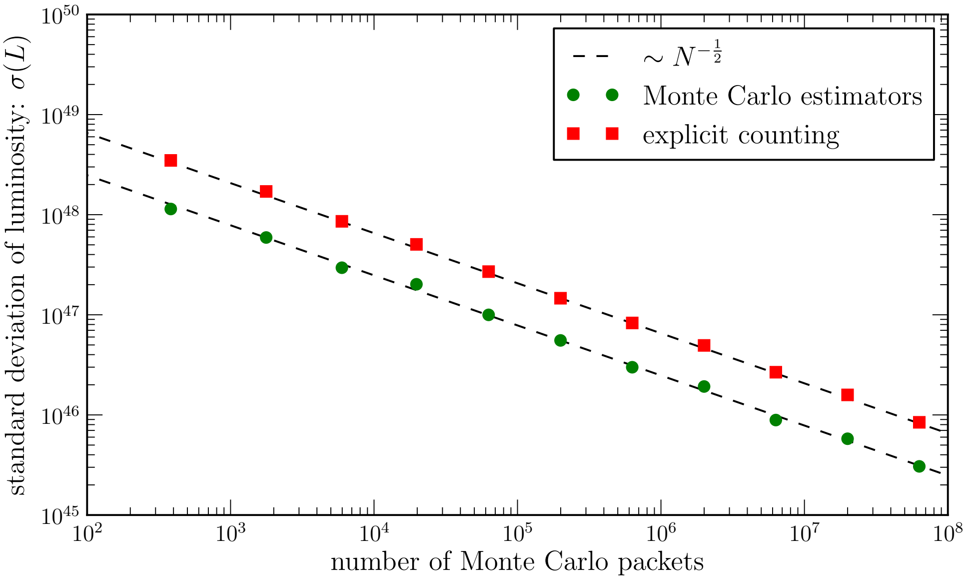

Figure 4.10.: The standard deviation in the reconstructed luminosity as a function of the number of Monte Carlo packets in the computational domain after the stationary state has established. The results of both reconstruction schemes, the volume-based estimator formalism (green circles) and the direct counting approach (red squares), are shown and compared with the expected trend, $\sim N^{-\frac{1}{2}}$. Both schemes exhibit the expected noise behaviour, but the estimator approach yields smaller absolute deviations.

larger sample sizes and follows the $N^{-\frac{1}{2}}$ trend. The higher absolute noise level in the direct counting results clearly advocates the use of the volume-based estimator formalism and lends credence to its superiority. Nevertheless, one has to bear in mind that the noise difference between the two reconstruction schemes depends on the properties of the investigated problem, in particular on the duration of the time step. If a small time step has to be used, for example due to characteristic time scale restrictions, the noise benefits of the estimator formalism abate. In the limit of very short time steps, the number of contributions to the estimator and to the final balancing in the direct counting picture converge, since packets do not have sufficient time to perform multiple events and consequently only contribute once to the estimator sums. For the test calculation at hand, we are interested in the steady-state solution and the dynamical effect of the radiation field on the ambient material is neglected. Thus, no immediate constraint is imposed on the duration of the radiative transfer step and the relation between the noise behaviour of the estimator scheme and the length of the time step may be investigated. In Fig. 4.11, the standard deviations of the two reconstruction techniques are compared and shown as functions of the time step duration. By using the same number of Monte Carlo packets to represent the steady-state radiation field, 2×10^6 packets, the statistical fluctuations of the direct counting results remain on the same level even if the time step duration changes. By contrast, the

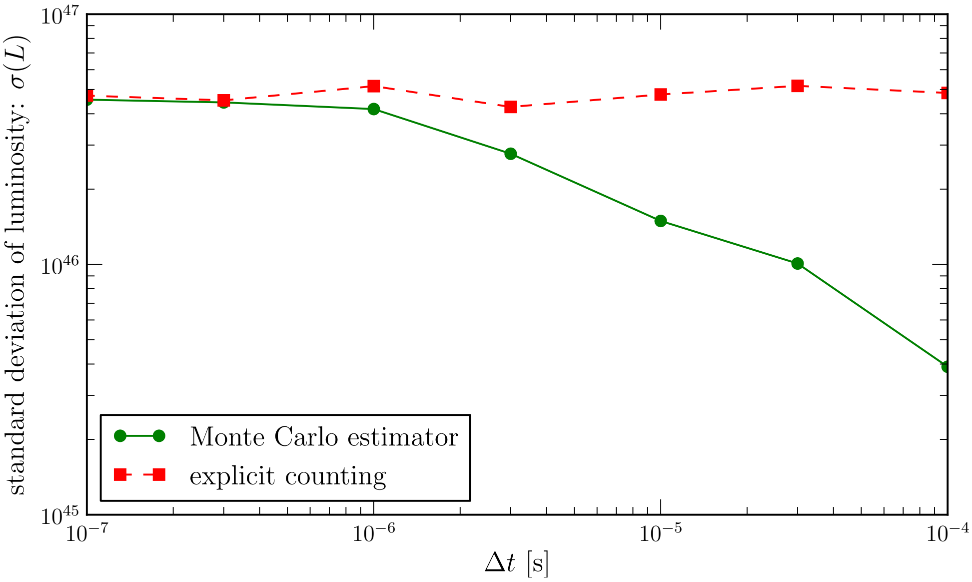

Figure 4.11.: Standard deviation of the direct counting and estimator reconstruction schemes as a function of the time step length. For small step sizes, the noise level is the same in both formalisms, since packets are not able to perform multiple events during the time step and thus only contribute once to the volume-based estimators. With increasing cycle duration, however, packets may contribute multiple times, thus leading to a decrease in the Monte Carlo noise of the estimator scheme.

accuracy of the estimator formalism clearly depends on the step size. Exhibiting the same noise behaviour as the direct counting scheme for short time steps, the fluctuation strength decreases with longer durations of the cycles, since packets may now contribute multiple times to the estimator according to the trajectory segments which link the different numerical and physical events the packets experience during the step.

Based on these results, we conclude that relying on the volume-based estimator formalism is always beneficial. Its noise behaviour never falls below that of the direct counting approach but may be significantly higher under favourable conditions. We emphasise, that the above investigation was restricted to the reconstruction of the specific intensity and its moments. The formalism for determining the energy and momentum terms is scrutinised in a different test calculation (see Section 4.3.1).

4.2.3. Homogeneous Sphere

So far only scattering interactions have been considered in the test calculations. However, in radiation hydrodynamics, absorption and emission processes often have to be incorporated, since they allow for energy transfer between the radiation field and the internal energy of the ambient material. Thus, in the final verification problem for the pure radiative transfer module of Mcrh, we focus on the working of the absorption and emission machinery. For this, we follow Abdikamalov et al. (2012) and consider a homogeneous sphere with constant emissivity and absorption opacity. Outside the sphere of radius R, no sources or sinks are present, thus radiation emerging from the sphere may stream freely. The analytic solution for the steady state was formulated, for example, by Smit et al. (1997). With the constant source function B and absorption opacity χ^{abs} inside the sphere, the steady-state specific intensity is given by

$$I(r,\mu) = B\left(1 - \mathrm{e}^{-\chi^{\mathrm{abs}} s(r,\mu)}\right), \tag{4.19}$$

with

$$s(r,\mu) = \begin{cases} r\mu + Rg(r,\mu) & \text{if} \quad r < R \\ 2Rg(r,\mu) & \text{if} \quad r \geq R, \quad \sqrt{1 - \left(\frac{R}{r}\right)^2} \leq \mu \leq 1 \\ 0 & \text{else} \end{cases} \tag{4.20}$$

and

$$g(r,\mu) = \sqrt{1 - \left(\frac{r}{R}\right)^2 (1 - \mu^2)}. \tag{4.21}$$

Adopting the parameters for this problem from Abdikamalov et al. (2012), in particular $R = 10^6$ cm, $B = 10\,\mathrm{erg\,cm^{-2}\,s^{-1}}$ and $\chi^{\mathrm{abs}} = 2.5 \times 10^{-4}\,\mathrm{cm^{-1}}$, we follow the evolution of the radiation field inside and outside the sphere in a spherical computational domain, extending from $r = 0$ to 5×10^6 cm and encompassing 100 equidistant grid cells. The resulting steady-state radiation field calculated with Mcrh is shown in Fig. 4.12 and compared with the analytic solution according to Eq. (4.19). During each simulation step, 10^7 packets represent the thermal emission in the sphere. The solid angle integration to obtain the expected mean intensity and the higher moments of the specific intensity is performed using numerical quadrature. To ensure the correct treatment of packet absorption and injection in planar geometries, we also present in the same figure the corresponding results of a homogeneous "plane", using the same simulation parameters as listed above. Applying the formal solution to the radiative transfer equation in planar symmetry [see Eq. (2.79) and Chandrasekhar (1960, chaps. 7 and 9)] and inserting the problem-specific form of the source function, the steady-state specific intensity follows:

$$I(r,\mu) = \begin{cases} B & \text{if} \quad 0 \le x \le R \\ B & \text{if} \quad R < x, \quad 0 \le \mu \le 1 \\ 0 & \text{else} \end{cases} . \tag{4.22}$$

This implies a mean intensity of

$$J(x) = \begin{cases} B & \text{if} \quad 0 \le x \le R \\ \frac{1}{2}B & \text{if} \quad R < x \end{cases} , \tag{4.23}$$

and the following higher moments of the specific intensity:

$$H(x) = \begin{cases} 0 \\ \frac{1}{4}B \end{cases} , \qquad K(x) = \begin{cases} \frac{1}{3}B & \text{if} \quad 0 \le x \le R \\ \frac{1}{6}B & \text{if} \quad R < x \end{cases} . \tag{4.24}$$

The excellent agreement between our results and the analytic solution confirms the correct working of the absorption and emission machinery of the Monte Carlo scheme in both geometries. When combined with the results of the other radiative transfer test calculations, we conclude that the basic routines governing the packet propagation process and the reconstruction of the radiation field quantities operate accurately and reliably. In the next step, we complete the general verification process by investigating the coupling to the ambient material.

4.3. Radiation Hydrodynamics Tests

The previous verification process focused on testing the fluid dynamical and radiative transfer techniques separately by considering the operator splitting steps as isolated problems. To ensure the physical accuracy and computational feasibility of the entire radiation hydrodynamical approach, we account for the interdependence of fluid dynamics and radiative transfer in the final set of test calculations. Here, we gradually approach the full radiation hydrodynamical coupling by first solely including the coevolution of the radiative and the internal gas energy. Then, in a

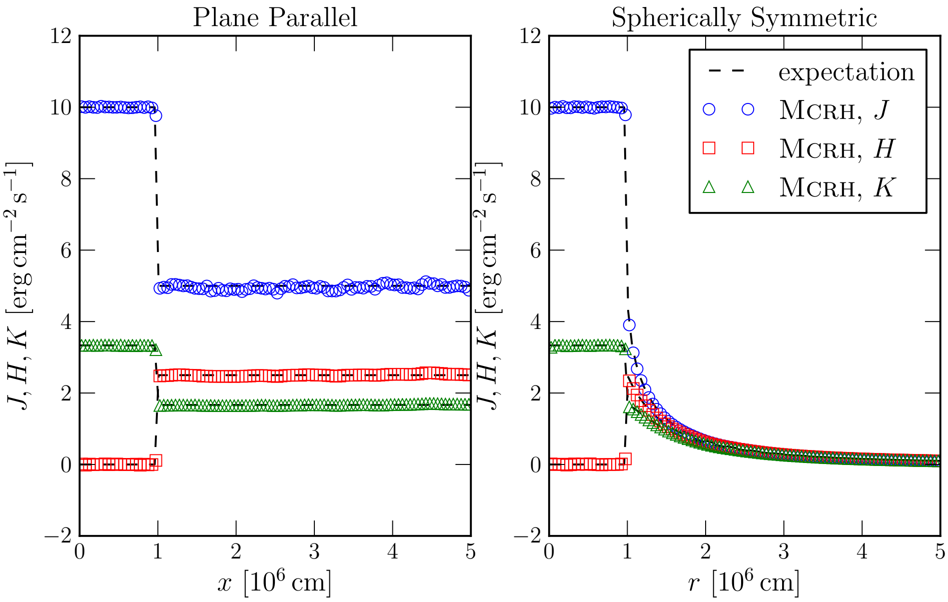

Figure 4.12.: Comparison between the first three moments of the specific intensity, calculated with MCRH (coloured symbols) and the analytic solution (dashed black) for the homogeneous plane (left panel) and sphere (right panel) test problems. The theoretical profiles follow from Eqs. (4.23) and (4.24) in the planar case and from numerical integration of Eq. (4.19) in the spherical case.

final test problem, dealing with the structure of radiative shocks, a full radiation hydrodynamical calculation, accounting for energy and momentum coupling, is performed.

4.3.1. Equilibration Calculations

By investigating the equilibration behaviour of a radiation–matter system which is initialised far from the equilibrium solution, we pose a first test on the applicability and accuracy of our operator-splitting approach to the radiation hydrodynamical coupling problem. For the numerical realisation of the test calculations, we adopt the configuration proposed by Turner & Stone (2001) and extended in Harries (2011). Versions of these test calculations have already been presented in Noebauer et al. (2012), but in less detail. We consider a purely absorbing gas in a plane-parallel box. If the radiation field or the gas temperature are initially set to non-equilibrium values, i.e. not fulfilling

$$J = \frac{\sigma_{\mathrm{R}}}{\pi} T^4, \tag{4.25}$$

the internal and radiative energy, E_{G} and E_{R}, evolve towards the equilibrium state according to

$$\frac{\partial}{\partial t} E_{\mathrm{G}} = \chi^{\mathrm{abs}} \left(c E_{\mathrm{R}} - 4 \sigma_{\mathrm{R}} T^4(E_{\mathrm{G}}) \right), \tag{4.26}$$

$$\frac{\partial}{\partial t} E_{\mathrm{R}} = - \frac{\partial}{\partial t} E_{\mathrm{G}}. \tag{4.27}$$

Following Harries (2011), we first consider the case in which the initial radiation field energy is much larger than the internal energy of the gas. For this configuration, the temporal change in the radiative energy pool may be neglected and Eqs. (4.26) and (4.27) reduce to a single ordinary differential equation. The test calculation is set up in a plane-parallel simulation box of length $L = 4\,\mathrm{cm}$ and with 4 grid cells[10]. A purely absorbing gas at rest with $\rho = 10^{-7}\,\mathrm{g\,cm^{-3}}$ and opacity $\chi^{\mathrm{abs}} = 4 \times 10^{-8}\,\mathrm{cm^{-1}}$ is considered. 10^6 Monte Carlo packets discretise the initial radiation field with, $E_{\mathrm{R}} = 10^{12}\,\mathrm{erg\,cm^{-3}}$. Under these circumstances, the equilibrium state of the ambient material is given by the internal energy density $E_{\mathrm{G}}^{\mathrm{eq}} = 4.228 \times 10^7\,\mathrm{erg\,cm^{-3}}$. This value may be obtained by inserting the initial radiative energy density into Eq. (4.25) and converting the resulting equilibrium gas temperature into an internal energy density. Initialising the equilibration calculations with[11] $E_{\mathrm{G}} = 10^{10}\,\mathrm{erg\,cm^{-3}}$ and, in the second case, with $E_{\mathrm{G}} = 10^2\,\mathrm{erg\,cm^{-3}}$, the resulting evolution towards equilibrium is shown in Fig. 4.13 (c.f. Noebauer et al., 2012, fig. 3) and compared with the expected trend following Eq. (4.26). The general agreement is excellent, which is further quantified in the lower panel of the same figure, displaying the relative deviation of the numerical Mcrh results from the expected solution. The approximately constant error is a consequence of the splitting approach and the use of logarithmically-increasing time steps

---

[10] The general code infrastructure of Mcrh requires a minimal domain size of 4 cells, owing to the PPM reconstruction.

[11] Note the obvious misprint of the initial internal energy in the legend of fig. 3 in Noebauer et al. (2012).

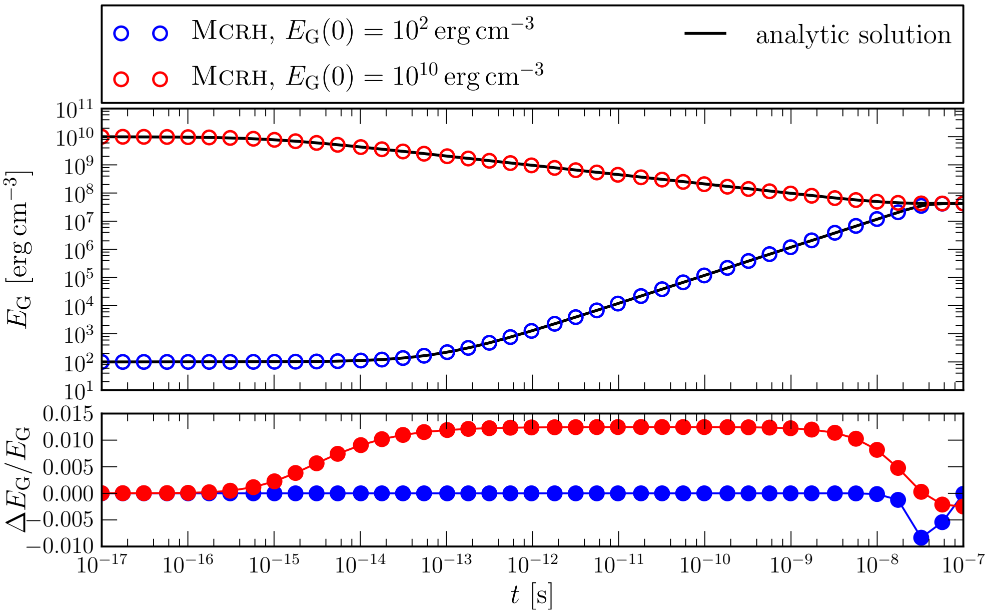

Figure 4.13.: Evolution of the internal energy density in the equilibration tests of Harries (2011). The MCRH results, depicted by open circles, are compared with the expected trend, E_G^{an}, following from Eq. (4.26) and shown as the black solid lines. The relative deviation from the analytic solution is shown for both calculations, with the initial internal energy below (blue) and above (red) the equilibrium value, in the lower panel. Specifically, $(E_G^{\mathrm{an}} - E_G)/E_G^{\mathrm{an}}$ is plotted. Also note that not all 410 logarithmically-spaced time steps of the interval $[10^{-17}\,\mathrm{s}, 10^{-7}\,\mathrm{s}]$ are shown, but only 41 representative ones.

(see also Noebauer et al., 2012, fig. 3 and associated discussion). Since the emissivity is assumed constant during the splitting step, it cannot adapt to the continuous decrease of the gas temperature during the time step, thus inducing a slightly too high a cooling rate. The error remains roughly constant, since the slowdown of the temperature decline and the associated decrease in the splitting error is compensated by using longer time steps. Only when the equilibrium value for the internal energy is approached, the numerical error drops. In the case of the low initial value for the internal gas energy, the error, as measured in the lower panel of Fig. 4.13, has a different sign. The relative error is, however, much smaller than in the corresponding calculation with high initial gas energy. During the rise of the gas energy at the beginning of the calculation, its evolution is dominated by the radiative heating process, $\chi^{\mathrm{abs}} c E_{\mathrm{R}}$. Since this term remains constant throughout the calculation, the numerical splitting error only becomes noticeable in the vicinity of the equilibrium region. Here, the cooling rate is of comparable size to the heating contribution.

We emphasise that the magnitude of the error in the equilibration tests scales with the length of the time step or the number of steps in the case of a logarithmic subdivision of the entire time interval. This general feature of the splitting approach (see Section 3.2.5) is illustrated in Fig. 4.14, in which the relative deviation from the expected internal energy evolution is shown for different numbers of logarithmically spaced time steps. A decrease of the numerical error with shorter time steps is clearly observed.

In the third equilibration test problem, we also include the evolution of the radiation field energy. The same basic simulation parameters as listed above are adopted, but the initial internal energy is set to $E_{\mathrm{G}} = 10^8\,\mathrm{erg\,cm^{-3}}$ and no radiative energy is initially present in the simulation box. For this choice of parameters, the full system of equations, Eqs. (4.26) and (4.27), has to be solved to obtain the expected evolution of the radiative and gas internal energy pools. In Fig. 4.15 (c.f. Noebauer et al., 2012, fig. 4), the MCRH results are compared with the expected trends, showing excellent agreement. While the numerical error of the gas energy exhibits the same behaviour as in the previous equilibration tests, the deviation in the radiation energy is governed by Monte Carlo noise, at least at the beginning where only few packets reside in the simulation box. At the end of the simulation, the radiation field is represented by about 8×10^4 packets.

The equilibration test calculations are ideally suited to illustrate the benefits of the estimator approach for the reconstruction of the radiation force terms. As pointed out in Section 3.4.5, the strategy of counting interaction events, despite being intuitive, fails in optically thin regions, in which only few or even no packets interact. In the estimator scheme, on the other hand, each packet contributes according to its interaction probability, leading to a well-behaved reconstruction technique also in optically thin regimes. This behaviour of the estimator approach and the deficits of the counting technique are strikingly illustrated in Fig. 4.16. Here, the evolution of the radiation force is shown for the equilibration calculation of Fig. 4.13 with the low initial gas internal energy: results obtained with the two different reconstruction techniques are compared with

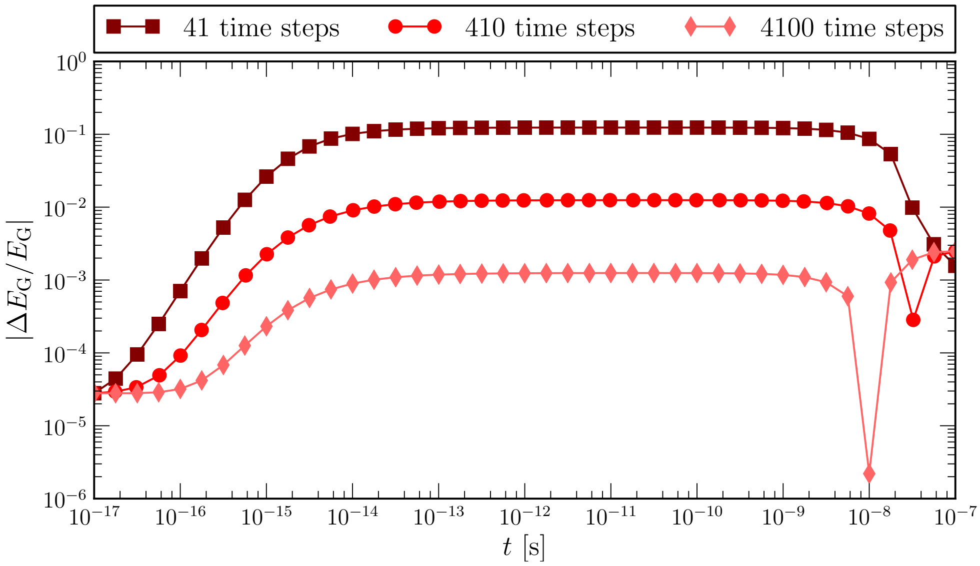

Figure 4.14.: Absolute values of the relative deviation of the calculated internal energy from the expected trend for a series of equilibration tests, equivalent to the high initial internal energy calculation presented in Fig. 4.13. The calculations differ only in the duration of the radiative transfer time steps, with the simulation time $[10^{-17}\,\mathrm{s}, 10^{-7}\,\mathrm{s}]$ being subdivided into 41 (dark red boxes), 410 (red circles, same as in Fig. 4.13) and 4100 (light red diamonds) logarithmically spaced simulation cycles. The relative error is measured analogously to Fig. 4.13, but its absolute value is now shown logarithmically to highlight the different magnitudes.

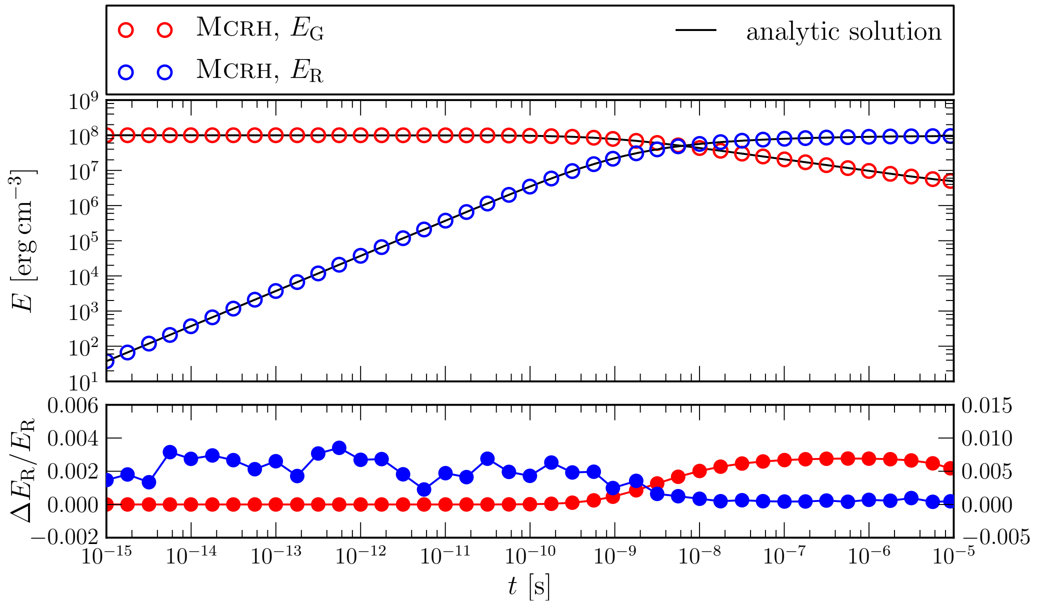

Figure 4.15.: Evolution of the internal (red circles) and radiative energy density (blue circles) in the equilibration test of Harries (2011) with no initial radiation field. The MCRH results (circles) are compared with the expected behaviour of the two energy pools (solid black line) according to Eqs. (4.26) and (4.27). In the lower panel, the relative deviation, measured in the same fashion as in Fig. 4.13, is plotted. Note, however, that the errors for internal and radiative energy do not share the same ordinate axis.

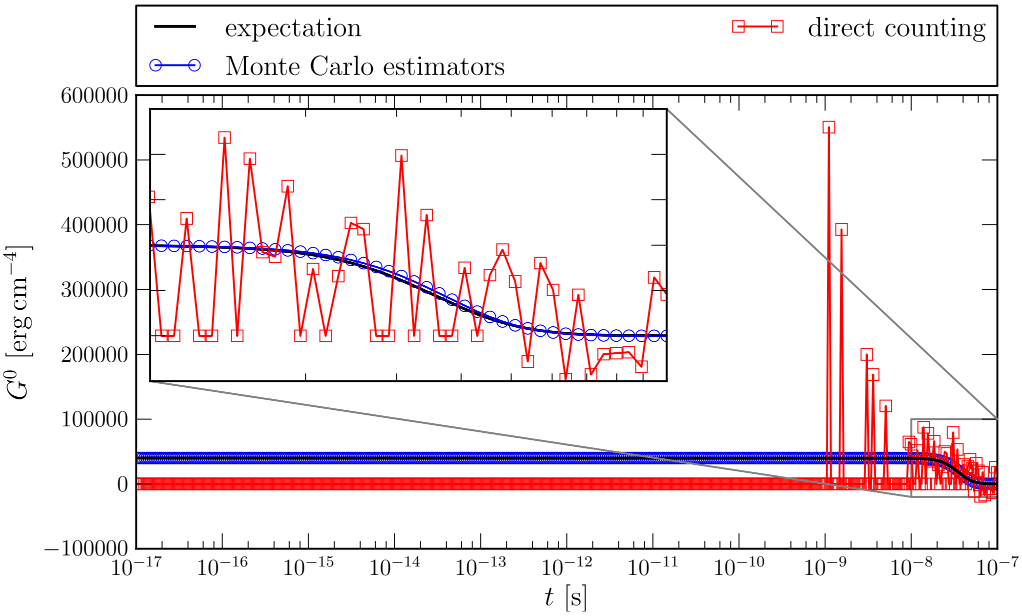

Figure 4.16.: Evolution of the radiation force component G^0, determined in the direct counting approach (red line and squares) and with the Monte Carlo estimators (blue line and circles), for the equilibration test with low initial internal gas energy (the same test as presented in Fig. 4.13). As a reference, the theoretically expected trend according to Eq. (4.26) is shown as the solid black line.

the analytic solution according to Eq. (4.26). The direct counting method yields indeterminate results for early times, in which the short duration of the time step and the low gas temperature prohibit any explicit packet absorption or emission events. Only at later times (see detail in Fig. 4.16), when the time step duration gradually approaches the characteristic mean interaction time, some packets experience an interaction event and contribute to the direct counting scheme. Nevertheless, even here the results are subject to much larger statistical fluctuations than the estimator values, which accurately track the theoretically expected trend of the energy transfer rate at all times. This behaviour highlights the superiority of the estimator approach over the intuitive direct counting scheme and, together with the findings of Section 4.2.2, argues strongly for generally relying on Monte Carlo estimators to reconstruct radiation field properties.

The successful outcome of all equilibration tests provides evidence that our numerical framework constitutes a valid approach to simulate the radiation–matter coevolution. In particular, incorporating a Monte Carlo radiative transfer approach via operator splitting yields physically accurate results in the simple energy-only coupling case. Further evidence to substantiate the applicability of our Monte Carlo approach to radiation hydrodynamics is gathered in the following test calculations, which go beyond equilibrium considerations.

4.3.2. Thermalisation Waves

In the equilibration test calculations, bulk motions of the radiation field were absent. The next logical step in the verification process is to include this additional dynamical component in the context of *thermalisation waves*. These phenomena are well-suited for testing radiation hydrodynamical schemes, since analytic expressions for the evolution of the material and radiation field properties may be formulated based on various assumptions. Consequently, thermalisation waves, in particular the realisation described by Marshak (1958), are commonly used to verify and validate numerical radiation hydrodynamical schemes (e.g. Hayes & Norman, 2003; Hayes et al., 2006; Sekora & Stone, 2010; Jiang et al., 2012). In the following we briefly introduce the thermal wave concept and discuss the particular incarnation according to Pomraning (1979), which we use to test our radiation hydrodynamical approach. For a more general and detailed discussion of this topic, the reader is referred to Zel'dovich & Raizer (1967, chap. 10). Useful summaries with a particular focus on radiative processes may be found in Mihalas & Mihalas (1984, §103) and Castor (2007, chap. 12.1).

Thermalisation waves may be interpreted as the conductive transport of energy, mediated by an energy flux which results from temperature gradients (Mihalas & Mihalas, 1984, §103):

$$\rho c_v \frac{\partial}{\partial t} T = \nabla \cdot (K \nabla T). \tag{4.28}$$

Here, c_v denotes the heat capacity of the ambient material and K its conductivity. Since the conduction time scale for astrophysical problems is typically much shorter than the characteristic time scale on which the ambient material is set into motion, changes in the material momentum may be neglected and a static medium may be considered (Mihalas & Mihalas, 1984, §103). The thermal wave phenomenon is also of astrophysical importance, since it may for example serve as an approximate description of stellar radiation shining onto the interstellar material after star formation (Mihalas & Mihalas, 1984, §103). Depending on the temperature dependence of the conductivity, linear and non-linear conduction waves can be realised.

Marshak (1958) studied a particular realisation of the non-linear conduction case. Here, a cold medium with semi-infinite extent is penetrated by a radiation front which emerges from the inner boundary. Marshak (1958) described the radiation–matter system in the equilibrium diffusion approximation, assumed Rosseland mean opacities[12] and imposed a constant temperature, T_0, at the inner boundary, $x = 0$, and zero temperature and radiative flux towards the outer edge of the domain, $x \to \infty$. Doing so, Marshak (1958) found a self-similar solution for the resulting non-linear conduction problem. The identified wave structure is commonly referred to as a *Marshak wave*.

Due to the approximations used, in particular the constant temperature boundary and the use of equilibrium diffusion, the Marshak wave propagates through the ambient medium too fast and also heats it too quickly (Mihalas & Mihalas, 1984, §103). As a consequence, Pomraning (1979) investigated the same problem with non-equilibrium diffusion techniques, i.e. allowing for different radiation[13] and gas temperatures. In this approximation, the internal and radiative energy evolution is governed by[14]

$$\frac{\partial}{\partial t}E_{\mathrm{R}} - \frac{\partial}{\partial z}\left(\frac{c}{3\chi^{\mathrm{abs}}(T)}\frac{\partial}{\partial z}E_{\mathrm{R}}\right) = c\chi^{\mathrm{abs}}(T)\left(a_{\mathrm{R}}T^4 - E_{\mathrm{R}}\right) \tag{4.29}$$

$$c_v(T)\frac{\partial}{\partial t}T = c\chi^{\mathrm{abs}}(T)\left(E_{\mathrm{R}} - a_{\mathrm{R}}T^4\right). \tag{4.30}$$

Instead of assuming a temporally constant temperature at the inner boundary, which is rather non-physical as pointed out by Castor (2007, chap. 12.1), the following condition is imposed, assuming an incident radiative flux of F_{inc}:

$$E_{\mathrm{R}}(z=0,t) - \left(\frac{2}{3\chi^{\mathrm{abs}}(T(z=0,t))}\right)\frac{\partial}{\partial z}E_{\mathrm{R}}(z=0,t) = \frac{4}{c}F_{\mathrm{inc}}. \tag{4.31}$$

This corresponds to the common strategy of including a black body radiation source by considering the constant emergent hemisphere flux. To remove the non-linearity and obtain a feasible problem, Pomraning (1979) ignored the temperature dependence of the opacity and assumed a particular form of the material heat capacity:

$$c_v(T) = \alpha T^3. \tag{4.32}$$

---

[12] These opacities typically scale with T^6 or T^7 (Mihalas & Mihalas, 1984, §103).

[13] The radiation temperature may be obtained by inverting Eq. (4.25).

[14] We introduce z as the spatial coordinate to be compatible with Pomraning (1979) and Su & Olson (1996).

With these simplifications, the introduction of the parameter

$$\varepsilon = \frac{4a_{\mathrm{R}}}{\alpha}, \tag{4.33}$$

and the dimensionless quantities

$$\begin{aligned} x &= \sqrt{3}\chi^{\mathrm{abs}} z, & \tau &= \varepsilon c \chi^{\mathrm{abs}} t, \\ u &= \frac{c}{4}\frac{E_{\mathrm{R}}}{F_{\mathrm{inc}}}, & v &= \frac{c}{4}\frac{a_{\mathrm{R}}T^4}{F_{\mathrm{inc}}}, \end{aligned} \tag{4.34}$$

the evolution equations [Eqs. (4.29) and (4.30)] reduce to

$$\varepsilon\frac{\partial u}{\partial \tau} - \frac{\partial^2 u}{\partial x^2} = v - u, \tag{4.35}$$

$$\frac{\partial v}{\partial \tau} = u - v. \tag{4.36}$$

Pomraning (1979) derived an analytic solution to the non-equilibrium thermalisation wave problem for $\varepsilon = 0$. This restriction corresponds to an infinite light propagation speed. With the additional simplification $u = v$, the original Marshak wave problem would be obtained. For the more general case, $\varepsilon \neq 0$, Pomraning (1979) only provided solutions in terms of integral expressions. The problem was revisited by Su & Olson (1996), who solved these integrals numerically for $\varepsilon = 0.1$ and $\varepsilon = 1$. We use the tabulated values for the latter case as a reference in our test calculations.

Since the comparison with the reference values of Su & Olson (1996) is performed in the non-dimensional form of Pomraning (1979), the particular choice of physical parameters for the test calculation is somewhat arbitrary. We consider an ambient material of $\rho = 1\,\mathrm{g\,cm^{-3}}$ and $\chi^{\mathrm{abs}} = 1\,\mathrm{cm^{-1}}$, which is at rest and at zero gas temperature. The material resides in a plane-parallel box of length $L = 11.547\,\mathrm{cm}$, which corresponds to the non-dimensional location $x = 20$, the maximum value for which Su & Olson (1996) recorded numerical solutions. To realise the particular temperature dependence of the heat capacity, we replace the ideal gas equation of state by one which resembles a radiation gas, i.e. $E_{\mathrm{G}} = a_{\mathrm{R}}T^4$. This corresponds to the case $\varepsilon = 1$. Within the Monte Carlo approach we realise the inner boundary condition by injecting in each simulation cycle new packets uniformly in time, with propagation directions chosen from Eq. (4.17). These discretise the flux

$$F_{\mathrm{inc}} = \sigma_{\mathrm{R}} T_0^4. \tag{4.37}$$

Here, T_0 denotes the temperature of the hypothetical perfect black body and is set to $T_0 = 1\,\mathrm{K}$ for our calculations. With this choice of simulation parameters, we follow the thermalisation of the cold ambient medium with MCRH. The resulting internal and radiative energy profiles are shown in Fig. 4.17 for a number of snapshots in terms of the dimensionless quantities of Eq. (4.34) and compared with the numerical values of Su & Olson (1996). The agreement between the MCRH

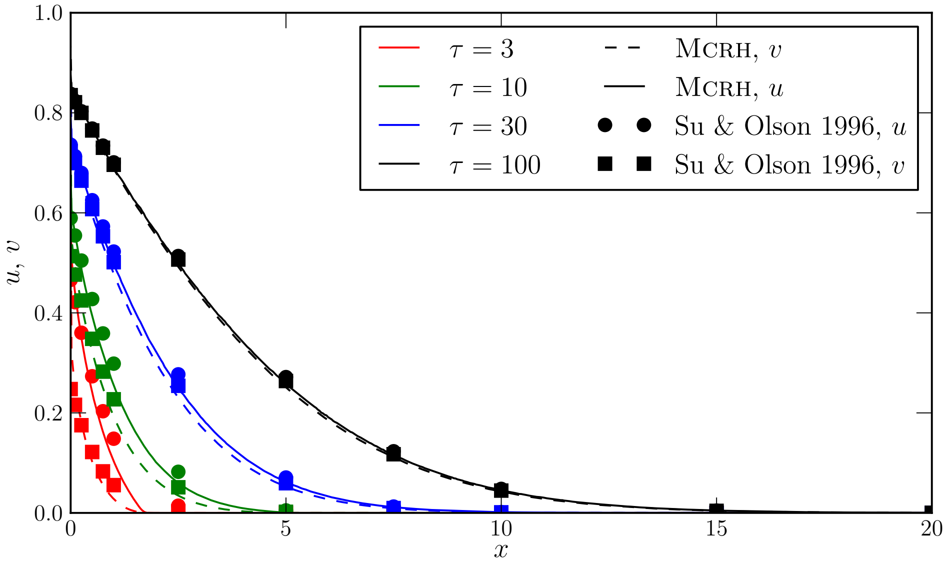

Figure 4.17.: MCRH results of the thermalisation wave test problem in terms of the dimensionless internal (dashed lines) and radiative energy densities (solid lines). The different snapshots are colour-coded and compared with the reference values of Su & Olson (1996) (circles and squares) for the case $\varepsilon = 1$.

results and the reference values is generally very good, in particular for later times. During the early phase, however, the Su & Olson (1996) solution penetrates the ambient medium faster. This seems to be connected with the use of the diffusion approximation in Pomraning (1979) and Su & Olson (1996). This formulation of the radiative transfer problem constitutes an excellent approximation to the physical reality for regions of high optical depth. It may, however, only be applied with caution to problems with intermediate or low optical depth, since the information propagation speed may exceed the speed of light. This well-know fact is accommodated in the numerical technique of flux-limited diffusion (Levermore & Pomraning, 1981) by restricting the propagation speed in low optical depth regions. In the problem at hand, the dimensionless length scale, x, is the optical depth of the domain, scaled with $\sqrt{3}$. Particularly the inner region, close to the boundary, may not be considered optically thick. Thus solving the diffusion equation directly without limiting the propagation speed leads to a too fast a penetrating of radiation into the medium. Our approach, which explicitly enforces the finite signal speed by propagating the Monte Carlo packets at the speed of light, constitutes a closer representation of the physical reality than the approximate results of Pomraning (1979) and Su & Olson (1996).

This observation is illustrated in Fig. 4.18, in which the dimensionless radiative energy is once more compared with the reference values. In addition, vertical dotted lines mark for each time step the maximum distance that photons, injected into the domain along the symmetry axis at

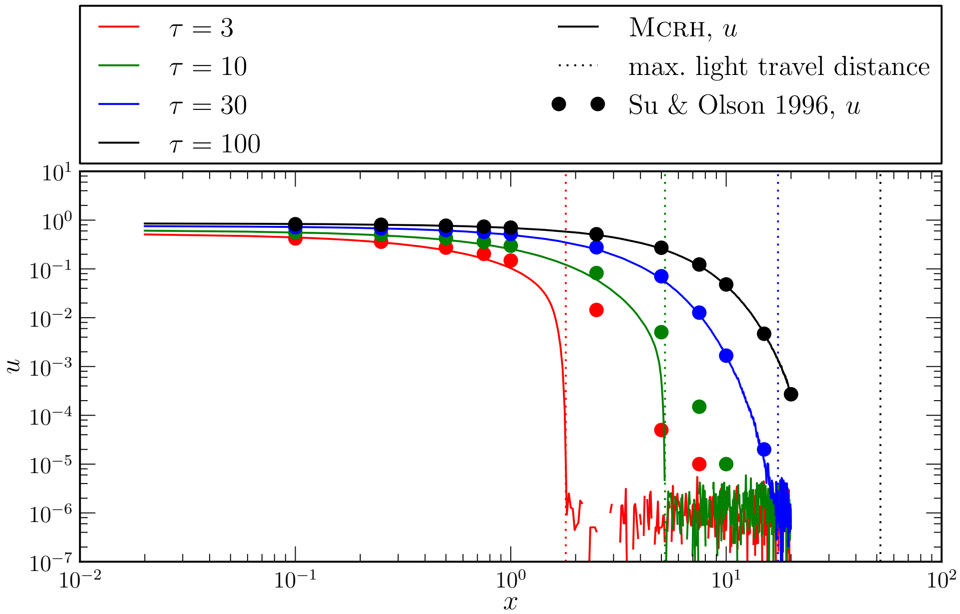

Figure 4.18.: Similar comparison between the MCRH and the Su & Olson (1996) results as in Fig. 4.17, but now restricted to the dimensionless radiation energy density. In addition, for each snapshot, the maximum distance that photons emitted from the inner boundary at $t = 0$ could have covered is marked as the vertical dotted line in the corresponding colour.

$t = 0$, may have covered (based on speed of light considerations). The sharp drop-off in the Mcrh results clearly traces this distance, while the numerical results of Su & Olson (1996) reach deeper into the ambient medium. Only at later times, when the light travel distance extends beyond the computational domain ($x = 20$), the two calculations agree very well throughout the entire optical depth range. This is consistent with the results of Hayes et al. (2006). Here, the authors test their radiation magneto-hydrodynamical code Zeus-mp2, which uses a flux-limited diffusion radiative transfer solver, against the results of Su & Olson (1996). Hayes et al. (2006) emphasise that no flux limiter is used, thus enabling a faster-than-light signal propagation, to achieve the excellent match with the reference values at all times (see Hayes et al., 2006, fig. 23). Taking these consideration and the agreement between the Mcrh and Su & Olson (1996) results at late times into account, we conclude that, in the presence of bulk motions of the radiation field, our radiation hydrodynamical scheme is well-suited to accurately follow the radiation–matter coevolution.

4.3.3. Radiative Shocks

We consider in the final suite of test calculations the full radiation hydrodynamical problem. Activating the complete energy and momentum coupling cycle and following the dynamical behaviour of the radiation field and the ambient material, we investigate the capability of our numerical approach to accurately determine the evolution of the radiation hydrodynamical state. Determining the structure of *radiative shocks* constitutes an ideal test problem to perform this last stage of the basic code verification process. Variants of these calculations have already been presented in Noebauer et al. (2012).

Initially proposed by Ensman (1994), radiative shocks have been established as a standard radiation hydrodynamics test case (e.g. Ensman, 1994; Turner & Stone, 2001; Hayes & Norman, 2003; Hayes et al., 2006; Sekora & Stone, 2010; Jiang et al., 2012), since the general structure of these shocks is well known and approximate analytic expressions for the expected fluid and radiation properties exist. The fundamental properties of the radiative shock phenomena have been derived by Raizer (1957a) and Zel'dovich (1957a)[15] and by Marshak (1958)[16]. Detailed numerical studies of the shock structure have been performed by Heaslet & Baldwin (1963) and Sincell et al. (1999). Recently, semi-analytic solution techniques have also been proposed to derive the shock profiles, based on the equilibrium (Lowrie & Rauenzahn, 2007) and the non-equilibrium (Lowrie & Edwards, 2008) diffusion approximation. In the following, we briefly introduce the basic properties of radiative shocks before presenting the actual test calculations. More exhaustive coverage of this topic may be found in the literature, for example in Zel'dovich & Raizer (1967, chap. 7, §14-18), Mihalas & Mihalas (1984, §104) and Castor (2007, chap. 12.4).

---

[15] English translations of the original works in Russian may be found in Zel'dovich (1957b); Raizer (1957b). Moreover, the authors summarised their original work in Zel'dovich & Raizer (1967).

[16] The Marshak wave may be interpreted as a simplified description of a radiative shock.

Considering a pure fluid dynamical shock wave, the jump in gas temperature induces a net flux of radiative energy into the cold unshocked material, due to the different thermal emissivities. This energy flow significantly affects the region close to the temperature discontinuity and changes the structure of the shock front with respect to the pure hydrodynamical solution (Zel'dovich & Raizer, 1967, chap. 7, §14). In case of very weak shocks, the radiation flux is a negligible contribution to the total energy budget and as a consequence, the discontinuous structure of a pure fluid dynamical shock is retained (see Section 3.3.6). However, as the shock strength increases, so does the magnitude of the thermal flux from the hot shocked material into the cold upstream material. The radiative energy emerging from the shock front is absorbed within a region corresponding to a few photon mean free paths (Zel'dovich & Raizer, 1967, chap. 7, §14) and heats the unshocked material to the temperature T_+ just ahead of the discontinuity[17]. Since the shock runs into a preheated region, the temperature T_- just after the shock front, is raised beyond the final temperature T_1, which follows from modified jump conditions (see, for example, Lowrie & Edwards, 2008). However, due to the net radiative flux, the region behind the shock gradually cools down to T_1. This basic structure prevails as the shock strength increases, until critical conditions are reached. At this point, which separates the distinct classes of *subcritical* and *supercritical* shocks, the radiative precursor raises T_+ to the value of T_1. In supercritical shocks, i.e. for strengths beyond the critical limit, the precursor does not raise the temperature in front of the shock further, but extends the preheating zone beyond the corresponding region in subcritical shocks. Despite the temperature behind and in front of the shock being equal, the compression still induces a sharp temperature increase, the so-called *Zel'dovich-spike*.

To verify the radiation hydrodynamical accuracy of MCRH, we investigate qualitatively the calculated sub- and supercritical shock structure, confront it with some of the approximate expressions of Zel'dovich & Raizer (1967) and compare explicitly with the results of numerical calculations performed with ZEUS-MP2 (Hayes et al., 2006). This massively-parallel and extended version of the original two-dimensional and serial radiation magneto-hydrodynamics code ZEUS (Stone & Norman, 1992) uses flux-limited diffusion and a variable Eddington tensor approach to determine the radiative pressure. The latest version of this code, which is used in the comparison calculations, is publicly available at `http://lca.ucsd.edu/portal/codes/zeusmp2/`[18]. In the shock calculations, we adopt the particular simulation setup of Hayes & Norman (2003) and Hayes et al. (2006) who were inspired by the initial shock calculations presented by Ensman (1994). In particular, we consider a plane-parallel box of length $L = 7 \times 10^{10}$ cm, which is discretised by 512 equidistant cells and in which a cold, purely absorbing gas of density $\rho_0 = 7.78 \times 10^{-10}\,\mathrm{g\,cm^{-3}}$ and constant opacity $\chi^{\mathrm{abs}} = 3.1 \times 10^{-10}\,\mathrm{cm^{-1}}$ resides. To initiate the shock, the material is sent towards the reflecting left boundary with an initial bulk velocity of $u = -6 \times 10^5\,\mathrm{cm\,s^{-1}}$ in the subcritical case and with $u = -2 \times 10^6\,\mathrm{cm\,s^{-1}}$ for the supercritical shock. Ensman (1994) originally used a linearly increasing temperature profile to avoid zero flux regions, which are numerically challenging for the radiation hydrodynamical framework that was used (VISPHOT

---

[17] We adopt the nomenclature of Zel'dovich & Raizer (1967).

[18] Unfortunately, at the time of finishing this work, the domain was not reachable any more.

Ensman, 1991). To be compatible with the original calculations, this temperature profile was adopted by Hayes & Norman (2003) and Hayes et al. (2006) and is employed here as well, in particular in the form of

$$T_0(x) = 10\,\mathrm{K} + \frac{L - x}{L} 75\,\mathrm{K}. \tag{4.38}$$

The resulting gas and radiation temperature profiles determined with Mcrh are shown in Fig. 4.19 (c.f. Noebauer et al., 2012, fig. 5) and compared with a corresponding Zeus-mp2 calculation for a number of snapshots ($t = 5.4 \times 10^3$, 1.7×10^4, 2.8×10^4 and 3.8×10^4 s). During the Mcrh simulations, we occasionally rescale the energy of the newly created packets to avoid that more than 10^4 packets are injected per cell and time step. This way, the total number of packets remains manageable and a total of 4.4×10^6 packets represents the total emission in the last simulation step, corresponding to the final snapshot in Fig. 4.19. We follow Hayes & Norman (2003) and Hayes et al. (2006) and display the shock structure in the reference frame of the upstream material (here, locations are measured by z) by performing the coordinate transformation

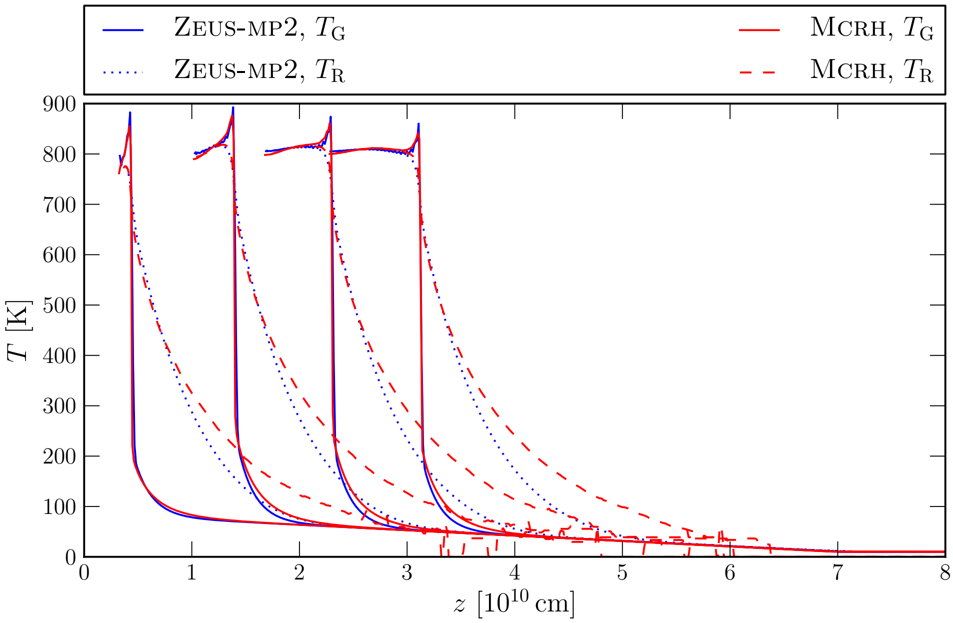

Figure 4.19.: Gas (solid line) and radiative temperature (dashed and dotted) profiles for a subcritical radiative shock following from the initial parameters of Hayes et al. (2006). The results obtained with Mcrh are shown in red and are compared with a corresponding Zeus-mp2 calculation in blue. All quantities are measured in the reference frame of the unshocked material [see Eq. (4.39)] and are displayed for the snapshots $t = 5.4 \times 10^3$, 1.7×10^4, 2.8×10^4 and 3.8×10^4 s.

$$z = x - ut. \tag{4.39}$$

Hayes & Norman (2003) pursued this strategy to facilitate a direct comparison with the original calculations of Ensman (1994), which were obtained in simulations with a Lagrangian code. The temperature profiles determined with MCRH exhibit the expected general shock structure, with a weak radiative precursor, a mild preheating of the cold material in the region in front of the shock and a gradual cooling of the shocked material. Moreover, the agreement with the ZEUS-MP2 calculations is excellent, apart from some small deviations in the precursor region. Following Sincell et al. (1999), we compare in Fig. 4.20 some of the fluid and radiation field properties of the subcritical shock with the analytic approximations of Zel'dovich & Raizer (1967, chap. 7, §14 - 17). In particular, the behaviour of the radiative flux near the shock front agrees very well with the theoretically derived structure (see Zel'dovich & Raizer, 1967, chap. 7, §16),

$$F = F_0 \exp\left(-\sqrt{3}|\tau|\right). \tag{4.40}$$

Here, τ measures the optical depth from the location of the shock front and F_0 the maximum attainable flux, $F_0 = \sigma_\mathrm{R} T_1^4$, with the final shock temperature T_1. From energy and momentum conservation, Zel'dovich & Raizer (1967, chap. 7, §15) derive expressions for the gas pressure, the temperature and the radiative flux as a function of the compression ratio $\eta = \rho_0/\rho$ (see also Sincell et al., 1999)

$$p(\eta) = \rho_0 D^2 (1-\eta), \tag{4.41}$$

$$T(\eta) = T_1 \frac{\eta(1-\eta)}{\eta_1(1-\eta_1)}, \tag{4.42}$$

$$F(\eta) = -\rho D R T_1 \frac{(1-\eta)(\eta-\eta_1)}{2\eta_1^2(1-\eta_1)}. \tag{4.43}$$

In these expressions, D denotes the propagation speed of the shock front, ρ_0 the initial constant density, R the gas constant and η_1 the maximum compression ratio. Reconstructing these quantities from the simulation results, the calculated shock profiles may be compared with the analytic compression curves by scaling them accordingly. The resulting comparison is shown in the right panel of Fig. 4.20. Despite the poor agreement in the intermediate compression range, our results correctly connect the initial and final fluid and radiation state. The deviation from the analytic curves is comparable to that found by Sincell et al. (1999, see figs. 2 and 3). Those authors argue that the relatively poor agreement in the intermediate compression regime is due to the approximations adopted by Zel'dovich & Raizer (1967) to derive the analytic estimates. A different view is offered by Jiang et al. (2012), who observe quite a good agreement between their numerical ATHENA results and the analytic compression curves (see Jiang et al., 2012, fig. 16). They suggest differences in the employed numerical techniques as the origin for the discrepancy between their and the Sincell et al. (1999) results. In particular, they attribute the success of their calculations to the use of a Riemann solver and the finite-volume approach, a statement which we cannot support since our approach also features these characteristics but yields results

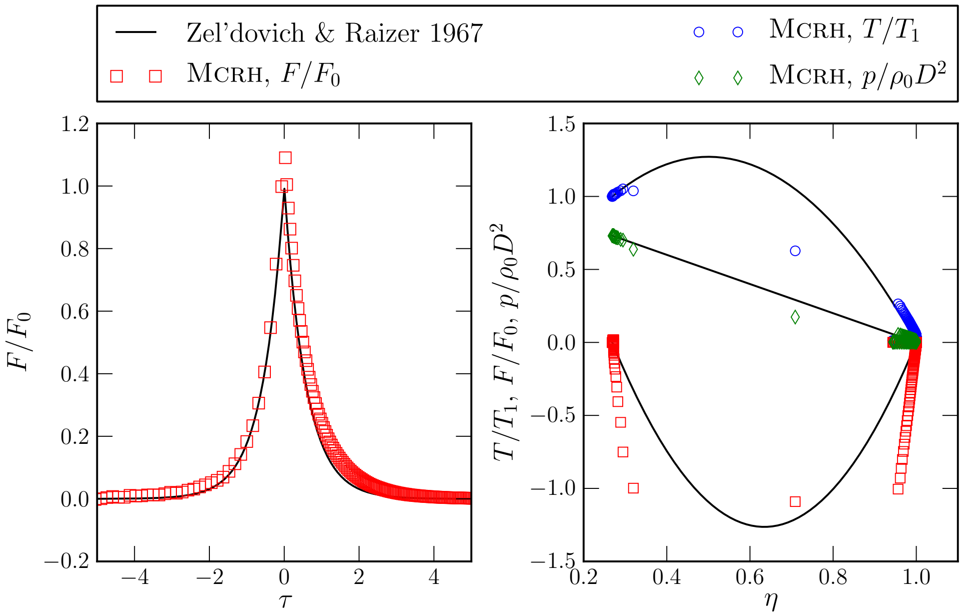

Figure 4.20.: The left panel shows a comparison between the radiative flux of the final snapshot of the subcritical shock presented in Fig. 4.19 (red squares) and the analytic expression, Eq. (4.40), of Zel'dovich & Raizer (1967) (solid black). In the right panel, the calculated subcritical fluid and radiation properties are compared to the compression curves, Eqs. (4.41) to (4.43). The analytic curves, which follow from Zel'dovich & Raizer (1967), are shown as solid black lines and the MCRH results are denoted by red squares (flux), blue circles (gas temperature) and green diamonds (gas pressure). Note that in both panels the displayed quantities are scaled to their reference values ($\rho_0 D^2$, T_1 and F_0).

comparable to Sincell et al. (1999). It may, however, be related to the hybrid Godunov scheme used by Jiang et al. (2012) to couple fluid dynamics and radiative transfer calculations (see Miniati & Colella 2007; Sekora & Stone 2010 and Section 5.3.5 for a discussion of the hybrid Godunov scheme).

We also carry out a comparison for the simulations with an increased bulk velocity, leading to the emergence of a supercritical radiative shock. In this case, our calculations again yield the characteristic features, as seen in Fig. 4.21 (c.f. Noebauer et al., 2012, fig. 6). The gas and radiation temperature are displayed for a series of snapshots ($t = 860$, 4×10^3, 7.5×10^3 and 1.3×10^4 s) in the reference frame of the upstream material [see Eq. (4.39)] and compared with the results of a Zeus-mp2 calculation. During the simulation step corresponding to the final snapshot, roughly 2.7×10^6 packets represent the aggregate emission effect. A strong radiative precursor deeply penetrates the upstream material, establishing a broad preheating region in which the temperature is raised to that of the shocked material. The Zel'dovich spike is also clearly visible. With respect to the Zeus-mp2 results, the location of the shock, the final gas temperature and parts of the preheating region are in very good agreement. However, distinct differences in the properties of the radiative precursor exist, most significantly, the deeper penetration in the Mcrh calculations. This behaviour is also observed in the shock calculations performed by Roth & Kasen (2014). As already pointed out in Noebauer et al. (2012), we attribute this discrepancy to differences in the numerical schemes, in particular to the

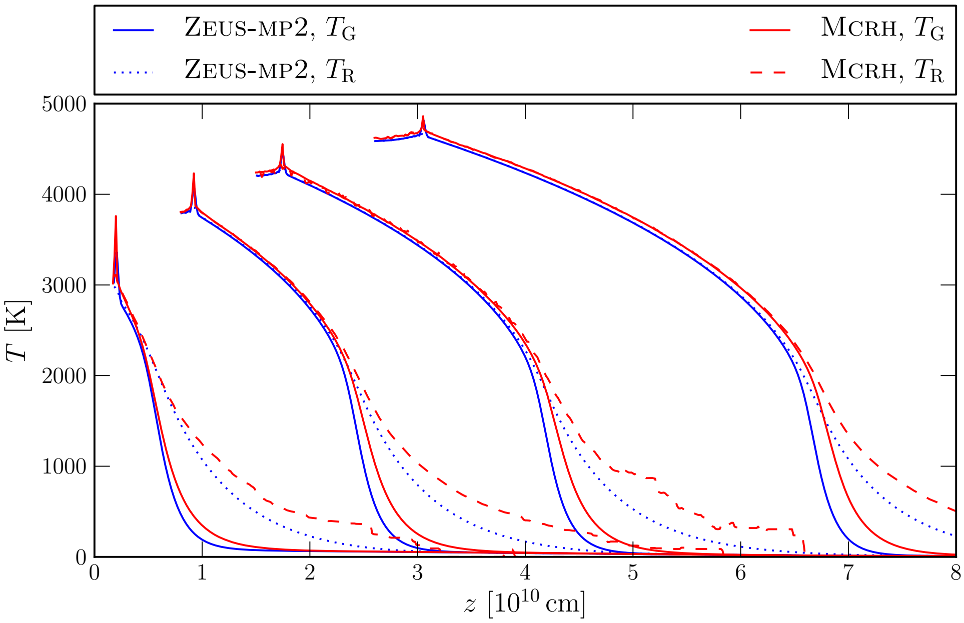

Figure 4.21.: Gas and radiation temperature for a supercritical shock according to the setup of Hayes et al. (2006). The colour-coding and the reference frame for the display are equivalent to Fig. 4.19. The snapshots $t = 860$, 4×10^3, 7.5×10^3 and 1.3×10^4 s are shown.

reliance on the diffusion formulation of radiative transfer in Zeus-mp2 and the use of flux-limited diffusion techniques (see Hayes et al., 2006). An influence of this approximate treatment on the precursor region has already been identified by Ensman (1994) when comparing the results of diffusion calculations and direct solution approaches to the radiation hydrodynamics equations (see Ensman, 1994, fig. 15). The reason for this discrepancy lies in a different angular distribution of the radiation field obtained with the two techniques. A measure for the isotropy of the radiation field is provided by the Eddington tensor, or, in the one-dimensional case, by the Eddington factor f (Section 2.3.6). The value of this quantity changes from 1/3 in the case of perfect isotropy to 1 for a radiation field that is aligned along the symmetry axis. Flux-limited diffusion restricts the magnitude of the Eddington factor in the precursor region to values below those found by a direct solution of the radiation hydrodynamical equations and thus partially inhibits the penetration of the cool unshocked material. This is illustrated in Fig. 4.22, in which the Eddington factors obtained with Mcrh and Zeus-mp2 for the final snapshots of the sub- and the supercritical shock calculations are compared. Our Mcrh calculations are very similar to those of Sincell

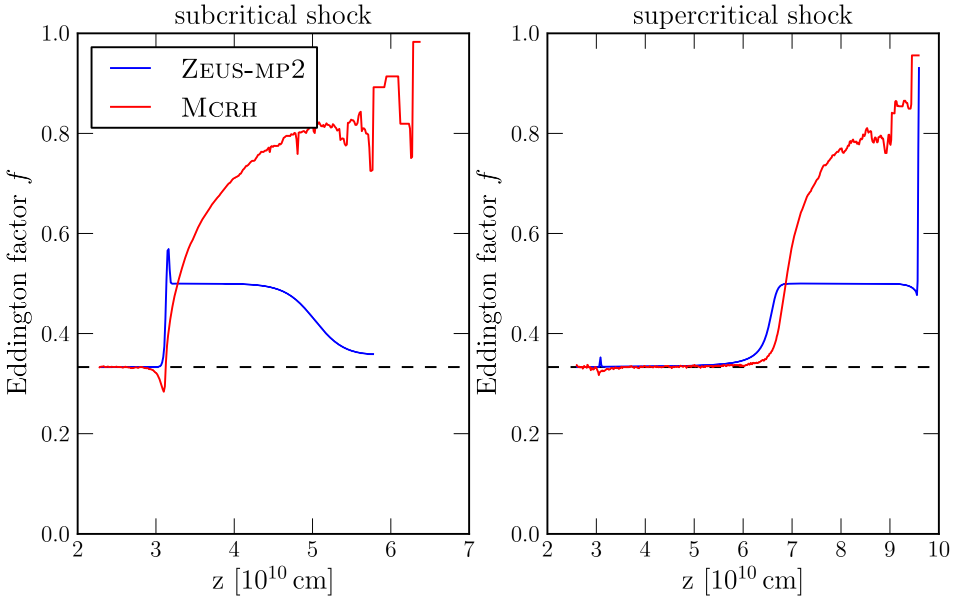

Figure 4.22.: Comparison between the Eddington factors in the final snapshots of the subcritical (left panel) and of the supercritical (right panel) radiative shock calculations, obtained with Mcrh (solid red) and with Zeus-mp2 (solid blue). The horizontal dashed black lines mark the value for an isotropic radiation field, i.e. 1/3. Again, we display the quantities in the reference frame of the unshocked material. Note the theoretically predicted drop below 1/3 at the shock front, a feature which is reproduced by Mcrh but not by Zeus-mp2.

et al. (1999, figs. 8 and 9), while the flux-limited diffusion calculations yield Eddington factors for the precursor region which are much smaller. Note also, that the Mcrh results exhibit the expected drop below 1/3 at the shock front (Sincell et al., 1999) – a behaviour of Monte

Carlo-based calculations which is reproduced in the simulations by Roth & Kasen (2014) as well. The inability of flux-limited diffusion to produce this feature has already been acknowledged by Turner & Stone (2001). The authors also point out, that the value of the Eddington factor in the precursor region may depend on the employed prescription of the flux limiter (see Turner & Stone, 2001, fig. 9). Taken all these findings into account, we conclude that deviations between the MCRH and ZEUS-MP2 shock structures are caused by the different numerical techniques and not by "[. . .] shortcomings of our approach to radiation hydrodynamics" (Noebauer et al., 2012).

The supercritical shock profiles are determined in simulations with a reduced time step (Noebauer et al., 2012). Instead of using the full CFL time step, which is comparable to the characteristic cooling time in the shocked region, a reduction by a factor of ten is required to obtain stable results in the simulations relying on the explicit treatment of the Monte Carlo radiative transfer step. This limitation of the simulation time step is not necessary when the implicit Monte Carlo technique is applied. As Fig. 4.23 illustrates, the implicit Monte Carlo scheme introduces an effective scattering opacity in the precursor region and the material behind the shock front, which reaches values up to 90% of the true absorption opacity. Due to resulting reduction in the

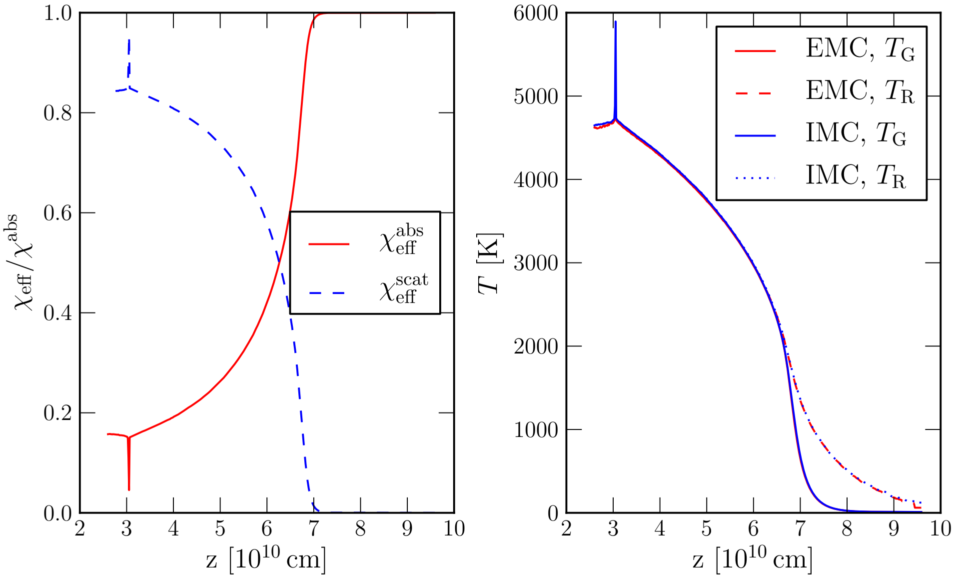

Figure 4.23.: The left panel shows the relative strength of the effective opacities in the implicit Monte Carlo (IMC) supercritial shock calculation. The right panel compares the gas (solid) and radiation temperature (dashed and dotted) for a supercritical shock, analogous to Fig. 4.21, determined with the explicit Monte Carlo (EMC) scheme of MCRH (red) and its implicit capability (green).

characteristic cooling time scale, the full CFL time step duration may be employed. The shock structure obtained is fully compatible with that determined in the explicit calculation with the smaller time step, as shown in the right panel of Fig. 4.23. Only in the height of the Zel'dovich spike, the two calculations disagree. This behaviour may be related to our current treatment of the S term in the implicit scheme. In the future, we will explore the inclusion of this term (see discussion in Section 5.3.4).

Before concluding the discussion of radiative shocks and thereby of the code verification process, we use these calculations to briefly comment on the computational costs and general properties of Mcrh simulations. In general, the bulk of the computational effort in a Mcrh calculation is spent on performing the radiative transfer step, in particular stepping through the packet propagation loop. In contrast, the time spent on the fluid dynamical splitting step is negligible. For example, to advance the subcritical radiative shock presented in Fig. 4.19 to the final snapshot, 3.4×10^4 s, the program runs for 1300 s on a 2.27 GHz Intel Xeon processor with 8 MB cache. In total, 8.9×10^{11} floating point operations are executed. A pure hydrodynamical calculation of the same setup requires only 2.0×10^8 floating point operations and concludes after 1.25 s on the same machine.[19] One should bear in mind, however, that all calculations presented here, and indeed throughout this thesis, are performed serially on a single processing core. A significant speed-up may be achieved by incorporating a parallelisation scheme – either with a shared, distributed or hybrid memory management – and migrating from single-core to multi-core processing architectures (Roth & Kasen 2014 present some parallelised Monte Carlo radiation hydrodynamics calculations). Due to the independence of each Monte Carlo quanta, Monte Carlo radiative transfer techniques are well-suited for parallel processing and thus ideal for high-performance computing. Consequently, even though not pursued in the scope of this work, a parallelisation scheme will be incorporated for future applications, in particular when generalising the approach to multidimensional geometries (see Chapter 7).

Given the findings presented in this paragraph, we consider the calculation of sub- and supercritical shock properties as the last successful step in the general verification process of the physical accuracy and computational feasibility of our radiation hydrodynamical framework. From the successful outcome of all test calculations presented in this chapter, we conclude that our approach is capable of accurately following the dynamical radiation–matter coevolution and that the Monte Carlo noise does not seem to be an inhibiting factor, also thanks to our volume-based estimator scheme. In summary, the tests indicate that our Monte Carlo radiation hydrodynamical technique constitutes a competitive numerical approach to radiation–matter coevolution problems.

---

[19] The program was compiled with the `gcc` compiler, using the optimisation level, `-O3`.

5. Application to Type Ia Supernovae

Radiation hydrodynamical effects are commonly encountered in the field of supernovae. These violent explosions mark the endpoints of stellar evolution and are either induced by thermonuclear burning processes in white dwarfs (Hoyle & Fowler, 1960) or a gravitational collapse in massive stars (Zwicky, 1938). The strategy of classifying supernovae according to their observational features dates back to Minkowski (1941), who first introduced the division into Type I and Type II objects (see Filippenko, 1997, for a more recent overview of supernova classification). With time, it became clear that the observationally motivated classification scheme also reflects the different explosion mechanisms. Nowadays, Type Ia supernovae are associated with thermonuclear explosions and their luminosity is in most cases traced back solely to the energy release accompanying the decay of radioactive material, primarily ^{56}Ni (Pankey, 1962; Truran et al., 1967; Colgate & McKee, 1969; Kuchner et al., 1994). All other supernovae, which are grouped into Type Ib, Type Ic and various Type II events, are linked to explosions following a gravitational collapse. Again, the light curve is mainly powered and shaped by radioactive energy. However, the prominent plateau in the light curve of Type IIP events, characterised by a roughly constant luminosity, is a consequence of a cooling and recombination wave propagating inwards. (e.g. Grassberg et al., 1971; Kirshner et al., 1973; Grassberg & Nadezhin, 1976; Woosley & Weaver, 1986; Utrobin, 2007). Radiation hydrodynamical processes play a role in all of these explosive events. For example, Type II light curves are initially dominated by the so-called *shock-breakout* effect (see Grassberg et al., 1971; Falk & Arnett, 1977, and references therein). During the explosion, the dying massive star is disrupted by a supercritical shock, which propagates outwards[1]. Its strength increases as it runs down the density gradient into regions with ever decreasing optical depth. At a certain point, the optical depth is small enough for the radiation in the precursor region to escape from the exploding object. This process is commonly referred to as the "break-out" of the shock. Provided the radiation hydrodynamical processes during the shock-breakout are well understood, the early light curve may be used to infer the outer structure of the progenitor star (see, for example, Schawinski et al., 2008), particularly its radius.

Another strategy of inferring properties of the supernova progenitor system also relies on radiation hydrodynamical effects, namely the interaction of the ejecta with circumstellar material (CSM; see, for example, Chugai et al., 2004b; Fryer et al., 2010; Blinnikov & Sorokina, 2010, for studies of interacting supernovae). Due to mass-loss episodes in the progenitor system, a

---

[1] See, for example, Mihalas & Mihalas (1984), §105 (c), for a brief summary, and Weaver (1976) for a detailed discussion of supernova shocks.

significant amount of material may be present in the immediate environment of the supernova explosion. Once the ejecta material comes into contact and interacts with the CSM, part of the kinetic energy stored in the ejecta expansion may be converted into internal energy by shock-heating. This internal energy excess is eventually fed into the radiation field and contributes to the light output of the interacting system (e.g. Grassberg & Nadezhin, 1986). Due to these processes, the interaction history and thus the CSM morphology imprints itself on the light curve shape (see, e.g., Chugai, 1992; Chugai et al., 2004a) and may also induce interaction signatures in the observed spectra, most prominently strong Hα emission (see, e.g., Henry & Branch, 1987; Cumming et al., 1996; Chugai et al., 2004a). Examples for such interacting supernovae are the Type IIn events (Schlegel, 1990), which exhibit narrow spectral features. These are a consequence of the circumstellar material being ionised by the X-ray emission from the radiative shock wave and the subsequent recombination (see, e.g., calculations by Chugai et al., 2004a). Recently also Type Ia supernovae have been found, showing indications of interaction with circumstellar material (see, for example, Hamuy et al., 2003; Dilday et al., 2012; Silverman et al., 2013). Modelling the interaction phase, predicting its observable signature and confronting it with observational data bears the prospect of inferring the properties of the CSM and in turn the mass-loss history of the progenitor system (for example, the shelluar CSM structure due to potential nova eruptions in the progenitor of SN PTF11kx, inferred by Dilday et al., 2012).

This brief listing is by no means exhaustive but serves as an illustration of the importance of radiation hydrodynamical processes in the supernova environment. In the following we present the first application of Mcrh to radiation hydrodynamical problems in the supernova context. Since we have for now limited these calculations to supernova Type Ia related problems, we first provide a brief overview of these explosions in Section 5.1. To establish the performance of our approach under conditions appropriate for the supernova environment, we revisit in Section 5.2 the problem of a potential influence of the radiation field on the expansion of Type Ia ejecta (see Pinto & Eastman, 2000; Woosley et al., 2007; Noebauer et al., 2012). Afterwards we report in Section 5.3 on our attempts to apply Mcrh to interacting supernovae.

5.1. Type Ia Supernovae

Type Ia supernovae today are intimately associated with the discovery of the accelerated expansion of the Universe (Riess et al., 1998; Perlmutter et al., 1999)[2]. Two basic properties render this type of explosions particularly useful for probing cosmic distances. Due to their intense brightnesses – around maximum, they can even outshine their host galaxies – they may be detected and observed at great distances. Moreover, an empirical relation between the width and the brightness peak of the light curve of Type Ia explosions has been identified (Pskovskii, 1984; Phillips, 1993), which empowers the observer to derive the true brightness from the apparent one and establish the distance to these events. By comparing supernova Type Ia distances with

---

[2] For this achievement, the Nobel Prize 2011 was awarded to Saul Perlmutter, Adam Riess and Brian Schmidt.

their cosmological redshift, a measure for how far these events lie in the past, the expansion history of the Universe may be reconstructed and compared with the predicted trends according to different cosmological models. The accelerated expansion, which has been established with this methodology, is commonly attributed to the effect of a new form of energy, which, due to the lack of concrete knowledge about its origin and nature, is labelled “dark energy”. Today, supernova cosmology focuses mainly on investigating the parameters of the dark energy equation of state. By pinpointing the relation between the density and pressure of this mysterious energy component, one strives at obtaining a better understanding of its nature. A recent review of supernova cosmology is given by Goobar & Leibundgut (2011).

Apart from their significance for cosmological studies, Type Ia supernovae have a major impact on many other branches of astrophysics. They play a key role in advancing the chemical enrichment of the Universe, not only by synthesising heavy elements but also by feeding the stellar and explosive burning products back into the stellar matter cycle (see, e.g., Kobayashi et al., 1998, for a galactic chemical evolution study with Type Ia supernovae). A major fraction of stable iron present in the Universe arises from this process (e.g. Matteucci & Greggio, 1986). In addition to the influence on chemical evolution processes, Type Ia supernovae contribute to heating the interstellar medium (Ciotti et al., 1991). Moreover, these explosions may have a regulating effect on the star formation process (Leibundgut, 2000) since significant mass may be expelled from galaxies due to supernova Type Ia activity (e.g. Ferrara & Tolstoy, 2000).

Despite the immense importance of Type Ia supernovae for cosmology and astrophysics, these phenomena are still not fully understood. The thermonuclear disruption of a carbon/oxygen white dwarf is the accepted explanation, but the details of the explosion mechanism are still heavily debated (see Hillebrandt & Niemeyer 2000 and Hillebrandt et al. 2013 for recent reviews on the topic). White dwarfs constitute the final evolution stage of low and intermediate mass stars (see, e.g., Kippenhahn et al., 2013, chaps. 34-36, on stellar evolution towards white dwarfs). These objects are stable and inert, nuclear burning has ceased and the pull due to self-gravity is compensated by the degeneracy pressure of free electrons (see, e.g., Shapiro & Teukolsky, 1983, chap. 3). An explosion in white dwarfs may only be induced through the interaction with a companion star. The interaction process alters the conditions within the white dwarf to enable thermonuclear carbon burning. The scenarios which are proposed as viable explanations for Type Ia supernovae differ in the mechanisms which lead to an ignition within the white dwarf. The emerging thermonuclear flame may either propagate in the form of a subsonic *deflagration* or a supersonic *detonation* (see Hillebrandt & Niemeyer, 2000, and references therein for details on thermonuclear flame propagation). During the burning process, a transition from a deflagration to a detonation may also occur (Khokhlov, 1991). The two flame manifestations differ in the way the necessary heating of the cold unburned material is achieved, with conductive energy transport being responsible in deflagrations and shock-heating in detonations. In the following only the most important Type Ia scenarios are briefly sketched. For a more detailed outline of the different Type Ia models, their flaws and strong points, the reader is referred to the recent review article by Hillebrandt et al. (2013).

In the classical textbook model for Type Ia supernovae, the *single degenerate* scenario (Whelan & Iben, 1973; Nomoto, 1982), mass is transferred onto a carbon/oxygen white dwarf from a main sequence or giant star companion via Roche-lobe overflow. Shortly before reaching the *Chandrasekhar mass limit* M_{Ch}[3], the maximum attainable mass for a self-gravitating object sustained by electron-degeneracy pressure (after Chandrasekhar, 1931), the conditions at the centre of the white dwarf ($\rho \sim 2 \times 10^9\,\mathrm{g\,cm^{-3}}$, see Woosley & Weaver 1986) enable the ignition of thermonuclear burning after an intermediate “simmering” phase.

In contrast to the single degenerate model, the companion star in the *double degenerate* scenario (Iben & Tutukov, 1984; Webbink, 1984) is also a white dwarf. Here, the explosion is ultimately a result of the merger of these two stars. By the emission of gravitational waves, the separation of the binary system decreases and the stars are brought into immediate contact. In the following collision and merging phase, the material at the shearing interface may reach conditions, which are sufficient to ignite a carbon detonation (e.g. Pakmor et al., 2010, 2012). The total mass of the binary system often exceeds the Chandrasekhar limit, but both white dwarfs individually are commonly less massive than M_{Ch}.

An alternate mechanism leading to explosions in sub-Chandrasekhar white dwarfs is provided by the *double detonation* scenario (Iben et al., 1987). Here, the primary star accretes helium from its companion. A detonation in the developing helium shell may occur already at a total mass of the white dwarf below M_{Ch}. As the helium-burning front sweeps around the carbon/oxygen core, shock waves are sent towards the central region. Particularly at the location where these shocks converge a carbon detonation may be initiated due to the induced rapid heating and compression (e.g. Fink et al., 2007, 2010). This scenario may be realised both in single and double degenerate progenitor systems.

It is still widely discussed which of these scenarios correctly describes Type Ia explosions (see details in Hillebrandt et al., 2013). Resolving this debate is further complicated by the wealth of recent observations, which have transformed what was once believed to be a homogeneous class of objects into a very diverse group of transients with a growing number of sub-classes (see for example Benetti et al., 2005; Branch et al., 2006; Wang et al., 2009; Li et al., 2011; Parrent et al., 2014). This diversity indicates that there may not be one unique Type Ia mechanism but that multiple scenarios may be realised in nature. In particular, the standard text-book explanation according to which Type Ia supernovae originate solely from explosions near the Chandrasekhar limit in the single-degenerate scenario is gradually being widely questioned. Arguments against this model include the absence of any direct detection of companion stars in nearby supernova remnants (e.g. Schaefer & Pagnotta, 2012; Kerzendorf et al., 2013), the direct constraints on the nature of the companion star derived from observations (the most stringent limits are based on the nearby supernova SN2011fe, see Nugent et al. 2011; Li et al. 2011; Brown et al. 2012 and

---

[3] For a non-rotating carbon/oxygen white dwarf, this limit amounts to $M_{\mathrm{Ch}} \simeq 1.4 M_{\odot}$ (see Shapiro & Teukolsky, 1983, chap. 3.1).

Bloom et al. 2012) and the observation of the X-ray flux from galaxies (Gilfanov & Bogdán, 2010).

On the road towards a firmer understanding of Type Ia supernovae, detailed numerical simulations constitute an important tool. With this strategy, the different explosion scenarios may be modelled (e.g. Jordan et al., 2008; Fink et al., 2010; Pakmor et al., 2010; Röpke et al., 2012), synthetic observables derived and confronted with actual data (e.g. Kasen et al., 2009; Sim et al., 2012; Kromer et al., 2013; Dessart et al., 2014), either giving credit or raising doubt about the plausibility of the proposed Type Ia mechanism. In particular, investigating the objects that are considered non-standard due to their violation of the width-luminosity relation provides valuable insights for our general understanding of Type Ia explosions. These "outliers" are often interpreted as extreme realisations of processes which potentially also contribute to normal Type Ia supernovae. For example, the sub-class of SN 2002cx-like objects have recently been associated with very weak pure-deflagration explosions (Kromer et al., 2013).

Another very interesting class of objects is formed by the super-luminous explosions. These objects challenge the standard model in which the entire light-output derives from the decay of radio-nuclei, since ejecta masses beyond the Chandrasekhar-mass limit would be required. This may be realised in massive mergers (Hicken et al., 2007) or in systems with rapidly rotating white dwarfs (Howell et al., 2006), but another promising candidate for the theoretical explanation of such intense luminosities invokes interactions of the ejecta with CSM (see Grassberg & Nadezhin, 1986; Chugai et al., 2004b, for studies of CSM interaction to explain intense luminosities in Type II explosions).

In addition to the unresolved question about the origin of the high energy output of these systems, they are potentially problematic for future supernova cosmology projects which are based on purely photometric surveys. Since, due to their intense brightness, the observational bias favours super-luminous events in high redshift samples and since a removal of these events based on photometric information alone proves challenging, they may induce a systematic error in distance determinations at high redshifts (see Taubenberger et al., 2011). A firm understanding of the physics underlying these powerful explosions is required to quantify the contamination effect of cosmological samples at high redshifts. Radiation hydrodynamical simulations constitute a valuable tool for this, in particular for investigating the plausibility of the interaction scenario.

Our MCRH approach offers some very appealing features for radiation hydrodynamical studies of Type Ia explosions. The spectra of Type Ia supernovae do not exhibit a black-body continuum but are dominated by a multitude of atomic line features, many of which originate in scattering interactions. Thus, any modelling effort must be able to deal with this complex microphysical situation. Moreover, the non-isotropic distribution of elemental abundances due to the multidimensional morphology of the thermonuclear burning front (see Hillebrandt & Niemeyer, 2000, and references therein) and the potential overall asymmetry of the Type Ia ejecta found in some simulations, for example by Jordan et al. (2008) and Pakmor et al. (2012), have to be taken into account in detailed modelling attempts. In addition, the circumstellar material in the interaction scenario may feature a complex geometrical configuration (see, for example, model in Chugai et al., 2004b, fig. 5). As pointed out in Section 3.4.1, the Monte Carlo approach is ideally suited to accommodate both requirements. Consequently, many current state-of-the-art pure radiative transfer codes for the derivation of synthetic observables of Type Ia explosions, such as Sedona (Kasen et al., 2006) and Artis (Sim, 2007; Kromer & Sim, 2009), rely on Monte Carlo techniques (see also Wollaeger et al., 2013, for a first report on a hybrid DDMC-IMC spectral synthesis code). For the same reason, the use of a Monte Carlo approach suggests itself for the study of radiation hydrodynamical effects in the Type Ia supernova field, in particular for investigating the plausibility of the interaction scenario. As a preparation for this, we first test the performance of our method under typical Type Ia supernova conditions by investigating the radiative influence on the ejecta expansion (see Section 5.2). Afterwards, we report on our attempts to use Mcrh for the study of interacting Type Ia supernovae (see Section 5.3).

5.2. Radiative Influence on Ejecta Expansion

5.2.1. Powering Type Ia Supernova Light Curves

The electromagnetic signature of Type Ia supernovae does not reflect the actual explosion event but its radioactive afterglow (Pankey, 1962; Truran et al., 1967; Colgate & McKee, 1969; Kuchner et al., 1994). The energy released in the explosion is primarily spent on accelerating the ejecta material. However, the thermonuclear burning produces the radioactive nickel isotope, ^{56}Ni, in large amounts. ^{56}Ni is β-unstable and the electron-capture reactions, which occur at a half-life of $T_{1/2} = 6.075\,\mathrm{days}$ (Audi et al., 2003), are accompanied by the emission of γ-rays (see Ambwani & Sutherland, 1988, tab. 1). These interact in the ejecta, get eventually absorbed and heat the ambient material (e.g. Kuchner et al., 1994). After the expansion has significantly reduced the density and the optical depth of the ejecta, electromagnetic radiation, emitted by the hot ejecta material, may escape and be detected by an external observer. Due to the efficient photon trapping at early times, the optical light curve peaks not before 17 to 20 days after the actual explosion (e.g Arnett, 1982). Since the electromagnetic energy output is initially (almost) exclusively powered by the radioactive nickel decay, its produced amount determines the peak luminosity of the light curve (e.g Arnett, 1982). In the later phases of the ejecta evolution, ^{56}Co, the daughter nucleus of ^{56}Ni, takes precedence in shaping the light curve. It decays[4] with a half-life of $T_{1/2} = 77.23\,\mathrm{days}$ (Audi et al., 2003) to the stable iron isotope ^{56}Fe, which de-excites by emitting γ-rays (see again Ambwani & Sutherland, 1988, tab. 1).

---

[4] The radio-nucleus ^{56}Co decays primarily by electron capture but, with a probability of roughly 20%, also by positron emission (Junde et al., 2011).

5.2.2. Homologous Ejecta Expansion

The explosion mechanism and the involved thermonuclear burning are complex physical processes. However, already shortly after the explosion, the evolution of the ejecta is governed by a very simple principle: *homologous expansion.* Burning has stopped and, compared to the large fluid velocities, all other forces are negligible and the ejecta evolve in a force-free and self-similar fashion. This homologous phase is governed by the simple relation

$$u = \frac{r}{t}, \tag{5.1}$$

connecting the fluid velocity u at any point to its distance from the expansion centre, r, and the time since the onset of the expansion, t. The formation of this homologous phase has been verified in numerical explosion simulations (e.g. Röpke, 2005), in which the ejecta material is found to evolve in this self-similar fashion after only a few seconds.

The question remains, however, if the homologous expansion persists in the presence of the radiation field which gradually builds up in the radioactive decay reactions. Due to the interaction with the ambient material, it may exert an appreciable force onto the ejecta and alter the expansion history. In particular regarding the derivation of synthetic observables for Type Ia supernovae, an answer to this question is crucial. To reduce the complexity of the problem, many numerical approaches, for example Artis (Kromer & Sim, 2009), Sedona (Kasen et al., 2006), Syn++ (Thomas et al., 2011) and Tardis[5] (Kerzendorf & Sim, 2014), neglect the influence of the radiation field on the dynamics of the ejecta material and perform a pure radiative transfer calculation in a homologously expanding medium (a notable exception is the radiation hydrodynamical code Stella). Earlier studies of this problem (Pinto & Eastman, 2000; Woosley et al., 2007) concluded that this approach is justified, since the radiative influence on the ejecta structure is small and has no significant effect on the observed (colour) light curves. We revisit this problem of the dynamical importance of the radiation field during the ejecta expansion phase and use it as a test case for the performance of Mcrh under typical supernova conditions. The results presented here have already been published in Noebauer et al. (2012).

5.2.3. Radioactive Decay and Gamma-Ray Transport in MCRH

For the investigation of the homologous expansion phase, additional physical effects, all associated with the energy injection due to radioactive decays, have to be incorporated into our numerical tool. The abundances of the radio-nuclei have to be tracked, their decay reactions followed and the energy release treated. In the following, we briefly present the extensions which are implemented, and verify their validity and accuracy in a simple toy calculation according to Lucy (2005).

---

[5] Publicly available at `https://github.com/tardis-sn/tardis`.

Incorporating arbitrary elemental or chemical compositions into a fluid dynamical code is a simple task and commonly encountered in simulations of reactive flows (e.g. Fryxell et al., 1989). Expressing the elemental abundances by their respective mass fractions

$$X_i = \frac{N_i A_i}{\sum_j N_j A_j}, \tag{5.2}$$

with N_i denoting the number of nucleons of an element i and A_i its mass number, the combination $X_i \rho$ constitutes a conserved quantity. Thus, various elements may be included into fluid dynamical calculations by additionally solving

$$\frac{\partial}{\partial t}(\rho X_i) + \nabla \cdot (\rho \mathbf{u} X_i) = 0 \tag{5.3}$$

for each elemental species (see, for example, Fryxell et al., 1989). If interactions between the elements, such as fusion or decay reactions, may occur, a source term appears on the right hand side of Eq. (5.3). The source terms may be incorporated into finite-volume hydrodynamical calculations using the operator-splitting technique described in Section 3.2. For the supernova ejecta simulations with Mcrh, we include the capability of advecting elemental abundances according to Eq. (5.3) during the fluid dynamics calculation and insert an additional splitting step, in which the decay chain

$$^{56}\mathrm{Ni} \rightarrow {}^{56}\mathrm{Co} \rightarrow {}^{56}\mathrm{Fe} \tag{5.4}$$

is treated. The changes in the number of radionuclei are governed by the differential equations

$$\frac{\mathrm{d}N_{^{56}\mathrm{Ni}}}{\mathrm{d}t} = -\lambda_{^{56}\mathrm{Ni}} N_{^{56}\mathrm{Ni}}, \tag{5.5}$$

$$\frac{\mathrm{d}N_{^{56}\mathrm{Co}}}{\mathrm{d}t} = -\lambda_{^{56}\mathrm{Co}} N_{^{56}\mathrm{Co}} + \lambda_{^{56}\mathrm{Ni}} N_{^{56}\mathrm{Ni}}. \tag{5.6}$$

Here, the decay constants λ_i are used (see Table 5.1) and the simultaneous destruction and production of cobalt is taken into account. A solution for the number of nuclei involved in the decay chain may be obtained from *Bateman's equation* (Bateman, 1910). Accordingly, the number of nickel and cobalt nuclei at time t is given by

$$N_{^{56}\mathrm{Ni}}(t) = N_{^{56}\mathrm{Ni}}(t_0) \exp\left(-\lambda_{^{56}\mathrm{Ni}}(t - t_0)\right), \tag{5.7}$$

$$\begin{aligned} N_{^{56}\mathrm{Co}}(t) &= N_{^{56}\mathrm{Co}}(t_0) \exp\left(-\lambda_{^{56}\mathrm{Co}}(t - t_0)\right) \\ &\quad + N_{^{56}\mathrm{Ni}}(t_0) \frac{\lambda_{^{56}\mathrm{Ni}}}{\lambda_{^{56}\mathrm{Co}} - \lambda_{^{56}\mathrm{Ni}}} \left[\exp\left(-\lambda_{^{56}\mathrm{Ni}}(t - t_0)\right) - \exp\left(-\lambda_{^{56}\mathrm{Co}}(t - t_0)\right)\right], \end{aligned} \tag{5.8}$$

assuming initial abundances $N_i(t_0)$ at t_0. Relying on this result, the mass fractions may be updated and the energy release calculated.

Each reaction of the decay chain is accompanied by the production of γ-rays, which are emitted at a number of different frequencies (see Ambwani & Sutherland, 1988, tab. 1). Propagating

	decay constant λ	energy release per nucleon q
^{56}Ni	$1.321 \times 10^{-6}\,\mathrm{s}^{-1}$	$2.7686 \times 10^{-6}\,\mathrm{erg}$
^{56}Co	$1.039 \times 10^{-7}\,\mathrm{s}^{-1}$	$5.7133 \times 10^{-6}\,\mathrm{erg}$

Table 5.1.: Parameters for the radioactive decay chain of ^{56}Ni via ^{56}Co to stable iron, Eq. (5.4).

through the ejecta, the γ-rays interact with the ambient material by Compton scatterings, the production of e^+-e^- pairs and by the photoelectric effect. With these interactions, the γ-rays eventually heat the ejecta material and contribute via the ensuing quasi-thermal emission to the radiation field in the ejecta. In our simulations, we explicitly follow the propagation of the γ-rays with the same Monte Carlo tools as are used for the optical[6] radiation field. Packets representing γ-rays are distinguished from normal radiation packets and separate opacities are used for their propagation. However, we simplify the γ-propagation process by replacing the numerous interactions possibilities by an effective absorption channel of $\sigma^{\mathrm{abs}}/\rho = 0.03\,\mathrm{cm}^2\,\mathrm{g}^{-1}$ (see Sutherland & Wheeler, 1984; Ambwani & Sutherland, 1988; Swartz et al., 1995). Also, we assume instantaneous thermalisation and immediately convert each absorbed γ-packet into an optical radiation packet of the same energy. Since we perform our MCRH simulations in the grey approximation, we integrate over the emitted γ-spectrum (see Ambwani & Sutherland, 1988, tab. 1), obtaining the energy release values listed in Table 5.1 (see also Lucy, 2005; Noebauer et al., 2012). At the beginning of each radiative transfer step, a number of new γ-packets, representing the radioactive energy release, are determined according to the decaying nickel and cobalt nuclei and the respective q-values. These packets are injected uniformly over the radiative transfer step and propagated together with the optical radiation packets according to the prescriptions mentioned above and explained in Section 3.4. In addition to the radiative effect on the ejecta structure, we are interested in the observable signature. Thus, all packets which reach the outer boundary of the computational domain are recorded to construct the light curve.

5.2.4. Lucy 2005 Model Ejecta Calculation

To verify the accuracy of the extensions discussed above, we consider the simplified and parameterised supernova ejecta model of Pinto & Eastman (2000) and Lucy (2005). The emergent light curve is calculated and compared with the results of Lucy (2005), who formulated this problem as a test case for Monte Carlo radiative transfer codes for supernovae. The results of this test calculation have already been presented in Noebauer et al. (2012).

The model consists of a spherical mass distribution that extends out to $u_{\mathrm{max}} = 10^4\,\mathrm{km}\,\mathrm{s}^{-1}$, encompasses a total mass of $M_{\mathrm{tot}} = 1.39 M_{\odot}$ and has a spatially constant density. During homologous expansion, the extent of the ejecta is most conveniently specified by the velocity, since fluid parcels move radially outwards at constant speed. Using Eq. (5.1), the linear velocity

---

[6] The term “optical” is chosen to distinguish it from γ-radiation

stratification may be converted into radial positions at all times during the expansion. The inner core of the ejecta is assumed to consist exclusively of nickel. Further out, the nickel concentration drops linearly and radioactive material is completely absent in the outermost layers. In summary, the nickel distribution, measured in mass coordinates[7], may be specified by

$$X_{^{56}\mathrm{Ni}}(r) = \begin{cases} 1 & \text{if} \quad M_r < 0.5 M_\odot \\ 3 - 4\frac{M_r}{M_\odot} & 0.5 M_\odot \leq M_r < 0.75 M_\odot \\ 0 & \text{else.} \end{cases} \tag{5.9}$$

The remaining material is assumed to be composed of carbon and oxygen in equal parts. We use the grey cross section of Lucy (2005) for interactions of the optical radiation field, $\chi/\rho = 0.1\,\mathrm{cm}^2\,\mathrm{g}^{-1}$, and adopt $\chi^{\mathrm{abs}}/\rho = 0.03\,\mathrm{cm}^2\,\mathrm{g}^{-1}$ as the effective γ-absorption opacity[8], following Sutherland & Wheeler (1984) and Ambwani & Sutherland (1988).

Shortly after the explosion, when thermonuclear burning has ceased and the ejecta are already in homologous expansion, the material is completely opaque for γ and optical radiation. For example, the model ejecta have a total optical depth of $\tau = 1.65 \times 10^{11}$ and $\tau = 4.95 \times 10^{10}$ for photons and γ-rays at 20 s after explosion. An effective use of the Monte Carlo radiative transfer scheme is virtually impossible in such an environment. We bridge the time until the expansion of the ejecta has decreased the optical depth far enough for Monte Carlo radiative transfer simulations to become feasible by a simple homology calculation. This strategy is very similar to the initialisation process of SEDONA Monte Carlo radiative calculation of Type Ia light curves and spectra (see Kasen et al., 2006). We evolve the ejecta material to the time of the onset of the simulation in a force-free homologous fashion, tracking the changes in the abundances of the radioactive material and recording the associated energy release. The energy release is assumed to instantly thermalise and contribute to the radiative pool. Together with energy losses due to adiabatic expansion, the final radiation energy may be determined, according to which the initial radiation field for the radiation hydrodynamics calculation is seeded.

During homologous expansion, the ejecta mass is conserved. Thus, changes in density occur solely due to the increase in volume. Since the radial location of any parcel of ejecta material changes according to

$$r(t) = r(t_0)\frac{t}{t_0}, \tag{5.10}$$

with $r(t_0)$ being the radius at a reference time t_0, the density decrease is governed by

$$\rho(t) = \rho(t_0)\left(\frac{t_0}{t}\right)^3. \tag{5.11}$$

---

[7] This coordinate, M_r, specifies the total mass enclosed by a spherical shell of radius r.

[8] Here, we deviate slightly from the test calculation presented by Lucy (2005), who resolves the emitted γ-spectrum and uses the frequency-dependent interaction cross section of Ambwani & Sutherland (1988).

Due to the high optical depth in the early expansion phase, we may assume LTE, i.e. gas and radiation energy are equal

$$T_{\mathrm{G}} = T_{\mathrm{R}} = \left(\frac{E_{\mathrm{R}}}{a_{\mathrm{R}}}\right)^{\frac{1}{4}}. \tag{5.12}$$

To determine the evolution of the radiation energy[9], $\mathcal{E}_{\mathrm{R}}$, we account for the radioactive energy input and the losses due to adiabatic expansion work[10], $-p\mathrm{d}V$:

$$\frac{\mathrm{d}\mathcal{E}_{\mathrm{R}}}{\mathrm{d}t} = q_{^{56}\mathrm{Ni}}\lambda_{^{56}\mathrm{Ni}}N_{^{56}\mathrm{Ni}}(t) + q_{^{56}\mathrm{Co}}\lambda_{^{56}\mathrm{Co}}N_{^{56}\mathrm{Co}}(t) - \frac{1}{3}\frac{\mathcal{E}_{\mathrm{R}}}{V}\frac{\mathrm{d}V}{\mathrm{d}t}. \tag{5.13}$$

The number of radionuclei follows from Eqs. (5.7) and (5.8) (see also Noebauer, 2011)[11]. Inserting into Eq. (5.13), the resulting non-linear ordinary differential equation may be solved analytically (Noebauer, 2011)[12], yielding the radiative energy evolution

$$\begin{aligned}
\mathcal{E}_{\mathrm{R}}(t) &= \mathcal{E}_{\mathrm{R}}(t_0)\frac{t_0}{t} \\
&+ \left\{\frac{N_{^{56}\mathrm{Ni}}(t_0)}{t}\left(q_{^{56}\mathrm{Ni}} - q_{^{56}\mathrm{Co}}\frac{\lambda_{^{56}\mathrm{Co}}}{\lambda_{^{56}\mathrm{Ni}} - \lambda_{^{56}\mathrm{Co}}}\right)\right. \\
&\times \left.\left[\frac{1}{\lambda_{^{56}\mathrm{Ni}}} + t_0 - \left(\frac{1}{\lambda_{^{56}\mathrm{Ni}}} + t\right)\exp\left(-\lambda_{^{56}\mathrm{Ni}}(t - t_0)\right)\right]\right\} \\
&+ \left\{\frac{q_{^{56}\mathrm{Co}}}{t}\left(N_{^{56}\mathrm{Co}}(t_0) + N_{^{56}\mathrm{Ni}}(t_0)\frac{\lambda_{^{56}\mathrm{Ni}}}{\lambda_{^{56}\mathrm{Ni}} - \lambda_{^{56}\mathrm{Co}}}\right)\right. \\
&\times \left.\left[\frac{1}{\lambda_{^{56}\mathrm{Co}}} + t_0 - \left(\frac{1}{\lambda_{^{56}\mathrm{Co}}} + t\right)\exp\left(-\lambda_{^{56}\mathrm{Co}}(t - t_0)\right)\right]\right\}.
\end{aligned} \tag{5.14}$$

This equation formulates the condition for initialising the packet population at time t in the Mcrh calculations. The initial fluid state at time t follows from Eq. (5.11) and from converting Eq. (5.14) into a gas temperature assuming LTE.

For the test simulation of the Lucy (2005) ejecta model, we start the simulation at $t = 3\,$days. The resulting initial state of the ejecta, determined in the homologous expansion calculation, is shown in terms of gas temperature and nickel and cobalt abundances in Fig. 5.1 (c.f. Noebauer et al., 2012, fig. 7). We map the ejecta model onto a spherical grid with 1000 cells, discretise the initial radiation field by 10^6 packets, use the γ-ray transport scheme outlined in Section 5.2.3 and, following Lucy (2005), assume radiative equilibrium. This way, we may treat the interactions of the optical radiation field with the ambient ejecta material exclusively as scatterings (see Noebauer et al., 2012). To enable a direct comparison to the results of Lucy (2005), which were obtained from pure radiative transfer calculations, we deactivate the influence of the radiation field on the dynamics of the ejecta material in our Mcrh calculation. We perform the simulation

---

[9] Recall that the energy is denoted by $\mathcal{E}$ and its corresponding volume density by E.

[10] For a radiation-dominated gas, pressure and energy are related by $p = 1/3E$ [see Eq. (2.31)]

[11] Note the typo in the corresponding formula of Noebauer (2011), eq. 6.1.7.

[12] Also the the analytic formula for the energy evolution in Noebauer (2011), eq. 6.1.8, contains a typo on the last line.

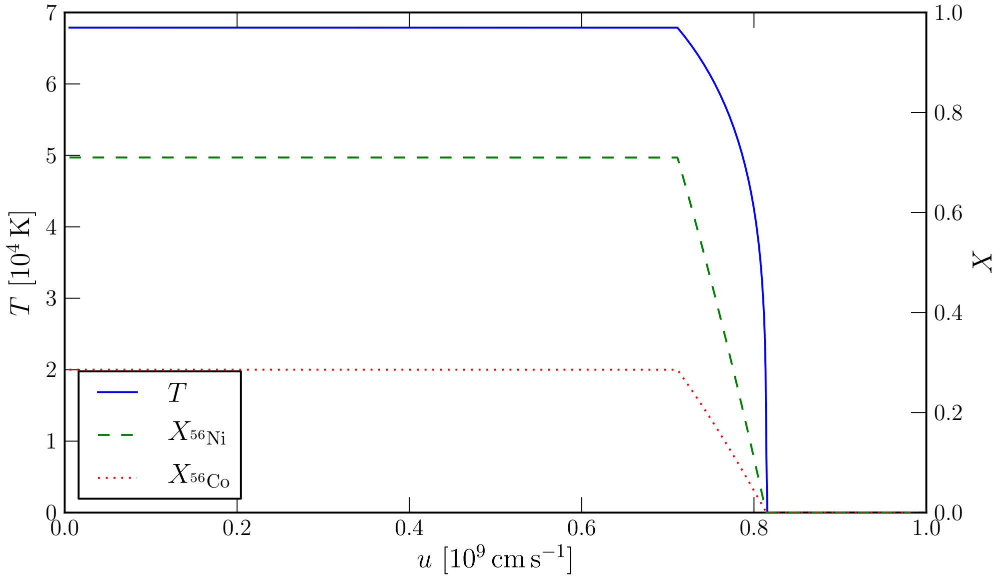

Figure 5.1.: Temperature profile and abundances of the radionuclei for the Lucy (2005) light curve test at $t = 3$ days. The initial radiation field in the MCRH calculation is seeded assuming LTE according to this temperature distribution.

in the Lagrangian mode of MCRH, since the bulk of the ejecta material would leave the computational domain of a static Eulerian grid during the simulation. In contrast, the grid follows the fluid flow and expands during the calculation in the Lagrangian description. Moreover, the dissipation, i.e. the conversion of kinetic to internal energy due to the numerical discretisation, is much lower in Lagrangian than in Eulerian schemes. This is particularly important for the supernova case since the energy stored in the expansive motion of the ejecta is much larger than the internal energy pool. Consequently, even a small amount of numerical dissipation would cause large changes in the gas temperature. However, relying on the Lagrangian scheme, this effect is largely absent in our simulations (see chap. 7.2 in Noebauer, 2011, for a detailed discussion).

With the configurations and the initial setup described above, we follow the evolution of the radiation field with MCRH from $t = 3$ days until $t = 50$ days. The emerging bolometric light curve is shown in Fig. 5.2 (c.f. Noebauer et al., 2012, fig. 8) and compared with the reference calculation of Lucy (2005). In addition, the γ-deposition rates of Lucy (2005) and of the MCRH simulation are displayed in the same figure. All results are presented in the magnitude system by converting the emergent luminosity (and decay and deposition rates) according to

$$m = -2.5 \log \left(L/L_{\odot}\right) + m_{\odot}, \tag{5.15}$$

using the solar luminosity, $L_\odot = 3.845 \times 10^{33}\,\mathrm{erg\,s^{-1}}$ and its bolometric magnitude, $m_\odot = 4.74$ (Cox, 2000). The match in the two light curves and in the γ-deposition rates is excellent. Taking into account that the Lucy (2005) results have been successfully verified by comparing with the outcome of a non-Monte Carlo calculation based on a solution to the momentum equations of Castor (1972), the agreement displayed in Fig. 5.2 demonstrates the accurate operation of the supernova-specific extensions of MCRH.

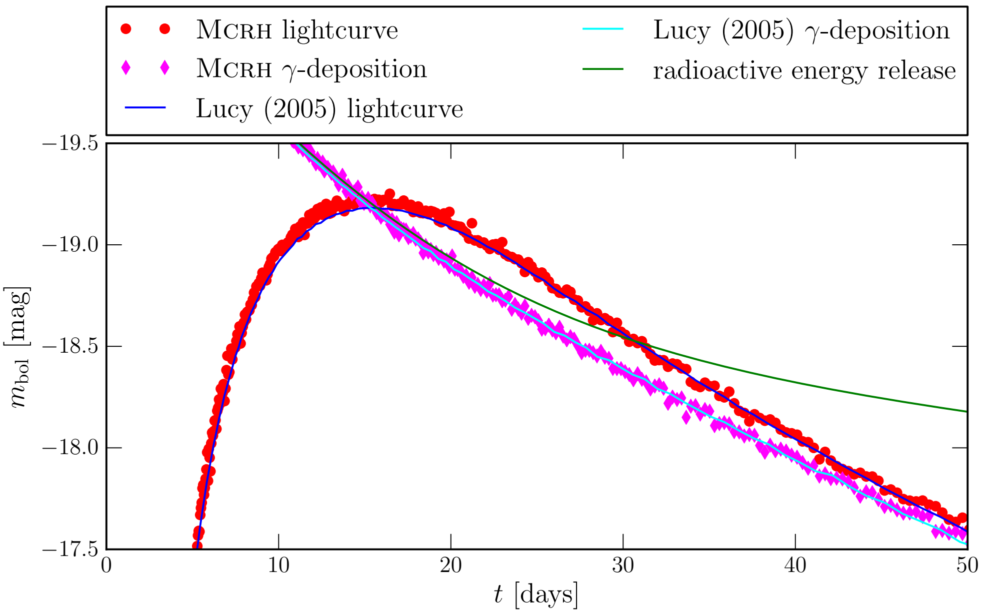

Figure 5.2.: Comparison between the bolometric light curve determined with MCRH (red circles) and the published results of Lucy (2005) (solid blue). Additionally, the γ-deposition rates are shown for both calculations, by magenta diamonds for MCRH and by the solid cyan line for the Lucy (2005) simulation. Initially, the γ-deposition follows the radioactive energy release (solid green), but as the ejecta expand and the optical depth decreases, γ-rays propagate further and less energy is deposited in the optical radiation field.

5.2.5. W7 Ejecta Calculations

Having established the correct working of the supernova-specific aspects of MCRH, we use our radiation hydrodynamical tool to investigate the influence of the radiation field on the evolution of ejecta of Type Ia supernovae. An initial study of this problem was already presented in Noebauer (2011), however, relying on unrealistic physical conditions, in particular on a plane-parallel geometry. Here, we report on the results of more sophisticated calculations, based on a more realistic representation of the physical conditions in Type Ia supernova ejecta. These calculations have partly been discussed already in Noebauer et al. (2012).

We perform the ejecta calculations using the example of the W7 model (Nomoto et al., 1984; Thielemann et al., 1986). This one-dimensional Chandrasekhar-mass explosion model relies on a parametrisation of the thermonuclear flame speed. Due to its success in reproducing many observational features, it has emerged as a reference model for Type Ia supernovae. In our simulations, we rely on the particular W7 calculation of Iwamoto et al. (1999), who incorporated a large nuclear reaction network. Relying on the same procedure as outlined in Section 5.2.4, we evolve the W7 density stratification and the abundance structure to the onset of the MCRH calculation, $t = 3\,\mathrm{days}$. As emphasised in Section 5.2.4, this strategy is owed to the computational inefficiency of the Monte Carlo approach in regions of high optical depths. Naturally, any dynamical influence of the radiation field onto the ejecta evolution during the time from the onset of homologous expansion to the start of the simulation is neglected. A noticeable amount of momentum transfer may, however, occur during early times, even though the radiation field is highly diffusive and thus almost isotropic. Due to the high opacity of the medium, the radiation field may exert an appreciable influence on the ambient material even for very low net fluxes. For now we ignore this effect and investigate the radiative influence during the early expansion times later, by successively decreasing the duration of the homology calculation.

The homologously expanded W7 ejecta are mapped onto a spherical grid with 2000 equidistant cells, to properly resolve the spatial distribution of the radioactive material. The original W7 velocity profile is not in perfect homologous expansion but exhibits slight departures from it (see, for example, Noebauer, 2011, fig. 6.1). To facilitate a clear identification of the radiation hydrodynamical effects, we ignore the ejecta velocity of the W7 model and initiate the material with the flow speed of homologous expansion [see Eq. (5.1)]. For the γ-transport scheme, we adopt the same effective absorption cross section as in Section 5.2.4, $\chi^{\mathrm{abs}}/\rho = 0.03\,\mathrm{cm}^2\,\mathrm{g}^{-1}$. In the treatment of the optical radiation field, we again follow Lucy (2005), rely on the assumption of radiative equilibrium and simplify the interaction processes with the ambient material to only occur as scatterings. However, compared to the simplified ejecta model calculation, we adopt a more realistic treatment of the opacity. In particular, we gear the interaction cross section to the distribution of heavy elements, since they are the main source of opacity. Following Mazzali & Podsiadlowski (2006) and Sim (2007), we adopt the opacity law

$$\chi/\rho = N(0.9X_{\mathrm{IGE}} + 0.1), \tag{5.16}$$

which involves the abundances of the iron group elements (IGE)[13] and a normalisation factor N, ensuring a mean interaction cross section in the ejecta of $\langle\chi/\rho\rangle = 0.1\,\mathrm{cm}^2\,\mathrm{g}^{-1}$. The distribution of iron group elements is shown in Fig. 5.3 (c.f. Noebauer et al., 2012, fig. 9), together with the initial gas temperature, which determines the radiation field at the onset of the MCRH calculation. The resulting cross section is shown together with the initial density at $t = 3\,\mathrm{days}$ in Fig. 5.4 (c.f. Noebauer et al., 2012, fig. 10). At that time, the ejecta have an optical depth of

---

[13] We include all elements with $Z \geq 20$ as part of the iron group.

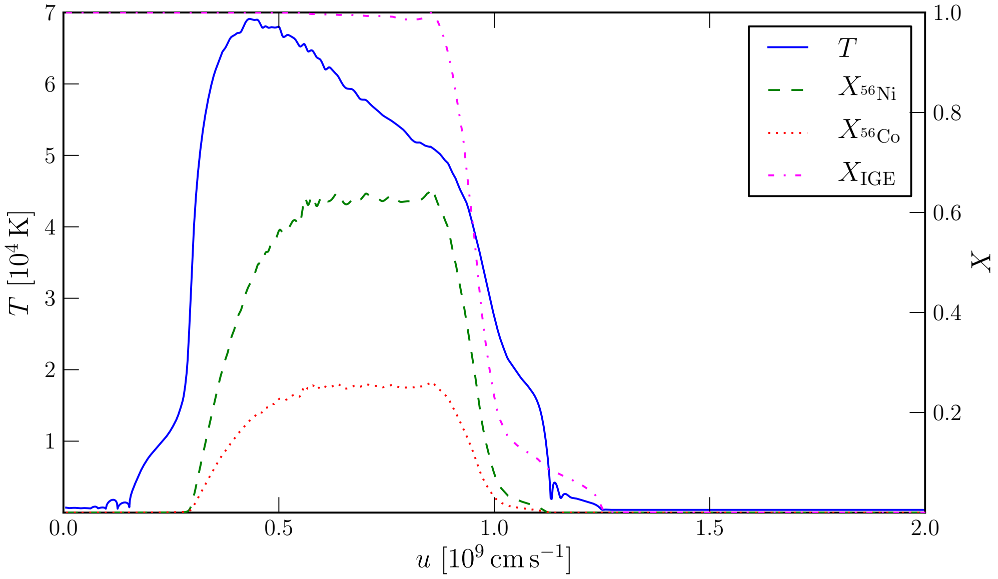

Figure 5.3.: Initial (at $t = 3\,$days) gas temperature (solid blue), abundances of the iron group elements (dash-dotted magenta) and of the radioactive nickel (dashed green) and cobalt (dotted red) for the W7 ejecta after the analytic homologous expansion procedure.

$\tau = 5.6 \times 10^2$ for γ-rays and $\tau = 3.7 \times 10^3$ for optical radiation which allows us to use Monte Carlo radiative transfer schemes efficiently (see discussion in Section 5.2.4). We discretise the initial radiation field by 10^6 Monte Carlo packets and evolve the radiation–matter state in the W7 ejecta with the Lagrangian mode of MCRH (see Section 5.2.4). In contrast to the previous toy calculation, we now explicitly include the dynamical effect of the radiation field. We halt the calculation when reaching $t = 50\,$days after explosion. In Fig. 5.5 (c.f. Noebauer et al., 2012, fig. 11), the evolution of the radiation field is illustrated in the $u \times t$ plane. Due to its origin in radioactive decay reactions, the initial radiation field tracks the location of the radioactive material, which in the W7 model resides in an extended shell between $u \simeq 0.3 \times 10^9\,\mathrm{cm\,s^{-1}}$ and $u \simeq 1.1 \times 10^9\,\mathrm{cm\,s^{-1}}$. As the optical depth of the ejecta material decreases with the advancing expansion, the radiation field streams in- and outwards (see Fig. 5.5). Consequently, the net radiation flux exerts a force on the ambient ejecta material, leading to a decelerated expansion in the inner regions and an acceleration in the “nickel shell” and the outer layers. These changes in the expansion velocities affect the density evolution, causing a dilution of the nickel shell and an accumulation of ejecta material at its edges. These effects are illustrated in Fig. 5.6 (c.f. Noebauer et al., 2012, fig. 12), in which the ejecta structure is shown with respect to a pure homologous expansion. In particular, u/u_0 and $\rho/\rho_0\ (t/t_0)^3$ are shown for the snapshots, $t = 4$, 6, 12, 20 and 45 days. Due to the dynamical effect of the radiation field, the ejecta velocity departs on a 2% level and the density stratification deviates on a 10% level from a pure homologous

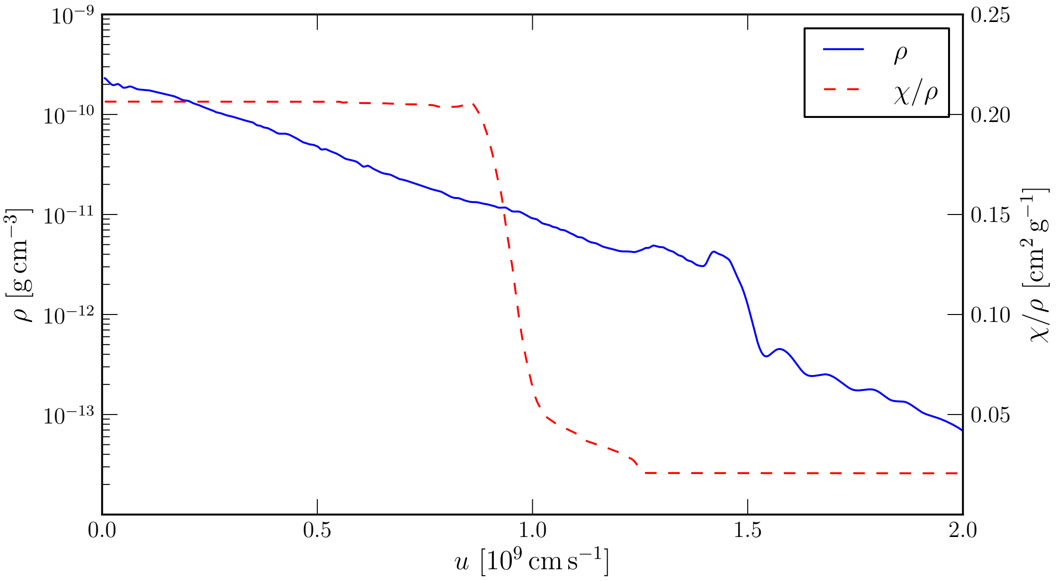

Figure 5.4.: Initial density (solid blue) and the composition-dependent scattering cross section (dashed red) for optical radiation, Eq. (5.16), in the W7 ejecta calculation.

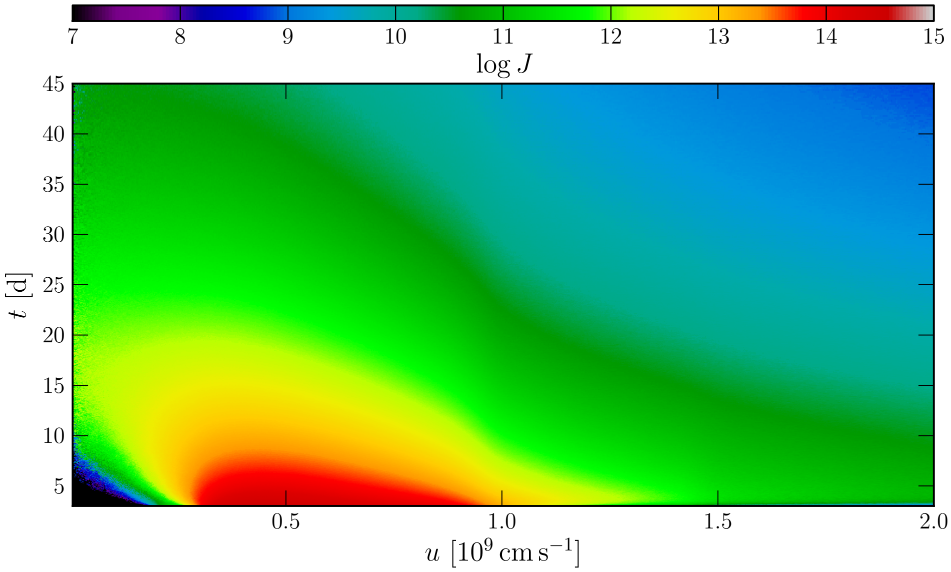

Figure 5.5.: Evolution of the radiation field in the W7 ejecta calculation. The mean intensity is colour-coded and displayed in the $u \times t$ plane. The initial confinement to the location of the radionuclei and the following diffusion out of this region is clearly visible.

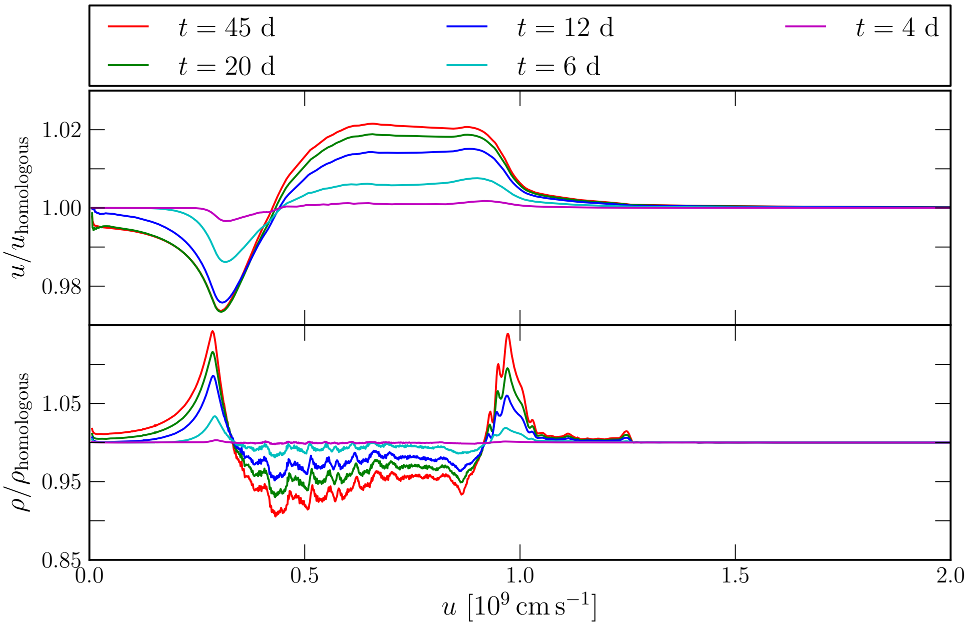

Figure 5.6.: Illustration of the radiative influence on the evolution of the W7 ejecta. In the upper panel the ejecta velocity is shown with respect to the one expected for a pure homologous expansion. Different snapshots of the calculation are colour-coded. In the lower panel, the changes in the density stratification are displayed in the same fashion.

expansion. The growth of these deviations slowly saturates with time as may be observed in the small difference in the ejecta structure between 20 and 45 days. Consequently, no significant radiative influence is expected beyond the reach of our calculation, 50 days. The structural changes in the ejecta, as shown in Fig. 5.6, do not seem to affect the (bolometric) observables of the supernova model. The bolometric light curve calculated in the radiation hydrodynamical simulation of the W7 ejecta is virtually identical with the one obtained in a analogous calculation in which the radiative influence on the ejecta evolution is deactivated (same simulation mode as in Section 5.2.4). This is illustrated in Fig. 5.7 (c.f. Noebauer et al., 2012, fig. 13), in which the light curves of these two simulations are compared, exhibiting no significant difference. These findings, which speak in favour of the common strategy to rely on a strict homologous ejecta expansion in the determination of synthetic supernova Type Ia observables, are compatible with previous studies by Pinto & Eastman (2000) and Woosley et al. (2007), which reached the same conclusions. In particular, Woosley et al. (2007) compared colour light curves, determined with the pure radiative transfer code Sedona (Kasen et al., 2006) with full radiation hydrodynamical simulations performed with Stella (Blinnikov & Bartunov, 1993; Blinnikov & Sorokina, 2000). The results of these calculations agree reasonably well and Woosley et al. (2007) argue that the differences are primarily caused by the different radiative transfer treatments in the two codes and not by the radiative influence on the ejecta evolution. Compared to this study, we have only investigated the influence on the bolometric light curve, but have the advantage of being able to

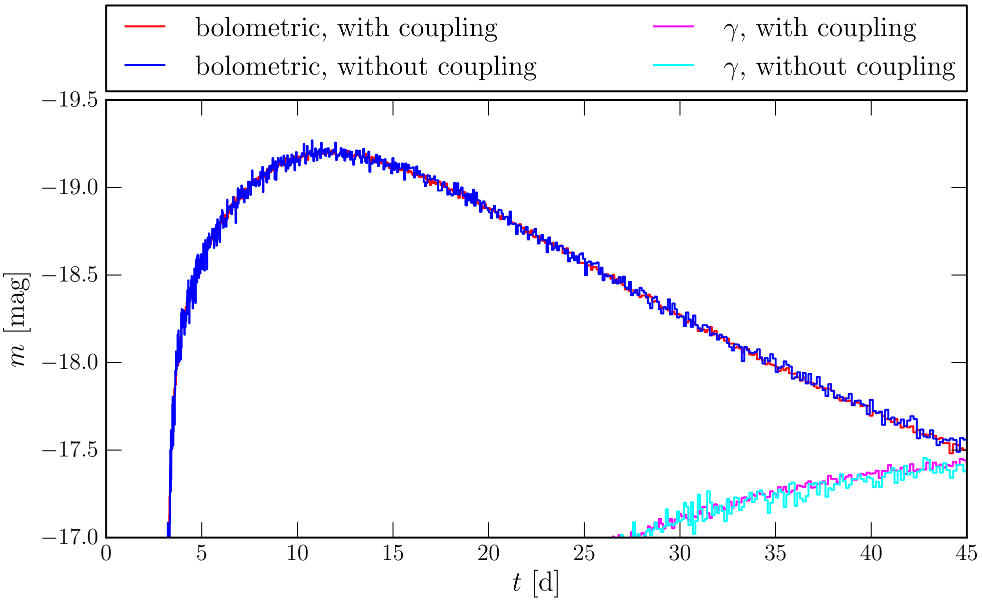

Figure 5.7.: Comparison between the bolometric light curve determined for the W7 ejecta with the radiative influence on the ejecta evolution included (solid red) and without (solid blue). The corresponding γ-light curves are shown in magenta and cyan.

clearly identify the effect of the radiation-hydrodynamical coupling since the radiative transfer treatment remains the same in both our calculations. However, despite the insensitiveness of the bolometric and colour light curves, the possibility remains that the induced changes in the ejecta structure, in particular in the expansion velocities, have a noticeable influence on the emergent spectra. Elements now lie at a slightly different velocity, which may induce shifts in the line profiles. A detailed study of this problem, however, is deferred to the future and the development of a fully-fledged frequency-dependent implementation of MCRH (see Chapter 7).

In contrast to the calculations performed with STELLA and discussed in Woosley et al. (2007), we cannot follow the radiative influence on the ejecta evolution during the early expansion phase. In an attempt to estimate the magnitude of this effect, which we ignore with our strategy of bridging the inaccessible early phase by an analytic homologous expansion calculation, we gradually shift the onset of the MCRH simulations to earlier times. In Fig. 5.8, we compare the departures in the ejecta structure from homologous expansions for calculations which start at 1, 2 and, as above, 3 days after explosion. The sooner we include the dynamical effect of the radiation field into the consideration, the higher the velocity and density changes are. However, even for the calculation starting 1 day after explosion, the changes are not strong enough to influence the bolometric light curve. This is illustrated in Fig. 5.9, in which the light curves of the radiation hydrodynamical calculations with different starting times are compared and

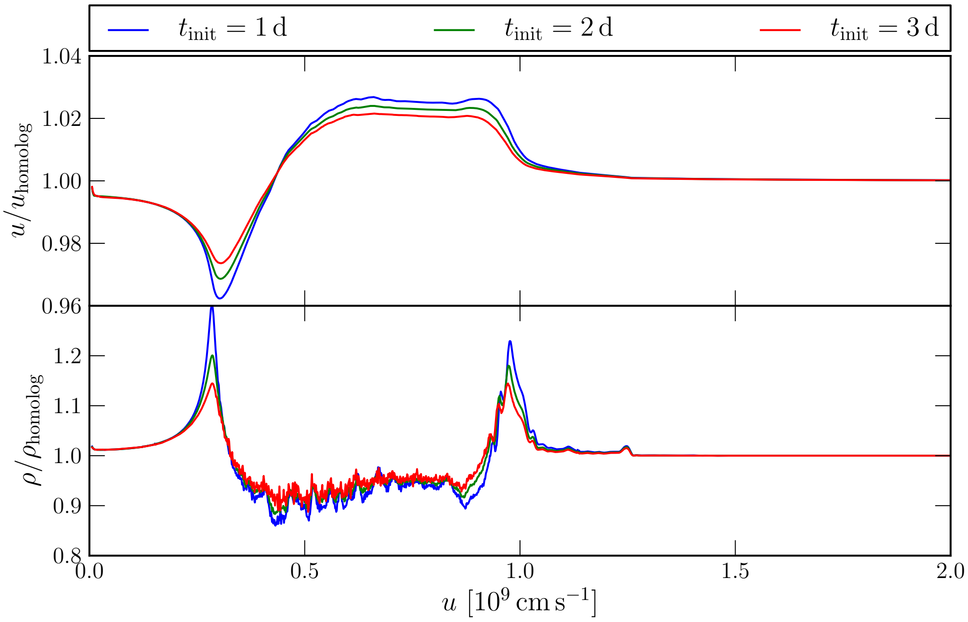

Figure 5.8.: Comparison of the ejecta structure for different durations of the homology calculations bridging the time to the onset of the MCRH simulation. The final (at $t = 45\,\text{d}$) velocity (upper panel) and density (lower panel) are shown with respect to a strict homologous expansion in analogy to Fig. 5.6.

agree perfectly within the uncertainties of the Monte Carlo noise. Based on these findings, we are confident that the conclusions drawn from the calculation at $t = 3\,$days are not affected by neglecting the dynamical influence of the radiation field during the early expansion phase.

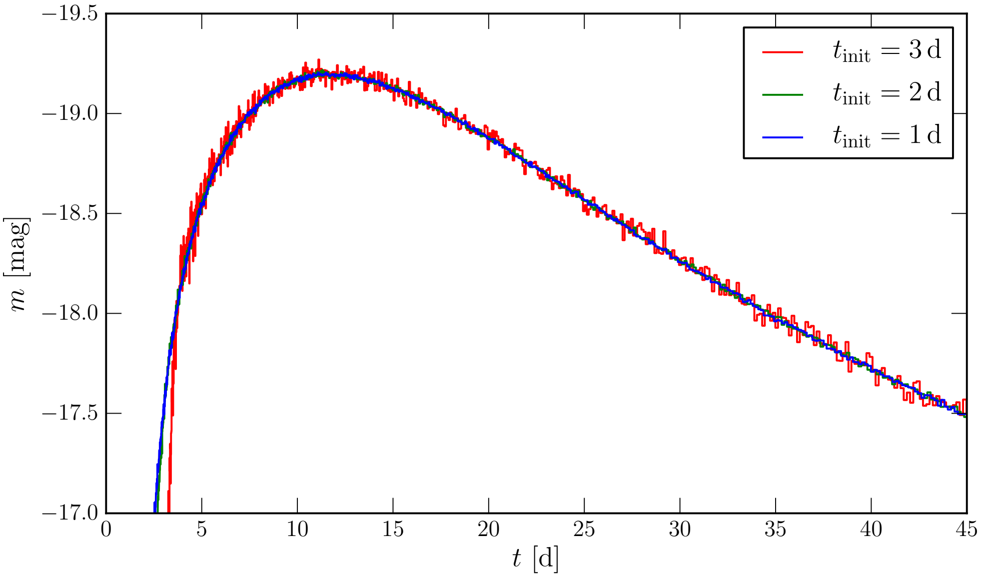

Figure 5.9.: Comparison of the bolometric light curves obtained in Mcrh simulations with different starting times. Apart from differences in the early rising phase of the light curve, all calculations agree very well within the Monte Carlo noise uncertainty.

Before concluding the discussion of the ejecta calculations, we emphasise that, in contrast to the calculations presented in Noebauer et al. (2012), no smoothing of the reconstructed radiation force terms is required here. This is due to the different estimator techniques used in the two studies. In Noebauer et al. (2012), we rely on estimators, in which each trajectory element simultaneously simulates the absorption and re-emission parts of the scattering interactions [see Eqs. (3.92) and (3.93)]. In contrast, we use estimators for the radiation force in the CMF in the current study and determine the momentum and energy transfer after the transformation into the LF [see Eqs. (3.102) to (3.104)]. The improved noise behaviour of the current technique is illustrated in Fig. 5.10, in which the cumulative momentum transfer during the ejecta calculation is shown for both techniques.

5.3. Ejecta–CSM Interactions

After having established the performance of the Mcrh method in the general supernova context, we attempt to perform Mcrh-based radiation hydrodynamical simulations of interacting supernovae. These calculations are mainly motivated by the relevance of the ejecta–CSM interaction

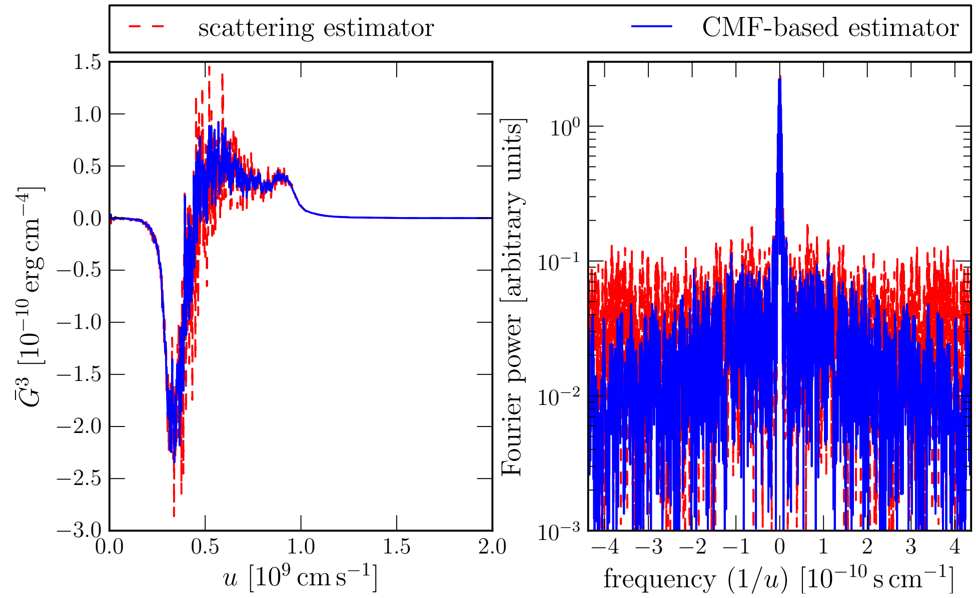

Figure 5.10.: The left panel shows the comparison between the mean radiation force component $\bar{G}^3$ during the entire ejecta simulation (starting at 3 days) obtained with the scattering estimators (dashed red) used in Noebauer et al. (2012) [described by Eqs. (3.92) and (3.93)] and with the CMF estimators (solid blue) employed throughout this work [captured by Eqs. (3.102) to (3.104)]. In the right panel, the corresponding Fourier analysis of the two results are shown. The CMF estimators clearly suffer from fewer high-frequency statistical fluctuations.

scenario as a potential explanation for super-luminous Type Ia explosions. After briefly providing the astrophysical background in Section 5.3.1, we present in Section 5.3.2 the first MCRH toy calculations of an interacting supernova ejecta and highlight in Section 5.3.3 the challenges associated with the stiffness of the radiative source terms we are facing in these calculations. In the remaining part, Sections 5.3.4 to 5.3.6, we discuss a number of numerical techniques that may potentially help in remedying these difficulties.

5.3.1. Super-luminous Type Ia Explosions

Our understanding of Type Ia supernovae is increasingly challenged by the various observational subclasses of these transients. In particular, the most luminous incarnations of Type Ia supernovae constitute a puzzle and elude a concise theoretical description. These events, of which SN 2009dc is a prominent example (Taubenberger et al., 2011), are characterised by intense peak luminosities ($M_{\mathrm{peak}} \sim -20$, see Taubenberger et al. 2011), which exceed those of all other Type Ia supernovae by about a factor of two. The high energy output of these systems severely contests the standard model for Type Ia supernovae, in which the observed radiative energy is solely traced back to the decay of the radio-nuclei in the ejecta material. To explain the high peak luminosity of SN 2009dc within this picture, radioactive nickel amounting to more than one solar mass would have to be present, which in turn implies a total ejecta mass beyond the Chandrasekhar-mass limit for non-rotating white dwarfs (see, for example, Taubenberger et al., 2011, 2013). Alternate scenarios have been put forward to explain these super-luminous events. By invoking rapid differential rotation, the stability limit for white dwarfs may be increased and the high amount of radioactive nickel motivated (Yoon & Langer, 2005; Howell et al., 2006; Branch, 2006). The merging of two massive white dwarfs is also discussed as a possible explanation for super-luminous events (Hicken et al., 2007), since the Chandrasekhar limit may be evaded in this scenario. The mass limit applies for the individual white dwarf stars, but not for the compound which is formed in the merger and in which a thermonuclear explosion is induced. The alternative to the above mechanisms is to invoke an energy source different from radioactivity, which contributes to the emergent luminosity. Here, interactions of the ejecta with circumstellar material, which may be present in the immediate explosion environment due to previous mass-loss episodes of the progenitor system, constitute a very promising scenario. Via shock-heating processes, the vast kinetic energy pool of the ejecta may be tapped and partly converted into internal energy, thus eventually contributing to the light output of the system (see, for example, Grassberg & Nadezhin, 1986; Chugai et al., 2004a, for similar calculations in the context of very luminous Type II explosions). Hachinger et al. (2012) demonstrated that a normal Type Ia supernova spectrum, amplified by the contribution of a continuum, which may be a result of ejecta–CSM interactions, fits the observed data of SN 2009dc very well. However, detailed radiation hydrodynamical investigations are required to establish if realistic interaction processes may indeed explain the high luminosity. Such studies may also predict the spectral appearance of such systems and establish which signatures may act as probes for the interaction scenario. This seems an ideal task for Monte Carlo-based calculations. With this motivation and the concrete aim of investigating super-luminous Type Ia explosions, we perform MCRH simulations of interacting supernovae. Similar radiation hydrodynamical simulations for Type Ia supernovae have already been performed before, for example by Fryer et al. (2010) and Blinnikov & Sorokina (2010), however not in the super-luminous context. In the remainder of this chapter we present the results and implications of our initial calculations. We note that the following discussion should be viewed as “work in progress” since the calculations and their results are preliminary and a concise picture has not yet formed. Nevertheless, we include a description of this work here, since it highlights some general challenges of explicit operator-split radiation hydrodynamical approaches in environments, where the radiation–matter coupling is energy dominated.

5.3.2. Toy Simulations of Ejecta–CSM Interaction

To establish whether the MCRH method is capable of following the interaction processes at the ejecta–CSM interface, we consider a simple toy setup. We again use the W7 model, according to which we initialise a supernova ejecta at $t = 1\,\mathrm{d}$ after explosion. At the edge of the ejecta, which is identified on the basis of the abundance pattern of the thermonuclear fuel (carbon and oxygen), we attach a power-law wind, following the density profile

$$\rho(r) = \rho_{\mathrm{ref}} r^{-4}. \tag{5.17}$$

The reference density is chosen to yield a total mass of $0.1\,M_{\odot}$ enclosed within the region of the wind we consider[14]: $r_{\mathrm{min}} = 1.2 \times 10^{14}\,\mathrm{cm}$ and $r_{\mathrm{max}} = 2 \times 10^{14}\,\mathrm{cm}$. For simplicity, and since we are initially only interested in the processes in the ejecta–wind interface, we initialise the entire computational domain at a temperature of $T = 10^4\,\mathrm{K}$ and consider the wind material at rest. Also, we ignore for now the energy release due to the radioactive decay within the ejecta and assume a grey absorption cross section of $\sigma = 0.1\,\mathrm{cm}^2\,\mathrm{g}^{-1}$ throughout the computational domain.

The challenges posed by the interactions between the ejecta and the CSM in the radiation hydrodynamical simulations may already be anticipated from a pure fluid dynamical treatment of the toy setup. The results of such a calculation are shown in Fig. 5.11, in which the evolution of density, velocity and gas temperature is illustrated. As expected, the ejecta material continues a homologous expansion in the inner regions. At the edge of the ejecta, however, the material runs into the wind and produces strong shocks. To guide the eye, the location of these shocks is marked by dashed white lines in Fig. 5.11. Since the (hydrodynamical) energy balance is dominated by kinetic energy – at the interface, the relation is $E_{\mathrm{kin}} \sim 1.1 \times 10^8\,\mathrm{erg\,cm^{-3}}$ to $E_{\mathrm{int}} \sim 8.4\,\mathrm{erg\,cm^{-3}}$ – already a small reduction of the kinetic energy pool by shock compression induces very high temperatures in the shocked region (see Fig. 5.11, bottom panel). The magnitude of

---

[14] These parameter choices are very crude. However, the results presented in the following are qualitatively the same if the density is changed by a few orders of magnitude.

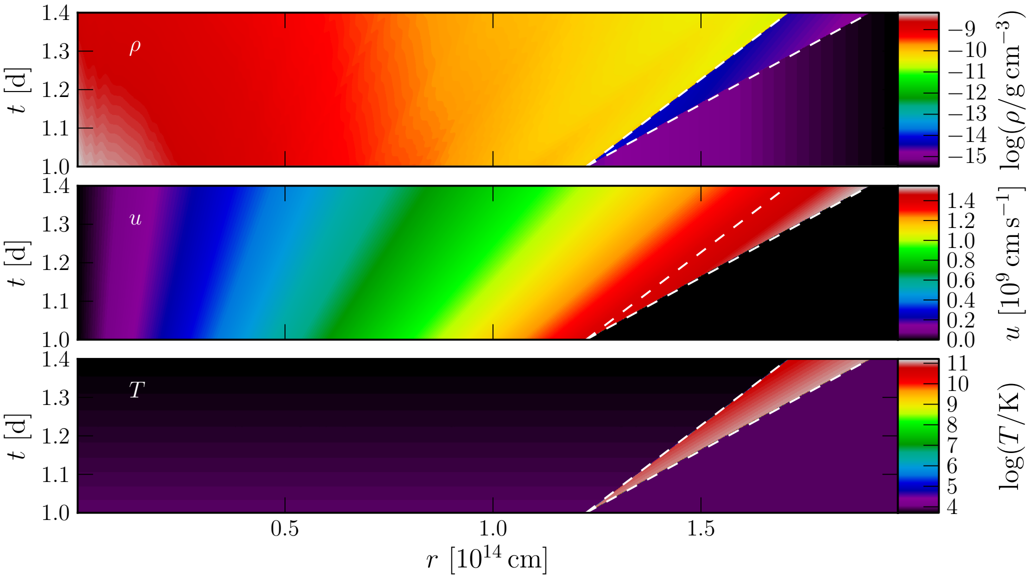

Figure 5.11.: Results of a pure hydrodynamical calculation of the ejecta–wind interaction toy setup. The evolution of density (top panel), velocity (middle panel) and gas temperature (bottom panel) is displayed in the $r \times t$ plane and colour-coded. The strong interaction at the ejecta–wind interface, which is initially located around $r \approx 1.2 \times 10^{14}$ cm, is clearly visible. The location of the emergent forward and backward shocks is marked in all panels by dashed white lines.

the temperature increase may be estimated from the jump conditions, approximated for very strong shocks (see, for example, Mihalas & Mihalas, 1984, §56):

$$\frac{T_2}{T_1} = \frac{\gamma - 1}{\gamma + 1} \frac{2u_1^2 \rho_1 - 2\gamma p_1}{(\gamma + 1) p_1}. \tag{5.18}$$

Here, the upstream and the shocked material are distinguished by subscripts 1 and 2, respectively. For the conditions at the ejecta–CSM interface and the adiabatic index $\gamma = 5/3$, the above relation predicts a jump of the order of $T_2/T_1 \sim 7.5 \times 10^6$. The temperature in the shock may be expressed as

$$T_2 = \frac{1}{2} u_1^2 \frac{3}{8} \frac{\mu}{k_\mathrm{B}} - \frac{5}{16} T_1, \tag{5.19}$$

which, for the current conditions ($\bar{\mu} = 5.4 \times 10^{-23}\,\mathrm{g}$) and as long as the temperature is negligible compared to the first term (i.e. $T_1 \ll 10^{10}\,\mathrm{K}$), only depends on the upstream specific kinetic energy

$$T_2 \approx 1.5 \times 10^{-7} e_{1,\mathrm{kin}}. \tag{5.20}$$

This implies a shock temperature of $T_2 \approx 1.5 \times 10^{11}\,\mathrm{K}$, which is of the order of the maximum temperature observed in the MCRH hydrodynamical simulation, $T_\mathrm{max} \approx 6.5 \times 10^{10}\,\mathrm{K}$.

Naturally, once radiative effects are included, such high temperatures do not manifest. Part of the kinetic energy, which in the pure hydrodynamical consideration is fully converted into internal energy, now feeds into establishing a strong radiation field. However, due to the reliance on the operator-splitting scheme, MCRH calculations are still limited by the consequences of the strong hydrodynamical shocks at the interface. These difficulties in our radiation hydrodynamical simulations are detailed below.

5.3.3. Stiff Source Terms

In Section 3.2.5, we highlighted the need to resolve all characteristic time scales in explicit schemes that are based on the operator splitting technique. This restriction leads to serious difficulties in cases when the source terms become *stiff* (see, for example, LeVeque, 2002, chap. 17), i.e. when the associated times scales are much shorter than the flow time, captured by the CFL criterion (see Section 3.3.3). In the current problem, the radiative cooling processes induce the stiffness. Since each radiation hydrodynamical step involves a pure hydrodynamical calculation, the shock temperature estimated above actually determines the radiative cooling time scale. For the high gas temperatures and low densities expected in the hydrodynamical shock, this time scale is of the order of $t_\mathrm{cool} \sim 10^{-21}\,\mathrm{s}$. If the overall duration of the simulation time step does not resolve this scale[15], radiative cooling processes deplete the entire internal energy pool during the radiative transfer step. Exactly this problem occurs if a MCRH radiation hydrodynamical

---

[15] This does not necessary imply that a time step duration of this order has to be used. After reducing the time step, the amount of shock-heating during the fluid dynamics step decreases and consequently the characteristic cooling scale grows.

simulation[16] is carried out with the full CFL time step ($t_{\mathrm{CFL}} \sim 10\,\mathrm{s}$): after the first time step the program crashes due to negative gas temperatures at the ejecta–wind interface.

Faced with the extremely short cooling time scale, the obvious remedy of reducing the time step until the associated processes are resolved is not feasible. An unmanageable number of time steps would have to be taken to follow the dynamics of the system. In fact, even after reducing the time step by a factor of 10^{-6} (a million time steps have to be spent to follow the fluid propagating the distance equivalent to one grid cell width), the cooling problem persists in the explicit Mcrh calculations.

Since stiff source terms are a generic problem in numerical treatments of fluid dynamics, a number of techniques have been developed and proposed to mitigate the associated difficulties. In the following we briefly discuss some of these methods and their relevance for the acute problem. Particularly, we focus on the implicit Monte Carlo technique of Fleck & Cummings (1971) in Section 5.3.4 and the hybrid Godunov scheme proposed by Miniati & Colella (2007) in Section 5.3.5. Also, we comment on approaches beyond the realm of Monte Carlo methods, which have been previously used to perform radiation hydrodynamical simulations of interacting supernovae (Fryer et al., 2010; Blinnikov & Sorokina, 2010).

5.3.4. Implicit Monte Carlo

Fleck & Cummings (1971) specifically developed the implicit Monte Carlo scheme to alleviate the problem with short characteristic time scales due to the radiative processes. By formally replacing the absorption and emission processes by an effective scattering component, much longer time steps may be adopted. We already demonstrated the utility of this technique when calculating the structure of supercritical shocks in Section 4.3.3. With the implicit scheme, the full CFL time step could be employed: without it, a reduction in the time step by about a factor of ten was needed. The benefits of the implicit Monte Carlo scheme have also been highlighted by Roth & Kasen (2014). It constitutes an integral part of their Monte Carlo-based radiation-hydrodynamical scheme and is tested in a number of verification problems, most prominently, strong steady and non-steady radiative shocks.

The implicit Monte Carlo scheme also improves the performance of Mcrh in the interaction problem. Since the cooling processes in the newly forming shock are drastically reduced and replaced by effective scatterings, the gas temperature remains positive everywhere, even if the full CFL time step is used. However, a different problem arises in the course of the simulation: the density at the ejecta–wind interface continuously grows. Since we perform the simulation in the Lagrangian mode, the width of the grid cell at the interface gradually decreases in order to maintain a constant mass enclosed by the cell. This causes the CFL stability criterion to drop as well and the simulation eventually to stagnate.

A detailed investigation of the processes occurring during the simulation reveals the following: the interface region is continuously shock-heated during the fluid dynamical calculation. In the

---

[16] Relying on the explicit treatment of Monte Carlo radiative transfer.

ensuing radiative transfer step, the temperature decreases due to radiative cooling. Here, the implicit scheme ensures that the relative temperature decrease is limited and does not deplete the internal energy. In contrast to the radiative shock calculations, however, in which the radiation field in the shocked region quickly adapts to equilibrium conditions, i.e. $T_\mathrm{R} \approx T_\mathrm{G}$, this never occurs in the interaction calculation. During the course of the simulation the radiation temperature is orders of magnitude smaller than the gas temperature in the cells where the shock is located. As a consequence, the total pressure, the sum of gas and radiation pressure, is insufficient to counteract a continuous compression of the fluid material in the involved cells.

Whether this behaviour of the density is physical or a numerical artefact still has to be firmly established. A physical origin may be supported by the findings of Blinnikov & Sorokina (2010). In their calculations of interacting Type Ia supernovae, using the fully-implicit code Stella (Blinnikov & Bartunov, 1993; Blinnikov & Sorokina, 2000), a very sharp and strong density peak at the interface, amounting to a relative jump by four to five orders of magnitude, was found for some model setups (see Blinnikov & Sorokina, 2010, fig. 11). Such shocks would seriously challenge the applicability of Mcrh. Even with the implicit Monte Carlo capability, our code uses an explicit time-marching scheme and is thus subject to the CFL time step restriction. Relying on the Lagrangian description is essential to capture such sharp shock structures which encompass a large amount of mass. This, however, leads to a very short explicit time-stepping as observed in our preliminary interaction simulations. Detailed comparison calculations using both approaches, Stella and Mcrh, are required to address these concerns and to better assess the applicability of Mcrh in the interacting supernova environment.

In addition to the question about the physical correctness of the continuous density increase, we highlight a still unresolved issue connected with the implicit Monte Carlo scheme. Compared to the approach described by Roth & Kasen (2014), we employ a different implementation of this implicit scheme. As outlined in Section 3.4.6, we follow the operator-split philosophy, determine the effective opacities and the cooling rate according to the intermediate fluid state calculated in the fluid dynamical step and assume S equal to zero. With this approach, we achieve very good agreement between the supercritical shock structures determined with the explicit and the implicit Monte Carlo capabilities of Mcrh (see Fig. 4.23). Roth & Kasen (2014), however, point out the importance of accounting for the S term, which should capture all internal energy changes that are not of radiative origin, and which modifies the cooling rate (as discussed in the original work by Fleck & Cummings, 1971). Thus, packets are created according to the emissivity

$$\xi = \frac{\sigma_\mathrm{R}}{\pi} \chi^\mathrm{abs} f_F T^4 + \frac{1}{4\pi}(1 - f_F) S. \tag{5.21}$$

When including the effect of S, however, we seem to be unable to reproduce the good agreement between the explicit and implicit supercritical shock results. Also, using this version of the implicit scheme in the interaction simulation does not change the picture qualitatively. The calculations still stagnate eventually for the same reason outlined above.

The findings of these preliminary interaction calculations do not dispute the utility of the implicit Monte Carlo scheme. The benefits of this approach have been highlighted and demonstrated in numerous studies (e.g. Fleck & Cummings, 1971; Abdikamalov et al., 2012; Roth & Kasen, 2014), including our own radiative shock calculations (see Section 4.3.3). However, to the best of our knowledge, it was never tested under such extreme conditions, with orders of magnitude separating the radiative and fluid-flow timescales. It is possible that such conditions are too challenging for radiation hydrodynamical approaches based on the operator-splitting scheme and on the implicit Monte Carlo technique[17]. Further exploration of this method is required to establish whether our implementation may be improved, in particular with respect to the handling of the source term S. Here, the steady radiative shock calculations very recently presented by Roth & Kasen (2014) should prove very useful. For these verification problems semi-analytic predictions are available also for very strong (i.e. short characteristic times) radiative shocks.

5.3.5. Hybrid Godunov Scheme

While the implicit Monte Carlo scheme lengthens the characteristic time scales of radiative processes, the so-called *hybrid Godunov approach*[18], developed by Miniati & Colella (2007), adapted to radiation hydrodynamics by Sekora & Stone (2010) and implemented into the ATHENA code by Jiang et al. (2012), provides an alternative way of incorporating source terms into finite-volume Godunov-type fluid dynamical calculations. This scheme was specifically designed for the handling of stiff source terms. Encouraged by the success of this scheme in radiation hydrodynamical applications, attested by the growing number of investigations carried out with the ATHENA code (Jiang et al., 2012; Davis et al., 2012; Jiang et al., 2013a,b, 2014), we discuss the utility of this approach for improving the behaviour of MCRH in the stiff source terms regime. In their recent work, Roth & Kasen (2014), also highlight the potential benefits of interfacing this hybrid scheme with a Monte Carlo-based radiation hydrodynamical approach.

The hybrid Godunov approach is based on the deferred predictor-corrector ideas of Dutt et al. (2000) and Minion (2003). Assuming that the divergence of the hydrodynamical fluxes of the conserved fluid quantities is known, for example through solving the Riemann problem in the context of the finite-volume approach (see Section 3.3.6), the fluid dynamical problem in the presence of source terms $\mathbf{S}(\mathbf{Q})$ may be approximated by an ensemble of ordinary differential equations

$$\frac{\mathrm{d}}{\mathrm{d}t}\mathbf{Q} = \mathbf{S}(\mathbf{Q}) - (\nabla \cdot \mathbf{F})^{n+\frac{1}{2}}, \tag{5.22}$$

---

[17] Fleck & Cummings (1971) state that the implicit scheme is unconditionally stable. However, Larsen & Mercer (1987) found that, while the correct steady-state solution is obtained eventually in the implicit scheme, the evolution towards this state "[. . .] becomes increasingly unphysical for increasingly many time steps" (from Larsen & Mercer, 1987).

[18] Miniati & Colella (2007) termed this approach "A modified higher order Godunov's scheme for stiff source conservative hydrodynamics". Only Sekora & Stone (2010) introduced the name "Hybrid Godunov method". To facilitate the nomenclature, we adopt this terminology.

one for each grid cell. Here, the vector $\mathbf{Q}$ combines the conserved fluid quantities, density, ρ, momentum, $m = \rho u$, and total energy, $E = \rho e$. The flux divergence is evaluated at the centre of the time step and is assumed to be constant. Relying on a semi-implicit approach, the fluid state at the end of the time step may be determined from

$$\frac{\mathbf{Q}^{n+1} - \mathbf{Q}^{n}}{\Delta t} = \mathbf{S}(\mathbf{Q}^{n+1}) - (\nabla \cdot \mathbf{F})^{n+\frac{1}{2}}. \tag{5.23}$$

This scheme is semi-implicit since only the source function depends on the new fluid state and the flux divergence term is treated explicitly, thus its evaluation is based on the old fluid state. A predictor $\tilde{\mathbf{Q}}$, i.e. a first guess for the new fluid state, $\mathbf{Q}^{n+1}$, is found by linearising the source function

$$\mathbf{S}(\mathbf{Q}^{n+1}) = \mathbf{S}(\mathbf{Q}^{n}) + \nabla_{\mathbf{Q}}\mathbf{S}|_{\mathbf{Q}^n}(\mathbf{Q}^{n+1} - \mathbf{Q}^{n}) \tag{5.24}$$

and solving Eq. (5.23) for $\mathbf{Q}^{n+1}$

$$\tilde{\mathbf{Q}} = \mathbf{Q}^{n} + (\mathbb{I} - \Delta t \nabla_{\mathbf{Q}}\mathbf{S}|_{\mathbf{Q}^n})^{-1} \left[\mathbf{S}(\mathbf{Q}^{n}) - (\nabla \cdot \mathbf{F})^{n+\frac{1}{2}}\right] \Delta t. \tag{5.25}$$

Here, the unity matrix, $\mathbb{I}$, appears. The expression $\nabla_{\mathbf{Q}}\mathbf{S}|_{\mathbf{Q}^n}$ denotes the Jacobian of the source function with respect to the conserved quantities, evaluated at the old fluid state. The final fluid state at the end of the time step is obtained by applying a corrector to the first guess. For this, the error in the predictor, i.e. its deviation from the true solution, is estimated (see Miniati & Colella, 2007, eqs. 6 and 7)

$$\varepsilon(\Delta t) = \mathbf{Q}^{n} + \frac{\Delta t}{2}\left[\mathbf{S}(\tilde{\mathbf{Q}}) + \mathbf{S}(\mathbf{Q}^{n})\right] - \Delta t (\nabla \cdot \mathbf{F})^{n+\frac{1}{2}} - \tilde{\mathbf{Q}}. \tag{5.26}$$

Based on this error estimate, a corrector is constructed

$$\delta(\Delta t) = \left(\mathbb{I} - \Delta t \nabla_{\mathbf{Q}} S|_{\tilde{\mathbf{Q}}}\right)^{-1} \varepsilon(\Delta t) \tag{5.27}$$

and the final fluid state calculated

$$\mathbf{Q}^{n+1} = \tilde{\mathbf{Q}} + \delta(\Delta t). \tag{5.28}$$

In addition to the implicit treatment of the source function in the predictor-corrector scheme, an integral piece of the hybrid Godunov approach involves a modification of the Riemann problem. This modification uses “[...]a propagation operator that projects the dynamics of the stiff source terms onto the hyperbolic structure[...]”[19] of the fluid dynamical equations. The operator takes the form (see Miniati & Colella, 2007; Sekora & Stone, 2010)

$$\mathcal{I}(\Delta t/2) = \frac{2}{\Delta t}\int_0^{\Delta t/2} \exp\left[\tau \nabla_{\mathbf{Q}} \mathbf{S}(\mathbf{Q})\right] \mathrm{d}\tau \tag{5.29}$$

and involves the exponential of a 3 × 3 matrix. Determining this term analytically for a given source function constitutes the main challenge of this approach. Once the propagation operator is found, a modified reconstruction scheme is devised, yielding left and right states for the Riemann problem. In contrast to the methodology described in Section 3.3.5, these states incorporate the effect of the stiff source terms. In the simplest case of constant reconstruction, the modifications amount to (see Miniati & Colella, 2007, eqs. 50 to 52, for the analogous expression in case of a piecewise linear reconstruction scheme)

$$\begin{aligned}\mathbf{Q}_{L,i} &= \mathbf{Q}_i + \frac{\Delta t}{2}\mathcal{I}(\Delta t/2)\mathbf{S}(\mathbf{Q}_i),\\ \mathbf{Q}_{R,i} &= \mathbf{Q}_{i+1} + \frac{\Delta t}{2}\mathcal{I}(\Delta t/2)\mathbf{S}(\mathbf{Q}_{i+1}).\end{aligned} \tag{5.30}$$

The Riemann problem emerging from these interface states is solved with the same standard Riemann solver techniques, which are used in the pure fluid dynamics problem and which are explained in Section 3.3.6. Based on the flux divergence terms determined this way, the predictor-corrector procedure is carried out and the new fluid state is determined. With the approach just outlined, Miniati & Colella (2007) demonstrated at the example of a generic cooling function that source terms may be efficiently included for a wide range of stiffness conditions.

Encouraged by these results, Sekora & Stone (2010) adapted this approach of incorporating stiff source terms into fluid dynamical calculations for the specific problem of radiation hydrodynamics. Starting from a non-dimensional formulation of the radiation hydrodynamical equations, the authors identified the terms in the source function (in this case, combinations of the radiation force components, see Eqs. (2.87) and (2.88)) and in the Jacobian matrix, $\nabla_{\mathbf{Q}}\mathbf{S}$, which are mainly responsible for the stiffness of the equations. By primarily accounting for these terms, analytic forms for the propagation operator and the matrix inverse involved in Eqs. (5.25) and (5.27) were found. Assuming only grey interaction processes, the Jacobian, reduced to the stiff contribution of the energy coupling term, is given by (see Sekora & Stone, 2010, eq. 62)[20]

$$\nabla_{\mathbf{Q}} S = \begin{pmatrix} 0 & 0 & 0 \\ 0 & 0 & 0 \\ -S^E_\rho & -S^E_m & -S^E_E \end{pmatrix}, \tag{5.31}$$

---

[19] From Sekora & Stone (2010).

[20] Differences in the notation with respect to the expressions given in Sekora & Stone (2010) stem from the non-dimensional formulation.

involving the derivatives of the radiative sources in the energy equation [see Eq. (B.4)] with respect to the fluid state

$$\begin{aligned} S^E_\rho &= 16\chi^{\mathrm{abs}}\sigma_{\mathrm{R}}T^3\frac{\mu}{k_{\mathrm{B}}}(\gamma-1)\left(-\frac{E}{\rho^2}+\frac{m^2}{\rho^3}\right)\\ S^E_m &= 16\chi^{\mathrm{abs}}\sigma_{\mathrm{R}}T^3\frac{\mu}{k_{\mathrm{B}}}(\gamma-1)\left(-\frac{m}{\rho^2}\right)\\ S^E_E &= 16\chi^{\mathrm{abs}}\sigma_{\mathrm{R}}T^3\frac{\mu}{k_{\mathrm{B}}}(\gamma-1)\left(\frac{1}{\rho}\right). \end{aligned} \tag{5.32}$$

Only the dependence of the source function on the radiative cooling contribution, the main cause for the stiffness of the source terms, is taken into account. This process depends strongly on the gas temperature, which in turn is sensitive to variations in the fluid state. For an ideal gas with mean molecular weight μ, this dependence amounts to

$$T = \frac{\mu}{k_{\mathrm{B}}}(\gamma-1)\left(\frac{E}{\rho}-\frac{1}{2}\frac{m^2}{\rho^2}\right). \tag{5.33}$$

From the Jacobian, Sekora & Stone (2010) derive the propagation operator

$$\mathcal{I}(\Delta t/2) = \begin{pmatrix} 1 & 0 & 0\\ 0 & 1 & 0\\ (1-\alpha)\left(\frac{E}{\rho}-\frac{m^2}{\rho^2}\right) & (1-\alpha)\frac{m}{\rho} & \alpha \end{pmatrix} \tag{5.34}$$

with

$$\alpha = \frac{2}{S^E_E\Delta t}\left[1-\exp\left(-S^E_E\frac{\Delta t}{2}\right)\right] \tag{5.35}$$

and the matrix inverse

$$\left(\mathbb{I}-\Delta t\nabla_{\mathbf{Q}}\mathbf{S}\right)^{-1} = \begin{pmatrix} 1 & 0 & 0\\ 0 & 1 & 0\\ \frac{-\Delta t S^E_\rho}{1+\Delta t S^E_E} & \frac{-\Delta t S^E_m}{1+\Delta t S^E_E} & \frac{1}{1+\Delta t S^E_E} \end{pmatrix}. \tag{5.36}$$

Based on these expressions, Sekora & Stone (2010) formulate a radiation hydrodynamical scheme. The source function $\mathbf{S}$, which depends on the radiative energy density, its momentum and pressure tensor, is determined by solving radiative transfer with an implicit backwards-Euler method. The radiative sources are then incorporated by the hybrid Godunov method outlined above into the finite-volume fluid dynamical calculation, which consists of a piecewise linear reconstruction scheme and a HLLE Riemann solver (Einfeldt, 1988)[21]. The method is successfully verified by a number of test calculations, most prominently by solving the Marshak wave (see Section 4.3.2) and the radiative shock problems (see Section 4.3.3). In the follow-up work by Jiang et al. (2012),

---

[21] A variety of flux functions have been implemented in the NIKE code by Sekora & Stone (2010), however all test calculations presented in the paper have been performed with this choice.

the scheme has been slightly modified and incorporated into the Athena code (Stone et al., 2008). Later, the simple radiative transfer solver of Sekora & Stone (2010) has been replaced by the multidimensional, frequency-dependent short-characteristics method of Davis et al. (2012). With this hybrid version of Athena, a number of radiation hydrodynamical studies has been performed (Jiang et al., 2012; Davis et al., 2012; Jiang et al., 2013a,b, 2014).

Encouraged by these studies, we attempt to adapt the hybrid technique for Mcrh calculations to improve the performance of our scheme in the regime of stiff source terms. Effectively, we replace the implicit backwards-Euler step of Sekora & Stone (2010) with our Monte Carlo radiative transfer calculation to evolve the state of the radiation field. To assess the feasibility of using the hybrid scheme in conjunction with a Monte Carlo based radiative transfer calculation, we alter the hydrodynamical module of Mcrh and use the same techniques as outlined in Sekora & Stone (2010): a linear-reconstruction scheme and a HLLE Riemann solver. We chose the Ensman (1994) supercritical shock setup as the testing environment and the results of the operator-split Mcrh calculations as a reference (see Section 4.3.3).

In our preliminary calculations with the hybrid scheme, we are unable to reproduce the operator-split results. Instead, we observe that, while the gas and radiation temperature profiles exhibit the characteristic shape, their evolution is "lagging" behind the expected trend significantly. Only if the CFL time step was reduced drastically, by factors of $\sim 10-100$, the expected results were retained. This is not surprising, however, since in the limit $\Delta t \rightarrow 0$, the hybrid scheme resembles the operator-split version of the radiation hydrodynamical problem. We emphasise, however, the preliminary character of these results and the fact that, in contrast to the large amount of tests performed on the split version (a subsets of these tests are presented in Chapter 4), the hybrid version of Mcrh is currently poorly tested. Thus, we do not interpret these first findings as an argument against the feasibility of a Monte Carlo-based hybrid radiation hydrodynamical approach. Instead, we advocate the use of caution in the future efforts of more detailed and careful investigations of this approach. This word of caution mainly derives from observations we made while investigating these preliminary results in detail.

Miniati & Colella (2007) devised their scheme for a source function that may be determined fully by the fluid state, for example a cooling function, only depending on the internal energy and density of the fluid. However, in radiation hydrodynamics, only the thermal emission contribution to the source function may be determined from the fluid properties alone. In general, a radiative transfer calculation has to be performed to predict how radiative heating adapts to changes in the fluid state. As a consequence, the Jacobian of the source function in Sekora & Stone (2010) only contain terms describing how the cooling rate reacts to variations in the fluid quantities. However, the absence of the reaction of the heating term may lead to difficulties in regimes in which heating and cooling terms are large and react quickly to fluid state changes.

Despite this concern and the preliminary testing results, we will pursue the investigation of the hybrid Godunov scheme for a use in Mcrh in the future. It remains unclear, however, if this technique mitigates the problems in the interacting supernova environment. Nevertheless, given the successful radiation hydrodynamical studies performed by the Athena community, the hybrid scheme bears the good prospect of also improving the behaviour of Mcrh calculations in the presence of stiff source terms.

5.3.6. Alternative Approaches

At the end of the discussion of the challenges in the interacting supernova environment in particular and problems of strong energy coupling in general, we briefly remark on successful radiation hydrodynamical treatments of ejecta–CSM interactions reported in the literature. Specifically, we comment on the studies performed by Fryer et al. (2010) and Blinnikov & Sorokina (2010) and briefly discuss why their numerical approaches were successful.

The calculations of Fryer et al. (2010) are based on the merger scenario for Type Ia explosions. After modelling the merger of the white dwarfs in an SPH approach and simulating the thermonuclear explosion with the Flash code (Fryxell et al., 2000), the interaction of the supernova ejecta with the remnant material of the merger compound is followed with the radiation hydrodynamical code Rage (Gittings et al., 2008). This numerical approach solves the radiative transfer subproblem with a flux-limited diffusion scheme (Levermore & Pomraning, 1981) and employs an operator-split approach to couple the radiative sources with the fluid dynamical equation. Here, however, a particular technique is chosen. During the radiative transfer step, the evolution of the material internal energy due to radiative heating and cooling is also considered. The resulting system is then solved by an implicit backwards-Euler time integration approach. In particular, a new technique ("exponential differencing") is used to solve the implicit equation. As a consequence of solving the coevolution of internal and radiative energy and not excluding the internal energy pool from the radiative transfer step, the Rage code is able to address the interacting supernova problem and follow the evolution of the radiative shock to its breakout and beyond (Fryer et al., 2010). With regard to Mcrh, correctly incorporating the S term into the implicit Monte Carlo scheme may provide a way of (partly) including the evolution of the internal energy pool into the radiative transfer step.

Inspired by the study of Fryer et al. (2010), Blinnikov & Sorokina (2010) performed one-dimensional radiation hydrodynamical studies of interacting supernovae with the code Stella (Blinnikov & Bartunov, 1993; Blinnikov & Sorokina, 2000). In general, no detailed explosion calculation may be performed with Stella. Instead, pre-supernova models are artificially exploded by "thermal bombs" (i.e. injecting a large amount of energy into the centre of the model), or the evolution of ejecta models provided by a separate explosion calculation is followed. For the interaction with material from the environment, Blinnikov & Sorokina (2010) attached different configurations of mass shells representing the CSM to the ejecta models. With their radiation hydrodynamical calculations Blinnikov & Sorokina (2010) could confirm the importance of the shock interactions concluded by Fryer et al. (2010) for Type Ia explosions enshrouded by carbon-oxygen material. The success of Stella in treating the interaction of the ejecta with surrounding material stems from the fully implicit nature of this numerical approach. This scheme does not separate fluid dynamics and radiative transfer but discretises the full unsplit system of radiation hydrodynamical equations. Thus, the competing processes in the interface region, i.e. shock heating, radiative cooling and radiative heating, are treated simultaneously. Unfortunately, it is unclear how to construct a fully implicit Monte Carlo-based radiation hydrodynamical scheme in which these processes do not have to be separated[22]. But we aim at performing simulations in the interacting supernova environment with STELLA in the future, which will help in better assessing the utility of MCRH for such problems.

---

[22] Monte Carlo methods are also used for fluid dynamical simulations, but they are primarily designed for calculations below the continuum limit. See Sagert et al. (2014), for a recent study investigating many-particle systems both in the continuum and out-of-continuum regime with a direct simulation Monte Carlo technique.

6. Application to Stellar Winds

In the last chapter, we have discussed the challenges faced by the operator-splitting scheme of Mcrh in problems with a strong coupling between the energy content of the radiation field and the internal energy of the ambient material. The ultimate cause for the stiffness in the source terms in this energy-dominated regime lies in the strong dependence of the thermal emissivity on the gas temperature. The complementary situation of strong momentum coupling bears the prospect of being less problematic. Here, changes in the velocity structure, induced by the exerted radiative pressure, generally have a weak feedback on the propagation behaviour of the radiation field, since only Doppler factors and the associated frequency shifts are affected.

Momentum transfer-dominated environments are frequently encountered in astrophysics, in particular in radiatively-driven mass outflows. Prominent examples are the winds driven by massive stars. In the case of hot O and B stars, the force exerted by the interaction of the radiation field with a multitude of atomic line transitions is responsible for driving and sustaining the wind outflow (Lucy & Solomon, 1970; Castor et al., 1975). Moreover, mass outflows from discs are observed in a wide variety of accreting systems, including cataclysmic variables (e.g. Drew, 1997), active galactic nuclei (e.g. Weymann et al., 1991) and young stellar objects (e.g. Mundt & Ray, 1994). While radiative processes do not seem to be solely responsible for driving the disc outflows in all cases, the line-driving effect is discussed as a substantial contribution to the acceleration of the wind material (e.g. Proga et al., 1999).

Monte Carlo techniques are very attractive for the study of line-driven mass outflows and have been frequently used in pure radiative transfer calculations of both stellar (e.g. Abbott & Lucy, 1985; Lucy & Abbott, 1993; Vink et al., 1999; Muijres et al., 2012a) and disc winds (e.g. Long & Knigge, 2002; Sim et al., 2010; Noebauer et al., 2010; Higginbottom et al., 2013). The main motivation for relying on this approach is the ease with which a multitude of atomic line interaction processes may be incorporated. In particular for line-driven winds of hot stars, the capability of Monte Carlo techniques to naturally track multiple scattering interactions is a substantial advantage. Studies relying on this technique have demonstrated that the multiple scattering phenomenon can have a significant influence on the wind properties (e.g. Vink et al., 2000). In addition to the advantages related to the realisation of complex microphysics, the ease with which Monte Carlo techniques cope with arbitrary multidimensional geometrical configurations renders this approach very attractive for radiatively-driven winds. There is strong observational evidence, for example the variability of spectral line features in hot-star winds (e.g. Markova et al., 2005), that the mass outflows exhibit spatial and temporal irregularity. Qualitatively, irregular mass outflows are also found in numerical simulations of radiatively-driven winds, for example in studies of the line-driving instability in stellar winds (e.g. Owocki et al., 1988) and in radiation hydrodynamical calculations of accretion disc winds (e.g. Proga et al., 2000). Despite the observational indications and the findings of numerical simulations, the nature of these wind flow irregularities and their effects on the properties of the outflow are still debated. Here, radiation hydrodynamical calculations have the potential to provide valuable insights. Due to the reliance on Monte Carlo techniques, the MCRH method should be particularly suited for studies of momentum-driven outflows. As a first step, we establish the utility and the accuracy of MCRH in the radiative-driven wind environment by addressing hot-star winds.

6.1. Hot-Star Winds

Massive stars may lose a substantial fraction of their initial mass during their lifetime by driving powerful winds. This mass loss can have severe impacts on the evolutionary path of massive stars. Since the luminosity of stars during the hydrogen core-burning phase is strongly correlated with the total mass, stars suffering from mass loss will shine at a lower luminosity and conversely also have a longer lifetime than without this mass-depletion mechanism (see discussion in Lamers & Cassinelli, 1999, chap. 13.1.2). Moreover, due to the action of stellar winds, the outer layers of the stars are gradually removed and regions that are increasingly enriched with products of the stellar burning cycles are laid bare. This significantly affects the spectral appearance of the star, for example, the presence of nitrogen features in WN stars (see Lamers & Cassinelli, 1999, chap. 13.1.1). Not only does the wind outflow influence the star itself, it also induces dramatic effects in the star's immediate environment, by injecting energy and momentum into the interstellar medium. This may cause the development of wind-blown bubbles or the creation of shells of circumstellar material. All these effects ultimately shape the environment in which the supernova explosion at the end of the stellar life cycle occurs, thus allowing for the interaction of the ejecta and the previously expelled wind material (see discussion in Chapter 5). Despite the importance of stellar winds for the evolution of massive stars and their environments, the details of the associated mass-loss mechanism are still not fully understood. Thus, the adopted mass-loss prescriptions constitute an uncertain ingredient of stellar evolution calculations.

In many incarnations of stellar winds, the radiation emitted by the central star is discussed as the main driver of the mass outflow[1]. Emerging from the stellar photosphere, the radiation field has a predominant propagation direction outwards. By interacting with the wind material, the radiation field is partly isotropised and loses a fraction of its bulk momentum, which is transferred onto the wind material. In the case of hot O and B stars, the interaction of the radiation field with a multitude of atomic line transitions is the dominating process in accelerating the wind material (Lucy & Solomon, 1970; Castor et al., 1975). One-dimensional, static investigations of

---

[1] The solar wind does not fall into this category. Instead, it is an example for a coronal wind driven by the effect of thermal pressure and heat conduction (see Parker 1958 and Lamers & Cassinelli 1999, chap. 5, for a general discussion of coronal winds).

hot-star winds have been very successful in reproducing observed mass-loss rates for a variety of different stars (e.g. Pauldrach et al., 1986; Vink et al., 1999, 2000). Modern stellar evolution calculations rely on the interpolated prescriptions (for example, on the mass-loss laws determined by Vink et al., 2000) derived from a large number of such global investigations, spanning a wide range of stellar parameters. Despite the success of the static description of line-driven winds, strong observational evidence exists, indicating that the wind flow is not smooth. For example, observed variability in helium (e.g. Grady et al., 1983) and hydrogen line profiles (e.g. Markova et al., 2005) and in spectrapolarimetric data (e.g. Lupie & Nordsieck, 1987) points towards the existence of clumps in the wind outflow. Studies of clumpy winds indicate that ignoring these flow irregularities in the derivation of wind mass-loss rates may lead to an overestimation of the mass-loss rates by a factor of two to ten (see discussion in the review by Puls et al., 2008). Consequently, properly accounting for the irregular flow structure may mitigate some discrepancies between observed and predicted mass-loss rates.

However, the origin of these clumps and how they exactly affect the properties of stellar winds are still debated (see Puls et al., 2008, and references therein). One possible mechanism responsible for clumpy wind outflows may be the line-driving instability, which has already been shown to induce temporal and spatial irregularity in radiation hydrodynamical calculations (e.g. Owocki et al., 1988). There are other scenarios contesting this picture and detailed radiation hydrodynamical studies of the multidimensional line-driven outflows are required to shed more light onto the nature and the consequences of clumpy winds. As mentioned above, Monte Carlo-based techniques have great potential for such studies, since the characteristics of the line-driven wind environment – complex microphysics and multidimensional flows without internal symmetries – are the conditions under which the Monte Carlo approach to radiative transfer typically excels. As a preparation for a general use of MCRH in momentum-driven outflow problems, we establish the accuracy and the applicability of this approach in a series of radiation hydrodynamical calculations of the structure of hot-star winds. Here, we derive mass-loss rates and terminal flow speeds self-consistently, and compare with the results of the so-called CAK theory (after Castor et al., 1975). By successively including more physical effects, which eventually go beyond the capabilities of CAK, we also demonstrate the utility of our approach in one-dimensional calculations. Before presenting the results of these calculations (see Section 6.3), we first introduce the standard model for hot-star winds (see Sections 6.1.1 to 6.1.3) and describe the extensions implemented into MCRH (see Section 6.2).

6.1.1. Static Wind Theory

Over the years, the theory of line-driven winds in hot stars has developed substantially (see review by Puls et al., 2008). Here, we do not aim to reproduce this work. Instead we rely on early simple semi-analytic versions of the theoretical model for hot-star winds to facilitate quantitative comparisons and in turn the assessment of the utility and accuracy of our Monte Carlo-based approach in this environment. For this purpose, we briefly outline the most basic formulation of the standard model for line-driven winds in the following. More details may be found in the literature, for example in Lamers & Cassinelli (1999), on which this presentation heavily draws.

In the standard model, the structure of line-driven winds is derived by considering a steady-state solution to the continuity and momentum equation of radiation hydrodynamics in spherical coordinates [see Eqs. (B.10) and (B.11)]. In the absence of any temporal density changes, the continuity equation predicts a constant mass-loss rate of

$$\dot{M} = 4\pi r^2 u \rho \tag{6.1}$$

in the wind. The stationary velocity profile follows from considering the various forces acting on the wind. On the one hand, the material is subject to the gravitational pull from the central star of mass $M_\star$ and to the decelerating effect of the so-called *velocity strain*, $u(\mathrm{d}u/\mathrm{d}r)$, which follows from the advective terms of the fluid dynamical equations (see derivation of the Lagrangian formulation of fluid dynamics in Section 2.2.4). On the other hand, this combined deceleration is overcome by the force due to the gas pressure gradient and, more importantly, by the accelerating effect of the radiation field

$$g_\mathrm{R} = \frac{G^1}{\rho}. \tag{6.2}$$

Here, the spatial component of the radiation force, G^1, enters [see Eqs. (2.69) and (2.91)]. Once a stationary wind state has established, the temporal velocity changes vanish and the momentum balance reduces to (see Lamers & Cassinelli, 1999, chap. 8.7)

$$0 = -u\frac{\mathrm{d}u}{\mathrm{d}r} - \frac{GM_\star}{r^2} - \frac{1}{\rho}\frac{\mathrm{d}p}{\mathrm{d}r} + g_\mathrm{R}. \tag{6.3}$$

In the second contribution, G denotes the gravitational constant. Typically, the acceleration exerted by the gas pressure gradient is small compared to the other terms in the force balance and may be neglected[2]. The radiative acceleration involves a frequency-independent contribution from the continuous radiation field being scattered by free electrons (i.e. *Thomson scattering*). Lucy & Solomon (1970) and Castor et al. (1975), however, demonstrated that the dominant effect derives from frequency-dependent interactions of the radiation field with a large number of atomic line transitions. The challenge in hot-star wind calculations is posed by determining the line-driving force as the aggregate effect of all possible line transitions.

6.1.2. Atomic Line Interactions and the Sobolev Approximation

Photons may interact with atoms by inducing a transition of an electron from a lower energy level to an upper one, provided that the photon frequency in the rest frame of the atom, ν_0, corresponds to the energy separation between these levels. Due to different processes, most prominently the

---

[2] The wind structure determined under this assumption is very similar to the results of a detailed study including gas pressure gradients (see Lamers & Cassinelli, 1999, chap. 8.7).

Doppler-broadening associated with the thermal motion of the atoms, u_{th}, photons within an entire CMF[3] frequency window may in fact come into resonance with the line transition. In the case of thermal broadening, for example, the characteristic width of that window is given by

$$\Delta\nu_{\mathrm{D}} = \nu_0 \frac{u_{\mathrm{th}}}{c}. \tag{6.4}$$

In general, the line-profile function $\phi(\Delta\nu)$ encodes the broadening of the line transition and provides the probability of a photon whose CMF deviates from the rest frame frequency of the line by $\Delta\nu = \nu - \nu_0$. With that, the opacity presented by a line transition is given in terms of the specific cross section χ_ν by (see Lamers & Cassinelli, 1999, chap. 8.3)

$$\begin{aligned} \chi_\nu \rho &= \kappa_l \rho \phi(\Delta\nu), \\ \kappa_l &= \frac{\pi e^2}{m_e c} f_l \frac{n_l}{\rho} \left(1 - \frac{n_u}{n_l}\frac{g_l}{g_u}\right). \end{aligned} \tag{6.5}$$

Here, f_l describes the oscillator strength of the transition, and the population of the lower and upper energy levels and their associated statistical weights are denoted by $n_{l,u}$ and $g_{l,u}$ respectively. Also, the electron mass m_e and elementary charge e appear[4]. Note that in this formulation, the contribution of stimulated emission is already included as negative absorption.

Only photons, whose CMF frequencies overlap with the frequency window defined by the line profile function may perform interactions with atomic line transitions. At first glance this seems to restrict the efficiency of the line-driving force dramatically since only a very small portion of the radiative flux, which lies in the appropriate frequency window, may exert an acceleration onto the wind material. However, due to the increasing flow velocity in the wind material, photons are significantly redshifted as they propagate outwards. Consequently, a much larger part of the stellar spectrum may contribute to the line driving force. With the effect of the relativistic Doppler shift in mind, the radiative acceleration resulting from a single absorption line may be formulated as (see Lamers & Cassinelli, 1999, chap. 8.5.3)

$$g_{\mathrm{line}} = \frac{2\pi}{c} \int_{\mu_\star}^{1} \mathrm{d}\mu \int_{-\infty}^{\infty} \mathrm{d}(\Delta\nu)\, \chi_{\nu_p}(\Delta\nu) \mu I_{\nu_p}(\mu). \tag{6.6}$$

Here, ν_p refers to the LF frequency of a photon emitted at the photosphere of the star. Also, we have simplified the force calculation by assuming that the mass element in which the acceleration occurs sees the photosphere directly and that the diffuse radiation field (i.e. scattered radiation) is irrelevant. Thus, the direction integration is restricted to the interval $[\mu_\star, 1]$ since, in the absence of a diffuse component, radiation originating from the photosphere, located at $R_\star$, may

---

[3] Note that co-moving frame relates to the bulk motion of the ambient material and does not include the stochastic motion of the individual particles.

[4] Note that the constant $\pi e^2/m_e c$ has a value of about $0.02654\,\mathrm{cm}^2\,\mathrm{s}^{-1}$ in cgs units, which is obtained by using the elementary charge in units of statcoulomb.

not reach the point r in the wind from an arbitrary direction. Instead, the incident direction is limited by

$$\mu_\star = \sqrt{1 - \left(\frac{R_\star}{r}\right)^2}, \tag{6.7}$$

which corresponds to the solid angle subtended by the stellar disc at radius r.

The integral with respect to $\Delta\nu$ in Eq. (6.6) has to be interpreted as an integration over the photon propagation path, along which the CMF frequency is continuously Doppler-shifted. Solving this integral poses a formidable challenge, since the varying wind structure and excitation and ionisation balance along the entire photon trajectory formally have to be taken into account. Moreover, the Doppler shift depends on the projection of the propagation direction onto the radial velocity field, introducing an interdependence between $\Delta\nu$ and μ. In the most basic version of the standard model for line-driven winds, these challenges are overcome by applying a number of approximations. In particular, the central star is considered a point source. In this simplified treatment, proposed by Castor et al. (1975), photons are forced onto radial trajectories with $\mu = 1$. The complications associated with the integration along the photon path are mitigated by applying the so-called *Sobolev Approximation* (after Sobolev, 1960). In this approach, interactions between photons and atomic line transitions are confined to a very narrow region, which is equivalent to replacing the line-width profile by a delta distribution around the rest-frame frequency

$$\phi(\Delta\nu) \to \delta(\Delta\nu). \tag{6.8}$$

Relying on these approximations, the radiative acceleration due to the interaction with a single line transition is given by (see Lamers & Cassinelli, 1999, chap. 8.5.3)

$$g_{\text{line}} = \frac{\kappa_l F_{\nu_0}}{c}\left(\frac{1 - e^{-\tau_{\nu_0}}}{\tau_{\nu_0}}\right). \tag{6.9}$$

The quantity τ_{ν_0} denotes the optical depth along the photon path and F_{ν_0} the monochromatic radiative flux (see Section 2.3.2). In the Sobolev approximation (see Lamers & Cassinelli, 1999, chap. 8.4, for a brief summary), the integration along the trajectory (measured by z) of a photon emitted at the photosphere with LF frequency ν_p (see Lamers & Cassinelli, 1999, chap. 8.4.1),

$$\tau_{\nu_p}(z') = \frac{\pi e^2}{m_e c} f_l \int_{z'}^{\infty} \mathrm{d}z\, n_l(z)\left(1 - \frac{n_u}{n_l}\frac{g_l}{g_u}\right)\phi(\Delta\nu), \tag{6.10}$$

reduces to a purely local quantity,

$$\tau_{\nu_p}(z') = (\kappa_l \rho)_{r_s}\left(\frac{\mathrm{dz}}{\mathrm{d}(\Delta\nu)}\right)_{r_s}, \tag{6.11}$$

only depending on the conditions at the so-called *Sobolev point*, r_s. This point marks the location at which the photon comes into resonance with the line transition:

$$\nu_0 = \nu_p \gamma \left(1 - \frac{u(r_s)\mu(r_s)}{c}\right). \tag{6.12}$$

For photons moving along arbitrary trajectories, the Sobolev optical depth, Eq. (6.11), takes the form[5]

$$\tau_{\nu_0} = \frac{c}{\nu_0} \frac{(\kappa_l \rho)_{r_s}}{\left[(1-\mu^2)\frac{u}{r} + \mu^2 \frac{\mathrm{d}u}{\mathrm{d}r}\right]_{r_s}}. \tag{6.13}$$

For radial paths, this expression simplifies to

$$\tau_{\nu_0}(\mu = 1) = (\kappa_l \rho)_{r_s} \frac{c}{\nu_0} \left(\frac{\mathrm{d}u}{\mathrm{d}r}\right)^{-1}, \tag{6.14}$$

which enters the formulation for the line acceleration, Eq. (6.9).

For the later discussion of the CAK theory (see Section 6.1.3), it is instructive to consider two extreme limits of the line acceleration (see Lamers & Cassinelli, 1999, chaps. 8.5.4 and 8.5.5). In the case of very optically thin lines, Eq. (6.9) reduces to

$$g_{\mathrm{line}} = \frac{F_{\nu_0}}{c} \kappa_l, \tag{6.15}$$

which exhibits no dependence on the velocity structure of the wind outflow but involves the number density of the interacting particles (κ_l depends on n_l). For the complementary limit of lines with a very high optical depth, the associated acceleration is

$$g_{\mathrm{line}} = \frac{F_{\nu_0}}{c} \frac{\kappa_l}{\tau_{\nu_0}}. \tag{6.16}$$

Since the line is optically thick, all incident photons are absorbed and the associated acceleration is independent of the number of scattering partners [τ_{ν_0} involves κ_l, see Eqs. (6.13) and (6.14)]. The wind structure, however, enters explicitly in this case via the Sobolev optical depth.

Before discussing the integral effects of all interactions with atomic line transitions in the following section, we conclude the discussion of the Sobolev approximation with a brief remark about its applicability. Locating the interaction between a photon and an atomic line transition in one point is only appropriate if the physical conditions of the wind do not change significantly within the true physical interaction region. The size of this area is given by the so-called *Sobolev length* (see Lamers & Cassinelli, 1999, chap. 8.4.3), which translates the width of the line-profile into a spatial extent[6]

$$L_s = u_{\mathrm{th}} \left(\frac{\mathrm{d}(\mu u)}{\mathrm{d}z}\right)^{-1}. \tag{6.17}$$

---

[5] In this expression, the assumption that $\nu_p \simeq \nu_0$ enters, which holds for winds in which the flow speed does not come close to the speed of light (see Lamers & Cassinelli, 1999, chap. 8.4.1).

[6] Here, we assume that the line width is primarily given by the thermal Doppler broadening.

Provided that the wind properties do not change significantly on the scale of the Sobolev length, the conditions at the Sobolev point provide a good representation of the true interaction region and the Sobolev approximation may be applied to simplify the determination of the line acceleration (see, for example, discussion in Lamers & Cassinelli, 1999, chaps. 8.4.3 and 8.4.4). In the case of hot-star winds, these requirements are reasonably well met, in particular in the supersonic regions of the wind flow (see, for example, comparison calculations performed by Pauldrach et al., 1986). As a consequence, many line-driven wind studies rely on the Sobolev approximation (e.g. Abbott & Lucy, 1985; Vink et al., 1999, 2000; Sim, 2004). However, for investigations of the line-driving instability, non-Sobolev descriptions of the radiative acceleration have to be used (see, for example, the simulations by Owocki et al. 1988 and the general discussion about the growth of instabilities in winds in the review by Puls et al. 2008).

6.1.3. CAK Theory

The difficulty of determining the radiative acceleration in hot-star winds arises from the possible contribution of not only a few atomic transitions but hundreds of thousands of resonance lines. Castor et al. (1975) evaded the necessity to individually account for the influence of each of these interaction channels and developed an approximate analytic formulation of the effective line-driving force. Relying on this simplified estimate for the radiative acceleration, the force balance in stellar winds may be solved directly, yielding analytic expressions for the velocity and density stratification. Due to its success, this approach of addressing the line-driving force and solving the wind structure is often referred to as the CAK theory[7]. The original approach has been significantly improved in follow-up works by Abbott (1982) and in particular by Pauldrach et al. (1986), who developed a modified CAK approach and highlighted some severe limitations of the initial CAK formulation. Nevertheless, we start with the most basic formulation of the theory here because it provides simple analytic expressions for the line-driving force and the wind structure, which facilitate quantitative comparisons with Mcrh calculations.

The CAK approach relies on a number of approximations, which render the line-interaction problem accessible and which are largely identical to the simplifications adopted above to identify the effect of one single line. In particular, the Sobolev approximation is used to localise the line interactions. Moreover, the central star is assumed to be a point source, which implies that radiation only streams radially. Finally, all regions of the wind are assumed to experience the influence of the unaltered stellar spectrum. This approximation is often termed the *unattenuation* of the radiation field.

An important motivation for the CAK approach lies in the realisation that the line-driving force derives from two contributions: one arises solely from atomic physics, capturing the level structure of the different atoms and the oscillator strengths of the transitions. The second contribution encodes the influence of the wind structure, i.e. its density, velocity and velocity

---

[7] After the initials of the authors of the paper Castor et al. (1975): John Castor, David Abbott and Richard Klein.

gradient. The CAK approach achieves a separation of these two contributions, providing the significant advantage of being able to rely on the same atomic physics part of the line-driving force for winds in which the same atomic line transitions are present (see discussion in Lamers & Cassinelli, 1999).

To realise this separation, the CAK approach encodes all information about the wind structure in a dimensionless optical depth parameter (Castor et al., 1975)

$$t = \sigma_e^{\mathrm{ref}} u_{\mathrm{th}} \rho \left(\frac{\mathrm{d}u}{\mathrm{d}r} \right)^{-1}, \tag{6.18}$$

involving the thermal velocity in the wind u_{th} and the specific electron-scattering cross section σ_e^{ref}. Effectively, these two quantities are reference values and may be chosen freely since they cancel in the final expression for the line-driving force. We follow Abbott (1982) and adopt the thermal velocity of protons for all our calculations, i.e.

$$u_{\mathrm{th}} = \sqrt{\frac{2 k_{\mathrm{B}} T}{m_{\mathrm{p}}}}. \tag{6.19}$$

The mass of the proton m_{p} appears here.

A second dimensionless quantity, the *force multiplier* $M(t)$, is introduced to characterise the strength of the radiative acceleration (Castor et al., 1975). It measures the efficiency of the line-driving mechanism with respect to electron scattering

$$g_{\mathrm{line}} = \frac{\sigma_e^{\mathrm{ref}} F}{c} M(t). \tag{6.20}$$

The force multiplier describes the aggregate effect of all line interactions by summing over the individual contributions (Castor et al., 1975; Abbott, 1982)

$$M(t) = \sum \frac{F_{\nu_0} \Delta\nu_{\mathrm{D}}}{F} \left(\frac{1 - e^{-t}}{t} \right). \tag{6.21}$$

Up to this point, no simplifications beyond the basic assumptions stated above have been applied and all expressions are merely a result of smart rearrangements. The fundamental insight of Castor et al. (1975) lies in removing the need for a direct evaluation of Eq. (6.21) by relying on an approximate power-law formulation[8]

$$M(t) \approx k t^{-\alpha}. \tag{6.22}$$

---

[8] Note that improved formulations of the force multiplier, e.g. by Abbott (1982), typically also account for a weak dependence on the ionisation state (see Lamers & Cassinelli, 1999). We omit this throughout this work and adopt the original formulation by Castor et al. (1975), Eq. (6.21), since we specifically assume the same constant ionisation state in all our calculations (see Section 6.3.4).

Castor et al. (1975) explicitly determined the aggregate line-driving force due to all lines of the C III ion for a number of different values of the optical depth parameter and confirmed that the force multiplier indeed follows roughly a power-law trend (see Castor et al., 1975, fig. 1). This statement also holds if the lines of a realistic wind composition and ionisation state are taken into account (see, for example, Abbott, 1982). However, the power-law fit is only a reasonable approximation in the transition region between the bulk of the lines being optically thick or optically thin. In the limits, the force multiplier reflects the behaviour of the single line transitions [see Eqs. (6.15) and (6.16)] and saturates or follows a $\sim t^{-1}$ evolution. The saturation in the optically thin limit may be accounted for by applying a modified power-law fit, such as proposed by Owocki et al. (1988).

The parameters of the force multiplier fit, k and α, have to be determined by explicitly performing the summation over all relevant lines for a given central star and pre-defined ionisation conditions in the wind. In particular, the effective temperature of the star, its effective surface gravity and the electron density in the wind are the relevant quantities. Figure 6.1 illustrates this process. Once determined, the CAK parameters may be used to solve the structure of the winds for stars that match the conditions assumed in the fitting process.

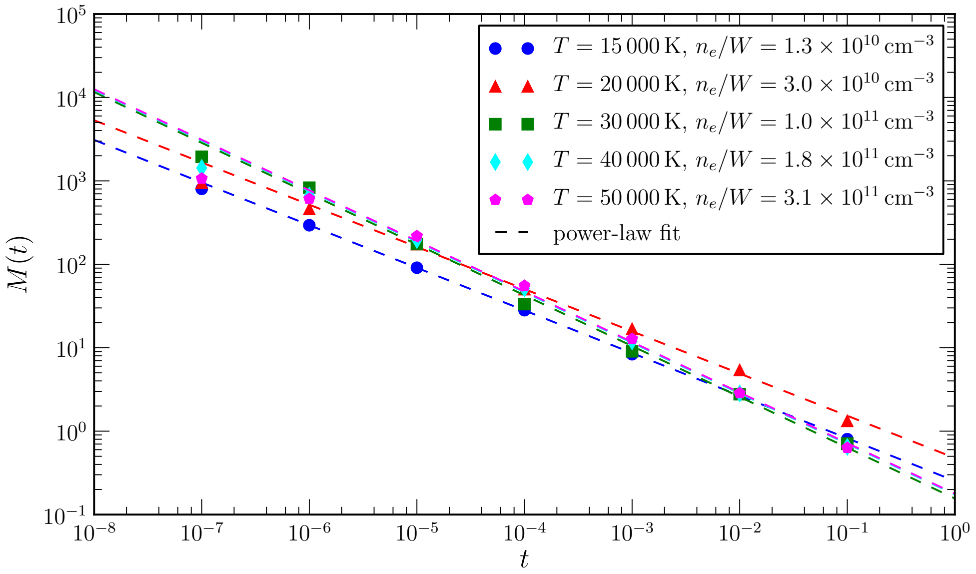

Figure 6.1.: Determination of the force multiplier parameters for a number of different physical conditions. Here, n_e denotes the electron density and W the dilution factor [see Eq. (6.46)]. The data and the resulting power-law fit (dashed lines) are taken from Abbott (1982, tab. 2).

Relying on the power-law formulation of the line-driving force, Eqs. (6.21) and (6.22), the force balance Eq. (6.3) may be solved analytically. The contribution of continuum scattering to the radiative acceleration may be absorbed into the gravitational force of the central star, effectively reducing its mass. Provided that the ionisation structure is constant throughout the wind, the electron number density, n_e, follows the mass density. As a consequence, also the specific cross section for Thomson scattering is constant (see Lamers & Cassinelli, 1999, chap. 8.7):

$$\sigma_e = \frac{n_e}{\rho}\sigma_\mathrm{T} = \frac{\sigma_\mathrm{T}}{m_\mathrm{p}}\sum_i (Q_i - 1)\frac{X_i}{A_i} = \text{const.} \tag{6.23}$$

Here, σ_T denotes the Thomson cross section and Q_i, X_i and A_i the mean ionisation stage[9], the mass fraction and the nucleon number of all elements present in the wind. As a consequence of Eq. (6.23) and of an approximately constant luminosity in the wind, the momentum transfer due to electron scattering has the same functional shape as the gravitational pull

$$g_{\mathrm{R,\,e}} = \frac{\sigma_e F}{c} = \frac{\sigma_e L}{4\pi c}\frac{1}{r^2}, \tag{6.24}$$

and may be accounted for by reducing the central mass of the star[10] to (see Lamers & Cassinelli, 1999, chap. 3.2)

$$M_\star^\mathrm{eff} = M_\star - \frac{\sigma_e L}{4\pi c G} \equiv M_\star(1-\Gamma). \tag{6.25}$$

Neglecting the influence of the gas pressure gradient, the force balance (with the velocity strain, the effective gravity of the central star and the CAK power-law line-driving force) has the following solution (see, for example, Lamers & Cassinelli, 1999, chap. 8.7.1 for a detailed outline of the solution procedure): at all locations in the wind, the combination $r^2 u(\mathrm{d}u/\mathrm{d}r)$ is constant and fulfils

$$r^2 u \frac{\mathrm{d}u}{\mathrm{d}r} = \frac{\alpha}{1-\alpha} G M_\star (1-\Gamma) = \text{const.} \tag{6.26}$$

This implies that the final wind solution is characterised by one unique value of the dimensionless optical depth parameter. From Eq. (6.26), the wind velocity law

$$u(r) = u_\infty \sqrt{1 - \frac{R_\star}{r}}, \tag{6.27}$$

is obtained (see Castor et al., 1975). Here, the terminal wind speed is a multiple of the escape speed from the stellar surface, u_esc,

$$u_\infty = \sqrt{\frac{\alpha}{1-\alpha}}\sqrt{\frac{2GM_\star(1-\Gamma)}{R_\star}} = \sqrt{\frac{\alpha}{1-\alpha}}u_\mathrm{esc}. \tag{6.28}$$

---

[9] We use the typical astronomical notation, thus $Q_i = 1$ for a neutral and $Q_i = 2$ for a singly ionised atom.

[10] Naturally, this approach neglects frequency changes of the scattered radiation due to Doppler shifts. Also, the overall propagation direction redistribution of the photons is not captured.

This structure corresponds to a generic β-type velocity law (a commonly adopted parametrisation of mass-loss velocity laws)

$$u(r) = u_c + (u_\infty - u_c)\left(1 - \frac{R_\star}{r}\right)^\beta \tag{6.29}$$

with $u_c = 0$ and $\beta = 0.5$. In the CAK approach, the mass-loss rate is given by (see Castor et al., 1975)

$$\dot{M} = \frac{4\pi}{\sigma_e^{\mathrm{ref}} u_{\mathrm{th}}}\left(k\alpha\frac{L_\star \sigma_e^{\mathrm{ref}}}{4\pi c}\right)^{\frac{1}{\alpha}}\left(\frac{1-\alpha}{\alpha}\right)^{\frac{1-\alpha}{\alpha}}\left(GM_\star(1-\Gamma)\right)^{\frac{\alpha-1}{\alpha}}. \tag{6.30}$$

These expressions are obtained by neglecting the influence of the gas pressure. However, even if typical gas pressure gradients prevalent in hot-star winds are taken into account, the above results are largely unaffected (see Castor et al. 1975; Cassinelli 1979 and the summary in chap. 8.7.2 of Lamers & Cassinelli 1999). By contrast, the point-source assumption for the central source has a significant effect on the velocity structure and mass loss rates of the line-driven wind. Castor et al. (1975) formulated a correction factor for the line driving force that accounts for the effect of radiation streaming along non-radial rays. Including the finite extent of the star, the correction factor

$$D_{\mathrm{f}} = \frac{(1+\sigma)^{\alpha+1} - (1+\sigma\mu_\star^2)^{\alpha+1}}{(1-\mu_\star^2)(\alpha+1)\sigma(1+\sigma)^\alpha}, \tag{6.31}$$

with

$$\sigma = \frac{r}{u}\frac{\mathrm{d}u}{\mathrm{d}r} - 1, \tag{6.32}$$

has to be applied to the force multiplier

$$M_{\mathrm{f}}(t) = M(t)D_{\mathrm{f}}. \tag{6.33}$$

With this functional form of the line-driving force, the force balance equation is significantly complicated and an analytic solution challenging (see Pauldrach et al., 1986; Kudritzki et al., 1989, for laborious solution techniques). Thus, a number of investigations have instead solved the momentum balance numerically (see, for example, Friend & Abbott, 1986), or derived the wind structure analytically by adopting some approximations, as done, for example, by Kudritzki et al. (1989). All these studies concur that accounting for the finite extent of the star raises the terminal velocity by a factor of about ~ 2.25 and changes the velocity structure to follow roughly a β-type law with $\beta \approx 0.8$. Other physical mechanisms and effects, such as rotation, a non-uniform ionisation and deviations from LTE, have been shown to also affect the wind structure and have been partly included in increasingly sophisticated formulations of the CAK theory (see, for example, the review by Puls et al., 2008, and references therein).

However, some physical processes, relevant for line-driven winds, lie beyond the capabilities of the CAK approach (including its extensions), for example, multiple-scatterings or non-resonant interaction processes. The Monte Carlo approach, which, contrary to the CAK strategy, solves the line-driving force directly, has been successfully and extensively used in radiative transfer studies to investigate the effect of these physical mechanisms (for example, Lucy & Abbott 1993 and Vink et al. 2000 studied the influence of multiple scattering and Sim 2004 the relevance of line branching). In particular, multiple-scattering events have been demonstrated to have a significant effect on the wind structure, in particular in dense winds, since the radiation field may raise the bulk wind momentum, measured by the wind efficiency number (see Lamers & Cassinelli, 1999, chap. 8.2)

$$\eta = \frac{\dot{M} u_\infty c}{L_\star} \tag{6.34}$$

beyond the single-scattering limit[11]

$$\dot{M}_{\mathrm{max},1} = \frac{L_\star}{u_\infty c}. \tag{6.35}$$

6.2. MCRH Code Extensions for Stellar Wind Studies

Encouraged by the success of Monte Carlo techniques in treating complex interaction physics, we aim at taking one step beyond previous pure radiative transfer investigations and treat the wind structure fully self-consistently. Typically[12], Monte Carlo studies of hot-star winds assume a static wind structure and follow the propagation of the radiation field emitted by the central star. Relying on global energy conservation, the momentum of the wind is found by considering the emergent luminosity, $L(\infty)$, and comparing with the amount of radiation injected into the wind at the stellar photosphere, $L(R_\star)$. Any difference between these terms has been transferred onto the wind material and accelerated it according to (e.g. Abbott & Lucy, 1985)

$$\frac{1}{2}\dot{M}(u_\infty^2 - u_{\mathrm{esc}}^2) = L(R_\star) - L(\infty). \tag{6.36}$$

This approach does not enforce local consistency, i.e. strict force balance will not exist at each location in the wind. Moreover, a certain velocity and density stratification has to be assumed. By using an iterative approach, in which the wind structure adapts in each cycle to the mass-loss rate determined with Eq. (6.36), the radiative influence on the wind structure may be approximately taken into account. Recent Monte Carlo studies also take the influence on the thermal structure of the wind into account (e.g. Muijres et al., 2012b).

Compared to other radiation hydrodynamical approaches to stellar winds, using MCRH has the benefit of retaining all advantages of the Monte Carlo technique – the capability of treating complex interaction physics and to cope with multidimensional irregular flow patterns – while

---

[11] This may be illustrated by the concept of hemispheric scattering: photons are continuously backscattered, thus transferring twice their momentum, reversing their propagation path and interacting in the opposite region of the wind. The photons may repeat this process until the continuous redshift has decreased their energy to zero. In reality, however, such extreme cases are not occurring, since photons will escape through frequency gaps in the spectrum which are not populated with lines (e.g. Springmann, 1994).

[12] Recent Monte Carlo-based studies, however, follow a dynamically self-consistent treatment of the wind structure (e.g. Müller & Vink, 2008; Muijres et al., 2012b).

taking the full feedback cycle between the radiation field and the wind material into account. These properties make the MCRH approach very attractive for detailed studies of the multidimensional morphology of stellar winds. In the following we introduce the extensions implemented into MCRH to account for the physical conditions in stellar winds. Afterwards, we present in Section 6.3 the first one-dimensional calculations of hot-star winds with MCRH, which demonstrate the applicability and accuracy of our approach in this environment and constitute the first step towards multidimensional simulations of line-driven mass outflows.

Since the interactions of the radiation field with atomic line transitions constitute the dominant contribution to the acceleration of the wind material, the most significant wind-related extension of MCRH concerns the inclusion of these frequency-dependent interaction processes into the radiative transfer scheme. Additionally, the deceleration due to the gravitational pull from the central star is taken into account. We simplify the wind calculations by adopting an isothermal description of fluid dynamics.

6.2.1. External Gravity

The gravitational pull of an external source acts as a generic body force **f** in the fluid dynamical momentum and energy equations [see Eqs. (B.11) and (B.12)]. We follow Colella & Woodward (1984) and include this body force in a "quasi-implicit"[13] fashion when performing the flux balance in each grid cell. Additional contributions, Δp_g^n and ΔE_g^n are taken into account when updating the fluid momentum and energy from time step n to $n+1$. These terms are given by

$$\Delta p_g^n = \frac{1}{2}\Delta t(\rho^n g^n + \rho^{n+1} g^{n+1}), \tag{6.37}$$

$$\Delta E_g^n = \frac{1}{2}\Delta t(\rho^n u^n g^n + \rho^{n+1} u^{n+1} g^{n+1}), \tag{6.38}$$

with the external gravity field [c.f. Eq. (6.25)]

$$g = -\frac{GM_\star(1-\Gamma)}{r^2}. \tag{6.39}$$

6.2.2. Isothermal Hydrodynamics

Many studies of line-driven hot-star winds rely on an isothermal stratification of the wind material (e.g. Abbott, 1982; Abbott & Lucy, 1985; Owocki et al., 1988; Vink et al., 1999, 2000; Sim, 2004). Due to the constant irradiation from the central star and since the cooling time is much shorter than the flow time, the wind material should be approximately at the effective temperature of the star (Klein & Castor, 1978). We follow this reasoning and rely on an isothermal description of fluid dynamics in our calculations of hot-star winds. This reduces the complexity of the hydrodynamical step and removes some of the numerical complications in flows

---

[13] This construction is not implicit since "[...] the values of ρ^{n+1} do not depend upon u^{n+1}; nor do those of $\rho^{n+1}u^{n+1}$ depend upon E^{n+1}[...]" (from Colella & Woodward, 1984, page 192).

that are dominated by kinetic energy (see Section 5.2.4). For an isothermal flow with constant temperature T_0, the pressure is directly related to the density via the isothermal sound speed, a:

$$p = a^2 \rho = \frac{k_\mathrm{B} T_0}{\mu} \rho. \tag{6.40}$$

This involves the mean molecular weight μ of the flow. Due to this relation, the dynamics of the flow is already fully determined by the continuum equation and by momentum conservation. Solving the energy equation is no longer required. As a consequence, in the isothermal version of MCRH we only reconstruct the density and velocity, determine the gas pressure according to Eq. (6.40) and solve the Riemann problem at the cell interfaces with a specific version of the Riemann solver, which accounts for the form of the simple waves in isothermal flows. In particular, we adopt the isothermal implementation of HLLC from the ATHENA code (Stone et al., 2008). Alternate isothermal Riemann solvers are described, for example, by Balsara (1994), who presents a high-order Godunov-type scheme for isothermal hydrodynamics, or by Toro (2009, chap. 12.2.1), who outlines an isothermal Riemann solver of the Roe family.

Figure 6.2 shows the result of a test calculation based on a variant of the Sod-Shocktube (see Balsara, 1994, sec. 6.1). The same parameters as in Section 4.1.2 are used, together with an isothermal sound speed of unity, $a = 1\,\mathrm{cm\,s^{-1}}$. The results obtained with the isothermal version of MCRH are compared with the analytic solution[14], yielding excellent agreement. In a second test calculation, the inclusion of an external gravitational force is verified. For this purpose, we consider a spherical shell around a central mass[15] with $M_\star = 52.5\,M_\odot$ and $R_\star = 1.317 \times 10^{12}\,\mathrm{cm}$, extending from $r_\mathrm{min} = R_\star$ to $r_\mathrm{max} = 5\,R_\star$. Through the lower boundary, we assume an inflow of material into the computational domain at the rate $\dot{M} = 10^{-7}\,M_\odot\,\mathrm{yr}^{-1}$ and with the local escape speed. Neglecting the influence of the pressure gradient, which is warranted by our choice of an isothermal sound speed of $a = 10^4\,\mathrm{cm\,s^{-1}}$, the steady-state solution to this problem may be readily formulated based on simple energy conservation arguments. In the stationary solution, the flow should adopt at every point the local escape speed and a density corresponding to the constant mass-inflow rate:

$$\begin{aligned} u(r) &= \sqrt{\frac{2GM_\star}{r}}, \\ \rho(r) &= \frac{\dot{M}}{4\pi r^2 u(r)}. \end{aligned} \tag{6.41}$$

Figure 6.3 displays the steady-state density and velocity structure resulting from a MCRH calculation. The excellent agreement between the MCRH results and the analytic solution according to Eq. (6.41) confirms the correct implementation of the effect of an external gravity field.

---

[14] The exact solution for the isothermal shocktube problem may be obtained in the same way as in Section 4.1.2, following the methods outlined in Toro (2009) and using an adiabatic index very close to one. We use the routine `exact_riemann.f`, provided by Franck Timmes at `http://cococubed.asu.edu/code_pages/exact_riemann.shtml` for this purpose.

[15] The same stellar parameters as in the final stellar wind calculations are used (see Section 6.3).

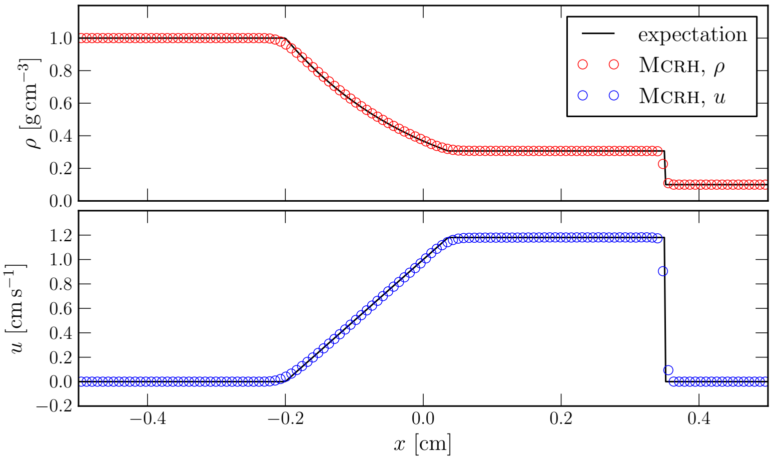

Figure 6.2.: Comparison between the analytic solution (solid black) and the MCRH results (coloured circles) at $t = 0.2\,\mathrm{s}$ for the isothermal version of the Sod-Shocktube (following Balsara, 1994). In the upper panel, the density is displayed and in the lower one the velocity. Notice the absence of a density jump in the contact discontinuity, a characteristic feature of isothermal flows (see, for example, Balsara, 1994).

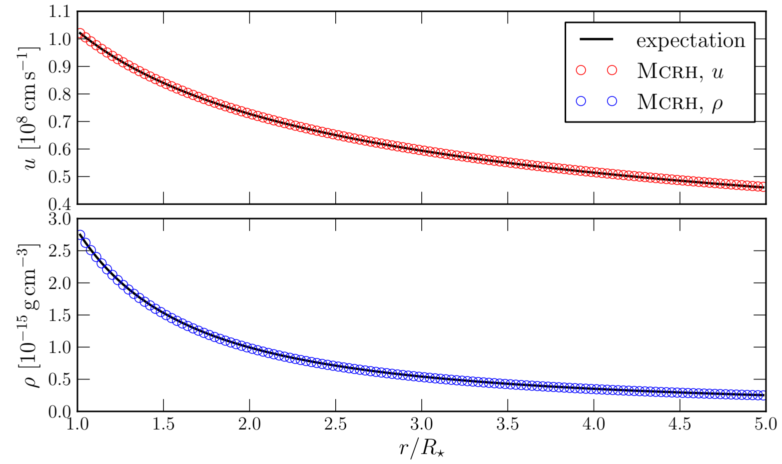

Figure 6.3.: Comparison between the velocity (upper panel) and density (lower panel) determined with MCRH (coloured circles) and the analytic solution (solid black) according to Eq. (6.41) for the test calculation of a spherical flow in the presence of an external point-source gravity field.

6.2.3. Resonant Line Interactions

Substantial changes are made to the radiative transfer scheme to include interactions with atomic line transitions. In addition to a fraction of the radiation field energy, all Monte Carlo packets are now identified with a frequency, which is assigned in the initialisation process by sampling the spectral energy distribution of the radiation field emitted by the star. Realistic atmosphere models may be used for this procedure (for example Kurucz, 1979). However, for simplicity we adopt a LTE initialisation scheme for this work. Under these conditions, the initial packet frequencies have to be drawn from the Planck function, Eq. (2.39). Due to the complex dependence of this expression on the frequency, we avoid the laborious task of inverting the probability distribution or the computationally expensive van-Neumann rejection sampling process and rely instead on an approximate method. The frequency interval of interest is subdivided into a number of bins. In each of those, the radiative flux is estimated by integrating Eq. (2.39) with the trapezoidal rule. The flux content in the bin with respect to the total radiative flux sets the number of packets whose frequencies have to lie within this bin. The individual frequencies of this packet subsample are finally assigned uniformly between the bin boundaries. Naturally, the fidelity of this approach in reproducing the physical spectral distribution increases with a finer binning of the overall frequency interval. After the initialisation process, the packet propagation proceeds according to the basic principles outlined in Section 3.4.4.

In addition to grey interactions of the continuum radiation field, the possibility of performing atomic line interactions is included. Here, the ability to use the Sobolev approximation is instrumental, since it reduces the computational complexity of the line-interaction problem dramatically. However, we emphasise that, with the reliance on this approximation, our scheme is unsuited for the investigation of the line-driving instability. Since line overlaps are not permitted within the Sobolev approximation, the next atomic line transition a packet comes into resonance with and may interact with may be immediately and unambiguously predicted based on the current CMF frequency and the local fluid velocity gradient. Whether a packet performs the line-interaction once it reaches the Sobolev point is decided according to the Sobolev optical depth of the line transition, which is a pure local quantity. In particular, at the onset of each packet trajectory element the optical depth to the next interaction event is determined in analogy to Eq. (3.69),

$$\tau = -\log z. \tag{6.42}$$

The nature of this interaction event is established with the help of a summation routine, adopted from Mazzali & Lucy (1993). As the packet propagates over a distance l, it steadily accumulates optical depth due to frequency-independent continuum processes,

$$\tau_{\mathrm{cont}} = l\chi_{\mathrm{cont}}. \tag{6.43}$$

Once the packet reaches the Sobolev point corresponding to the next line interaction, the accumulated optical depth is instantaneously raised by the full Sobolev optical depth associated with the line transition. This summation process is repeated to the next Sobolev point and beyond until the aggregate optical depth equals the one initially determined by Eq. (6.42). If this occurs during the instantaneous increment at one of the Sobolev points, the packet performs the associated line interaction. Throughout this work, we follow Abbott & Lucy (1985) and assume that all line interactions occur as resonant scatterings. In case the accumulated optical depth surpasses the limit of Eq. (6.42) between two Sobolev points, the packet experiences a continuum process at the location determined from Eq. (6.43). The exact nature of the continuum interaction event may be determined in analogy to Eq. (3.71) by comparing the opacities of all constituting processes. Figure 6.4 graphically illustrates the summation process and the identification of the interaction location and nature.

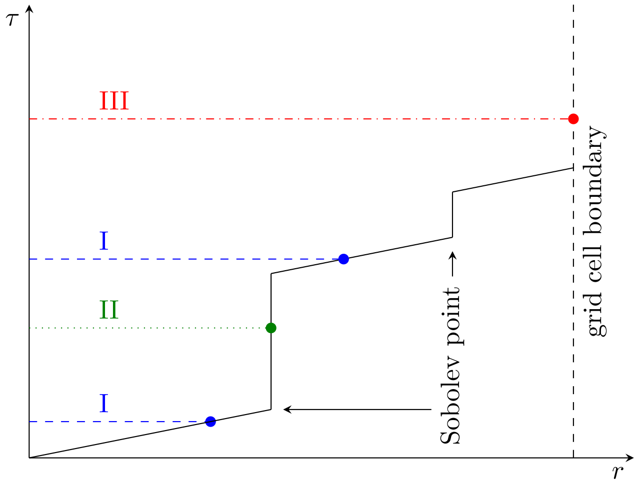

Figure 6.4.: Illustration of the optical depth summation process to determine the details of the physical interaction processes Monte Carlo packets experience (adapted from Mazzali & Lucy 1993). The x-axis traces the distance a packet covers during the propagation and the y-axis shows the accumulated optical depth. Until reaching the next Sobolev point, continuum opacity steadily increases the accumulated optical depth of the packet path. At the resonance points, the full Sobolev optical depth is instantaneously added. Depending on when the aggregate optical depth reaches the value determined by Eq. (6.42), different events occur. Three representative possibilities are highlighted in this illustration: in the first case (I, dashed blue), the optical depth value is reached in one of the continuum segments and the packet performs the corresponding continuum process. If the increment at one of the Sobolev points surpasses the critical value, as in the second case (II, dotted green), the packet experiences a line interaction. Finally, the third case (III, dashed dotted red) illustrates the situation in which the packet reaches the cell boundary before the optical depth value of the next interaction is accumulated.

6.2.4. Excitation and Ionisation

The probability of a photon to excite a certain atomic line transition depends on the number of ions with the lower energy level of the transition being populated. Thus, to calculate the Sobolev optical depths for the summation process outlined above, the ionisation and excitation balance has to be determined. Consequently, at the onset of each radiative transfer step, we perform an ionisation and excitation calculation, following the approach of Vink et al. (1999).

In LTE, the ionisation balance is governed by the Saha equation (see Mihalas, 1978, chap. 5.1), which connects the number densities of two successive ionisation stages, $j+1$, and j, of a certain elemental species l with the overall electron number density n_e

$$\frac{N_{l,j+1} n_e}{N_{l,j}} = C \frac{Z_{l,j+1}(T)}{Z_{l,j}(T)} T^{\frac{3}{2}} \exp\left(-\frac{\chi_{l,j}}{k_{\mathrm{B}} T}\right) . \tag{6.44}$$

Here, the ionisation potential $\chi_{l,j}$, the numeric constant $C = 4.83 \times 10^{15}\,\mathrm{cm}^{-3}\,\mathrm{K}^{-3/2}$ and the partition function $Z_{l,j}$ are used. This involves a summation over all energy levels i of the ion j, with the excitation potentials $\varepsilon_{l,j,i}$ and the statistical weights $g_{l,j,i}$:

$$Z_{l,j}(T) = \sum_i g_{l,j,i} \exp\left(-\frac{\varepsilon_{l,j,i}}{k_{\mathrm{B}} T}\right) . \tag{6.45}$$

The Saha equation may be solved by successive insertion of Eq. (6.44), finally linking the ground state with the highest possible ionisation state. By iteratively solving for the electron density the LTE ionisation balance may be solved (see, for example, Mihalas, 1978, chap. 5.1 and 5.2, for a detailed presentation of a solution strategy).

However, in stellar winds, the radiation field exhibits departures from LTE, for example due to its non-isotropy. Since radiation predominantly streams radially outwards once emitted by the stellar photosphere, an effective dilution of radiation energy occurs. This effect is captured by the geometric dilution factor $W(r)$ (Mihalas, 1978, chap. 5.3), which describes the solid angle subtended by the stellar disc at distance r

$$W(r) = \frac{1}{2}\left(1 - \sqrt{1 - \left(\frac{R_\star}{r}\right)^2}\right) . \tag{6.46}$$

At the stellar surface, the dilution factor is exactly $1/2$, which reflects the absence of any radiative source just above the photosphere. With the dilution factor, a so-called modified nebular approximation of the ionisation balance may be formulated (see, for example, Vink et al., 1999)

$$\frac{N_{l,j+1} n_e}{N_{l,j}} = [\zeta_j W + (1-\zeta_j) W^2] \sqrt{\frac{T_e}{T_r}} \left(\frac{N_{l,j+1} n_e}{N_{l,j}}\right)^*_{T_r} . \tag{6.47}$$

Here, the expression in round brackets represents the LTE ion fractions following from Eq. (6.44), however, now relying on non-LTE partition functions (see our treatment of these below). In addition to the dilution of the radiation field other non-LTE effects are also approximately captured. For example deviations between the electron and the radiation temperatures, T_e and T_r, and the possibility of recombinations not to proceed directly into the ground state (captured by the fraction of ground state recombinations ζ_j). This implies that some of the ionisation processes require two or more interactions with the (diluted) radiation field, which is approximately captured by the term $(1-\zeta_j)W^2$.

For the calculation of line interaction probabilities, also the excitation balance has to be known. Here, we again follow Vink et al. (1999) and distinguish so-called *meta-stable* levels, which are not connected to the ground state by any electric dipole transitions. The population of these levels is then assumed to be collisionally dominated and consequently follows from LTE Boltzmann statistics (Mihalas, 1978, chap. 5.1)

$$\frac{n_{l,j,i}}{n_{l,j,1}} = \frac{g_{l,j,i}}{g_{l,j,1}} \exp\left(-\frac{\varepsilon_{l,j,i}}{k_{\mathrm{B}T}}\right). \tag{6.48}$$

For all remaining levels, the excitation balance also involves the influence of the radiation field in an approximate fashion, entering in terms of the dilution factor (Vink et al., 1999):

$$\frac{n_{l,j,i}}{n_{l,j,1}} = W \left(\frac{n_{l,j,i}}{n_{l,j,1}}\right)^{*}_{T_r}. \tag{6.49}$$

This excitation treatment of meta-stable levels is less sophisticated and realistic than the scheme employed by Abbott & Lucy (1985). Nevertheless, Springmann & Puls (1998) showed that the excitation and ionisation description according to Eqs. (6.47) to (6.49) provides an adequate approximation of the physical conditions in hot O and B stars.

6.2.5. Velocity Interpolation

To determine the Sobolev points and the Sobolev optical depths in the Monte Carlo scheme, the local CMF frequencies of the Monte Carlo packets and the fluid velocity gradient have to be accessible. This requires an interpolation between the cell-averaged mean velocity values to approximate the velocity structure within the grid cells. Here, it is essential to construct a velocity interpolation scheme that retains the full line-driving force. Due to the Doppler shift, packets may scan over an extended region of the CMF frequency space as they propagate through the wind. Any discontinuity in the interpolated velocity would introduce an abrupt change in the CMF frequency causing packets to skip a region of the spectrum, which is potentially populated by many lines. Their contribution to the line-driving force would be lost and the total radiative acceleration would be erroneously determined[16]. To avoid this, our velocity interpolation scheme for the radiative transfer step insists on continuity at the grid cell boundaries. In particular, we determine the fluid velocity at the interfaces by linearly interpolating between the finite-volume values in the adjacent cells. The velocity structure within the grid cell is then in turn set by linear interpolation between the left and right interface values. This process is illustrated in Fig. 6.5.

---

[16] For this work, we are not considering any stellar wind problems in which shocks and thus abrupt velocity changes are expected.

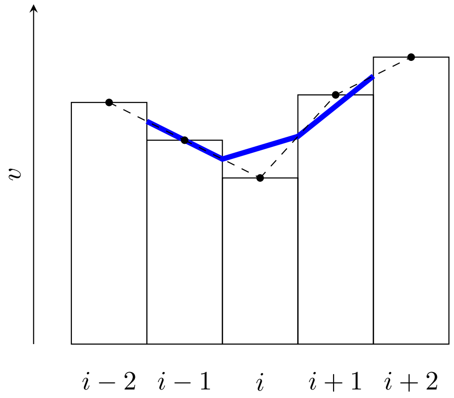

Figure 6.5.: Illustration of the velocity interpolation scheme used in the Monte Carlo radiative transfer scheme to track the CMF frequency shift and to determine the local velocity gradient entering the determination of the Sobolev point and of the Sobolev optical depth. The cell-averaged velocity values are shown by black dots. The linear interpolation segments to determine the interface values are depicted as dashed black lines and the resulting linear velocity structure within the cells as solid blue ones.

Equally important to the spatial continuity is a smooth transition of packet CMF frequencies between successive time steps. The changes induced by the hydrodynamical calculation would again induce discontinuous jumps for packets that have survived the last radiative transfer step and now resume their propagation at a different fluid velocity. To avoid this, we assume that during the radiative transfer step from n to $n+1$, the cell-averaged fluid velocities linearly change from $\tilde{u}_i^{n-1}$ to $\tilde{u}_i^n$. Here, the tilde highlights that the flow speeds right after the hydrodynamical calculation are used:

$$u_i^n \xrightarrow{\text{Fluid Dynamics}} \tilde{u}_i^n \xrightarrow{\text{Momentum Transfer}} u_i^{n+1} \tag{6.50}$$

Relying on these intermediate values ensures that the CMF frequencies remain continuous for packets that are stored and revisited in the next time step. In summary, the velocity interpolation scheme is based on the method outlined in Fig. 6.5, but with temporally varying values of the cell averages (again linearly interpolated between $\tilde{u}_i^{n-1}$ and $\tilde{u}^n$).

6.2.6. Instantaneous Packet Propagation

Since we are primarily interested in the properties of the steady-state solution of the wind outflow, we simplify the radiative transfer scheme and assume an instantaneous propagation of Monte Carlo packets. This strategy is commonly encountered in Monte Carlo calculations of pure radiative transfer problems, for example in the Python code (Long & Knigge, 2002) or in Tardis (Kerzendorf & Sim, 2014). Adopting this approach, we circumvent the need to follow the initial build-up of the radiation field in the wind via the continuous feeding by the emission from the star through the lower boundary. Numerically we realise the instantaneous packet transport by using a propagation speed which greatly exceeds the speed of light

$$c_{\text{prop}} \gg c. \tag{6.51}$$

However, for all occurrences of the speed of light unrelated to the packet propagation process, for instance the calculation of Doppler factors or the translation from J to E, the physical value of c is used. We emphasise that, as long as we are interested only in the final stationary state of the problem, the reliance on a faster-than-light propagation of packets merely reduces the computational costs of the calculations but not the physical accuracy. As long as we rely on the instantaneous packet propagation, the time-dependent aspect of the velocity interpolation scheme may be omitted, since no packet will be present in the wind at the end of the time step.

6.2.7. Monte Carlo Estimators

Determining the line-driving force exerted by the radiation field on the wind material constitutes an integral part of the radiation hydrodynamical calculations of the structure of stellar winds. However, the energy and momentum transfer associated with line interactions cannot be reconstructed in the same fashion as in the case of continuum processes. Since the opacity associated with a line transition is not easily formulated, the estimators presented in Section 3.4.5 are not directly applicable to the reconstruction of the line-driving force. In contrast, we adapt the direct counting approach and, following Lucy (1999b), combine it with the fundamental principle of the volume-based estimator technique: all packets that may interact contribute according to their interaction probability. For the matter at hand, this implies that all packets that come into resonance with a line transition, i.e. that reach the associated Sobolev point, are taken into account. In a line interaction occurring as a resonant scattering, energy and momentum amounting to

$$\Delta E = \varepsilon^i \left[1 - \gamma^2(1 + \beta\mu_0^f)(1 - \beta\mu^i)\right], \tag{6.52}$$

$$\Delta p = \frac{\varepsilon^i}{c} \left[\mu^i - \gamma^2(\mu_0^f + \beta)(1 - \beta\mu^i)\right], \tag{6.53}$$

are transferred in the LF onto the ambient wind material[17]. These transfer terms are weighted by the interaction probability, which depends on the Sobolev optical depth of the line transition, $1 - \exp(-\tau_s)$, and summed up to form the estimators for the radiation force exerted by line interactions in the LF:

$$G^0_{\text{line}} = \frac{1}{\Delta V c \Delta t} \sum (1 - e^{-\tau_s})\varepsilon[1 - \gamma^2(1 - \beta\mu)], \tag{6.54}$$

$$G^1_{\text{line}} = \frac{1}{\Delta V c \Delta t} \sum (1 - e^{-\tau_s})\varepsilon[\mu - \gamma^2\beta(1 - \beta\mu)]. \tag{6.55}$$

---

[17] The same notation as in Section 3.4.5 is used.

Here, we have already summed over all CMF directions emergent from the resonant scatterings, exploiting the isotropy of the scattering events[18] and thus cancelled all appearances of the re-emission direction.

6.2.8. CAK Radiation Force

We aim at establishing the accuracy and utility of our MCRH approach in solving the structure of hot-star winds by comparing with the predictions of the CAK theory. For this purpose, we also implement an alternative calculation mode into MCRH, in which the Monte Carlo radiative transfer scheme is replaced by a CAK module. Relying on the CAK parameters k and α, which are externally provided and remain constant throughout the simulation, the line-driving force is determined in each cell according to the power-law

$$\frac{G^1}{\rho} = kt^{-\alpha}\frac{\sigma_e^{\mathrm{ref}} L_\star}{4\pi c r^2} \tag{6.56}$$

and the local value of the dimensionless optical depth t [see Eq. (6.18)]. The velocity gradient needed to reconstruct t from the instantaneous velocity profile is determined by means of finite differences, using a symmetric five-point stencil assuming an uniform grid (see Fornberg, 1988, for an algorithm to compute finite differences for arbitrarily spaced grids)

$$\frac{\mathrm{d}u_i}{\mathrm{d}r} = \frac{u_{i-2} - 8u_{i-1} + 8u_{i+1} - u_{i+2}}{12\Delta r_i}. \tag{6.57}$$

The above formulation of the line-driving force holds in the point-source limit. For more sophisticated simulations and comparison calculations, the finite extent of the star is taken into account and the formulation Eq. (6.33) is used instead.

6.2.9. Comparison with Syn++

As a test of the code extension associated with the frequency-dependent line interactions, we consider a sphere in homologous expansion which is illuminated by a central source emitting a perfect black-body spectrum. Within the expanding material, the radiation is able to perform resonance interactions with the line transitions of a pre-defined ion. We record the emergent spectrum, which is expected to exhibit strong P-Cygni features around the rest-frame frequencies of the line-transitions. This line profile is a characteristic feature of the interaction with an outflowing material. It results from the superposition of a blue-shifted absorption trough due to the material along the line of sight and of an emission contribution, which originates from the complete wind region and which is symmetrically Doppler-shifted around the rest-frame frequency of the line transition (see, for example, Lamers & Cassinelli, 1999, chap. 2.2). The calculated spectrum is compared with the result of a corresponding SYN++ (Thomas et al.,

---

[18] Strictly speaking, re-emission within the Sobolev theory is not isotropic. Due to its fore-aft symmetry, however, a summation over all possible directions also cancels exactly.

2011) simulation[19]. This spectral synthesis code, which has been developed for the analysis of supernova observables, is ideally suited for this task. The code also relies on the Sobolev approximation and grants the user great flexibility in choosing the composition, the ionisation and excitation balance in the ambient material[20].

We perform the test calculation by comparing the Lyman-α ($\lambda = 1215.7\,\text{Å}$[21]) and Lyman-$\beta$ ($\lambda = 1025.7\,\text{Å}$) line profiles emerging from a homologously expanding shell, extending from $r_{\mathrm{min}} = 6.96 \times 10^{10}\,\mathrm{cm}$ to $r_{\mathrm{max}} = 6.96 \times 10^{11}\,\mathrm{cm}$ and in velocity space from $u_{\mathrm{min}} = 0.001\,c$ to $u_{\mathrm{max}} = 0.01\,c$. The density stratification is chosen to be compatible with the standard input profile for SYN++:

$$\rho(r) = \rho_{\mathrm{ref}} \exp\left(\frac{u_{\mathrm{ref}} - u(r)}{u_{\mathrm{e}}}\right). \tag{6.58}$$

For the reference density, ρ_{ref}, we use a value that yields a mass loss rate of $\dot{M} = 10^{-13}\,M_{\odot}\,\mathrm{yr}^{-1}$ at the reference velocity $u_{\mathrm{ref}} = 10^{8}\,\mathrm{cm\,s}^{-1}$. For simplicity, we set the second velocity parameter to the same value, i.e. $u_{\mathrm{e}} = u_{\mathrm{ref}}$. Furthermore, we assume that the material is entirely composed of neutral hydrogen, H I, and that the excitation balance is set by the gas temperature $T = 10^{4}\,\mathrm{K}$. For this purpose, we define the Sobolev optical depth of the Lyman-α line, which acts as the reference line in the SYN++ calculation, at u_{ref} to $\tau_{\mathrm{ref}} = 1.2428$. This value follows from Eq. (6.11), when solved for the chosen conditions at the reference location. At the lower boundary, a photosphere, emitting a black-body spectrum at the effective temperature $T_{\mathrm{eff}} = 4 \times 10^{4}\,\mathrm{K}$ is adopted. The inflow flux is discretised by 10^{6} Monte Carlo packets, which sample the frequency distribution according to the technique outlined at the beginning of Section 6.2.3. The line profiles, determined with MCRH are shown in Fig. 6.6 and compared with the SYN++ results. Both spectra have been normalised to the incident black-body flux. The agreement between the two calculations is excellent, confirming the correct implementation of the frequency-dependent transfer processes.

6.3. Hot-Star Wind Calculations with MCRH

With the inclusion of the additional physical effects as outlined in the previous section, the first radiation hydrodynamical calculations of the structure of hot-star winds with MCRH are performed. As stated previously, the prime purpose of these calculations is to establish the accuracy and utility of our approach in the line-driven mass-outflow environment. To this end, we carry out a series of MCRH simulations with increasing level of sophistication and compare the obtained wind structure with the predictions of the CAK theory. As an additional verification process, we confront the MCRH results with calculations in which we rely on the CAK power-law fits to determine the line-driving force (see Section 6.2.8).

---

[19] The source code is freely available and may be obtained at `https://c3.lbl.gov/es/`.

[20] In fact, the ion fractions may be pre-defined individually and without maintaining physical consistency. The excitation balance is also set externally by choosing the strength of a reference line.

[21] Throughout this work, information about rest-frame wavelengths of atomic line transitions is taken from Kurucz & Bell (1995).

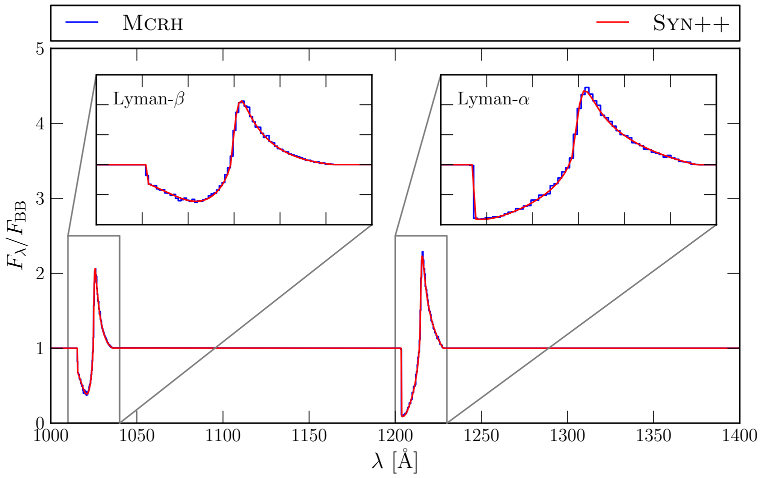

Figure 6.6.: Comparison between the Lyman-α and Lyman-β line profiles emerging from the homologous shell determined with SYN++ (solid red) and with MCRH (solid blue). The fluxes are normalised to the incident black-body flux, F_{BB}.

6.3.1. General Parameters

In all our calculations, we consider the mass outflow from a well-studied O-star, ζ-Puppis, and adopt its parameters from Puls et al. (1996). The star has a mass of $M_\star = 52.5\,M_\odot$ and sends out radiation at luminosity $L_\star = 10^6 L_\odot$ with effective temperature $T_{\rm eff} = 4.2 \times 10^4$ K. For simplicity, we assume that the star emits a perfect black-body spectrum. We emphasise, however, that the incorporation of a realistic stellar spectrum, from which the frequency of the incident Monte packets are sampled, would not present any significant challenges (conceptually or in terms of implementation).

In all calculations, we follow the evolution of the wind material in the region from $r_{\rm min} = R_\star$ to $r_{\rm max} = 5\,R_\star$ until a stationary state has established. The wind is assumed to be composed of material with a solar-like abundance pattern. For this, we adopt the values derived by Asplund et al. (2009) and take all elements up to nickel with solar abundances $X_i/X_{\rm H} > 3 \times 10^{-8}$ into account (similar to Sim, 2004). These elements, together with their associated ionisation stages, which are considered in our studies, are listed in Table 6.1. The details of the atomic structure and the line transitions present in these ions are extracted from an atomic database which has been compiled by Stuart Sim for a study of colliding winds, Parkin & Sim (2013), and which is based on the Kurucz & Bell (1995) atomic data set[22].

During the stellar wind calculations, the ionisation and excitation balance is not determined on a first principle basis by iteratively solving the Saha-Boltzmann equation, since this approach typically yields an ionisation balance inconsistent with observations of hot-star winds. This dis-

---

[22] The Kurucz & Bell (1995) atomic data may be obtained at `http://www.cfa.harvard.edu/amp/ampdata/kurucz23/sekur.html`.

Element	Ions	Element	Ions
H	I,II	He	I-III
C	I-IV	N	I-VI
O	I-VI	F	I-VI
Ne	I-VI	Na	I-VI
Mg	I-VI	Al	I-VI
Si	I-VI	P	I-VI
S	I-VI	Cl	I-V
Ar	I-V	K	I-V
Ca	I-VI	Ti	I-VI
Cr	I-VI	Mn	I-VI
Fe	I-VI	Co	I-VI
Ni	I-VI		

Table 6.1.: Summary of the elements and their ionisation stages incorporated in our stellar wind calculations.

crepancy has been noted, for example, by Olson & Castor (1981) and Abbott (1982), and may be attributed to the presence of a clumpy wind structure. Regions with over-dense mass concentrations may reduce the overall ionisation state to be in accordance with observational findings. Instead of the first-principle approach, we follow the common strategy of one-dimensional wind studies and adopt a characteristic electron density, and a radiation and a gas temperature for the wind. Since our primary interest lies in establishing the applicability of Mcrh for line-driving problems and in comparing with predictions from the CAK theory, we adopt rather simplified choices for these parameters. In particular, we set the ratio n_e/W to the constant value $10^{-15}\,\mathrm{cm}^{-3}$ throughout the wind and adopt the temperature stratification

$$T_{\mathrm{R}} = T_{\mathrm{e}} = T_{\mathrm{eff}}. \tag{6.59}$$

For simplicity, we also set the recombination fraction ζ_i to unity for all ions and assume that all level populations used in the ionisation calculations follow Boltzmann statistics (i.e. assume LTE excitation). Since these choices induce a constant ionisation and excitation state throughout the wind, we may approximately account for the effect of electron scattering by adjusting the mass of the central star as outlined in Section 6.1.3. Relying on Eq. (6.24), the specific electron scattering cross section in our calculations amounts to $\sigma_{\mathrm{e}} = 0.343\,\mathrm{cm}^2\,\mathrm{g}^{-1}$, which lies within the typical range of 0.28 to $0.35\,\mathrm{cm}^2\,\mathrm{g}^{-1}$ for hot stars (see Lamers & Cassinelli, 1999, chap. 8.7) and which implies an Eddington factor of $\Gamma = 0.502$.

All the assumptions listed above oversimplify the physical processes dramatically but yield roughly the characteristic ionisation balance of hot-star winds. We emphasise again that our main motivation for adopting this simplified description is computational convenience and the facilitation of a direct comparison between Mcrh and CAK line-driving results. As outlined in Section 6.2.4, all necessary prescriptions and techniques are already implemented into Mcrh to readily adopt a more realistic ionisation and excitation treatment, analogous to, for example

Vink et al. (1999). The Monte Carlo scheme would also allows us, in principle, to determine the dilution factor W directly from the properties of the radiation field and not rely on the geometric approximation Eq. (6.46) (see, for example, Sim, 2004). Moreover, electron scattering processes may be followed explicitly, without the need of approximating their effect by reducing the stellar gravity. All these improvements, however, are deferred to future calculations, once the utility and accuracy of MCRH has been fully established.

6.3.2. CAK Fitting

For a confrontation of the MCRH results with the CAK predictions, values for the power-law fit parameters k and α are required. Since the mass-loss rate and the terminal wind speed are very sensitive to the values of these parameters [see Eqs. (6.27) and (6.30)], we perform the fitting process ourselves instead of relying on literature values. This way, we avoid obscuring any fundamental deviations between the MCRH and CAK line-driving force, which may exist, by differences in the ionisation prescription and in the underlying stellar parameters. For the fitting procedure, we evaluate the force-multiplier sum for a number of different values of the optical depth parameter with the line-interaction module of MCRH. Thus, we ensure that the CAK line-driving force corresponds to the same microphysics conditions prevalent in the MCRH simulations. Following Sim (2004), we reduce the list of possible line transitions, by only including those whose strength exceeds the threshold $\log(g_l f) > -6$. This step, which is again owed to computational convenience, results in an effective line list containing roughly 1.6×10^5 transitions. We have ensured that a reduction of the threshold, thus including more weak transitions, does not influence the outcome of the radiation hydrodynamical simulations. In Fig. 6.7, the force multiplier explicitly calculated with MCRH is shown, together with the resulting power-law fit. As a reference, the results of the study by Abbott (1982) for comparable physical conditions are included. Deviations between our findings and the Abbott (1982) results are most likely a result of the combined effect of differences in the ionisation treatment, the atomic data set and Abbott's use of realistic stellar spectra instead of a black body. The CAK fit parameters determined in our power-law fit are listed in Table 6.2, together with the resulting properties of the wind according to the CAK theory[23]. Note that the Eddington factor and the implied mass-loss rate are higher than what is usually derived (however, Abbott 1982 also derived rather high mass-loss rates) and observed for ζ-Puppis (see, for example Lamers & Cassinelli, 1999, tab. 8.1). This is most likely a consequence of our crude ionisation and excitation treatment.

6.3.3. Boundary Conditions

For the radiation hydrodynamical calculations, we construct particular boundary conditions, which extrapolate the wind flow into the inner ghost cells. In particular, we use the velocity in the innermost cells of the computational domain to fit a β-type law (with $\beta = 0.5$ for the

---

[23] If not specifically stated otherwise, CAK theory always refers to the most basic formulation in the point-source limit, neglecting the pressure gradient and assuming an unattenuated radiation field.

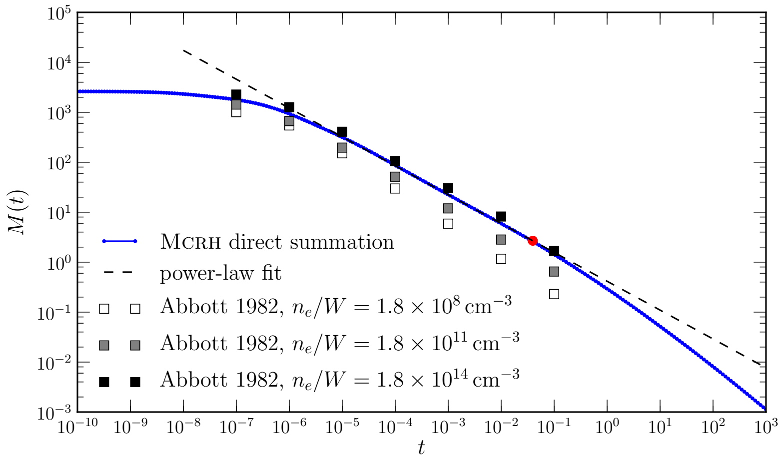

Figure 6.7.: The force multiplier as a function of the dimensionless optical depth, determined by direct evaluation of Eq. (6.21) with MCRH (blue circles). The result of the power-law fit, summarised in Table 6.2, is shown as the dashed black line. The red circle highlights the value of the force multiplier, which is predicted by the CAK theory to prevail in the wind with the determined fit parameters. In addition to our results, the findings of Abbott (1982) for a star with $T_{\mathrm{eff}} = 4 \times 10^{4}\,\mathrm{K}$ and $n_e/W = 1.8 \times 10^{8}$, 1.8×10^{11}, $1.8 \times 10^{14}\,\mathrm{cm}^{-3}$ are shown (white, grey and black squares).

Parameter	Value
k	0.4152
α	0.5776
Γ	0.5022
Quantity	**Value**
t	0.0396
$M(t)$	2.6815
$\dot{M}$	$4.717 \times 10^{-5}\, M_{\odot}\, yr^{-1}$
v_{∞}	$8.488 \times 10^{7}\,\mathrm{cm\,s^{-1}}$

Table 6.2.: Summary of the CAK power-law fit parameters and the resulting characteristics of the wind according to the CAK theory. Note that Γ is repeated here for completeness, but is unrelated to the power-law fit.

calculations in the point-source limit and $\beta = 0.8$ for simulations which account for the extent of the stellar disc), according to which the flow speed is set in the ghost cells. During the entire simulation, the density in the ghost cells is held at the values dictated by the CAK theory. We found it necessary to anchor the wind this way to avoid the outflow material completely detaching from the star. However, due to the possibility of the velocity at the inner boundary to float, the mass-loss rate may adjust itself, despite the constant density at this location. With this general design of fixing the density and letting the velocity vary, our boundary conditions are similar to those used by Owocki et al. (1988). Concerning the radiation field, the inner edge of the computational domain constitutes an inflow boundary. During each time step, packets are created at this location in accordance with the luminosity of the star. Their frequencies are assigned from a black-body spectrum corresponding to the effective temperature of the star. Any packet which is back-scattered inwards and intersects the boundary sphere automatically is absorbed by the photosphere and is no longer considered. The outer boundary of the wind material is also transparent for the Monte Carlo packets. All packets escaping through this boundary surface, however, are recorded in order to construct the emergent spectrum. We mimic the outflow of wind material at this location by linearly extrapolating the fluid flow into the ghost cells beyond the outer boundary[24].

6.3.4. MCRH Simulation Series

With the general parameters listed in Section 6.3.1, the boundary conditions described in Section 6.3.3 and the CAK parameters determined in Section 6.3.2, we perform a series of stellar wind simulations with MCRH[25]. With each step of this series we increase the complexity level, beginning with a reproduction of the original CAK conditions, later including the finite extent of the stellar disc and finally also accounting for the attenuation of the radiation field. In this last stage of the series we go beyond the capabilities of the CAK theory. Where possible, we compare our results with the analytic or approximate predictions of the CAK theory. Moreover, we also confront the MCRH calculations during the first two stages of the series with corresponding simulations in which the Monte Carlo scheme is replaced by a CAK-like determination of the line-driving force (see Section 6.2.8). From the differences of this confrontation, we assess the utility and accuracy of our approach for line-driven outflow problems in general and the stellar wind problems in particular.

To realise the point-source approximation of the central star in the MCRH calculations during the first stage of the series, all Monte Carlo packets injected through the inner boundary are assigned a propagation direction parallel to the radial direction. Once the finite extent of the star is taken into account, packets are injected without any limb darkening along the directions

---

[24] Due to the Monte Carlo noise we determine the parameters of the extrapolation function by linear regression of the fluid state in a number of cells at the outer edge of the domain.

[25] In contrast to previous uses of MCRH, we found it necessary to slightly deviate from our default implementation of the splitting scheme. We use the same values of the fluid state for the fluid dynamics and the radiative transfer step. Otherwise, we obtain unstable results.

sampled from Eq. (4.17). The unattenuation of the radiation field, used in the first and second stage of the simulation series, is achieved in the Monte Carlo scheme by insisting that the packet properties, in particular the propagation direction, do not change during any physical interaction event. At this point, a clarification of terminology is advisable. Unattenuation of the radiation field merely implies that all portions of the wind may interact with the unaltered stellar spectrum. Nevertheless, the same photon may contribute to the line-driving force in different parts of the wind, since it may scan over a number of lines as its CMF frequency is redshifted by the increasing wind velocity. This effect, however, is not commonly referred to as “multiple scattering”. The term describes the effect resulting from the lengthening of the photon propagation path once the directional change during interaction events is taken into account. As a consequence to the longer propagation path, photons may scan over a broader CMF frequency interval, come into resonance with a larger number of lines and effectively exert a stronger accelerating force onto the wind material. This effect is only accounted for in the last stage of the simulation series. Here, the full Monte Carlo propagation scheme, as detailed in Sections 3.4.4 and 6.2.3 is used, which implies that Monte Carlo packets change their properties during interactions according to Eqs. (3.51) and (3.73). Since a fraction of the packets will be back-scattered into the photosphere, the luminosity in the wind material would significantly drop. We counter this effect by rescaling the packet energies proportionally to this energy loss. Doing so, we ultimately change the effective temperature of the photosphere[26] and perform a colour correction of the incident stellar spectrum. Naturally, this is an approximate treatment of the reaction of the stellar atmosphere to the backscattered radiation. Ideally, the stellar wind simulation should be coupled to a detailed atmosphere calculation, which determines the stellar spectrum by taking the illumination from the diffuse radiation field into account. In the future, we may attempt such coupled calculations.

The MCRH simulations are performed on a computational grid with 256 equidistant cells and with 5×10^4 packets representing the incident radiation field between $\lambda_{\min} = 228\,\text{Å}$ and $\lambda_{\max} = 22\,800\,\text{Å}$. The lower wavelength limit corresponds to the ionisation edge of He II. Following Sim (2004), we do not consider radiation which is more energetic than that, since such photons are assumed to be immediately absorbed by helium in bound-free processes. Due to our choice of the number of injected Monte Carlo packets, the computational effort is kept manageable and the statistical fluctuations in the line-driving force within reasonable limits. We have explicitly checked that increasing the number of Monte Carlo packets yields the same radiative acceleration just with a reduced noise level. All simulations are initialised with the CAK density and a wind velocity that is twice as high as predicted by CAK. These choices are somewhat arbitrary, but lead to a relatively fast settling towards the final stationary solution. The results of our calculations seem to be invariant with respect to the particular choice of the initial state. For example, starting from the CAK velocity, half their values or even using a

---

[26] The effective temperature of a star follows from comparing its surface flux with the Stefan-Boltzmann law, Eq. (2.40). Since the radius of the photosphere is unaffected, an increase in luminosity results in a higher effective temperature.

homologous velocity profile eventually leads to the same steady wind state. Since determining the wind structure analytically within CAK is not straightforward anymore once the finite extent of the star is included, we rely on the solution procedure proposed by Kudritzki et al. (1989) to predict the wind stratification and initialise the simulations. The resulting density profile is also used to fill the ghost cells at the lower boundaries during the second and third stage of the simulation series.

The results of the simulation series are summarised in Fig. 6.8, displaying the velocity, density and mass-loss rate of the steady-state wind structure. Considering the first stage of the series, the agreement between the MCRH results, the wind structure determined in the radiation hydrodynamical simulation with the CAK line-driving force and the analytic predictions of the CAK theory is excellent. In particular, the good match between the MCRH calculation and the analytic CAK solution demonstrates that our approach is able to accurately determine the structure of line-driven hot-star winds.

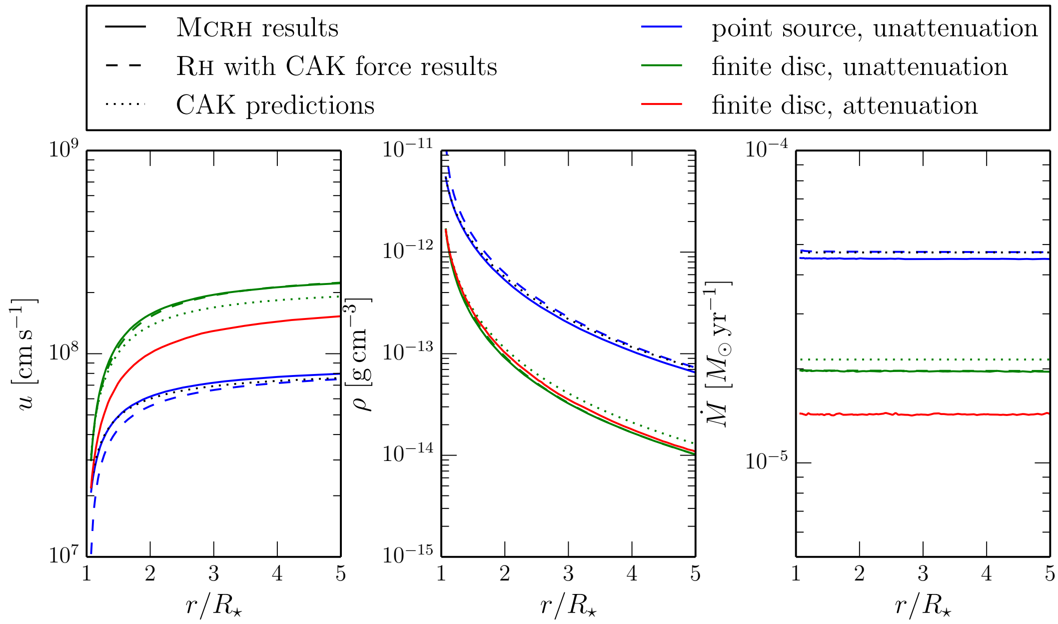

Figure 6.8.: Results of a series of MCRH simulations to determine the wind structure with an increasing level of physical detail. The resulting wind structure is shown in terms of the determined steady-state velocity (left panel), density (central panel) and mass-loss rate (right panel) for the MCRH calculations (solid lines). As a comparison, the results of radiation hydrodynamical simulations, in which the Monte Carlo scheme is replaced by a CAK power-law determination of the line-driving force, are shown (dashed lines). The results of the first stage, in which the central star is assumed to be a point source, are displayed in blue. The second stage, in which the finite extent of the stellar disc is taken into account, is colour-coded in green. The results of the most sophisticated calculation, in which also the attenuation of the radiation field is considered, is shown in red. Where possible, we confront the simulation results with the predictions of the CAK theory (dotted lines). In the second stage of the simulation series, the predictions are based on the formulation by Kudritzki et al. (1989).

Also the second stage of the series exhibits good agreement between the results of the two variants of the radiation hydrodynamical calculations, relying on the Monte Carlo scheme and the CAK power-law expression of Eq. (6.33) to determine the line-driving force. Compared to the point-source calculations, the wind outflow emerges with roughly twice the velocity, but carrying a lower mass flux. These wind features are characteristic for the inclusion of the finite-disc effect and have been observed in previous numerical and analytic studies (e.g. Friend & Abbott, 1986; Pauldrach et al., 1986; Kudritzki et al., 1989). To better quantify this statement, and due to the difficulties in predicting the wind structure once the point-source approximation is abandoned, we compare our results with the solution technique developed by Kudritzki et al. (1989). Our MCRH results agree reasonably well with this predicted wind structure, but appreciable deviations are present. The exact nature of these discrepancies is not fully resolved but it may be connected with the assumptions adopted by Kudritzki et al. (1989) to formulate the solution. Another possible source may lie in the reliance on the fixed density values at the lower boundary. Since this density profile slightly deviates from the true solution, the MCRH calculations may solve the wind structure arising from a slightly different star than originally set up (i.e. slight changes in the stellar mass, luminosity, effective temperature or the Eddington factor). Nevertheless, the small scale of the discrepancies between the different results of the second stage of the simulation series, in particular of the two radiation hydrodynamical calculations, emphasises the utility and accuracy of MCRH in more complex stellar wind calculations.

The assumption of an unattenuated radiation field, on which the derivation of the CAK line-driving force relies, is only an approximate representation of the physical reality. Interactions of the radiation field with the ambient material in the inner parts of the wind alter the spectral energy distribution of the radiation field which then contributes differently to the accelerating force in regions of the wind that lie further out. We account for this attenuation effect in the final stage of the simulation series and reach with these calculations beyond the capabilities of the CAK theory. Moreover, since packets now change their propagation direction in line-interactions, the multiple-scattering effect is fully incorporated. The result of this MCRH calculation is also shown in Fig. 6.8. Compared to the results of the previous stage, the wind velocity decreases slightly. Two effects, which counteract each other, are important. Since packets are allowed to back-scatter into the photosphere, a number of packet trajectories are significantly shorter than in the unattenuated case. Thus, a lower radiation force derives from these packets. In contrast to that, the length of some packet trajectories may be drastically increased due to multiple-scattering interactions, leading to a stronger radiative acceleration associated with these propagation paths. As detailed below (see Fig. 6.10), a large fraction of the escaping packets actually experience multiple-scattering events. The two mechanisms, back-scattering and multiple scattering, which seem to nearly cancel in our simulation, are closely intertwined and may not be clearly separated as one may think from the above presentation. Packets which undergo many scattering interactions may eventually still reach the photosphere.

6.3.5. Additional Diagnostics

The series of simulations presented above vividly demonstrates that MCRH is able to accurately solve the structure of line-driven outflows. With the inclusion of the attenuation of the radiation field, the results of the last calculation in this series highlight the capability of MCRH to treat complex interaction processes, which are beyond the scope of analytic descriptions. The utility of the MCRH approach to line-driven outflows is further emphasised by its diagnostic power. In the following, some of these diagnostics possibilities are outlined, always at the example of the last calculation of the simulation series presented above.

Since the details of the interactions Monte Carlo packets experience can be easily recorded, the nature of the line-driving force may be closely investigated. Figure 6.9 shows the importance of the different ions present in the wind for forming the line-driving force. The same figure also illustrates how this "composition" of the line-driving force varies within the wind outflow. It is striking how the line-driving force is dominated by the contribution of the iron ions with their many line transitions. However, the importance of this element for the line-driving force seems to be most dominant in the lower parts of the wind. With increasing distance from the central star,

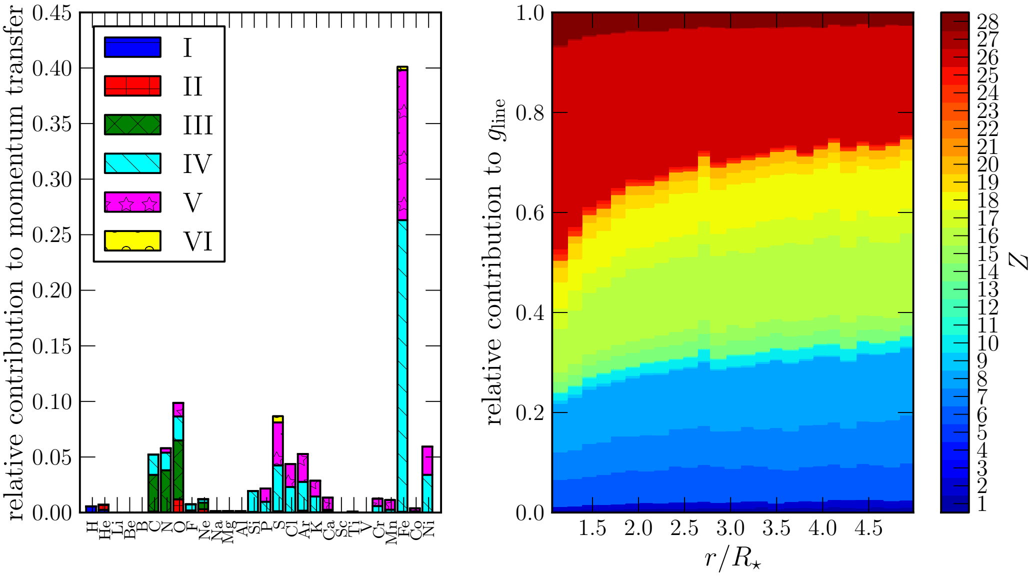

Figure 6.9.: Composition of the line driving force: the left panel illustrates the extent to which each ion contributes to the average line-driving force in the wind. The importance of iron, the CNO group and some intermediate mass elements is clearly visible. The "composition" of the line-driving force seems, however, to depend on the location in the wind as indicated by the right panel. Here, the contributions to the line-driving force exerted by the ions of one element are colour-coded and plotted as a function of the location in the wind. Ten grid cells have been grouped together to form one data point.

other elements grow in significance. This is most likely a consequence of the attenuation of the radiation field and of the scattering of packets back into the photosphere. From these changes in the composition of the line-driving force we may conclude that the iron elements are crucial for setting the mass-loss rate of the wind, which is determined in the subsonic region close to the photosphere (see, for example, Vink et al., 1999). The intermediate mass elements seem to be more important for establishing a particular terminal wind speed, since this process occurs in the supersonic part of the wind (e.g. Vink et al., 1999). This interpretation is compatible with the findings of Vink et al. (1999), who attribute the increasing mass-loss rate around the bi-stability jump (see, for example, Puls et al., 2008, and references therein) to a stronger line-driving force due to iron in the subsonic region of the wind.

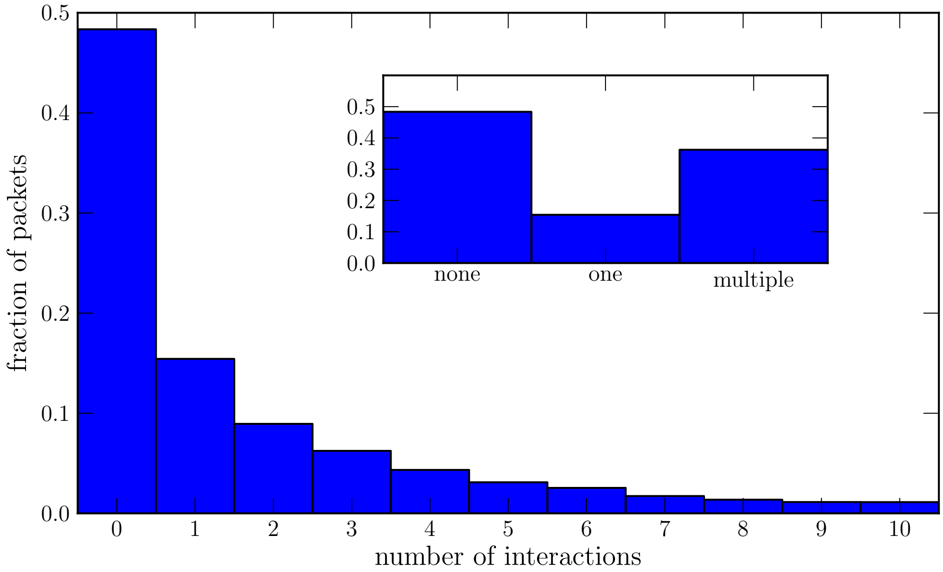

Figure 6.10.: Number of interactions the escaping Monte Carlo packets experienced. Almost half of all escaping packets never interacted. The majority of the remaining packets, however, interacted multiple times, as illustrated by the histogram in the inlay.

Figure 6.10 demonstrates the capability of our approach to follow multiple scattering events. The histogram reveals that for the particular wind conditions considered here, roughly half of all escaping packets never undergo an explicit interaction event. However, the majority of packets that interact do this multiple times, stressing once more the importance of following and handling these multiple scattering events. The Monte Carlo approach is well capable of tracking these complex propagation histories and of taking the competing effect of back-scattered radiation into account as well. These benefits of the Monte Carlo scheme will be particularly relevant for future studies of dense winds, for example in Wolf-Rayet stars. Previous studies, such as Lucy

& Abbott (1993) and Sim (2004), suggest that multiple scattering has a significant effect on the structure of these outflows.

As an advantageous byproduct, our MCRH simulations also provide the means to determine the spectrum of the radiation field emergent from the wind material. Figure 6.11 shows the wavelength distribution of the radiation field emitted by the wind in the window of interest between $\lambda_{\mathrm{min}} = 228\,\mathrm{Å}$ and $\lambda_{\mathrm{max}} = 22\,800\,\mathrm{Å}$. Zoom-ins focus on a few prominent spectral features, for example the Lyman-α line ($\lambda = 1215.7\,\mathrm{Å}$), N V ($\lambda\lambda = 1238.8\,,1242.8\,\mathrm{Å}$) and C IV ($\lambda\lambda = 1548.2\,,1550.8\,\mathrm{Å}$) doublets and strong C III lines ($\lambda = 1247.4\,\mathrm{Å}$, $\lambda = 2296.0\,\mathrm{Å}$). The P-Cygni shape of the spectral lines, a characteristic feature for the presence of outflowing material, is clearly visible. To achieve the high spectral resolution necessary to investigate the line features, we restart the simulation with the steady-state wind condition and use 10^6 packets for one time step. We have ensured that the line-driving force determined with the larger number of packets is compatible with the low-resolution runs.

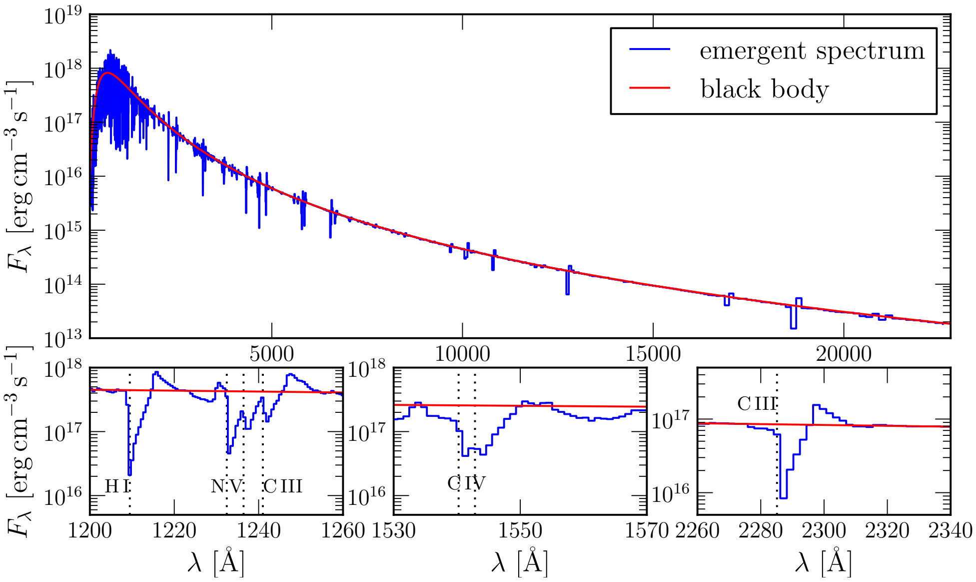

Figure 6.11.: Emergent spectrum of the stellar wind calculation with the attenuated radiation field. The upper panel shows the monochromatic flux emergent at the surface of the wind (at $r = 5\,R_\star$) as a function of wavelength. In particular in the short-wavelength region, many line features are present – some prominent lines are detailed in the panels below. Here, the rest frame wavelengths, Doppler-shifted via the terminal flow speed into the LF, are shown in dotted vertical lines to guide the eye. In all panels, the incident black-body flux is shown as the solid red line as a comparison.

The successful outcome of the hot-star wind simulation series performed with MCRH and the diagnostic power of our approach confirm its utility for the study of line-driven outflows. In the future, we intend to use our method to investigate various hot-star wind phenomena, for example revisit the bi-stability jump (Vink et al., 1999). Eventually, we aim at generalising our approach to multidimensional geometries, which will allow us to study radiatively-launched outflows from accretion discs. In such multidimensional simulations, our Monte Carlo-based approach will unfold its full potential.

7. Conclusions

7.1. Summary

In this work we have introduced a new approach to numerically solve radiation hydrodynamical problems in astrophysics. The key feature of this technique is the reliance on a time-dependent Monte Carlo radiative transfer simulation (see Section 3.4). The energy and momentum transfer terms determined in this step are coupled to a finite-volume fluid dynamical calculation (see Section 3.3), which is based on the piecewise parabolic method of Colella & Woodward (1984), using a simple Godunov-splitting algorithm (see Section 3.2). The main motivation for constructing such a radiation hydrodynamical scheme lies in the advantages presented by the Monte Carlo approach. Namely, the applicability to arbitrary geometrical configurations and the capability of treating complex interaction physics, in particular scattering processes, render this technique very attractive for astrophysical investigations. We have invested significant effort into mitigating the major drawbacks of Monte Carlo approaches, namely the introduction of stochastic fluctuations and the high computational effort. Two concepts are particularly important: the indivisible energy packet formalism of Abbott & Lucy (1985); Lucy (1999a, see Section 3.4.3) and the volume-based estimator concept of Lucy (1999a, see Section 3.4.5). The former facilitates the realisation of strict energy conservation and avoids an inflation of the number of Monte Carlo packets in the simulations in cases with non-resonant interactions. With the estimator strategy, the sample size in the counting experiments used to reconstruct the radiation field characteristics is maximised and thus the level of stochastic noise minimised (see particularly Figs. 4.10 and 4.16). Adopting the ideas of Lucy (1999a, 2003, 2005), a powerful estimator formalism was devised to reconstruct the moments of the specific intensity and the radiation force components from the ensemble of packet trajectories (see Section 3.4.5). Our scheme also includes the possibility of performing the Monte Carlo radiative transfer step in accordance with the implicit techniques of Fleck & Cummings (1971, see Section 3.4.6). In this way, the restrictions on the duration of the simulation time step due to the characteristic time scales of the radiative source terms (i.e., the cooling time scale) are partially alleviated (see Section 4.3).

The scheme has been implemented into the numerical code Mcrh, which currently operates on plane-parallel or spherically symmetric one-dimensional geometric meshes (see implementation summary in Section 3.5.1). The physical accuracy of the scheme and its computational feasibility have been verified in a series of test calculations (see Chapter 4). These problems have been chosen to probe all aspects of the numerical scheme, ranging from the fluid dynamical step (see

Section 4.1) over the pure radiative transfer calculation (see Section 4.2) to the full coupling of the two subproblems (see Section 4.3). The successful outcome of all these test calculations demonstrates that our method accurately follows the coevolution of the radiation field and the ambient fluid state. These test calculations also highlight the benefits of using the volume-based reconstruction techniques for minimising the stochastic noise in the radiation field characteristics, particularly in the challenging optically thin regime (see Figs. 4.10 and 4.16). Moreover, the determination of the structure of radiative shocks demonstrates the utility of the implicit Monte Carlo scheme for radiation hydrodynamical calculations. With the explicit mode, the time step had to be reduced by a factor of ten compared to the CFL time step to obtain stable results. Relying instead on the implicit Monte Carlo capability allowed us to use the full duration of the time step according to the CFL criterion, while retaining the expected evolution of the gas and radiation temperature (see Section 4.3.3).

We applied our radiation hydrodynamical scheme to astrophysical problems in which either the energy or the momentum transfer between the radiation field and the ambient material is the dominating dynamical effect. For the energy-dominated case, we consider the Type Ia environment (see Chapter 5), in particular the interaction of the ejecta with circumstellar material (see Section 5.3). As a first example, we demonstrated the performance of MCRH under typical supernova ejecta conditions by investigating the radiative influence on the expansion of the material of Type Ia ejecta. With our radiation hydrodynamical calculations we were able to reproduce the findings of previous studies (Pinto & Eastman, 2000; Woosley et al., 2007), namely that the changes in the ejecta structure, which lie on the ten per cent level, do not affect the bolometric light curve significantly (see Section 5.2).

Our preliminary toy calculations of the interacting Type Ia supernova scenario revealed difficulties of the operator-splitting scheme in the stiff source term regime (see Section 5.3). Due to the high kinetic energy of the ejecta, the shock-heating rate at the ejecta-CSM interface was very high, inducing a ruinously short characteristic cooling time scale. Reducing the explicit time step has turned out to be unfeasible given the large discrepancy between the dynamical fluid time scale and the cooling time. Again, we emphasise that these challenges are not unique to our approach, but generally apply to explicit operator-splitting schemes that incorporate stiff source terms. We have explored the utility of the implicit Monte Carlo scheme and of the hybrid Godunov scheme of Miniati & Colella (2007, see Section 5.3.5) for improving the behaviour of MCRH in the stiff source term regime posed by the interaction problem. Given the preliminary character of these calculations, we consider their implications inconclusive. Further detailed exploration of these techniques is required and will be carried out in the future to assess their value for MCRH applications.

In contrast to the problems in the strongly energy-dominated case, applications with momentum transfer being the main dynamical effect are less problematic. As an example for such environments, we performed radiation hydrodynamical calculations of line-driven hot-star winds with MCRH (see Chapter 6). Our simulations, determining the steady-state wind structure with a variant of the Mcrh method, featuring a Sobolev-type frequency-dependent radiative transfer calculation (see Sections 6.1.2 and 6.2.3), demonstrated that our approach accurately accounts for the accelerating effect exerted by the interaction of the radiation field with a multitude of atomic line transitions (see Section 6.3). In particular the comparisons between the Mcrh results and the predictions of the CAK theory (Castor et al., 1975, see Section 6.1.3), which show very good agreement, highlight the accuracy and performance of our approach in stellar wind calculations (see Section 6.3.4). Even the Mcrh simulations with a detailed treatment of the interaction physics are in accordance with expectations and demonstrate the capacity of our approach to go beyond the capabilities of CAK-based calculations. The utility of our method for studies of line-driven outflows is further underlined by the diagnostic power it offers, including the calculation of emergent spectra, packet interaction histories and the investigation of the line-driving force composition (see Section 6.3.5).

7.2. Outlook

The main focus of this work was to establish the feasibility, accuracy and applicability of our Monte Carlo radiation hydrodynamical method. As a consequence, we chose idealised and simplified treatments of physical reality in our astrophysical calculations. These choices facilitated the assessment of the utility of our approach for radiation hydrodynamical problems in different astrophysical environments. In the future, we intend to use our approach to perform more realistic investigations of astrophysical radiation hydrodynamical phenomena.

The current implementation of the method may, for example, be used to refine the study of the expansion of Type Ia supernova ejecta presented in this work (see Section 5.2). Relying on the frequency-dependent transfer scheme, which for now has been exclusively used for the stellar wind application, colour light curves and spectra may be determined and the influence of the radiation hydrodynamical coupling on these observables established. This is relevant, since the spectral line features may shift due to velocity changes induced by the effect of the radiation field. The findings of a previous study (Woosley et al., 2007) were partly obscured by differences in the radiative transfer methods used to determine the decoupled and the coupled results. Our approach provides the advantage of relying on the same method and the same radiation–matter interaction description in both cases.

In addition to the supernova study, a variety of stellar wind phenomena may already be investigated with the current one-dimensional, Sobolev-type implementation of Mcrh. Here, we are particularly interested in studying the so-called *bi-stability jump* (see, for example Vink et al., 1999). This effect describes a sudden increase in the mass-loss rate of stellar winds with decreasing effective temperature of the central star. In the important study by Vink et al. (1999), the cause for this change in the mass-loss rate and in the line-driving force was found in changes of the ionisation conditions in the wind. Due to the decrease in effective temperature, iron ions recombine from Fe IV to Fe III. This recombination is accompanied by an increase in the line-driving force in the subsonic region associated with iron. Compared to the original study by Vink et al. (1999), our approach offers the possibility of investigating this phenomenon without invoking a fixed velocity law with a predefined terminal wind speed. These investigations will contribute to consolidating the ionisation/recombination picture as the theoretical explanation for the bi-stability jump.

In addition to astrophysical studies that may already be carried out with the current version of Mcrh, we intend to significantly invest into improving the method. As a start, this includes a thorough exploration of the implicit Monte Carlo method and the inclusion of the source term S (see discussion in Sections 3.4.6 and 5.3.4). For this task, the steady radiative shock tests presented by Roth & Kasen (2014) seem to provide the ideal testbed. Since semi-analytic predictions for the shock structure exist (Lowrie & Edwards, 2008), the accuracy and the performance of the implicit Monte Carlo implementation may be investigated for strong shocks, in which the characteristic radiative time scales are shorter than the fluid flow timescale. Related to this, we aim to perform a detailed investigation of the feasibility of interfacing the hybrid Godunov scheme with our Mcrh approach. These two steps will allow us to firmly assess the applicability of the Mcrh technique to problems in which the radiative sources are stiff, such as the interacting supernova scenario. Here, the intended reference calculations with the radiation hydrodynamical code Stella (Blinnikov & Bartunov, 1993; Blinnikov & Sorokina, 2000) will help in forming a clear picture of the expected physical conditions and processes in the ejecta–CSM interaction region.

Monte Carlo methods typically suffer from computational inefficiency in regions with high optical depths. Since the physical radiation–matter interactions have to be tracked explicitly, a high computational effort has to be invested in solving radiative transfer in this regime. This property limits, to a certain extent, a general applicability of Monte Carlo-based techniques. However, special algorithms, such as DDMC (Gentile, 2001, see also Section 3.4.6), have been developed to treat radiative transfer in optically thick regions also with Monte Carlo methods. In the future, we aim to investigate the possibility of interfacing our Mcrh approach with the DDMC technique to achieve a hybrid Monte Carlo scheme (similar to Abdikamalov et al., 2012; Wollaeger et al., 2013), that switches from explicit/implicit Monte Carlo to DDMC in optically thick regions.

The full potential of Monte Carlo radiative transfer techniques truly unfolds in multidimensional calculations. Since detailed studies of radiation hydrodynamical phenomena in astrophysics often require a multidimensional treatment, an important future goal of the Mcrh development constitutes this transition. We plan to generalise our approach from relying on one-dimensional computational grids to being applicable to multidimensional geometries. This step will enable us to investigate complex radiation hydrodynamical flows. In particular, we are interested in the radiatively-driven mass outflows from accretion discs and in performing studies similar to Proga & Kallman (2004), but with a higher level of physical sophistication in the description of the radiation field. Additionally, we will consider the development of a non-Sobolev treatment of the frequency-dependent radiation–matter interactions (potentially similar to the schemes presented by Knigge et al. 1995 and Kusterer et al. 2014). This step would allow us to perform multidimensional investigations of clumpy stellar winds, studying the temporal and spatial flow irregularities.

With these intended extensions and improvements – specifically the handling of multidimensional geometries, the interfacing with a special technique for optically thick regimes and an improved treatment of the stiff source terms – the MCRH method has the potential of becoming a general multi-purpose approach. Here, the rapid increase in the availability of computational resources over the last few decades (and its expected continuation) should be kept in mind. The main limitation of Monte Carlo techniques is not of a conceptual nature, but due to the available computational power. In the light of these developments, our Monte Carlo-based radiation hydrodynamical approach has a good prospect of proving its utility for a variety of different astrophysical radiation hydrodynamics problems and of contributing to an increased understanding of complex systems such as supernovae, stellar winds, accretion disc outflows and potentially also radiative feedback in star-formation[1].

---

[1] Haworth & Harries (2012) and Harries et al. (2014) present successful applications of Monte Carlo-based radiation hydrodynamical approaches to the star formation environment.

A. Frame Transformations

The following listing summarises the most important transformation laws to relate properties of the radiation field defined in the two important reference frames for the theory of radiative transfer [see Section 2.3.4 for an in-depth presentation]. On the left hand side, the CMF quantities are expressed in terms of their counterparts in the LF. The right hand side contains the corresponding inverse transformation. Note that all these transformation laws are formulated for one-dimensional geometries, and that the explicit dependence of the quantities on frequency, propagation direction, location and time have been omitted to simplify the notation.

$$\begin{aligned} \nu_0 &= \gamma(1-\beta\mu)\nu & \nu &= \gamma(1+\beta\mu_0)\nu_0 \\ &= \left(\frac{\nu_0}{\nu}\right)\nu & &= \left(\frac{\nu}{\nu_0}\right)\nu_0 \end{aligned} \tag{A.1}$$

$$\begin{aligned} \mu_0 &= \frac{\mu-\beta}{1-\beta\mu} & \mu &= \frac{\mu_0+\beta}{1+\beta\mu_0} \\ &= \gamma\left(\frac{\nu}{\nu_0}\right)(\mu-\beta) & &= \left(\frac{\nu_0}{\nu}\right)(\mu_0+\beta) \end{aligned} \tag{A.2}$$

$$\mathrm{d}\nu_0 = \left(\frac{\nu_0}{\nu}\right)\mathrm{d}\nu \qquad \mathrm{d}\nu = \left(\frac{\nu}{\nu_0}\right)\mathrm{d}\nu_0 \tag{A.3}$$

$$\mathrm{d}\mu_0 = \left(\frac{\nu}{\nu_0}\right)^2\mathrm{d}\mu \qquad \mathrm{d}\mu = \left(\frac{\nu_0}{\nu}\right)^2\mathrm{d}\mu_0 \tag{A.4}$$

$$\chi_0 = \left(\frac{\nu}{\nu_0}\right)\chi \qquad \chi = \left(\frac{\nu_0}{\nu}\right)\chi_0 \tag{A.5}$$

$$\eta_0 = \left(\frac{\nu_0}{\nu}\right)^2\eta \qquad \eta = \left(\frac{\nu}{\nu_0}\right)^2\eta_0 \tag{A.6}$$

$$I_0 = \left(\frac{\nu_0}{\nu}\right)^3 I \qquad I = \left(\frac{\nu}{\nu_0}\right)^3 I_0 \tag{A.7}$$

$$J_0 = \gamma^2(J - 2\beta H + \beta^2 K) \qquad J = \gamma^2(J_0 + 2\beta H_0 + \beta^2 K_0) \tag{A.8}$$

$$H_0 = \gamma^2[H(1+\beta^2) - \beta(J+K)] \qquad H = \gamma^2[H(1+\beta^2) + \beta(J_0+K_0)] \tag{A.9}$$

$$K_0 = \gamma^2(K - 2\beta H + \beta^2 J) \qquad K = \gamma^2(K_0 + 2\beta H_0 + \beta^2 J_0) \tag{A.10}$$

B. Radiation Hydrodynamics in One Dimension

We briefly present the simplified version of the radiation hydrodynamical equations suitable to address one-dimensional geometries. These equations are the foundation of the current, one-dimensional implementation of our numerical method Mcrh. If the problem features plane-parallel symmetry, the equations reduce to

$$p = \frac{1}{\gamma - 1}\left(e - \frac{1}{2}u^2\right), \tag{B.1}$$

$$\frac{\mathrm{D}}{\mathrm{D}t}\rho + \rho\frac{\partial}{\partial x}u = 0, \tag{B.2}$$

$$\rho\frac{\mathrm{D}}{\mathrm{D}t}u + \frac{\partial}{\partial x}p = f + G^1, \tag{B.3}$$

$$\rho\frac{\mathrm{D}}{\mathrm{D}t}e + \frac{\partial}{\partial x}(up) = uf + cG^0, \tag{B.4}$$

$$\left(\frac{1}{c}\frac{\partial}{\partial t} + \mu\frac{\partial}{\partial x}\right) I = \xi - \chi I, \tag{B.5}$$

$$G^0 = \frac{2\pi}{c}\int_0^\infty \mathrm{d}\nu \int_{-1}^{1} \mathrm{d}\mu(\chi I - \xi), \tag{B.6}$$

$$G^1 = \frac{2\pi}{c}\int_0^\infty \mathrm{d}\nu \int_{-1}^{1} \mathrm{d}\mu(\chi I - \xi)\mu. \tag{B.7}$$

with the substantial derivative given by

$$\frac{\mathrm{D}}{\mathrm{D}t} = \frac{\partial}{\partial t} + u\frac{\partial}{\partial x}. \tag{B.8}$$

For spherically symmetric applications, the radiation hydrodynamical equations take the following form:

$$p = \frac{1}{\gamma - 1}\left(e - \frac{1}{2}u^2\right), \tag{B.9}$$

$$\frac{\mathrm{D}}{\mathrm{D}t}\rho + \rho\frac{1}{r^2}\frac{\partial}{\partial r}(r^2 u) = 0, \tag{B.10}$$

$$\rho\frac{\mathrm{D}}{\mathrm{D}t}u + \frac{\partial}{\partial r}p = f + G^1, \tag{B.11}$$

$$\rho\frac{\mathrm{D}}{\mathrm{D}t}e + \frac{1}{r^2}\frac{\partial}{\partial r}(r^2 up) = uf + cG^0, \tag{B.12}$$

$$\left(\frac{1}{c}\frac{\partial}{\partial t} + \mu\frac{\partial}{\partial r}\right)I = \xi - \chi I, \tag{B.13}$$

$$G^0 = \frac{2\pi}{c}\int_0^\infty \mathrm{d}\nu \int_{-1}^1 \mathrm{d}\mu(\chi I - \xi), \tag{B.14}$$

$$G^1 = \frac{2\pi}{c}\int_0^\infty \mathrm{d}\nu \int_{-1}^1 \mathrm{d}\mu(\chi I - \xi)\mu. \tag{B.15}$$

Again, the pseudo-Lagrangian notation has been used in the fluid dynamical part with the substantial derivative

$$\frac{\mathrm{D}}{\mathrm{D}t} = \frac{\partial}{\partial t} + u\frac{\partial}{\partial r}. \tag{B.16}$$

It is worth noting that the plane-parallel equations, and the ones defined in a spherically symmetric coordinate system, formally only differ in the hydrodynamical flux terms, which in the latter case include geometrical form factors. Consequently, the same solution techniques may be employed in both cases.

C. Corrections to the Original PPM Publication

Unfortunately the original publication (Colella & Woodward, 1984) describing the piecewise parabolic method, PPM, contains a number of typos. These hamper a direct implementation of the method. In the following a (possibly incomplete) list of these typos and errors are given, which have been spotted and thus been accounted for in the PPM implementation of Mcrh.

- Index error on the first line of Equation (1.8). It should read instead:

$$\delta_m a_j = \min(|\delta a_j|, 2|a_j^n - a_{j-1}^n|, 2|a_{j+1}^n - a_j^n|)\mathrm{sgn}(\delta a_j) \tag{C.1}$$

- On the bottom section of Page 178 the determination of left and right values is mixed-up. $a_{L,j}$ and $a_{R,j}$ represent the left and right ends of the parabolic reconstruction in the cell j. Thus, $a_{j+1/2}$, which is the value at the interface between cell j and $j+1$, will be assigned to $a_{L,j+1}$ and $a_{R,j}$ (and **not** to $a_{L,j}$ and $a_{R,j-1}$ as written in the original paper).

- In Section 3, there is an asymmetry in the expression of $\beta^{\pm}_{j+1/2,S}$. The last addend should be the following to yield a symmetric result:

$$\beta^{\pm}_{j+1/2,S} = \cdots \pm \Delta t \left(\frac{\alpha u^{\pm}_{j+1/2,S}\, c^{\pm}_{j+1/2,S}}{r^{\pm}_{j+1/2,S}} - \pm g^{\pm}_{j+1/2,S} \right) \tag{C.2}$$

- In the appendix, the criterion to determine if a shock is present is wrong. Since flattening can only occur in zones where w_j is 1 (see Colella & Woodward, 1984, Equation A.6), criterion (A.1) has to detect all possible shock fronts, not only the ones propagating to the right. Thus, the criterion should read:

$$\begin{aligned} w_j &= 1 \qquad \text{if} \quad \frac{|p_{j-1} - p_{j+1}|}{\max(p_{j+1}, p_{j-1})} > \varepsilon \quad \text{and} \quad u_{j-1} - u_{j+1} > 0 \\ w_j &= 0 \qquad \text{else} \end{aligned} \tag{C.3}$$

- Some typos in the indices of the Eulerian dissipation scheme, in particular in (A.9) and (A.10). Instead they should read:

$$\tilde{\kappa}_j = \left| \frac{W_j^E - u_{j+2s_j} + s_j c_{j+2s_j}}{W_j^E} \right| \tag{C.4}$$

$$W_j^E = s_j \frac{W_j}{\rho_{j-2s_j}} u_{j-2s_j} \tag{C.5}$$

$$f_j = \max(\tilde{f}_j, \tilde{f}_{j+s_j}) \tag{C.6}$$

Bibliography

Abbott, D. C. 1982, ApJ, 259, 282

Abbott, D. C. & Lucy, L. B. 1985, ApJ, 288, 679

Abdikamalov, E., Burrows, A., Ott, C. D., et al. 2012, ApJ, 755, 111, [arXiv:1203.2915]

Acreman, D. M., Harries, T. J., & Rundle, D. A. 2010, MNRAS, 403, 1143, [arXiv:0912.2030]

Ambwani, K. & Sutherland, P. 1988, ApJ, 325, 820

Ames, W. 1992, Numerical Methods for Partial Differential Equations (Academic Press)

Arnett, W. D. 1982, ApJ, 253, 785

Asplund, M., Grevesse, N., Sauval, A. J., & Scott, P. 2009, ARA&A, 47, 481, [arXiv:0909.0948]

Audi, G., Bersillon, O., Blachot, J., & Wapstra, A. H. 2003, Nuclear Physics A, 729, 3

Auer, L. H. 1968, ApJ, 153, 783

Avery, L. W. & House, L. L. 1968, ApJ, 152, 493

Balbus, S. A. & Hawley, J. F. 1991, ApJ, 376, 214

Balsara, D. S. 1994, ApJ, 420, 197

Bateman, H. 1910, Proc. Cambridge Philos. Soc., vol. 15, 423

Batten, P., Clarke, N., Lambert, C., & Causon, D. 1997, SIAM Journal on Scientific Computing, 18, 1553

Benetti, S., Cappellaro, E., Mazzali, P. A., et al. 2005, ApJ, 623, 1011, [arXiv:astro-ph/0411059]

Blinnikov, S., Lundqvist, P., Bartunov, O., Nomoto, K., & Iwamoto, K. 2000, ApJ, 532, 1132, [arXiv:astro-ph/9911205]

Blinnikov, S. I. & Bartunov, O. S. 1993, A&A, 273, 106

Blinnikov, S. I. & Sorokina, E. I. 2000, A&A, 356, L30, [arXiv:astro-ph/0003247]

Blinnikov, S. I. & Sorokina, E. I. 2010, ArXiv e-prints, [arXiv:1009.4353]

Bloom, J. S., Kasen, D., Shen, K. J., et al. 2012, ApJ, 744, L17, [arXiv:1111.0966]

Bodenheimer, P., Laughlin, G. P., Rózyczka, M., & Yorke, H. W. 2007, Numerical Methods in Astrophysics: An Introduction, ed. P. Bodenheimer, G. P. Laughlin, M. Rózyczka, & H. W. Yorke (Boca Raton, FL: Taylor and Francis Group)

Book, D. 1994, Shock Waves, 4, 1

Branch, D. 2006, Nature, 443, 283

Branch, D., Dang, L. C., Hall, N., et al. 2006, PASP, 118, 560, [arXiv:astro-ph/0601048]

Brown, P. J., Dawson, K. S., de Pasquale, M., et al. 2012, ApJ, 753, 22, [arXiv:1110.2538]

Bryan, G. L., Norman, M. L., O'Shea, B. W., et al. 2014, ApJS, 211, 19, [arXiv:1307.2265]

Buchler, J. R., Kolláth, Z., & Marom, A. 1997, Ap&SS, 253, 139, [arXiv:astro-ph/9707145]

Cannon, C. J. 1973, ApJ, 185, 621

Canuto, C. 1988, Spectral Methods in Fluid Dynamics, Springer series in computational physics (Springer-Verlag)

Caroff, L. J., Noerdlinger, P. D., & Scargle, J. D. 1972, ApJ, 176, 439

Cassinelli, J. P. 1979, ARA&A, 17, 275

Castor, J. I. 1972, ApJ, 178, 779

Castor, J. I. 2007, Radiation Hydrodynamics (Cambridge, UK: Cambridge University Press)

Castor, J. I., Abbott, D. C., & Klein, R. I. 1975, ApJ, 195, 157

Chandrasekhar, S. 1931, ApJ, 74, 81

Chandrasekhar, S. 1960, Radiative Transfer (New York: Dover)

Chugai, N. N. 1992, Soviet Ast., 36, 63

Chugai, N. N., Blinnikov, S. I., Cumming, R. J., et al. 2004a, MNRAS, 352, 1213, [arXiv:astro-ph/0405369]

Chugai, N. N., Chevalier, R. A., & Lundqvist, P. 2004b, MNRAS, 355, 627, [arXiv:astro-ph/0408508]

Ciotti, L., D'Ercole, A., Pellegrini, S., & Renzini, A. 1991, ApJ, 376, 380

Clarke, C. & Carswell, B. 2007, Principles of Astrophysical Fluid Dynamics (Cambridge, UK: Cambridge University Press)

Cleveland, M. A., Gentile, N. A., & Palmer, T. S. 2010, Journal of Computational Physics, 229, 5707

Colella, P. & Sekora, M. D. 2008, Journal of Computational Physics, 227, 7069

Colella, P. & Woodward, P. R. 1984, Journal of Computational Physics, 54, 174

Colgate, S. A. & McKee, C. 1969, ApJ, 157, 623

Courant, R., Friedrichs, K. O., & Lewy, H. 1928, Math. Ann., 100, 32

Cox, A. N. 2000, Allen's Astrophysical Quantities, 4th edn., ed. A. N. Cox (New York, AIP Press)

Cumming, R. J., Lundqvist, P., Smith, L. J., Pettini, M., & King, D. L. 1996, MNRAS, 283, 1355, [arXiv:astro-ph/9610020]

Davis, S. 1988, SIAM J. Sci. and Stat. Comput., 9, 445

Davis, S. W., Stone, J. M., & Jiang, Y.-F. 2012, ApJS, 199, 9, [arXiv:1201.2222]

Densmore, J. D., Thompson, K. G., & Urbatsch, T. J. 2012, Journal of Computational Physics, 231, 6924

Densmore, J. D., Urbatsch, T. J., Evans, T. M., & Buksas, M. W. 2007, Journal of Computational Physics, 222, 485

Dessart, L., Hillier, D. J., Blondin, S., & Khokhlov, A. 2014, MNRAS, 439, 3114, [arXiv:1310.7750]

Dilday, B., Howell, D. A., Cenko, S. B., et al. 2012, Science, 337, 942, [arXiv:1207.1306]

Drew, J. E. 1997, in Astronomical Society of the Pacific Conference Series, Vol. 121, IAU Colloq. 163: Accretion Phenomena and Related Outflows, ed. D. T. Wickramasinghe, G. V. Bicknell,

& L. Ferrario, 465

Dupree, S. A. & Fraley, S. K. 2002, A Monte Carlo Primer (New York: Kluwer Academic/Plenum Publishers)

Dutt, A., Greengard, L., & Rokhlin, V. 2000, BIT Numerical Mathematics, 40, 241

Edelmann, P. 2010, Master's thesis, Technische Universität München

Edelmann, P. 2014, Dissertation, Technische Universität München

Einfeldt, B. 1988, SIAM Journal on Numerical Analysis, 25, 294

Ensman, L. 1994, ApJ, 424, 275

Ensman, L. M. 1991, PhD thesis, California Univ., Santa Cruz.

Falk, S. W. & Arnett, W. D. 1977, ApJS, 33, 515

Feautrier, P. 1964, Comptes rendus hebdomadaires des seances de l'Academie des sciences, 258, 3189

Ferrara, A. & Tolstoy, E. 2000, MNRAS, 313, 291, [arXiv:astro-ph/9905280]

Filippenko, A. V. 1997, ARA&A, 35, 309

Fink, M., Hillebrandt, W., & Röpke, F. K. 2007, A&A, 476, 1133, [arXiv:0710.5486]

Fink, M., Röpke, F. K., Hillebrandt, W., et al. 2010, A&A, 514, A53, [arXiv:1002.2173]

Fleck, J. A. & Cummings, J. D. 1971, Journal of Computational Physics, 8, 313

Fornberg, B. 1988, Mathematics of Computation, 51, pp. 699

Friend, D. B. & Abbott, D. C. 1986, ApJ, 311, 701

Fryer, C. L., Ruiter, A. J., Belczynski, K., et al. 2010, ApJ, 725, 296, [arXiv:1007.0570]

Fryxell, B., Olson, K., Ricker, P., et al. 2000, ApJS, 131, 273

Fryxell, B. A., Müller, E., & Arnett, W. D. 1989, Hydrodynamics and nuclear burning, MPA Green Report 449, Max-Planck-Institut für Astrophysik, Garching

Gentile, N. A. 2001, Journal of Computational Physics, 172, 543

Gilfanov, M. & Bogdán, Á. 2010, Nature, 463, 924, [arXiv:1002.3359]

Gilks, W. R. & Wild, P. 1992, Journal of the Royal Statistical Society. Series C (Applied Statistics), 41, pp. 337

Gingold, R. A. & Monaghan, J. J. 1977, MNRAS, 181, 375

Gittings, M., Weaver, R., Clover, M., et al. 2008, Computational Science and Discovery, 1, 015005, [arXiv:0804.1394]

Godunov, S. K. 1959, Matematicheskii Sbornik, 47, 271

Goobar, A. & Leibundgut, B. 2011, Annual Review of Nuclear and Particle Science, 61, 251, [arXiv:1102.1431]

Grady, C. A., Snow, Jr., T. P., & Timothy, J. G. 1983, ApJ, 271, 691

Grassberg, E. K., Imshennik, V. S., & Nadyozhin, D. K. 1971, Ap&SS, 10, 28

Grassberg, E. K. & Nadezhin, D. K. 1976, Ap&SS, 44, 409

Grassberg, E. K. & Nadezhin, D. K. 1986, Soviet Astronomy Letters, 12, 68

Hachinger, S., Mazzali, P. A., Taubenberger, S., et al. 2012, MNRAS, 427, 2057, [arXiv:1209.1339]

Hamuy, M., Phillips, M. M., Suntzeff, N. B., et al. 2003, Nature, 424, 651, [arXiv:astro-ph/0306270]

Harries, T., Haworth, T., & Acreman, D. 2014, in Astrophysics and Space Science Proceedings, Vol. 36, The Labyrinth of Star Formation, ed. D. Stamatellos, S. Goodwin, & D. Ward-Thompson (Springer International Publishing), 395–399

Harries, T. J. 2000, MNRAS, 315, 722

Harries, T. J. 2011, MNRAS, 416, 1500, [arXiv:1105.5571]

Harten, A., Lax, P., & Leer, B. 1983, SIAM Review, 25, 35

Haworth, T. J. & Harries, T. J. 2012, MNRAS, 420, 562, [arXiv:1110.5266]

Hayek, W., Asplund, M., Carlsson, M., et al. 2010, A&A, 517, A49+

Hayes, J. C. & Norman, M. L. 2003, ApJS, 147, 197, [arXiv:astro-ph/0207260]

Hayes, J. C., Norman, M. L., Fiedler, R. A., et al. 2006, ApJS, 165, 188, [arXiv:astro-ph/0511545]

Heaslet, M. A. & Baldwin, B. S. 1963, Physics of Fluids, 6, 781

Heng, K. 2014, ArXiv e-prints, [arXiv:1404.6248]

Henry, R. B. C. & Branch, D. 1987, PASP, 99, 112

Hicken, M., Garnavich, P. M., Prieto, J. L., et al. 2007, ApJ, 669, L17, [arXiv:0709.1501]

Higginbottom, N., Knigge, C., Long, K. S., Sim, S. A., & Matthews, J. H. 2013, MNRAS, 436, 1390, [arXiv:1308.5973]

Hillebrandt, W., Kromer, M., Röpke, F. K., & Ruiter, A. J. 2013, Frontiers of Physics, 8, 116, [arXiv:1302.6420]

Hillebrandt, W. & Niemeyer, J. C. 2000, ARA&A, 38, 191, [arXiv:astro-ph/0006305]

Hirose, S., Krolik, J. H., & Blaes, O. 2009, ApJ, 691, 16, [arXiv:0809.1708]

House, L. L. & Avery, L. W. 1968, in Resonance Lines in Astrophysics, 133

Howell, D. A., Sullivan, M., Nugent, P. E., et al. 2006, Nature, 443, 308, [astro-ph/0609616]

Hoyle, F. & Fowler, W. A. 1960, ApJ, 132, 565

Hummer, D. G. & Rybicki, G. B. 1971, MNRAS, 152, 1

Iben, Jr., I., Nomoto, K., Tornambe, A., & Tutukov, A. V. 1987, ApJ, 317, 717

Iben, Jr., I. & Tutukov, A. V. 1984, ApJS, 54, 335

Iwamoto, K., Brachwitz, F., Nomoto, K., et al. 1999, ApJS, 125, 439, [arXiv:astro-ph/0002337]

Janka, H. & Mueller, E. 1996, A&A, 306, 167

Jiang, Y.-F., Davis, S. W., & Stone, J. M. 2013a, ApJ, 763, 102, [arXiv:1212.1742]

Jiang, Y.-F., Stone, J. M., & Davis, S. W. 2012, ApJS, 199, 14, [arXiv:1201.2223]

Jiang, Y.-F., Stone, J. M., & Davis, S. W. 2013b, ApJ, 778, 65, [arXiv:1309.5646]

Jiang, Y.-F., Stone, J. M., & Davis, S. W. 2014, ApJ, 784, 169, [arXiv:1402.2979]

Jordan, IV, G. C., Fisher, R. T., Townsley, D. M., et al. 2008, ApJ, 681, 1448, [arXiv:astro-ph/0703573]

Junde, H., Su, H., & Dong, Y. 2011, Nuclear Data Sheets, 112, 1513

Kalos, M. H. & Whitlock, P. A. 2008, Monte Carlo Methods: Second Revised and Enlarged Edition (Wiley-VCH Verlag)

Kamm, J. R. 2000, Evolution of the Sedov-von Neumann-Taylor Blast Wave Solution, Tech. rep., Integrated Physics Group, MS D413, Applied Physics Division, Los Alamos National Laboratory

Kamm, J. R. & Timmes, F. X. 2007, On Efficient Generation of Numerically Robust Sedov Solutions, Tech. Rep. 2849, Applied Physics Division, Los Alamos National Laboratory, Los Alamos

Kasen, D., Röpke, F. K., & Woosley, S. E. 2009, Nature, 460, 869, [arXiv:0907.0708]

Kasen, D., Thomas, R. C., & Nugent, P. 2006, ApJ, 651, 366, [arXiv:astro-ph/0606111]

Kasen, D., Woosley, S. E., & Heger, A. 2011, ApJ, 734, 102, [arXiv:1101.3336]

Kerzendorf, W. E. & Sim, S. A. 2014, MNRAS, 440, 387, [arXiv:1401.5469]

Kerzendorf, W. E., Yong, D., Schmidt, B. P., et al. 2013, ApJ, 774, 99, [arXiv:1210.2713]

Khokhlov, A. M. 1991, A&A, 245, 114

Kippenhahn, R., Weigert, A., & Weiss, A. 2013, Stellar Structure and Evolution (Springer-Verlag Berlin Heidelberg)

Kirshner, R. P., Oke, J. B., Penston, M. V., & Searle, L. 1973, ApJ, 185, 303

Klein, R. I. & Castor, J. I. 1978, ApJ, 220, 902

Knigge, C., Woods, J. A., & Drew, J. E. 1995, MNRAS, 273, 225

Kobayashi, C., Tsujimoto, T., Nomoto, K., Hachisu, I., & Kato, M. 1998, ApJ, 503, L155, [arXiv:astro-ph/9806335]

Korobeilnikov, V., Mel'nikova, N., & Ryazanov, Y. 1961, Teoriya Tochechnogo Vzryva (Leningrad: FizMatLit), transl.: The theory of point explosion, JPRS 14, 334, U.S. Dept. of Commerce, Washington, DC, 1962

Kromer, M., Fink, M., Stanishev, V., et al. 2013, MNRAS, 429, 2287, [arXiv:1210.5243]

Kromer, M. & Sim, S. A. 2009, MNRAS, 398, 1809, [arXiv:0906.3152]

Krumholz, M. R., Klein, R. I., & McKee, C. F. 2007, ApJ, 656, 959, [arXiv:astro-ph/0609798]

Krumholz, M. R., Klein, R. I., McKee, C. F., Offner, S. S. R., & Cunningham, A. J. 2009, Science, 323, 754, [arXiv:0901.3157]

Kuchner, M. J., Kirshner, R. P., Pinto, P. A., & Leibundgut, B. 1994, ApJ, 426, L89

Kudritzki, R. P., Pauldrach, A., Puls, J., & Abbott, D. C. 1989, A&A, 219, 205

Kunasz, P. & Auer, L. H. 1988, Journal of Quantitative Spectroscopy and Radiative Transfer, 39, 67

Kurucz, R. L. 1979, ApJS, 40, 1

Kurucz, R. L. & Bell, B. 1995, Atomic Line List (Kurucz CD-ROM, Cambridge, MA: Smithsonian Astrophysical Observatory)

Kusterer, D.-J., Nagel, T., Hartmann, S., Werner, K., & Feldmeier, A. 2014, A&A, 561, A14

Lamers, H. J. G. L. M. & Cassinelli, J. P. 1999, Introduction to Stellar Winds (Cambridge, UK: Cambridge University Press)

Landau, L. D. & Lifshitz, E. M. 1959, Fluid Mechanics, ed. Landau, L. D. & Lifshitz, E. M. (Oxford: Pergamon Press)

Larsen, E. W. & Mercer, B. 1987, Journal of Computational Physics, 71, 50

Leibundgut, B. 2000, A&A Rev., 10, 179, [arXiv:astro-ph/0003326]

LeVeque, R. J. 2002, Finite-Volume Methods for Hyperbolic Problems (Cambridge, UK: Cambridge University Press)

Levermore, C. D. & Pomraning, G. C. 1981, ApJ, 248, 321

Li, W., Leaman, J., Chornock, R., et al. 2011, MNRAS, 412, 1441, [arXiv:1006.4612]

Long, K. S. & Knigge, C. 2002, ApJ, 579, 725, [arXiv:astro-ph/0208011]

Lowrie, R. & Edwards, J. 2008, Shock Waves, 18, 129

Lowrie, R. & Rauenzahn, R. 2007, Shock Waves, 16, 445

Lucy, L. B. 1977, AJ, 82, 1013

Lucy, L. B. 1983, ApJ, 274, 372

Lucy, L. B. 1999a, A&A, 344, 282

Lucy, L. B. 1999b, A&A, 345, 211

Lucy, L. B. 2003, A&A, 403, 261, [arXiv:astro-ph/0303202]

Lucy, L. B. 2005, A&A, 429, 19, [arXiv:astro-ph/0409249]

Lucy, L. B. & Abbott, D. C. 1993, ApJ, 405, 738

Lucy, L. B. & Solomon, P. M. 1970, ApJ, 159, 879

Lupie, O. L. & Nordsieck, K. H. 1987, AJ, 93, 214

Magnan, C. 1968, Astrophys. Lett., 2, 213

Markova, N., Puls, J., Scuderi, S., & Markov, H. 2005, A&A, 440, 1133, [arXiv:astro-ph/0505613]

Marshak, R. E. 1958, Physics of Fluids, 1, 24

Marti, J. M. A., Mueller, E., Font, J. A., Ibanez, J. M. A., & Marquina, A. 1997, ApJ, 479, 151

Matsumoto, M. & Nishimura, T. 1998, ACM Trans. Model. Comput. Simul., 8, 3

Matteucci, F. & Greggio, L. 1986, A&A, 154, 279

Mazzali, P. A. & Lucy, L. B. 1993, A&A, 279, 447

Mazzali, P. A. & Podsiadlowski, P. 2006, MNRAS, 369, L19, [arXiv:astro-ph/0604032]

McKee, C. F. & Ostriker, E. C. 2007, ARA&A, 45, 565, [arXiv:0707.3514]

Miczek, F. 2013, Dissertation, Technische Universität München

Mignone, A., Bodo, G., Massaglia, S., et al. 2007, ApJS, 170, 228, [arXiv:astro-ph/0701854]

Mihalas, D. 1978, Stellar Atmospheres, 2nd edn. (San Francisco: W. H. Freeman and Co)

Mihalas, D. 2001, J. Quant. Spec. Radiat. Transf., 71, 61

Mihalas, D., Auer, L. H., & Mihalas, B. R. 1978, ApJ, 220, 1001

Mihalas, D. & Mihalas, B. W. 1984, Foundations of Radiation Hydrodynamics (New York: Oxford University Press)

Miniati, F. & Colella, P. 2007, Journal of Computational Physics, 224, 519

Minion, M. L. 2003, Communications in Mathematical Sciences, 1, 471 – 500

Minkowski, R. 1941, PASP, 53, 224

Mohr, P. J., Taylor, B. N., & Newell, D. B. 2012, Reviews of Modern Physics, 84, 1527, [arXiv:1203.5425]

Monaghan, J. J. 1992, ARA&A, 30, 543

Muijres, L., Vink, J. S., de Koter, A., et al. 2012a, A&A, 546, A42, [arXiv:1209.5934]

Muijres, L. E., Vink, J. S., de Koter, A., Müller, P. E., & Langer, N. 2012b, A&A, 537, A37, [arXiv:1112.0944]

Müller, P. E. & Vink, J. S. 2008, A&A, 492, 493, [arXiv:0810.1901]

Mundt, R. & Ray, T. P. 1994, in Astronomical Society of the Pacific Conference Series, Vol. 62, The Nature and Evolutionary Status of Herbig Ae/Be Stars, ed. P. S. The, M. R. Perez, & E. P. J. van den Heuvel, 237

Nayakshin, S., Cha, S.-H., & Hobbs, A. 2009, MNRAS, 397, 1314, [arXiv:0905.2896]

Noebauer, U. M. 2011, Master's thesis, Technische Universität München

Noebauer, U. M., Long, K. S., Sim, S. A., & Knigge, C. 2010, ApJ, 719, 1932, [arXiv:1007.0209]

Noebauer, U. M., Sim, S. A., Kromer, M., Röpke, F. K., & Hillebrandt, W. 2012, MNRAS, 425, 1430, [arXiv:1206.6263]

Nomoto, K. 1982, ApJ, 253, 798

Nomoto, K., Thielemann, F., & Yokoi, K. 1984, ApJ, 286, 644

Nordlund, A. 1982, A&A, 107, 1

Nugent, P. E., Sullivan, M., Cenko, S. B., et al. 2011, Nature, 480, 344, [arXiv:1110.6201]

Och, S. R., Lucy, L. B., & Rosa, M. R. 1998, A&A, 336, 301

Olson, G. L. & Castor, J. I. 1981, ApJ, 244, 179

Olson, G. L. & Kunasz, P. 1987, Journal of Quantitative Spectroscopy and Radiative Transfer, 38, 325

Owocki, S. P., Castor, J. I., & Rybicki, G. B. 1988, ApJ, 335, 914

Pakmor, R., Kromer, M., Röpke, F. K., et al. 2010, Nature, 463, 61, [arXiv:0911.0926]

Pakmor, R., Kromer, M., Taubenberger, S., et al. 2012, ApJ, 747, L10, [arXiv:1201.5123]

Pankey, T. J. 1962, PhD thesis, Howard University

Parker, E. N. 1958, ApJ, 128, 664

Parkin, E. R. & Sim, S. A. 2013, ApJ, 767, 114, [arXiv:1302.6228]

Parrent, J., Friesen, B., & Parthasarathy, M. 2014, Astrophysics and Space Science, 1

Pauldrach, A., Puls, J., & Kudritzki, R. P. 1986, A&A, 164, 86

Perlmutter, S., Aldering, G., Goldhaber, G., et al. 1999, ApJ, 517, 565, [arXiv:astro-ph/9812133]

Phillips, M. M. 1993, ApJ, 413, L105

Pinto, P. A. & Eastman, R. G. 2000, ApJ, 530, 744

Piran, T. 1978, ApJ, 221, 652

Pomraning, G. 1979, Journal of Quantitative Spectroscopy and Radiative Transfer, 21, 249

Proga, D. & Kallman, T. R. 2004, ApJ, 616, 688, [arXiv:astro-ph/0408293]

Proga, D., Stone, J. M., & Drew, J. E. 1999, MNRAS, 310, 476, [arXiv:astro-ph/9907177]

Proga, D., Stone, J. M., & Kallman, T. R. 2000, ApJ, 543, 686, [arXiv:astro-ph/0005315]

Pskovskii, Y. P. 1984, Soviet Ast., 28, 658

Puls, J., Kudritzki, R.-P., Herrero, A., et al. 1996, A&A, 305, 171

Puls, J., Vink, J., & Najarro, F. 2008, The Astronomy and Astrophysics Review, 16, 209

Raizer, Y. P. 1957a, Zh. Eksp. Teor. Fiz., 32, 1528

Raizer, Y. P. 1957b, Soviet Physics JETP, 5, 1242

Riess, A. G., Filippenko, A. V., Challis, P., et al. 1998, AJ, 116, 1009, [arXiv:astro-ph/9805201]

Roe, P. 1981, Journal of Computational Physics, 43, 357

Röpke, F. K. 2005, A&A, 432, 969, [arXiv:astro-ph/0408296]

Röpke, F. K., Kromer, M., Seitenzahl, I. R., et al. 2012, ApJ, 750, L19, [arXiv:1203.4839]

Roth, N. & Kasen, D. 2014, ArXiv e-prints, [arXiv:1404.4652]

Rybicki, G. B. & Lightman, A. P. 1979, Radiative Processes in Astrophysics (New York: Wiley-Interscience)

Sagert, I., Bauer, W., Colbry, D., et al. 2014, Journal of Computational Physics, 266, 191

Schaefer, B. E. & Pagnotta, A. 2012, Nature, 481, 164

Schawinski, K., Justham, S., Wolf, C., et al. 2008, Science, 321, 223, [arXiv:0803.3596]

Schlegel, E. M. 1990, MNRAS, 244, 269

Sedov, L. 1946, Dokl Akad Nauk SSSR, 52, 17

Sedov, L. I. 1959, Similarity and Dimensional Methods in Mechanics (New York: Academic Press)

Sekora, M. D. & Stone, J. M. 2010, Journal of Computational Physics, 229, 6819, [arXiv:1005.4246]

Shakura, N. I. & Sunyaev, R. A. 1973, A&A, 24, 337

Shakura, N. I. & Sunyaev, R. A. 1976, MNRAS, 175, 613

Shapiro, S. L. & Teukolsky, S. A. 1983, Black Holes, White Dwarfs, and Neutron Stars: The Physics of Compact Objects (New York: Wiley-Interscience)

Silverman, J. M., Nugent, P. E., Gal-Yam, A., et al. 2013, ApJS, 207, 3, [arXiv:1304.0763]

Sim, S. A. 2004, MNRAS, 349, 899, [arXiv:astro-ph/0401149]

Sim, S. A. 2005, MNRAS, 356, 531, [arXiv:astro-ph/0410090]

Sim, S. A. 2007, MNRAS, 375, 154, [arXiv:astro-ph/0611677]

Sim, S. A., Long, K. S., Miller, L., & Turner, T. J. 2008, MNRAS, 388, 611, [arXiv:0805.2251]

Sim, S. A., Proga, D., Kurosawa, R., et al. 2012, MNRAS, 426, 2859, [arXiv:1207.7194]

Sim, S. A., Proga, D., Miller, L., Long, K. S., & Turner, T. J. 2010, MNRAS, 408, 1396, [arXiv:1006.3449]

Sincell, M. W., Gehmeyr, M., & Mihalas, D. 1999, Shock Waves, 9, 391

Smit, J. M., Cernohorsky, J., & Dullemond, C. P. 1997, A&A, 325, 203

Sobolev, V. V. 1960, Moving Envelopes of Stars (Cambridge, MA: Harvard University Press)

Sod, G. A. 1978, Journal of Computational Physics, 27, 1

Springel, V. 2010, MNRAS, 401, 791, [arXiv:0901.4107]

Springel, V., White, S. D. M., Jenkins, A., et al. 2005, Nature, 435, 629, [arXiv:astro-ph/0504097]

Springmann, U. 1994, A&A, 289, 505

Springmann, U. & Puls, J. 1998, in Astronomical Society of the Pacific Conference Series, Vol. 131, Properties of Hot Luminous Stars, ed. I. Howarth, 286

Stein, R. F. & Nordlund, A. 1998, ApJ, 499, 914

Stone, J. M., Gardiner, T. A., Teuben, P., Hawley, J. F., & Simon, J. B. 2008, ApJS, 178, 137, [arXiv:0804.0402]

Stone, J. M., Mihalas, D., & Norman, M. L. 1992, ApJS, 80, 819

Stone, J. M. & Norman, M. L. 1992, ApJS, 80, 753

Strang, G. 1968, SIAM Journal on Numerical Analysis, 5, pp. 506

Su, B. & Olson, G. L. 1996, Journal of Quantitative Spectroscopy and Radiative Transfer, 56, 337

Sumiyoshi, K. & Yamada, S. 2012, ApJS, 199, 17, [arXiv:1201.2244]

Sutherland, P. G. & Wheeler, J. C. 1984, ApJ, 280, 282

Swartz, D. A., Sutherland, P. G., & Harkness, R. P. 1995, ApJ, 446, 766, [arXiv:astro-ph/9501005]

Swesty, F. D. & Myra, E. S. 2009, ApJS, 181, 1

Taubenberger, S., Benetti, S., Childress, M., et al. 2011, MNRAS, 412, 2735, [arXiv:1011.5665]

Taubenberger, S., Kromer, M., Hachinger, S., et al. 2013, MNRAS, 432, 3117, [arXiv:1304.4952]

Taylor, G. 1941, Brit. Rept RC-210, reprinted in (1950) Proc Roy Soc A 186:159

Teyssier, R. 2002, A&A, 385, 337, [arXiv:astro-ph/0111367]

Thielemann, F., Nomoto, K., & Yokoi, K. 1986, A&A, 158, 17

Thomas, L. H. 1930, The Quarterly Journal of Mathematics, os-1, 239

Thomas, R. C., Nugent, P. E., & Meza, J. C. 2011, PASP, 123, 237

Timmes, F. X. & Arnett, D. 1999, ApJS, 125, 277

Toro, E. 2009, Riemann Solvers and Numerical Methods for Fluid Dynamics, 3rd edn. (Springer Berlin Heidelberg)

Toro, E., Spruce, M., & Speares, W. 1994, Shock Waves, 4, 25

Truran, J. W., Arnett, W. D., & Cameron, A. G. W. 1967, Canadian Journal of Physics, 45, 2315

Turner, N. J. & Stone, J. M. 2001, ApJS, 135, 95, [arXiv:astro-ph/0102145]

Utrobin, V. P. 2007, A&A, 461, 233, [arXiv:astro-ph/0609642]

van Marle, A. J. & Keppens, R. 2011, Computers & Fluids, 42, 44

Vink, J. S., de Koter, A., & Lamers, H. J. G. L. M. 1999, A&A, 350, 181, [arXiv:astro-ph/9908196]

Vink, J. S., de Koter, A., & Lamers, H. J. G. L. M. 2000, A&A, 362, 295, [arXiv:astro-ph/0008183]

Vogelsberger, M., Genel, S., Springel, V., et al. 2014, Nature, 509, 177, [arXiv:1405.1418]

Vögler, A., Shelyag, S., Schüssler, M., et al. 2005, A&A, 429, 335

von Neumann, J. 1941, NDRC Division B Rept AM-9, reprinted in (1963) Taub AH (ed) John von Neumann collected works. Pergamon, Oxford, pp 219-237

von Neumann, J. 1951, Applied Math Series, 12, 1

Wang, X., Filippenko, A. V., Ganeshalingam, M., et al. 2009, ApJ, 699, L139, [arXiv:0906.1616]

Weaver, T. A. 1976, ApJS, 32, 233

Webbink, R. F. 1984, ApJ, 277, 355

Weymann, R. J., Morris, S. L., Foltz, C. B., & Hewett, P. C. 1991, ApJ, 373, 23

Whelan, J. & Iben, Jr., I. 1973, ApJ, 186, 1007

Wollaeger, R. T., van Rossum, D. R., Graziani, C., et al. 2013, ApJS, 209, 36, [arXiv:1306.5700]

Wongwathanarat, A. 2014, private communication

Wongwathanarat, A., Hammer, N. J., & Müller, E. 2010, A&A, 514, A48, [arXiv:1003.1633]

Woodward, P. & Colella, P. 1984, Journal of Computational Physics, 54, 115

Woodward, P. R., Herwig, F., & Lin, P.-H. 2013, ArXiv e-prints, [arXiv:1307.3821]

Woosley, S. E., Kasen, D., Blinnikov, S., & Sorokina, E. 2007, ApJ, 662, 487, [arXiv:astro-ph/0609562]

Woosley, S. E. & Weaver, T. A. 1986, ARA&A, 24, 205

Yoon, S.-C. & Langer, N. 2005, A&A, 435, 967, [arXiv:astro-ph/0502133]

Zel'dovich, Y. B. 1957a, Zh. Eksp. Teor. Fiz., 32, 1126

Zel'dovich, Y. B. 1957b, Soviet Physics JETP, 5, 919

Zel'dovich, Y. B. & Raizer, Y. P. 1967, Physics of Shock Waves and High-Temperature Hydrodynamic Phenomena, ed. R. F. Hayes, W.D.; Probstein (New York: Academic Press)

Zwicky, F. 1938, ApJ, 88, 522

Acknowledgments

First and foremost, I am deeply indebted to Wolfgang Hillebrandt, my supervisor during the last three years. With his support and guidance but even more with his encouragement for developing and pursuing my own research ideas, he holds a significant stake in the formation of this work.

No less important were the countless discussions with Stuart Sim, who has been a firm guide during the capricious journey of harnessing the powers of Monte Carlo techniques in particular and of taming radiative transfer calculations in general. Moreover, his quick but careful assessments more than once revealed treacherous pitfalls in the paths that I've chosen. Markus Kromer and Fritz Roepke deserve equal gratitude: I benefited greatly from their expertise in Monte Carlo radiative transfer and hydrodynamical techniques and their intimate knowledge of supernova research.

My thanks also go out to the entire supernova/stellar hydrodynamics community at MPA. Countless discussions have increased my understanding of astrophysical fluid dynamics. Here, I would like to point out particularly the code comparison calculations done together with Hannes Grimm-Strele, which paved the way for identifying the (hopefully) last errors in our PPM implementation. Also, I would like to thank Philipp Edelmann for the advice he offered with respect to physical and numerical properties of various fluid dynamical methods. Moreover, his knowledge of the inner workings of the Linux operating system, his familiarity with a plethora of programming languages and software packages are unrivalled and more than once saved the day. Also Michael Klauser, who is developing the same aptitude for solving IT problems, repeatedly came to the rescue. During the supernova-related part of the project, Stefan Taubenberger, our living supernova encyclopedia, offered many helpful insights and evaluations.

Finally, my family, first and foremost my parents, deserve much gratitude. They provided me with all the support to embark on an academic career and their constant encouragement accompanied me through my university years and my PhD project. And you, my dearest Silvia: you gave me strength and endurance, comfort and encouragement to enjoy all the ups and master all the downs of the last years. Thank you so much!